University of Southern Queensland

School of Mechanical and Electrical Engineering

PHD DISSERTATION

Cooperative Systems Based Signal Processing Techniques with Applications to Three-Dimensional Video Transmission

Omar Hazim Salim

Student Number: 0061007275

2015

Certification of Dissertation

I certify that the ideas, designs and experimental work, results, analyses and conclusions set out in this dissertation are entirely my own effort, except where otherwise indicated and acknowledged.
I further certify that the work is original and has not been previously submitted for assessment in any other course or institution, except where specifically stated.

_____ / /
Omar Hazim Salim, Candidate

_____ / /
A/Prof. Wei Xiang, Principal supervisor

_____ / /
A/Prof. John Leis, Associate supervisor

_____ / /
A/Prof. Hani Mehrpouyan, Associate supervisor

_____ / /
Dr. Ali Arshad Nasir, Associate supervisor

Abstract

Three-dimensional (3-D) video has recently emerged to offer an immersive multimedia experience that can not be offered by two-dimensional (2-D) video applications. Currently, both industry and academia are focused on delivering 3-D video services to wireless communication systems. Modern video communication systems currently adopt cooperative communication and orthogonal frequency division multiplexing (OFDM) as they are an attractive solution to combat fading in wireless communication systems and achieve high data-rates. However, this strong motivation to transmit the video signals over wireless systems faces many challenges. These are mainly channel bandwidth limitations, variations of signal-to-noise ratio (SNR) in wireless channels, and the impairments in the physical layer such as time varying phase noise (PHN), and carrier frequency offset (CFO). In response to these challenges, this thesis seeks to develop efficient 3-D video transmission methods and signal processing algorithms that can overcome the effects of error-prone wireless channels and impairments in the physical layer.

In the first part of the thesis, an efficient unequal error protection (UEP) scheme, called video packet partitioning, and a new 3-D video transceiver structure are proposed. The proposed video transceiver uses switching operations between various UEP schemes based on the packet partitioning to achieve a trade-off between system complexity and performance. Experimental results show that the proposed system achieves significantly high video quality at different SNRs with the lowest possible bandwidth and system complexity compared to direct transmission schemes.

The second part of the thesis proposes a new approach to joint source-channel coding (JSCC) that simultaneously assigns source code rates, the number of high and low priority packets, and channel code rates for the application, network, and physical layers, respectively. The proposed JSCC algorithm takes into account the rate budget constraint and the available instantaneous SNR of the best relay selection in cooperative systems. Experimental results show that the proposed

JSCC algorithm outperforms existing algorithms in terms of peak signal-to-noise ratio (PSNR).

In the third part of the thesis, a computationally efficient training based approach for joint channel, CFO, and PHN estimation in OFDM systems is proposed. The proposed estimator is based on an expectation conditional maximization (ECM) algorithm. To compare the estimation accuracy of the proposed estimator, the hybrid Cramér-Rao lower bound (HCRB) of hybrid parameters of interest is derived. Next, to detect the signal in the presence of PHN, an iterative receiver based on the extended Kalman filter (EKF) for joint data detection and PHN mitigation is proposed. It is demonstrated by numerical simulations that, compared to existing algorithms, the performance of the proposed ECM-based estimator in terms of the mean square error (MSE) is closer to the derived HCRB and outperforms the existing estimation algorithms at moderate-to-high SNRs. Finally, this study extends the research on joint channel, PHN, and CFO estimation one step forward from OFDM systems to cooperative OFDM systems. An iterative algorithm based on the ECM in cooperative OFDM networks in the presence of unknown channel gains, PHNs and CFOs is applied. Moreover, the HCRB for the joint estimation problem in both decode-and-forward (DF) and amplify-and-forward (AF) relay systems is presented. An iterative algorithm based on the EKF for data detection and tracking the unknown time-varying PHN throughout the OFDM data packet is also used. For more efficient 3-D video transmission, the estimation algorithms and UEP schemes based packet portioning were combined to achieve a more robust video bit stream in the presence of PHNs. Applying this combination, simulation results demonstrate that promising bit-error-rate (BER) and PSNR performance can be achieved at the destination at different SNRs and PHN variance.

The proposed schemes and algorithms offer solutions for existing problems in the techniques for applications to 3-D video transmission.

List of publications

The following publications were produced during the period of candidature:

[1] **Omar H. Salim**, Wei Xiang, and John Leis, "An efficient unequal error protection scheme for 3-D video transmission," in *Proc. IEEE Wireless Communications and Networking Conference (WCNC)*, Shanghai, China, Apr. 2013, pp. 4077-4082.

[2] **Omar H. Salim** and Wei Xiang, "A novel unequal error protection scheme for 3-D video transmission over cooperative MIMO-OFDM systems," *EURASIP J. Wirel. Commun. Netw.*, vol. 2012:269, no. doi:10.1186/1687-1499-2012- 269, Aug. 2012.

[3] **Omar H. Salim** and Wei Xiang, "Prioritized 3-D video transmission over cooperative MIMO-OFDM systems," in *Proc. IEEE International Conference on Digital Image Computing Techniques and Applications (DICTA)*, Noosa, QLD, Australia, Dec. 2011, pp. 225-230.

[4] **Omar H. Salim**, Wei Xiang, and John Leis, "Error-resilient video transmission for 3-D signal over cooperative-MIMO system," in *Proc. European Signal Processing Conference (EUSIPCO)*, Barcelona, Spain, Aug. 2011, pp. 1372-1376.

The work in the papers is presented in Chapter 3.

[5] **Omar H. Salim**, Wei Xiang, John Leis, and Lei Cao, "Cross-layer optimization for 3-D video transmission over cooperative relay systems," *Signal Processing-Image Communication* 29 (2014), pp. 1102-1120,
doi: 10.1016/j.image.2014.08.003.

The work in the paper is presented in Chapter 4.

[6] **Omar H. Salim**, Ali A. Nasir, Hani Mehrpouyan, Wei Xiang, Salman Durrani, and Rodney A. Kennedy, "Channel, Phase Noise and Frequency Offset in OFDM Systems: Joint Estimation, Data Detection and Hybrid Cramér-Rao Lower Bound," *IEEE Trans. Commun.*, vol. 62, no. 9, pp. 3311-3325, Sep. 2014.

[7] **Omar H. Salim**, Ali A. Nasir, Hani Mehrpouyan, and Wei Xiang, "Phase Noise and Carrier Frequency Offset in OFDM Systems: Joint Estimation and Hybrid Cramér-Rao Lower Bound," in *Proc. International Workshop on Signal Processing Advances in Wireless Communications (SPAWC)*, Darmstadt, Germany, June 2013, pp. 649-653.

The work in the papers is presented in Chapter 5.

[8] **Omar H. Salim**, Ali A. Nasir, Wei Xiang, and Rodney A. Kennedy, "Joint Channel, Phase Noise, and Carrier Frequency Offset Estimation in Cooperative OFDM systems," in *Proc. IEEE International Conference on Communications (ICC)*, Sydney, NSW, Australia, June 2014, pp. 4384-4389.

The work in the paper is presented in Chapter 6.

Dedicated to my lovely wife Sadeem for her unconditional love, patience and all the sacrifices. Also, dedicated to my children (Qutaiba, Sadeel , Razn and Nasam) and my dear parents, who have been my pillar of strength

Acknowledgments

First and the foremost, I would like to express my deepest gratitude to my principal supervisor A/Prof. Wei Xiang for his endless commitment to directing the research and invaluable guidance. Without his motivation and guidance, this thesis would not have been completed.

I would like to express my sincere thanks to my associate supervisor A/Prof. John Leis, for his support and encouragement throughout my PhD studies.

I am also genuinely grateful to my associate supervisor A/Prof. Hani Mehrpouyan from California State University, and my associate supervisor Dr. Ali Arshad Nasir from The Australian National University for their instructive discussions and constructive suggestions to my thesis. They are always willing to have in-depth discussion whenever I approach them for help.

I would like to gratefully acknowledge the funding support provided by the MHED scholarship in Iraq for supporting my study at USQ during my PhD studies. A special thank to all my friends and colleagues at USQ. Last, but not the least, my thanks go to Sandra Cochrane, who helped me in proofreading the thesis.

Omar Hazim Salim

University of Southern Queensland
2015

Acronyms & Abbreviations

2-D	Two-dimensional
3-D	Three-dimensional
5G	Fifth generation
AF	Amplify-and-forward
AVC	Advanced video coding
AWGN	Additive white Gaussian noise
BER	Bit-error-rate
BIM	Bayesian information matrix
BPSK	Binary phase-shift keying
CFO	Carrier frequency offset
CIR	Channel impulse response
CPE	Common phase error
CRC	Cyclic redundancy check
CRLB	Cramér-Rao lower bound
CSI	Channel state information
CSV	Conventional stereo video
DF	Decode-and-forward
DFT	Discrete Fourier transform
DIBR	Depth image-based rendering
DP	Direct path
EEP	Equal error protection
ECM	Expectation conditional maximization
EM	Expectation-maximization
FEC	Forward error correction

FIM	Fisher's information matrix
GOP	Group of pictures
HEVC	High efficiency video coding
HP	High-priority
ICI	Inter-carrier interference
IDFT	Inverse discrete Fourier transform
IEEE	Institute of electrical and electronics engineers
i.i.d.	independent and identically distributed
JMVC	Joint multiview video coding
JSCC	Joint source-channel coding
LDPC	Low-density parity-check
LLF	log-likelihood function
LP	Low-priority
MAP	maximum a posteriori
MBs	Macroblocks
MIMO	Multi-input multi-output
MMSE	Minimum mean-square error
MPEG	Moving picture expert group
MRC	Maximum ratio combining
MRC	Mixed-resolution stereo coding
MVC	multi-view video coding
MSE	Mean-square error
NAL	Network abstraction layer
OFDM	Orthogonal frequency division multiplexing
PP	Partitioning path
PHN	Phase noise
PPS	Picture parameter sets
PSK	Phase-shift keying
PSNR	Peak signal-to-noise ratio
Q_p	Quantization parameter
QAM	Quadrature amplitude modulation

QPSK	Quadrature phase-shift keying
R_{budget}	Rate budget
R-D	Rate-distortion
RF	Radio frequency
SC	Simulcast coding
SISO	Single-input-single-output
SNR	Signal-to-noise ratio
SPA	Sum-product algorithm
SPS	Sequence parameter sets
STBC	Space-time block codes
SVC	Scalable video coding
TDMA	Time division multiplexing acess
UEP	Unequal error protection
VLC	Variable-length code
VpD	Video plus depth
WLAN	Wireless local area network

$\|\cdot\|$	absolute value operator
$(\cdot)^*$	conjugate operator
$(\cdot)^H$	conjugate transpose operator
$(\cdot)^T$	transpose operator
$\mathbf{x}$	vector variable
$\mathbf{X}$	matrix variable
$[\mathbf{X}]_{x,y}$	element in row x and column y of $\mathbf{X}$
$\mathbf{I}_X$	$X \times X$ identity matrix
$\mathbf{0}_{X\times X}$	$X \times X$ matrix of all zeros
$\mathbf{1}_{X\times X}$	$X \times X$ matrix of all ones
$\hat{x}$	estimated value of x
$\mathbf{X}(n_1 : n_2, m_1 : m_2)$	submatrix of $\mathbf{X}$ from row n_1 to row n_2 and from column m_1 to column m_2
$\|\mathbf{x}\|$	element-wise absolute value of a vector $\mathbf{x}$
$\text{diag}(\mathbf{x})$	diagonal matrix with the diagonal elements are given by vector $\mathbf{x}$
$\mathbf{X} \succeq \bar{\mathbf{X}}$	matrix ($\mathbf{X} \succeq \bar{\mathbf{X}}$) is positive semi-definite
$\mathbb{E}_{x,y}[\cdot]$	expectation over x and y
$\Re\{\cdot\}$	real part of a complex quantity
$\Im\{\cdot\}$	imaginary part of a complex quantity
$\nabla_{\mathbf{x}}$	first-order partial derivative operator, i.e., $\nabla_{\mathbf{x}} = [\frac{\partial}{\partial x_1}, \cdots, \frac{\partial}{\partial x_N}]^T$
$\triangle_{\mathbf{y}}^{\mathbf{x}}$	second-order partial derivative operator, i.e., $\triangle_{\mathbf{y}}^{\mathbf{x}} = \nabla_{\mathbf{y}} \times \nabla_{\mathbf{x}}^T$
$\mathcal{N}(\mu, \sigma^2)$	real Gaussian distribution with mean μ and variance σ^2

$\mathcal{CN}(\mu, \sigma^2)$	complex Gaussian distribution with mean μ and variance σ^2
$\otimes$	circular convolution
$\dot{z}$	Jacobian of z

Contents

List of Figures

List of Tables

Chapter 1

Introduction

1.1 Background

Three-dimensional (3-D) video applications have recently emerged to offer immersive video content that can not be offered by two-dimensional (2-D) video services. Although 3-D illusions have captured people's imagination since the 19th Century, they have only recently become feasible on consumer electronics platforms due to advances in display technology and the physical layer [1]. Currently, there is intensive research activity pursuing 3-D video technology over wireless systems, similar to its applications in 3-D cinema and television [2]. This strong motivation is due to the 3-D video environment's ability to create a more realistic experience for the viewers [3]. However, many obstacles in wireless systems limit the transmission of 3-D video though wireless video channels. These obstacles are mainly channel bandwidth limitations, requirement for higher data-rates, variations of signal-to-noise ratio (SNR) in wireless channels, and the impact of synchronization between the transmitter and the receiver.

To overcome the channel bandwidth limitations, the source must compress the original video sequence as much as possible. This allows for the transmission of high video quality over a smaller bandwidth. However, the video compression operation usually makes the resulting bitstream very sensitive to the errors caused by the channel and the noise in the system. Therefore, error-resilient video methods are essential for providing reliable video communication between the source and the destination [4].

Generally, high data-rates are required for video transmission, and even higher rates are required for 3-D video services. Spatial multiplexing techniques such

as multi-input multi-output (MIMO) have been developed to address this issue. However, MIMO systems have limitations such as the size and power constraints with an increased number of antennae. Another approach is through the use of cooperative diversity [5]. The concept of "cooperative communication" is presented that each terminal user is sharing its antennae and partnering with other terminals to format a virtual diversity system. Therefore, each user terminal can receive its partner signal and share data with its neighboring partners [6]. Hence, cooperative communication systems employ cooperation among nodes in a wireless network to increase data throughput and robustness to signal fading. Recently, the combination of MIMO technology with one to three antennae and cooperative communications has been proposed as means of enhancing the video transmission over wireless systems [5, 7].

Modern video communication systems currently adopt orthogonal frequency division multiplexing (OFDM) as it is a powerful multi-carrier modulation technique for increasing the bandwidth efficiency of wireless communication systems. By converting a frequency-selective channel into multiple frequency-flat subchannels, OFDM can mitigate the detrimental effects of frequency-selective fading [8, 9]. Hence, OFDM has been adopted by existing and future wireless local area network (WLAN) standards such as IEEE 802.11ac and IEEE 802.11ad [10, 11]. However, OFDM systems are much more sensitive to synchronization errors than single-carrier systems. Therefore, the imperfect synchronization in OFDM systems can lead to the degradation of video system performance [12, 13].

It is important to note that the advantages of cooperative communications can only be realized if there is perfect synchronization amongst all the nodes in the network. Impairments such as channel multipath, time varying phase noise (PHN), and carrier frequency offset (CFO) result in the loss of synchronization and diversity performance of cooperative communication systems. Joint estimation of these impairments is necessary to correctly detect the received signal in cooperative systems.

To realize the goal of 3-D video transmission through wireless channels, this study focuses on designing efficient 3-D video transmission methods and signal processing algorithms to overcome the effects of error-prone wireless channels and imperfect synchronization amongst the nodes in cooperative networks. The outcome of this project can be further developed to improve the quality of 3-D video transmission methods and to achieve synchronization within cooperative networks.

1.2 Motivation

Video systems generally use compression techniques such as H.264/AVC (advanced video coding) based on variable-length codes (VLCs) to overcome the problem of channel bandwidth limitation. The resulting bitstream is usually very sensitive to bit errors because of high interdependency between the coded bits. A single-bit error can propagate to many subsequent VLCs. Moreover, error propagation causes a synchronization loss between the encoder and decoder. In the worst cases, this can lead to an entire system decoding failure.

The use of error resilience tools in source coding does not completely overcome error propagation. Thus, many different types of error resilient video and channel coding techniques, such as unequal error protection (UEP), have been proposed to improve video transmission over wireless communication systems. UEP partitions the video data into different fractions of visual importance, with the most important fraction called the high-priority (HP) stream and the remaining fractions called the low-priority (LP) stream. In addition, UEP is mostly combined with forward error correction (FEC) methods, such as turbo codes or low-density parity-check (LDPC) codes, to achieve more robust video bit streams.

Many different types of error resilient video and channel coding techniques have been proposed in the literature. However, they depend on fixed design without taking into account the priority of protection of video packets inside the 3-D video views. As a result, their design cannot be adopted to the time-varying wireless channel. In addition, these designs require high data rates for transmission to overcome the effects of error propagation in the video bit streams.

Significant improvement in 3-D video systems can be achieved by adopting new video systems based on a 3-D video transceiver architecture that adopts various UEP schemes based on a packet partitioning scheme. The switching operation between the selected UEP schemes can be used to achieve high video quality with the lowest bandwidth and system complexity. The new video system is inspired by the advantage of protection of video packets inside the 3-D video views. In addition, the new video system exploits the channel state information (CSI) in the slow time-varying wireless channel as feedback to the source and the destination.

The joint source-channel coding (JSCC) algorithm for video streaming aims to optimally share the available R_{budget} between the source and channel coding rates. This can be very useful in combatting the combined effects of source quantization noise and packet losses from the wireless channels.

The current JSCC studies for 3-D video transmission are based on the fixed UEP operation. Consequently, the UEP scheme based on packet partitioning has not been considered. Therefore, a new JSCC algorithm is proposed. This algorithm changes the UEP operation according to the throughput requirements and the available instantaneous SNR. Moreover, the proposed algorithm achieves cross-layer optimization that simultaneously assigns the number of high and low priority packets for the video packet partitioning in the network layer as well as the source and channel code rates in the application and physical layer, respectively. The aim of this approach is to maximize the quality of video at the destination and minimize the complexity of the system.

Bit errors in the video bitstream may be produced by the noise within the channel or by the Doppler shift from the wireless channel. The impairments in the physical layer, such as PHN and CFO, caused by unstable local oscillators or Doppler shift, respectively, result in a common phase error (CPE) and inter-carrier interference (ICI) at the receiver. Both of these factors can lead to the degradation of system performance and error bits on the transmitted video signal [12, 13].

Given that the received signal is affected by PHN and CFO at the destination, the challenge of this research is to propose the channel, PHN and CFO estimation and detection techniques that overcome the CPE and ICI effects. In addition, the estimation of channel impulse response (CIR) using training symbols in the presence of CFO and PHN is challenging. Moreover, the proposed estimation and detection have to be low in computational complexity and suitable for video applications.

In the context of estimation of synchronization parameters, the Cramér-Rao lower bound (CRLB) is a lower bound to assess the achievable estimation accuracy of any unbiased estimator. However, the hybrid Cramér-Rao lower bound (HCRB) for joint channel, PHN, and CFO estimation in OFDM systems has not been studied in the existing literature. Therefore, a new expression for the HCRB for joint estimation of the channel, PHN and CFO in OFDM systems is derived in this thesis.

A conventional MIMO system is affected by a single PHN and CFO as the antenna elements are co-located on a single device. However, a cooperative diversity can be only achieved if these impairments are estimated and removed from the received signal. A cooperative network consists of multiple distributed nodes, where each one has its own local oscillator. Thus, this gives rise to *multiple phase noises* (PHNs) and *multiple carrier frequency offsets* (CFOs) that affect the re-

ceived signal at the receiver. Moreover, accurate estimation of these multiple impairments, i.e., CIR, CFOs, and time-varying PHNs, is required for coherent detection of OFDM signals at the receiver.

Most of the existing work in the literature focuses on estimating either CFOs while assuming perfect estimation of PHNs, or targets the estimation PHN parameters while assuming perfect CFOs estimation. More importantly, the HCRB for joint estimation of multiple impairments in cooperative OFDM systems is not provided. Thus, there is a need for a comprehensive study of these impairments in cooperative networks.

Given the time-varying nature of PHN, it must be tracked not only during the training interval but also during the data transmission interval. Hence, following the training period, a receiver structure for joint data detection and PHN mitigation in the data transmission period is required. In the existing literature, joint data detection and PHN mitigation has been analyzed [14, 15]. However, the existing PHN tracking schemes require the application of pilots throughout an OFDM symbol to compensate the CPE. This adversely affects the bandwidth efficiency and data detection performance of the overall system.

The existing video work reported in the literature focuses on transmitting 2-D and 3-D video signals while assuming perfect channel, PHN and CFO synchronization. Therefore, this thesis provide new insight into streaming 3-D video in cooperative relay networks in the presence of PHNs and CFOs. Since UEP schemes based on packet partitioning, and joint estimation of channels, PHN, and CFO can be considered solutions of different problems (robustness and ICI mitigation), it is useful to exploit a combination of these two methods in order to obtain powerful video transmission schemes.

1.3 Research Problems and Scope

1.3.1 Research Problems

The delivery of 3-D video services over wireless systems such as mobile systems poses new challenges. This is due to the wireless channel environment, which negatively affects the video transmission. 3-D video transmission over wireless channels will face significant hurdles until the problems caused by the oscillators' fluctuation and the wireless channel are studied and resolved in detail.

1.3.1.1 Unequal error protection schemes for 3-D video transmission

Many different types of error resilient video and channel coding schemes have been proposed in the literature to mitigate the effects of the wireless channel on the 3-D video sequence [3, 16–19]. However, the proposed UEP schemes in [3, 16, 19] basically depend on the direct transmission schemes that give more protection to the independently-encoded view such as the right (/or colour) view than to the dependent view, i.e., left view (/or depth). In addition, they depend on fixed design without taking into account the protection priority of video packets inside the views. Therefore, they are unable to change their design to adapt to the time-varying wireless channel. In addition, these designs require high date rates for transmission to overcome the effects of error propagation in the wireless channel.

The proposed UEP schemes in [17, 18] are based on the slice interleaving method. However, this method is only used when the SNR in the wireless channel is high. In this thesis, an efficient UEP scheme and a new video transceiver structure for 3-D video transmission are proposed. The proposed UEP scheme can be applied for the modern 3-D video techniques, i.e., multi-view video coding (MVC) and video plus depth (VpD). The proposed video transceiver takes into consideration the SNR variations in the wireless channel to enable the 3-D video system to be adaptive to SNR changes in the channel and achieve a trade-off between system complexity and system performance.

1.3.1.2 Joint source-channel coding for 3-D video transmission

JSCC algorithms have been proposed for 3-D video transmission [20–22]. However, the proposed JSCC algorithms in [20–22] adopted for transmission based on direct schemes, requires high data rates for transmission and has lower performance compared to packet partitioning schemes. In addition, the JSCC algorithms in [20–22] have lower performance compared to packet partitioning schemes. Moreover, the unequal importance of packets inside the right (/or colour) and left (/or depth) is not considered in [20–22] in formatting the HP and LP of the JSCC algorithm. Therefore, in this thesis, a new approach via the JSCC algorithm based on the video packet partitioning scheme is proposed. The proposed algorithm simultaneously assigns the number of high and low priority packets for the video packet partitioning in the network layer as well as the source and channel code rates in the application and physical layer. The new algorithm can minimize system complexity and overall video distortion at the destination. The cooperative system also utilizes the specific properties of

best relay selection and estimated SNR between the source-destination and the source-relay-destination to control the proposed JSCC algorithm.

1.3.1.3 Joint channel, phase noise, carrier frequency offset estimation and data detection in OFDM systems

In data-aided OFDM systems, a training-based transmission scheme is used, in which the training signals are used to assist joint estimation of the channel parameters, PHN, and CFO at the destination receiver. In the context of point-to-point systems, joint channel, PHN, and CFO estimation was proposed in [23–25]. However, the estimation approach in [23] and [24] is based on a small angle approximation, which adversely affects the performance of the estimation and data detection algorithms. In addition, the complexity of the estimation approaches in [23–25] are very high. More importantly, in [23–25], the HCRB for the joint estimation of channel impulse response (CIR), PHN, and CFO in the OFDM systems is not derived. For data detection, an efficient receiver structure for joint data detection and PHN mitigation during the data transmission interval must be designed. In the existing literature, joint data detection and PHN mitigation are analyzed in [26, 27]. However, the data detection algorithms in [26, 27] may not be used in practical implementations due to their high computational complexity and poor bit-error-rate (BER) performance when using high order modulations. In this thesis, an efficient new estimator that jointly estimates the channel, PHN, and CFO for OFDM systems is proposed. An algorithm for joint data detection and phase noise mitigation to detect OFDM data symbols in the presence of PHN is proposed. As shown in this thesis, both the proposed estimator and data detection algorithms outperform existing algorithms in terms of the MSE and BER. In addition, it is shown that the proposed receiver structure has lower computational complexity and could be suitable for video applications.

1.3.1.4 Synchronization of cooperative communication systems and its effects on 3-D video applications

The transmitted packet from the source to relays to destination consists of training and data signals. During the training signal, the destination has to estimate multiple channel parameters, PHNs, and CFOs. Then, during the data detection and PHN mitigation, the estimated values of the impairments are used to compensate the effect of the channel parameters, PHNs, and CFOs. Various algorithms have been proposed (in the literature) for joint estimation of multiple channel

parameters, PHNs, and CFOs in cooperative communication systems [14, 28–30]. However, most of this work focuses on estimating either CFOs, while assuming perfect PHN estimation [28–30], or PHNs while assuming perfect CFO estimation [14]. In addition, the HCRB for joint estimation of channel parameters, PHNs and CFOs is not addressed in the existing studies. In this thesis, a computationally efficient training based approach for joint channel gain, PHN, and CFO estimation in OFDM-based decode-and-forward (DF) and amplify-and-forward (AF) relay systems is proposed. The HCRB for the joint estimation problem is derived. In order to detect the data symbols at the destination in the presence of time-varying PHN, an iterative algorithm for data detection and PHN mitigation at the destination is proposed. As shown in this thesis, both proposed estimator and data detection algorithm can significantly improve the average BER performance of relay systems compared to existing algorithms.

The delivery of 3-D video services over cooperative systems was proposed in [31–35]. However, the video transmission approaches in [31–35] are based on perfect estimation of channel gains, PHNs, and CFOs. Therefore, the effects of channel gains, PHNs, and CFOs on the performance of video transmission systems are not take into account. Moreover, the study of the impact of channel estimation in the presence of PHN and CFO on the system performance and complexity for 3-D video transmission has not been addressed in the literature, to date. In this thesis, an efficient combination of UEP schemes based on video packet partitioning and estimation algorithms of channel parameters in the presence PHNs and CFOs is proposed. A computationally efficient training based approach for joint channel, CFOs, and PHNs estimation in OFDM-based relay systems is proposed. The performance of 3-D video transmission under the effects of PHN and CFO in OFDM-based AF relay network is investigated. Finally, in order to detect the data symbols in the presence of time-varying PHNs, an iterative data detection algorithm is proposed.

1.3.2 Research Scope

The scope of the thesis is to provide efficient solutions for the problems caused by the oscillators' fluctuation and the wireless channel on 3-D video signals. This can be achieved by adopting efficient communication and signal processing techniques to transmit 3-D video signals over wireless communication systems. It is nearly impossible to cover all approaches that can be used to improve the video transmission over the wireless channel. As a result, this thesis will focus primarily

on five important approaches. These are UEP, JSCC, cooperative diversity, joint channel, PHN and CFO estimation, and data detection in the presence of PHN and CFO. The proposed systems are applied for the modern 3-D video techniques, i.e., MVC and VpD. The H.264/AVC reference software in [36] and MVC codec based on H.264/AVC in [21, 37] are used for encoding the 3-D video sequences throughout this thesis.

1.4 Original Contributions

This thesis makes four original contributions to the knowledge of science:

- **A New Unequal Error Protection Scheme for 3-D Video Transmission:** A comparison between 3-D video representations (i.e., VpD, mixed-resolution stereo coding (MRSC), simulcast coding (SC), and MVC) is investigated to study the noise effect on each format and determine the representation that is most suitable for video transmission over the wireless channel. Simulation results demonstrate that VpD is most suitable for wireless video communication. Next, a new UEP scheme, called video packet partitioning is proposed for 3-D video transmission. A new 3-D video transceiver structure is also proposed. It adopts various UEP schemes based on the packet partitioning. The UEP schemes are tested over cooperative MIMO-OFDM systems. Switching operations between the proposed schemes are proposed to achieve a trade-off between the system complexity and performance. Experimental results show that the proposed schemes achieve significantly high video quality at different SNRs over the wireless channel with the lowest possible bandwidth and system complexity compared to the direct transmission schemes. The proposed schemes are published in [32–35].

- **Joint Source-Channel Coding Algorithm for 3-D Video Transmission:** The rate budget constraint and the available instantaneous SNR of the best relay selection in cooperative systems can dramatically impact system performance and complexity of video applications, since they determine the video distortion. By taking these constraining factors into account, the signal model and formulate the system optimization problem are outlined first. Next, a new approach to cross-layer optimization for 3-D video transmission over a cooperative relay systems is proposed. Procedures for estimation of the end-to-end instantaneous SNR using an estimate of the

available instantaneous SNRs between the source-destination, and source-relay-destination are proposed. These estimation procedures are performed before beginning to send the video signal to the best relay and destination. A novel approach using Lagrange multipliers is developed to solve the optimum bit allocation problem. Based on the rate budget constraint and the estimated end-to-end instantaneous SNR, the proposed JSCC algorithm simultaneously assigns source code rates for the application layer, the number of high and low priority packets for the network layer, and channel code rates for the physical layer based on criteria that maximize the quality of video, whilst minimizing the complexity of the system. Finally, the impact of the estimated end-to-end instantaneous SNR on video system performance and complexity is investigated. Experimental results show that the proposed JSCC algorithm outperforms existing algorithms in terms of peak signal-to-noise ratio (PSNR). Moreover, the proposed JSCC algorithm is found to be computationally more efficient as it can minimize the overall video distortion in a few iterations. The proposed JSCC algorithm is published in [38].

- **Joint Channel, Phase Noise and Frequency Offset Estimation and Data Detection in OFDM Systems:** An expectation conditional maximization (ECM) based algorithm for joint estimation of channel, PHN, and CFO in OFDM systems is proposed. The signal model for the estimation problem is presented and the hybrid Cramér-Rao lower bound (HCRB) for the joint estimation problem is derived. Next, an iterative receiver based on the *extended Kalman filter* for joint data detection and PHN tracking is proposed. Numerical results show that, compared to existing algorithms, the performance of the proposed ECM-based estimator is closer to the derived HCRB and outperforms the existing estimation algorithms at moderate-to-high SNRs. In addition, the combined estimation algorithm and iterative receiver are more computationally efficient than existing algorithms and result in improved average uncoded and coded BER performance. The proposed ECM estimator and the *iterative* algorithm for joint data detection and phase noise mitigation is published in [39, 40].

- **Synchronization of Cooperative Communication Systems and Its Effects on 3-D Video Applications:** An iterative pilot-aided algorithm is proposed based on the ECM approach that jointly estimate of multiple channels, Wiener PHNs, and CFOs in DF and AF based cooperative

OFDM systems. Next, an iterative receiver is proposed based on an *extended Kalman filter* for joint data detection and PHN tracking. The effects of PHNs and CFOs on the performance of OFDM-based AF relay networks for 3-D video applications is also investigated. Numerical results show that the proposed estimator achieves mean square error performance close to the derived HCRB at moderate-to-high SNR for different PHN variances. In addition, the combined estimation algorithm and iterative receiver can significantly improve average BER performance compared to the existing algorithms and non-cooperative systems. In addition, experimental results show that the accurate estimation of channel parameters, PHNs and CFOs directly affects the performance and complexity of cooperative systems for video applications. In addition, the proposed system of the combination of the estimation algorithms and UEP schemes based packet portioning can achieve high performance in terms of PSNR over a wide range of SNRs. Part of the proposed system was published in [41].

1.5 Organization

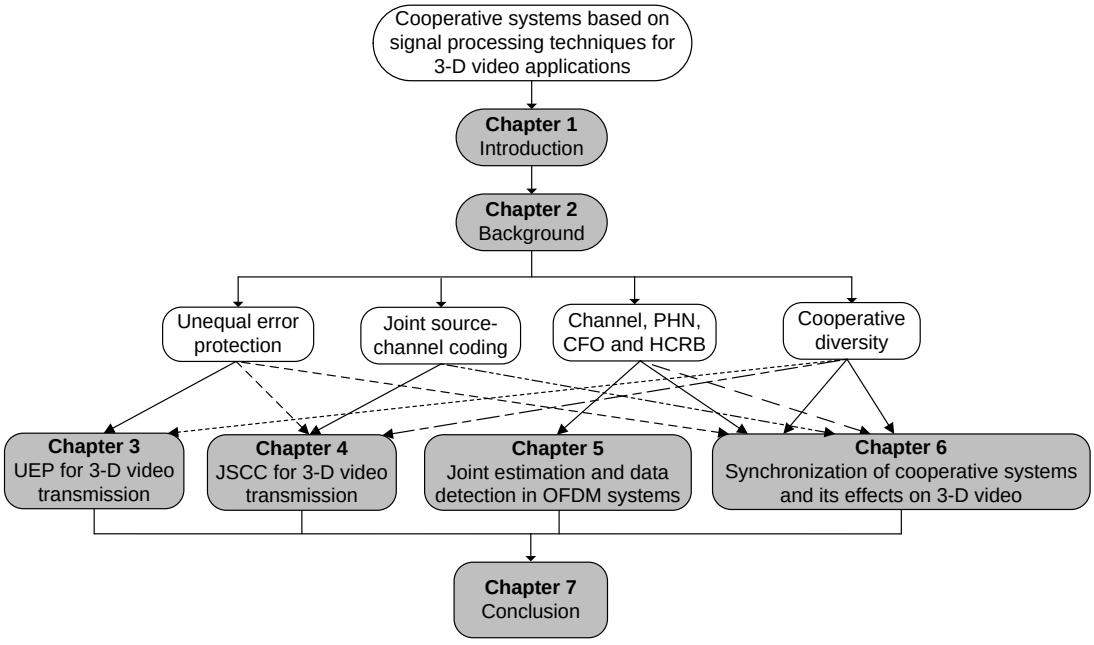

Figure 1.1: Block diagram of dissertation outline and coverage.

Figure 1.1 shows the overall scope and the coverage of the thesis. Chapter 2 is dedicated to the basic concepts of 3-D video transmission and a review of the existing literature related to this thesis. Chapter 3-6 present the specific technical contributions of the thesis. Each chapter summary is given as follows:

- **Chapter 2**: This chapter reviews the basic concepts of 3-D video representation and coding standards. In addition, error-resilient source and channel coding tools that could be used to improve 3-D video transmission are discussed. The effects of imperfect synchronization and impairments on the physical layer of OFDM systems is also covered.

- **Chapter 3**: A comparison between different 3-D video representations is investigated in this chapter. A new UEP scheme based on video packet partitioning for 3-D video transmission over wireless channels is proposed. A new 3-D video transceiver structure that adopts switching operations between the proposed UEP schemes is also proposed.

- **Chapter 4**: In this chapter, a new approach to the JSCC algorithm for 3-D video transmission over cooperative relay systems is proposed. The estimation procedures of the instantaneous SNRs between the source-destination, and source-relay-destination are proposed to control the proposed 3-D video transceiver. A novel optimization method using the Lagrange multiplier approach is derived to solve the system optimization problem. Finally, the impact of the instantaneous signal-to-noise ratio estimation on the video system performance and complexity is investigated.

- **Chapter 5**: A new ECM algorithm for joint estimation of channel, PHN, and CFO in OFDM systems is proposed. The signal model for the estimation problem is outlined in detail and the HCRB for the joint estimation of channel, PHN, and CFO in OFDM systems is derived. An *iterative* algorithm for joint data detection and phase noise mitigation is proposed for OFDM data symbols.

- **Chapter 6**: A new ECM algorithm for joint estimation of multiple channels, Wiener PHNs, and CFOs in DF and AF based cooperative OFDM systems is proposed. The signal model for the estimation problem is outlined in detail and the HCRB for the joint estimation problem is derived. An *iterative* algorithm for joint data detection and phase noise mitigation is proposed for OFDM data symbols at the destination. An investigation

of the performance of the proposed system in the presence of PHNs and CFOs for 3-D video applications at different SNRs is carried out.

- **Chapter 7**: This chapter summarizes the thesis and outlines future research directions.

Chapter 2

Background

This chapter provides an overview of 3-D video transmission and its applications in cooperative relay systems. Error-resilient techniques that are applicable to 3-D video transmission are also included, and the effect of imperfect synchronization on the performance of OFDM systems is presented.

Section 2.1 presents an overview of 3-D video representation and coding standards. Section 2.2 presents error-resilient source and channel coding tools that could be used to improve 3-D video transmission. Section 2.3 reviews the cooperative system and its transmission protocols adopted in the relay nodes. Section 2.4 discusses the synchronization in communication systems and the effects of PHN and CFO on their performance. Section 2.5 reviews the Cramér-Rao Lower bound. Finally, Section 2.6 concludes the chapter.

2.1 Three-Dimensional (3-D) Video Coding

Source 3-D video coding generally uses compression techniques to overcome the problem of channel bandwidth limitation. Although there are many different methods of source coding, this thesis will focus on 3-D video coding.

The input of the 3-D video signal is captured by two cameras. These two captured signals or views represent the left and right views. Several video representations for 3-D video signals have been proposed. As a consequence, various 3-D video compression and coding approaches are designed to process 3-D signals with different methods.

2.1.1 3-D Video Representations

The literature explores various approaches for processing the 3-D video signal. In this thesis, VpD and MVC are considered due to their suitability for low-rate applications such as mobile services. VpD and MVC are also evaluated compared to conventional stereo video (CSV) and MRSC representations. Figure 2.1 shows different representations and formats of 3-D video signal.

The MRSC method encodes the left and right views separately. As shown in Figure 2.1-(b), MRSC is implemented by down-sampling one of the views and up sampling back to the original resolution at the decoder. This operation yields different views with unequal resolution and the overall 3-D video quality is almost retained. This method is similar to the CSV method, as shown in Figure 2.1-(a), which encodes the left and right views separately without down-sampling [42].

The VpD method, as shown in Figure 2.1-(c), encodes one of the views (such as the right view) with auxiliary depth information. At the decoder, the left view can be reconstructed using the depth-image-based rendering (DIBR) technique [43].

MVC exploits the correlation between two close views in CSV format to increase compression efficiency. This correlation between the left and right views yields redundancies between views, which can be exploited by inter-view prediction scheme. Therefore, a coding method can exploit this feature to achieve high compression gain [44].

It can be concluded that, the relationship between the colour video and depth data in VpD, and the correlation between the left and right view in MVC, improves the compression efficiency for the 3-D video signal compared to CSV and MRSC representations.

Many studies have been proposed to examine and evaluate MRSC, VpD and MVC techniques for mobile 3-DTV applications. Brust et. al. [42] evaluated the MRSC scheme for different video sequences, and Gotchev et. al. [2] demonstrated that VpD and MVC are the preferable coding techniques for mobile applications.

2.1.2 3-D Video Coding Standards

The literature proposes many different coding standards to encode the 3-D video representations. In this thesis, the H.264/AVC is adopted because it is the most widely used international video coding standard [45]. Furthermore, the H.264/AVC codec provides almost twice the compression efficiency with the same quality compared to the previous standards [45]. Therefore, state-of-the-art video

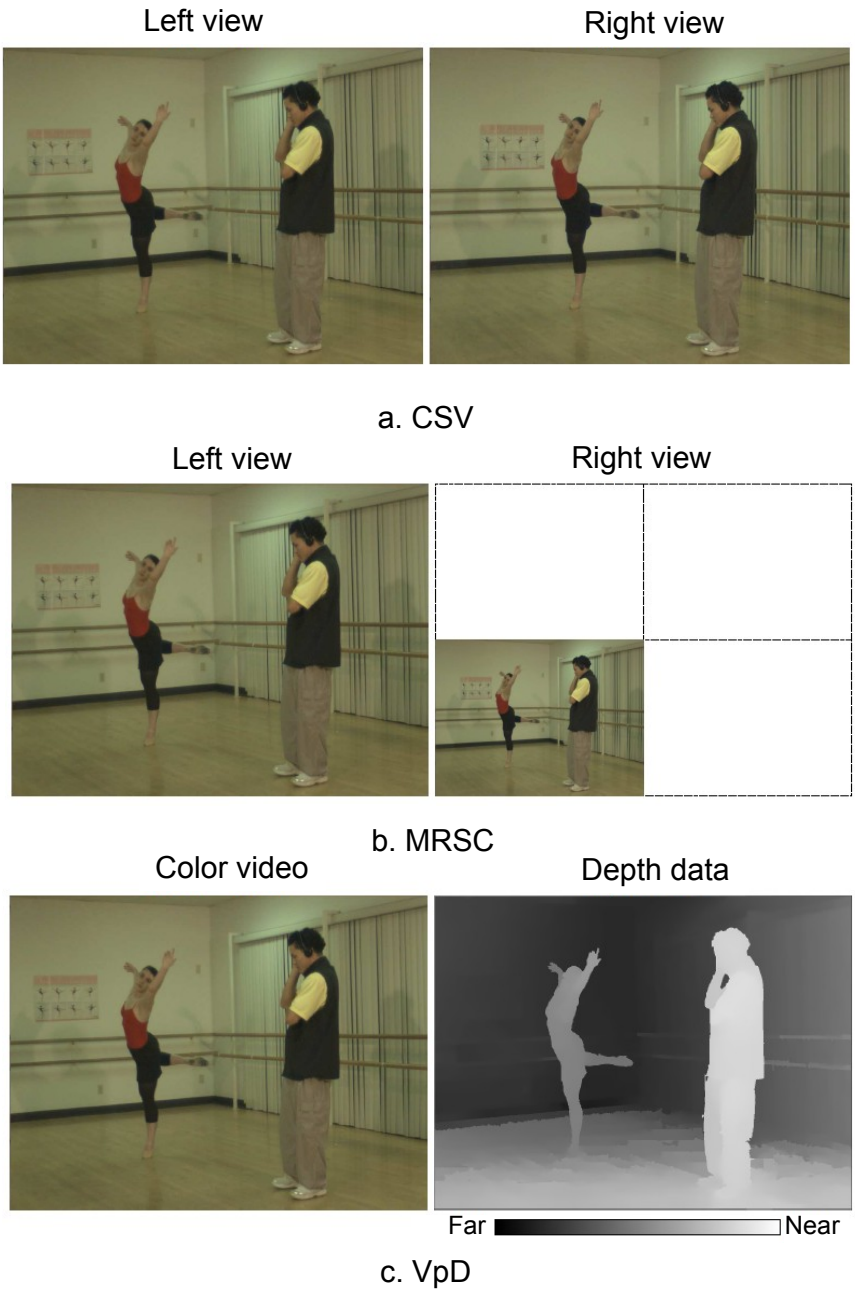

Figure 2.1: Different representations of 3-D video signals.

codec uses the H.264/AVC technique to compress the 3-D video sequence.

In general, two coding methods, called simulcast coding (SC) and multi-view

video coding (MVC) are used to encode the 3-D video sequences, as shown Figure 2.2, where GoP is the group of pictures. Simulcast coding, as shown in Figure 2.2-(a), encodes the left and right view separately using two 2-D video codec based on H.264/AVC. In simulcast coding, inter prediction is performed in each view individually. Multi-view video coding, as shown in Figure 2.2-(b), exploits the inherent redundancies in a multi-view scene by introducing predictions between views. The inter-view prediction can be used by AVC/MVC codec to achieve high compression gain.

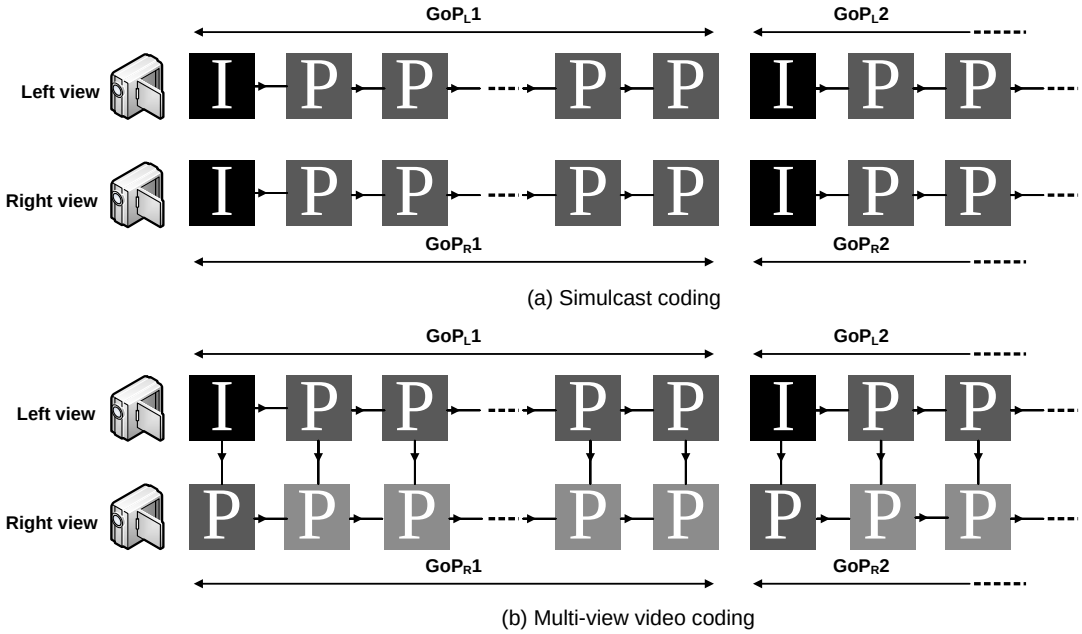

Figure 2.2: Simulcast and multi-view video coding.

A new 3-D video coding standard is referred to as the high-efficiency video coding (HEVC) extension. It is based on H.265 and expected to be used in the near future. The HEVC extension is developed to support the coding of multiple views and associated depth data. In addition, it achieves the same video quality as H.264 standard and improves the bit rate by 50% on average [46]. However, the improvements in HEVC extension comes at the cost of higher encoding and decoding complexity [47].

2.1.3 3-D Video Signal Transmission

In H.264/AVC encoding, the video encoder produces H.264/AVC bit stream as shown in Figure 2.3. As shown in this figure, the bit stream consists of a series of network abstraction layer (NAL) units or packets. The first two packet sequence parameter sets (SPS) and picture parameter sets (PPS) are used as common control parameters to the video decoder. The subsequent packets contain header information and an integer number of macroblocks (MBs), which contain coded video data [44].

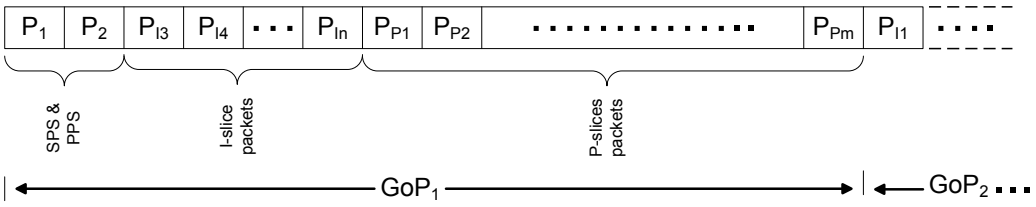

Figure 2.3: Different representations of 3-D video signals.

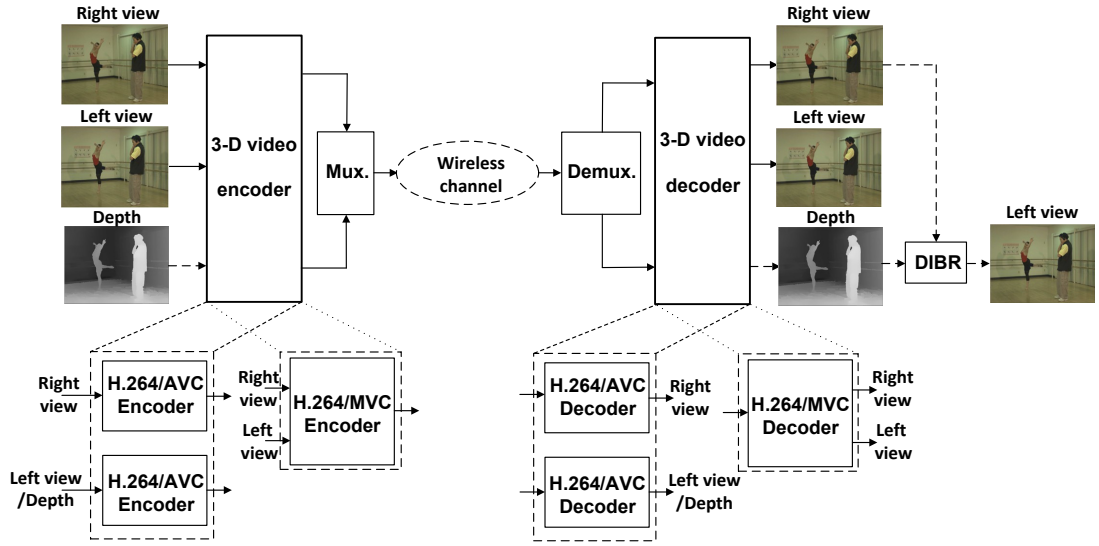

Figure 2.4: Simulcast and multi-view video coding.

The transmission of 3-D video bit streams is determined according to the adopted 3-D video representation. As shown in Figure 2.4, two H.264/AVC en-

coders and decoders are usually used to encode and decode the right and left/or depth sequence in the CSV, MRSC, and VpD formats. Meanwhile, a single H.264/MVC encoder and decoder are used for the MVC format. Therefore, the complexity of encoding and decoding operations for the VpD format is higher than the MVC format.

The output bit streams after a 3-D video encoder, as shown in Figure 2.4, are rearranged to a single output at the multiplexer. Subsequently, the output from the multiplexer is transmitted over the wireless channel. At the receiver, the received data stream is separated back to two data streams before being decoded by the H.264/AVC decoders. Meanwhile, the multiplexer is not needed for MVC transmission. When VpD is adopted for transmission, the DIBR technique is used at the receiver to reconstruct the left view from the right view (colour) and depth map.

2.2 Error-Resilient Source and Channel Coding Tools for 3-D Video Transmission

The H.264/AVC video standard is supported by many error resilience tools. The main tools are: data partitioning, slice interleaving and flexible macroblock ordering (FMO) [48]. Some of these tools are unsuitable for real time video applications. For example, the FMO technique typically produces a simple improvement in the system performance in spite of its implementation complexity [49]. Therefore, H.264/MVC is expected to use some error resilient tools such as data partitioning and slice interleaving in its reference software. Nevertheless, none of these tools are applied to H.264/MVC reference software [18].

A slice interleaving method was proposed to split video frames into several slices. In the decoder side, each slice is decoded independently. With this method, the errors in each slice are seriously restricted, thereby preventing error propagation to other slices. As a result, the increase in the number of slices per frame improves the quality of reconstructed video sequences, while reducing the efficiency of the video compression.

Many 3-D video studies have been interested to evaluate the slice interleaving method. Tech et al. [18] implemented and integrated joint multiview video coding (JMVC) reference software version 5.0.5 using the slice interleaving method. Micallef and Debono [17] also applied the slice interleaving method with different slice sizes to JMVC reference software version 8.0. It can be concluded that,

although this method is useful for minimizing and isolating the effects of error propagation, it is only suitable when the SNR value is high in the wireless channel. Moreover, the increase in the number of slices per frame leads to a reduction in the video compression efficiency.

In source coding, the use of error resilience tools does not completely overcome error propagation. Therefore, error-resilient channel coding techniques are necessary. A variety of error-resilient video and channel coding tools have been proposed to improve video transmission over wireless communication systems. The main schemes are UEP with aid of FEC methods, and JSCC.

2.2.1 Unequal Error Protection (UEP)

The channel coding (also known as FEC) is required to enable the error detection and/or correction method. To enable error detection and correction, the channel coding technique adds redundant bits to the video bit stream. As a result, bit streams may be different sizes and, thus, is represented to as the UEP scheme [4].

UEP involves on partitioning the video data (which comes from the source coding stage) into different fractions of visual importance. The most important fraction is called the HP-streams while the remaining fractions are called the LP-streams. HP-streams can be decoded to reconstruct the video with acceptable quality, while LP-streams are utilized to improve the video quality. Therefore, by partitioning the video data and applying better error protection to the video streams, a more robust video bit stream can be achieved [50].

The UEP technique for 3-D video transmission will be discussed in more detail in Chapter 3.

2.2.2 Joint Source-Channel Coding (JSCC)

The main goal of the JSCC algorithm is to make the video system adaptive to changes in the wireless channels. In this case, if the CSI is perfectly available at the transmitter, maximization of the channel capacity can be achieved to transmit video data through reliable channels. In order to achieve this scheme, the receiver needs to periodically feedback the CSI to the transmitter.

The JSCC algorithm is designed to maximize compression efficiency with minimal distortion. The increase of source rates leads to an improvement of video performance with low distortion. At the same time, the rise of channel coding

rates leads to a high bit error rate with low system performance. Therefore, to achieve a high data rate with low distortion, source rates must be increased and channel coding rates must be decreased under available channel capacity [51].

In wireless systems, there is a fixed rate budget (R_{budget}) related to the system parameters such as the target rate for each video frame according to its energy and type, channel coding rate, and the modulation scheme [4, 44]. The target rate for each video frame refers to the source coding rate (R_s), which is varied by quantization parameters in the video encoder. The channel coding rate (R_c) is determined by the forward error correction algorithm employed. Joint source-channel coding (JSCC) optimization for video streaming aims to optimally share the available R_{budget} between the source and channel coding rates. This can be very useful to combat the combined effects of source quantization noise and packet losses from the wireless channel [52].

The JSCC technique for 3-D video transmission will be covered in Chapter 4, where JSCC will take into account the R_{budget} and the available instantaneous SNR in cooperative channels to improve 3-D video performance.

2.3 Cooperative Systems

The main goal of the communication system is to transfer a maximum amount of information from the source to the destination through reliable wireless channels. Diversity techniques using MIMO systems have been proposed to achieve this goal using multiple antennas at the transmitter and/or receiver to provide multiple independent replicas of the same information to the receiver [5, 53, 54]. Moreover, space-time coding techniques have been used in MIMO systems to increase diversity gain [55, 56].

Due to size, power, and/or hardware limitations caused by an increase in the number of antennas in MIMO-mobile devices, cooperative diversity has been proposed as a very promising techniques for solving the limitations of MIMO systems [57, 58]. In other words, cooperative relay systems provide diversity by forming a virtual MIMO system that promises significant performance gains in terms of link reliability, spectral efficiency, system capacity, and transmission range [5]. More recently, the MIMO system with two to three antennas has been proposed for use in combination with cooperative diversity to improve the diversity of cooperative systems for video applications [7, 32–35].

The cooperative MIMO architecture with video applications is shown in Figure 2.5. It consists of three types of nodes: source (S), relay (R) and destination

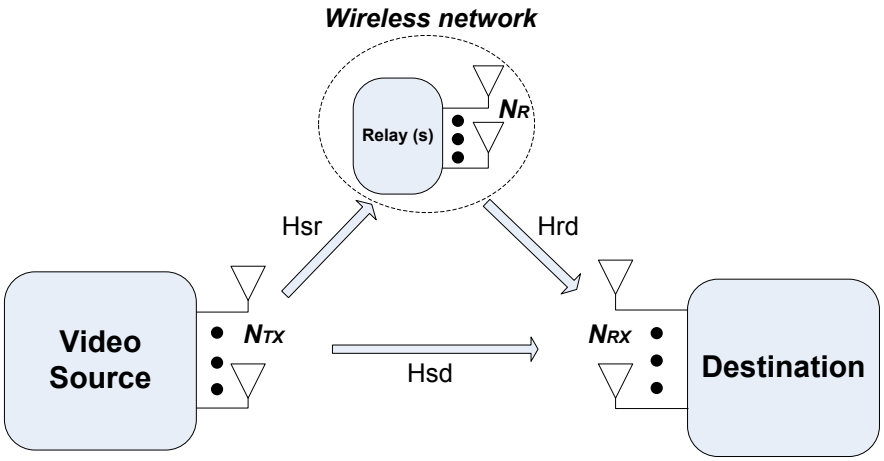

Figure 2.5: A cooperative MIMO system with video applications.

(D). Each node is equipped with two to three antennas to increase the diversity gain at the destination. The source node represents the video sequence with the least number of possible bits, without losing the video quality, using a compression method such as the H.264/AVC standard.

In cooperative systems, there are usually three types of links called direct, relay, and cooperative links. The direct link represents the signal path between source and destination, and the relay link is the signal path between source,relay, and destination. Furthermore, the cooperative link combines the signals of both the direct and relay links at the destination node. Since the channels in the direct and relay links are independent, each relay node can assist the source node to communicate with the destination node to achieve special diversity.

Usually, a half-duplex mode is adopted for all nodes in cooperative systems, i.e., a node cannot transmit and receive simultaneously, but on different time/ frequency slots. In this setup, in the first hop, the source node broadcasts its message to both relay and destination simultaneously. In the second hop, the relay processes the received signal and then forwards it to the destination. In general, the transmission using a half-duplex mode is performed over $K+1$ time slots, where K is the number of relays. It is clear that there is no collision between the received signals during the two consecutive hops at the destination. However, a half-duplex mode maintains orthogonality throughout the cooperative system at the expense of loss in spectral efficiency [58].

Two most commonly applied protocols are recorded in the literature. The

first protocol is called the decode-and-forward (DF), and the second is called the amplify-and-forward (AF) protocol. Usually, one or a hybrid combination of these two protocols is adopted to provide copies of transmitted signals via the relay link to the distinction node.

2.3.1 Relay Protocols

In the DF approach, the relay decodes the received signal, and then re-encodes the decoded data before forwarding it to the destination. Thus, the DF approach is known as a regenerative transmission protocol. Figure 2.6 shows the relay block

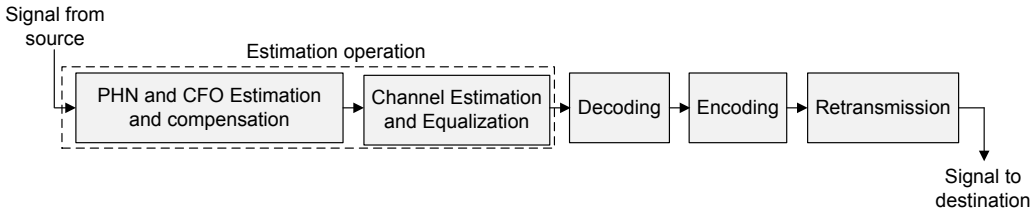

Figure 2.6: Relay block diagram using DF protocol.

diagram using the DF protocol. As shown in this figure, the DF relay estimates first the source to relay channel, PHN, and CFO between the source and relay. The compensation of PHN and CFO and channel equalization are performed depending on the estimated channel and offsets. Next, source information is decoded, encoded, and retransmitted to the destination node. Usually, when the channel between the source and the relay is good, the DF protocol is used and achieves superior performance in error correction compared to the AF protocol. However, the performance of the DF protocol is limited when the relay link suffers from deep fading. In this case, the error will propagate to the destination [5].

The second relay protocol is AF. Figure 2.7 shows the relay block diagram using the AF protocol. As shown in this figure, a relay using the AF protocol simply multiplies the received signal by the gain factor and forwards the resultant signal to the destination.

Unlike the DF relaying, AF relaying does not estimate the PHN, CFO, and the channel parameters between the source and the relay and does not perform PHN and CFO compensation and channel equalization. Thus, the source data signal is not decoded and directly retransmitted to the destination node.

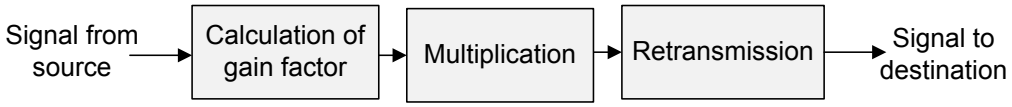

Figure 2.7: Relay block diagram using DF protocol.

2.3.2 Comparison between DF and AF Protocols for Video Applications

In cooperative systems, one or a hybrid version of the DF and AF protocols are usually adopted according to the system application. For example, FEC techniques are usually used and require a decoding method that is performed in an iterative manner such as the sum-product algorithm (SPA) of the LDPC codes [59]. Therefore, the DF protocol may not be suitable for use in relay networks for video applications because it results in both a high computational complexity and time delay. The increase in complexity may also lead to an increase in power consumption [60]. On the other hand, the AF protocol amplifies the received signal, including noise, and forwards it to the destination. However, the AF protocol has a lower complexity and hence processing time [60]. Therefore, in this thesis, the AF protocol is considered through the adoption of the best relay selection for video applications to reduce the system complexity.

The concept of the best relay selection has previously been proposed in the literature to efficiently implement the AF protocol in relay systems [61–65]. The best relay selection depends on selecting a single relay out of the set of available relays which has maximum instantaneous signal-to-noise ratio (γ_{SRD}) between the source-relay-destination. In addition, the selection procedures are automatically repeated every time the channel gains vary [62]. This concept is adopted in this thesis.

Both AF and the best relay selection schemes for video applications will be addressed in more detail in Chapter 4, where the accuracy estimation of instantaneous SNRs through the channels on the performance of the 3-D video system and complexity will be discussed in detail.

2.4 Synchronization in OFDM Communication Systems

Recently, OFDM has been widely adopted in many wired and wireless communication applications and standards because it achieves high spectral efficiency and robustness to multi-path fading distortions. Moreover, an OFDM receiver is relatively simple compared to signal carrier based systems because the detection of transmitted symbols can be performed via a one-tap channel equalizer [66, 67]. However, OFDM systems are very sensitive to synchronization imperfections between the source and the destination compared to signal carrier based systems [68]. The PHN and CFO are two of the common impairments in OFDM wireless communication systems. In this context:

- CFO is a deterministic parameter that is caused by the frequency difference between the source and the destination nodes, or by Doppler shift,

- PHN is a random process caused by instable local oscillators of the source and the destination.

In general, the frequency deviations at the oscillator output is related to the accuracy design of the local oscillators. Usually, oscillators are implemented with low-cost. Thus, it is difficult to develop a low cost oscillator with sufficient frequency stability [69]. Therefore, the effects of CFO and PHN can not be avoided and have to be considered in the design of wireless communications systems. The effect of PHN maybe more noticeable at higher carrier frequencies, e.g., V-band/60 GHz and E-band/70–80 GHz [70].

2.4.1 Phase Noise Modeling

Phase noise $\theta(t)$ is generated at the source and destination oscillators when the signals are translated between baseband and radio frequency (RF) band. It can be described as a phase disturbances that is accumulated over time and can be modeled by a random Wiener process given by

$$\theta(t) = \int_0^t u(t)dt, \tag{2.1}$$

where $u(t)$ is a white Gaussian process with a power spectral density $S_u(f)$ and the oscillator power spectrum is a Lorentzian in shape [71]

$$\mathcal{L}(f) = \frac{1}{\pi\beta\big(1+(\frac{f}{\beta})^2\big)}. \tag{2.2}$$

Here, β denotes the 3dB bandwidth. The discrete-time Wiener process is sampled every T_s seconds, i.e., the sampling time period. Then, the discrete time phase noise is given by

$$\theta_n \;=\; \theta_{n-1} + \delta_n, \quad \forall n, \tag{2.3}$$

where $\delta_n \sim \mathcal{N}(0, \sigma_\delta^2)$ is the PHN innovation and $\sigma_\delta^2 \triangleq 2\pi\beta T_s$ is the variance of the innovation process [71, 72].

2.4.2 Basics of Phase Noise and Carrier Frequency Offset

PHN and CFO produce a shift of the received OFDM symbols in the frequency domain and result in the loss of orthogonality between the subcarriers. This leads to significant performance degradation since it results in time varying channels and rotation of the signal constellation from symbol to symbol. The CFO and PHN basics can be illustrated in a simple model as shown in Figure 2.8 [73].

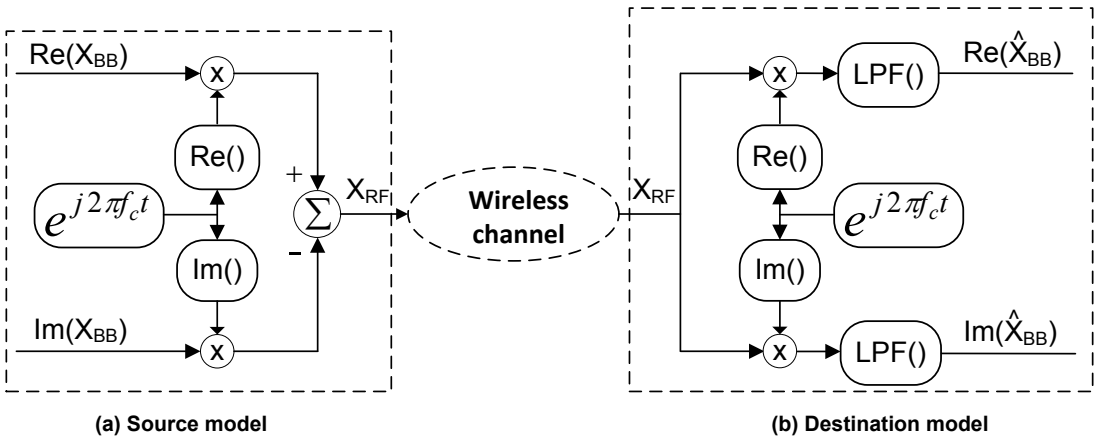

Figure 2.8: A simple model of RF conversion at the source and the destination nodes

The transmitted OFDM signal is given by

$$\begin{aligned} \mathrm{X_{RF}} &= \big(\mathrm{Re}\{\mathrm{X_{BB}}\}\cos(2\pi f_c t) - \mathrm{Im}\{\mathrm{X_{BB}}\}\sin(2\pi f_c t)\big)e^{j\theta_s(t)}, \\ &= \frac{1}{2}\big(\mathrm{X_{BB}}e^{j2\pi f_c t} + \mathrm{X_{BB}^*}e^{-j2\pi f_c t}\big)e^{j\theta_s(t)}, \end{aligned} \tag{2.4}$$

where $\theta_s(t)$ is the phase noise at the source, $\mathrm{X_{BB}}$ is a complex baseband signal after inverse discrete Fourier transform (IDFT), $\mathrm{X_{RF}}$ is the RF generated version of $\mathrm{X_{BB}}$ and f_c is the carrier frequency.

At the destination node, the received RF signal, $\mathrm{X_{RF}}$, is down converted and passed through a low-pass filter (LPF) with gain of 2. The carrier frequency at the destination node is assumed to be $f_c \pm f_o$, where f_o represents the frequency offset of the carrier. The received baseband signal, $\hat{\mathrm{X}}_{\mathrm{BB}}$, after LPF is given by

$$\begin{aligned} \hat{\mathrm{X}}_{\mathrm{BB}} &= \mathrm{LPF}\left[\frac{1}{2}e^{j2\pi(f_c \pm f_o)t}e^{j\theta_d(t)}\big(e^{j2\pi f_c t} + \mathrm{X_{BB}^*}e^{-j2\pi f_c t}\big)e^{j\theta_s(t)}\right], \\ &= \mathrm{X_{BB}}e^{\pm j2\pi f_o t}e^{j\theta_s(t)}e^{j\theta_d(t)}. \end{aligned} \tag{2.5}$$

where $\theta_d(t)$ is the phase noise at the destination. It is clear that the received baseband signal in (2.5) is modulated by three complex sinusoid signals, one signal is produced from CFO (f_o) which is frequency difference between carrier frequencies between the source and destination nodes, and two signals from the phase noises $\theta_s(t)$ and $\theta_d(t)$ at the source and destination, respectively.

2.4.3 Effects of Phase Noise and Carrier Frequency Offset on OFDM Systems

The CFO and PHN destroy the orthogonality of the symbols at the DFT output and lead to interferences amongst the OFDM subcarriers, i.e., a CPE and ICI. Substantially, the CPE and ICI affect the performance of the detector at the destination. This causes drastic performance degradation [12, 13, 68]. Moreover, PHN and CFO may affect the performance of other estimation processes. In fact, the estimation of CIR is impossible in the presence of CFO and PHN [23]. To better illustrate this concept, a simple OFDM system is considered as shown in Figure 2.9.

The baseband OFDM signal (s) can be obtained as follows. A set of modulated data $d = [d_0, d_1, \cdots, d_{N-1}] \in \mathcal{C}^{1\times N}$ after M-PSK or M-QAM modulation is normalized by IDFT, at the transmitter, as

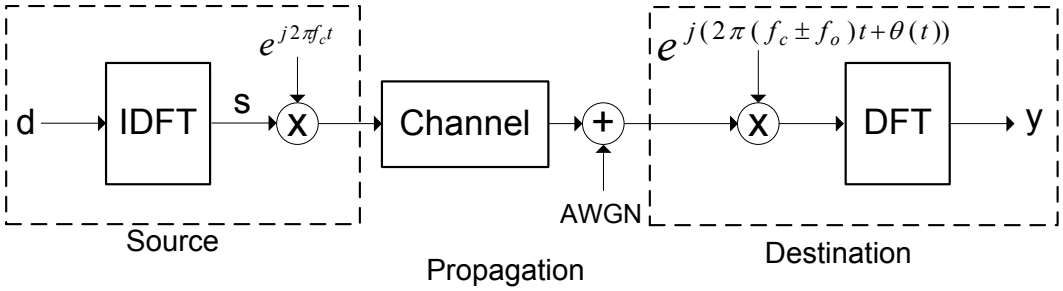

Figure 2.9: Block diagram of an OFDM system with CFO and oscillator instabilities.

$$s_n = \frac{1}{\sqrt{N}} \sum_{k=0}^{N-1} d_k e^{\frac{j2\pi kn}{N}} \qquad n = 0, 1, \ldots, N-1, \tag{2.6}$$

where k denotes the kth sample of the OFDM symbol and N is the number of subcarriers. At the receiver, after removing the cyclic prefix (CP), the complex baseband received signal of an OFDM symbol at rate N/T , where T is the symbol period, is given by

$$r_n = \frac{1}{\sqrt{N}} e^{j(\theta_n + 2\pi n\epsilon/N)} \sum_{k=0}^{N-1} h_k d_k e^{j2\pi kn/N} + z_n \tag{2.7}$$

where $\epsilon = \triangle fT$ is the normalized CFO; $\{\theta_n\}_{n=0}^{N-1}$ is the discrete-time PHN sequence; $\{h_k\}_{k=0}^{N-1}$ is the channel frequency response at subcarriers 0 to N-1; and $\{z_n\}_{n=0}^{N-1}$ is complex additive white Gaussian noise (AWGN) with variance σ^2 per dimension.

To illustrate the effects of the CFO and PHN on the received signal as follows. After FFT, the received signal corresponding to the kth subcarrier, y_k, is given

by

$$
\begin{aligned}
y_k &= \mathrm{FFT}\{r_n\} \\
&= \frac{1}{\sqrt{N}} \sum_{n=0}^{N-1} r_n e^{-j2\pi kn/N} \\
&= \sum_{n=0}^{N-1} \left[\frac{1}{N} e^{j(\theta_n + 2\pi n\epsilon/N)} \sum_{m=0}^{N-1} h_m d_m e^{j2\pi mn/N} + z_n \right] e^{-j2\pi kn/N} \\
&= \frac{1}{N} \sum_{n=0}^{N-1} e^{j(\theta_n + 2\pi n\epsilon/N)} \sum_{m=0}^{N-1} h_m d_m e^{j2\pi mn/N} e^{-j2\pi kn/N} + \sum_{n=0}^{N-1} z_n e^{-j2\pi kn/N} \\
&= \frac{1}{N} \sum_{n=0}^{N-1} \sum_{m=0}^{N-1} h_m d_m e^{j(\theta_n + 2\pi n\epsilon/N + 2\pi(m-k)n/N)} + Z_k \qquad (2.8) \\
&= h_k d_k \underbrace{\frac{1}{N} \sum_{n=0}^{N-1} e^{j(\theta_n + 2\pi n\epsilon/N)}}_{\text{CPE}} + \underbrace{\frac{1}{N} \sum_{\substack{m=0 \\ m\neq k}}^{N-1} h_m d_m \sum_{n=0}^{N-1} e^{e^{j(\theta_n + 2\pi n\epsilon/N + 2\pi(m-k)n/N)}}}_{\text{ICI}} + Z_l[k]
\end{aligned}
$$

Therefore, the CPE term is denoted by $\frac{1}{N} \sum_{n=0}^{N-1} e^{j(\theta_n + 2\pi n\epsilon/N)}$ and the ICI term is given by $\frac{1}{N} \sum_{\substack{m=0 \\ m\neq k}}^{N-1} h_m d_m \sum_{n=0}^{N-1} e^{e^{j(\theta_n + 2\pi n\epsilon/N + 2\pi(m-k)n/N)}}$.

The CPE term represents the amplitude and phase distortion of the kth subcarrier frequency component due to CFO and PHN. Meanwhile, the ICI term represents the ICI from other sub-carriers into the kth subcarrier frequency component, which implies that the orthogonality among subcarrier frequency components is not maintained any longer due to the CFO and PHN.

There has been much interest in investigating the effects of PHN and CFO in OFDM systems. In [68], Pollet *et al.* showed that PHN and CFO more significantly deteriorate the performance of OFDM systems compared to single carrier systems. The PHN and CFO in OFDM systems cause a number of impairments such as attenuation and rotation of each of the subcarriers and ICI between subcarriers [68]. Tomba in [74] derived the error probability of an OFDM system in the presence of PHN for different modulation schemes. The study in [74] showed that the degradation of BER performance is worst when increasing the PHN variance and the modulation order. Wu and Ness in [75] exhibited the effects of PHN on the performance of OFDM systems in terms of signal-to-noise-plus-interference ratio (SINR). The study in [75] illustrated that SINR is worst in the

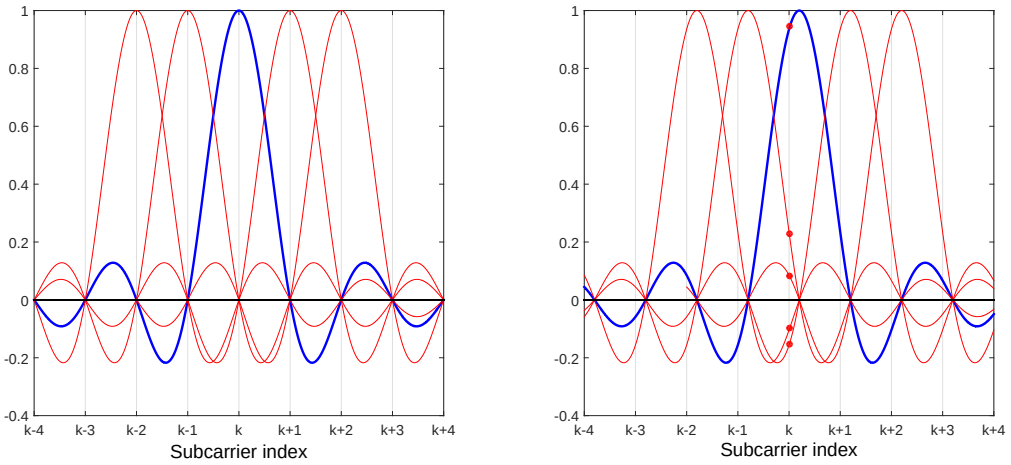

(a) $\epsilon = 0$ **(b)** $\epsilon = 0.2$

Figure 2.10: The CFO effects on the subcarriers orthogonality.

increasing of PHN bandwidth (β) and as the number of subcarrier increases.

The effect of CFO on OFDM signals is illustrated in Figure 2.10, where the dotted lines with circle markers denote the signal at the DFT output. It is clear from Figure 2.10-(b) that at $\epsilon = 0.2$, there is interference from the neighboring subcarriers on the corresponding subcarrier.

The effect of PHN and CFO on a 16-QAM constellation is shown in Figure 2.11. From Figure 2.11-(b), it is obvious that the PHN and CFO rotate the desired signal into a wrong decision area, and deteriorate the BER performance accordingly.

In conclusion, accurate estimation of these imperfections (i.e., channel, CFO, and PHN) is required before the DFT operation to mitigate the resulting CPE and ICI and perform data detection [76, 77].

The effects of PHN and CFO on channel estimation and OFDM system performance will be covered in Chapter 5, where new algorithms for joint estimation and data detection are used to mitigate the PHN and CFO effects and improve system performance.

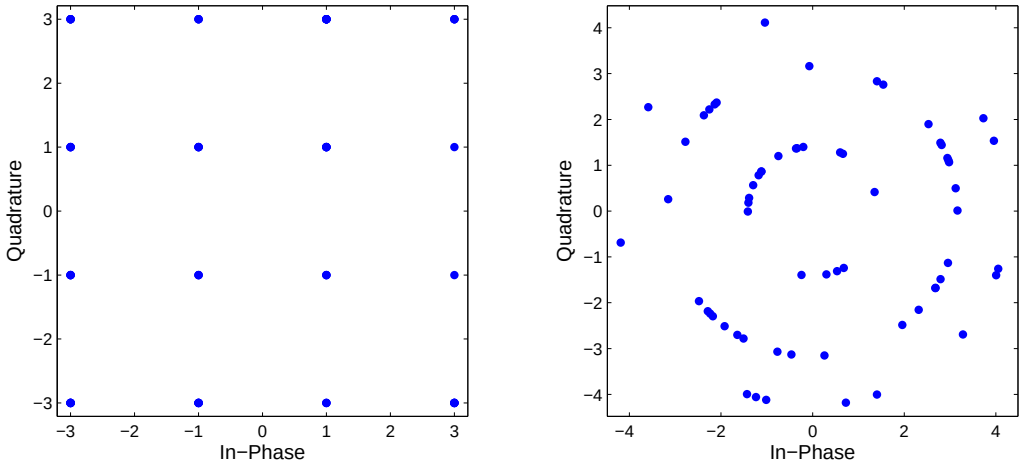

(a) $\sigma_\delta^2 = 0, \epsilon = 0$ **(b)** $\sigma_\delta^2 = 10^{-3}, \epsilon = 0.2$

Figure 2.11: 16-QAM constellation rotated by PHN and CFO.

2.5 Cramér-Rao Lower Bound (CRLB)

The CRLB is the lower bound to evaluate an unbiased estimator's performance in terms of MSE of estimated parameter $\hat{\lambda}$, i.e., $\text{MSE}(\hat{\lambda}) \succeq \text{CRLB}(\lambda)$. For applications of signal processing in communication systems, the CRLB has been widely applied to examine the performance of estimators [78]. This bound is adopted when the estimated parameter is deterministic such as the CFO, while the Bayesian Cramér-Rao lower bound (BCRB) is utilized for random parameters such as PHN [79]. Therefore, such bounds are very important tools as they can be used as performance benchmarks for unbiased estimators.

Recently, the HCRB has been adopted to provide an accurate lower bound for evaluating the performance of estimators in the presence of deterministic and random parameters [80]. For instance, in the joint estimation of PHN and CFO parameters, the HCRB is a lower bound on the joint estimation of random, e.g., PHN, and deterministic, e.g., CFO parameters. Let $\boldsymbol{\lambda} = [\boldsymbol{\theta}^T \ \epsilon]^T$ be the vector of hybrid parameters of interest, where $\boldsymbol{\theta}$ is a vector of random PHN parameters and the CFO, ϵ, is modeled as a deterministic parameter. The accuracy of estimating $\boldsymbol{\lambda}$ is lower bounded by the HCRB, $\boldsymbol{\Omega}$, as [79, pp. 1-85]

$$\mathbb{E}_{\mathbf{r},\boldsymbol{\theta}|\epsilon}\left[(\hat{\boldsymbol{\lambda}}(\mathbf{r}) - \boldsymbol{\lambda})(\hat{\boldsymbol{\lambda}}(\mathbf{r}) - \boldsymbol{\lambda})^T\right] \succeq \boldsymbol{\Omega}, \tag{2.9}$$

where $\boldsymbol{\Omega}$ is given by the inverse of the hybrid information matrix (HIM), $\mathbf{B}$, i.e., $\boldsymbol{\Omega} = \mathbf{B}^{-1}$. Here, $\mathbf{B}$ can be written as [79, pp. 1-85]

$$\mathbf{B} = \boldsymbol{\Xi}_D + \boldsymbol{\Xi}_P, \tag{2.10}$$

where $\boldsymbol{\Xi}_D \triangleq \mathbb{E}_{\boldsymbol{\theta}}\left[\boldsymbol{\Psi}(\boldsymbol{\theta}, \epsilon)\right]$, $\boldsymbol{\Psi}(\boldsymbol{\theta}, \epsilon)$ denotes the Fisher's information matrix (FIM) and $\boldsymbol{\Xi}_P$ is the prior information matrix for PHN.

The HCRB for joint channel, PHN and CFO estimation will be addressed in Chapter 5, where a new HCRB derivation is presented to evaluate the proposed estimator.

2.6 Conclusion

This chapter provided an overview of error-resilient source and channel tools for 3-D video transmission over wireless cooperative relay networks. Several types of 3-D video representation for low-rate video applications such as mobile services were reviewed. The efficient 3-D video coding standards in the literature were discussed. The cooperative system with its relay protocols and a comparison between the relay protocols for video applications were addressed. This chapter also discussed the synchronization tasks and effects of PHN and CFO synchronization imperfections on the system performance. The chapter concluded that the transmission of 3-D video signals over wireless communication systems can be achieved by adopting UEP, JSCC, and cooperative diversity, which enhances the system to be adapting to the time-varying wireless channel and provide high date rates for transmission to overcome the effects of error propagation in the wireless channels. Furthermore, it is indicated that PHN and CFO estimator with low computational complexity is required for video applications to overcome the effects of Doppler shift and the impairments in the physical layer. These communication and signal processing techniques can enhance the cooperative relay systems to provide reliable 3-D video communication over error-prone wireless channels.

Chapter 3

A New Unequal Error Protection Scheme for 3-D Video Transmission

3.1 Introduction

Unequal error protection (UEP) of the video bitstream is one of the most effective strategies for improving system video performance caused by an error-prone environment. Usually, a compressed video bitstream can be represented with different partitions according to their sensitivity to bit error in the wireless channel. Therefore, the degradation of video quality at the destination occurs when bit error propagates throughout the important partitions. Thus, the important partitions should have higher protection than other partitions.

In this chapter, a 3-D video transceiver based on a new UEP scheme, called video packet partitioning is proposed to achieve high video quality at different SNRs in the wireless channel with the lowest possible bandwidth and system complexity. Note that the delay and jitter are ones of the typical parameters in evaluating the quality of service (QoS) over communications networks. However, the delay does not affect the video streaming services compared to the packet loss if it can tolerate a delay of five seconds [81, 82]. In this case, the packet loss impacts more on the video streaming services [81, 82].

The advantages of exploiting diversity and multiplexing gains of multi-antenna systems promotes the application of MIMO technology in wireless video communications systems. Wu *et al.* [83] investigated the system performance of a

MPEG coding scheme with joint convolutional coding and MIMO-based space-time block codes (STBC) techniques over Rayleigh fading channels. The feedback information from the performance control unit (PCU) was employed to control the assigned rates to the MPEG source code and convolutional coding stages. Although this study demonstrated that BER can be improved using STBC and convolutional coding systems, it did not propose any techniques to mitigate error propagation in video signals at the video decoder. Song and Chen [84] proposed a MIMO system based on the adaptive channel selection (ACS) method. The suggested scheme was to load more important video layers to the MIMO sub-channel which has a high SNR. Song and Chen [85] also proposed another method to increase the transmission throughput by reallocating the excess power of certain sub-channel to other sub-channels. Zheng *et al.* [86] proposed a hybrid space-time coding structure to achieve the UEP scheme for multiple description coding (MDC) over a MIMO-OFDM system. Besides, several hybrid MIMO systems were proposed in [87, 88]. Although these works have suggested different methods to improve video transmission over wireless channels, they depend on the direct transmission of video signals. Therefore, they require high data rates for transmission and have lower PSNR performance than the packet partitioning proposed in this chapter.

Most of the existing work for 3-D video delivery over wireless communication channels focus on fixed designs such as the one proposed by Hewage *et al.* [16] which was based on VpD. In their paper, a UEP method based on unequal power allocation (UPA) was proposed to transmit 3-D video signals over WiMAX communication channels. The VpD map was coded with backward compatibility using scalable video coding (SVC) architecture. Akar *et al.* [89] utilized the previous method to transmit 3-D video signals over the Internet. Furthermore, Hewage *et al.* [90, 91] demonstrated that the depth map information is less important than the colour data in terms of perceived video quality. For this reason, the proposed UEP scheme in [90, 91] allocates more protection for the colour image than the depth map. It was also determined based on UPA method. Aksay *et al.* [3] studied the digital video broadcasting-handheld (DVB-H) system at different coding rates for transmitting left and right views. The study recommended that more protection be given to the independently-encoded view, i.e., the left view than the dependent view, i.e., the right view. Tech *et al.* [18] implemented and integrated the JMVC reference software version 5.0.5 using the slice interleaving method. Micallef and Debono [17] applied the same idea of the slice interleaving method with different slice sizes to the JMVC reference software version 8.0.

Recently, Hellge *et al.* [19] proposed a layer-aware FEC method to improve the MVC video performance over the DVB-H system. It can be concluded that the slice interleaving method is useful only when the SNR in the wireless channel is high. Furthermore, the slice interleaving method requires a high data rate for transmission due to the increase in the number of slices per frame.

3.2 Contributions

In this chapter, the issues raised above are addressed by contributing the following:

1. A comparison of 3-D video representations, i.e., VpD, MVC, MRSC and SC. The comparison is useful for studying noise effect on each representation and provide the format most suitable for video transmission over wireless video communication systems;

2. The proposal of a new 3-D video transceiver architecture that adopts various UEP schemes for transmission. The proposed schemes are based on video packet partitioning which classifies the video packets based upon the GoP for the MVC and VpD into sub-groups. Each sub-group is classified according to the HP or LP streams according to the position of the sub-group between the GoP packets. The classification method depends on isolating the HP and LP streams inside each view of MVC. The proposed schemes also applied for VpD to classify the video packets inside the colour and depth sequences;

3. A new transmission protocol is also proposed. The protocol selects the best UEP schemes between the proposed schemes and adopts a switching operation between the selected schemes to achieve high video quality with the lowest bandwidth and system complexity;

4. The combination of two error-resilient video methods to overcome the effects of noisy channels. The first method depends on resynchronization patterns and the second uses the channel state information (CSI) signal to control the LDPC encoders to allocate equal or unequal protection to the HP and LP streams;

5. An efficient algorithm called the approximate lower triangular form (ALTF) in [92] for the LDPC with different coding rates is adopted and integrated

into the 3-D video system. The adopted LDPC code is adaptive to the channel state according to the proposed JSCC algorithm; and

6. Several experiments are conducted with typical 3-D video sequences to investigate the performance of the proposed UEP schemes and transceiver over cooperative MIMO-OFDM systems. Experimental results show that the proposed UEP schemes achieve significantly high video quality at different SNRs in the wireless channel with the lowest possible bandwidth and system complexity compared to the direct transmission schemes.

The remainder of this chapter is organized as follows. Section 3.3 describes the proposed system model. Section 3.4 introduces proposed UEP schemes and problem formulation. Section 3.5 provides experiential results and discussion. Finally, Section 3.6 concludes this chapter.

3.3 System Model

Figure 3.1 illustrates the proposed cooperative MIMO-OFDM system for 3-D video transmission. The following sub-sections describe each major component of the proposed system.

3.3.1 3-D Video Encoder

The 3-D video input is generally captured by two cameras representing the left and right views. After that, the stereoscopic views are represented by the MVC or VpD representation [93]. The use of these methods is determined by the underlying 3-D video application and display techniques. In this thesis, MVC and VpD representations are used and tested because they are appropriate for low-rate applications such as mobile video services [93].

3.3.2 Rate-Distortion Analysis for 3-D Video Compression

The distortion of a video signal generally consists of source distortion (D_s) and channel distortion (D_c). D_s is due to the compression process in the video encoder, and D_c is caused by video packet losses introduced by the wireless channel. Hence, the total distortion of the left (D_L) and right (D_R) views can be formed

as:

$$D_L = D_{s_L} + D_{c_L} \tag{3.1}$$

and

$$D_R = D_{s_R} + D_{c_R} \tag{3.2}$$

where source distortion (D_{s_L} and D_{s_R}) can be calculated by measuring the MSE between the decoded video sequences from the uncorrupted bit-stream at the source and the original ones, while the channel distortion (D_{c_L} and D_{c_R}) can be calculated by measuring the MSE between the decoded video sequences after the video decoder and the original ones. Therefore, the overall video distortion at the end of the receiver can be defined as the MSE between the decoded video sequences after the video decoder and the original ones. The average distortion of the 3-D video signal (D_T) can be described as [3, 32]

$$D_T = \frac{D_L + D_R}{2} \tag{3.3}$$

To minimize D_T, two methods are followed. The first method uses a rate-distortion (R-D) model to estimate the source encoding rate that minimizes the D_{s_L} and D_{s_R}. The second method reduces the D_{c_L} and D_{c_R} by choosing suitable code rates of the LDPC encoders.

In the first method, the D_{s_L} and D_{s_R} can be modeled as [94]

$$D_{s_L} = \frac{\theta_L}{R_L - R_{0_L}} + D_{0_L} \tag{3.4}$$

$$D_{s_R} = \frac{\theta_R}{R_R - R_{0_R}} + D_{0_R} \tag{3.5}$$

where R_L and R_R are source encoding rates in bit per second (bps) of the left and right views, respectively. In addition, θ_L, R_{0_L} and D_{0_L} represent the sequence-dependent parameters of the R-D model of the left view encoder, and θ_R, R_{0_R} and D_{0_R} for the right view [94]. The source distortion of depth D_{s_D} can also be calculated

$$D_{s_D} = \frac{\theta_D}{R_D - R_{0_D}} + D_{0_D} \tag{3.6}$$

where R_D in bps is the encoding rate of the depth encoder.

Using some non-linear curve fitting tools, the relevant R-D curves of left, right and depth sequences for 'Car', 'Hands', 'Horse' videos in [95] are plotted in Figure 3.2. Hence, the distortion parameters in (3.4), (3.5) and (3.6) can be calculated

Table 3.1: Encoder rate-distortion curve parameters for 'Car' Video.

R-D parameters			
Left view	θ_L	R_{0_L}	D_{0_L}
	5.48×10^3	6.39	-1.755
Right view	θ_R	R_{0_R}	D_{0_R}
	2.14×10^3	10.85	-1.38
Depth sequence	θ_D	R_{0_D}	D_{0_D}
	842.69	23.09	-0.11

for each video sequence. For example, for the adopted 'Car' video, the distortion parameters can be calculated as shown in Table 3.1.

As can be seen from Figure 3.2-(a),(b), the variation in MSE becomes very small when R_L and R_R is greater than 1.2 Mbps. Therefore, the encoding rate R_L=R_R=1.206 Mbps is used to encode the right and left (colour) sequences. Similarly, as can be seen in Figure 3.2-(c), the variation in MSE becomes very small when R_D is greater than 350 kbps. In addition, the distortion effect on the depth sequence is less than on the colour sequence. Therefore, R_D=0.378 Mbps is utilized for encoding the depth sequence in VpD format. Thus, these selected rates achieve a good balance between video quality and bandwidth.

3.3.3 Video Packet Partitioning

In H.264/AVC coding, a number of coding profiles are defined according to the codec capabilities. In this thesis, the baseline profile is chosen due to its suitability for low rate video applications [44]. Figure 3.3 illustrates the video packets and their types after the H.264/AVC video encoder. As shown in Figure 3.3, P_1 and P_2 represent the sequence parameter set (SPS) and picture parameter set (PPS) packets. These packets contain common control parameters to the decoder which are used to identify the entire video sequence. The packets P_1 and P_2 are followed by I-frame packets ($P_{I3}, \ldots, P_{In}$) and P-frames packets ($P_{P3}, \ldots, P_{Pm}$),

From the error protection point of view, the SPS, PPS and I-frame packets can be classified to HP packets, while the rest P-frame packets can be classified as LP packets. This due to the fact that any error in the SPS and PPS packets may lead to an entire system decoding failure. Furthermore, any error in the I-frame packets will propagate to the P-frames packets. However, as shown in Figure 3.3, it is possible to enhance the video transmission and reduce the data rates

Table 3.2: The video system performance at different loss of groups

Tested sequence	Group	PSNR	Distortion
Car	g_1	27.45	116.713
	g_2	31.94	41.59
	g_3	35.9	16.7
	g_4	39.57	7.17
Hands	g_1	25.08	201.47
	g_2	30.14	62.91
	g_3	35.07	20.19
	g_4	39.7	6.95
Horse	g_1	31.24	48.85
	g_2	34.07	25.45
	g_3	36.62	14.148
	g_4	38.6	8.96

for transmission by dividing the video packets per GoP into a number of packet groups (GP) (g_1,g_2,. . .,g_{Ng}). These groups can be classified according to their loss effects on the total video quality when they are lost in the video decoder.

To illustrate the loss effects of each group on the quality of reconstructed video sequence, each GoP is divided into several video sequences such as 'Car', 'Hands' and 'Horse' videos in [95], with 30 frames per second (fps) of 432×240 pixels and a GoP of 10 frames, into four groups ($Ng = 4$) g_1, g_2,g_3, g_4. Each sequence is tested by discarding each group of packets individually. In the first test, the g_1 only is discarded, while g_2,g_3 and g_4 are reconstructed perfectly. This usually happens when the video decoder loses the g_1 packets because there is still bit error left in g_1 packets even after LDPC decoding. In the second, third and fourth tests, the same procedure is performed on g_2, g_3 and g_4, respectively. In addition, the video system performance for each test is measured in terms of the peak signal-to-noise ratio (PSNR) and video distortion.

Table 3.2 reveals the video system performance for each test sequence. As shown in this table, the worst PSNR occurs when the g_1 packets are lost, while the distortion is minimal when error propagation takes place within the packets in g_4. In conclusion, the priority order of the GP from high to low is g_1, g_2,. . ., g_{Ng}. Therefore, the video packet partitioning operation classifies the packets to HP and LP streams according to their position in the GoP packets.

In this chapter, two methods of video transmission are proposed as shown in Figure 3.1. The first method is based on the packet partitioning scheme. In this method, the video packets are classified to HP and LP packets and the HP packets have higher protection than LP packets. The second method uses the direct transmission. In this method, the independent view, i.e., colour and left view for VpD and MVC, respectively, and the dependent view, i.e., depth and right view for VpD and MVC, respectively, are sent directly without applying packet partitioning. In the direct transmission, the colour and left view for VpD and MVC, respectively, have higher protection for transmission because the left and right view for VpD and MVC, respectively, are reconstructed depending on the relationship between the colour and depth for VpD, and the left view and residual from the right view for MVC. Therefore, any error in the colour or left view for VpD or MVC will spread to the reconstructed view.

3.3.4 Source and Destination Control Units

As shown in Figure 3.1, the proposed system utilizes two control units at the network layer of the source and destination. The control unit in the transmitter is proposed to control the coding rates for 3-D video and LDPC encoders, and allocate a number of packets for HP and LP streams according to the CSI which is fed by the destination. In addition, the control units are responsible for:

1. Switch the switch circuits to the partitioning path (PP) or the direct path (DP) according to the scheme to be used for the transmission. This is can be achieved by switching switch circuits, called Switch-1, Switch-2, Switch-3 and Switch-4, to the PP or the DP path according to the control signals SW_T and SW_R. For example, if the partitioning schemes are adopted for transmission, the switch circuits connect the input to the PP path;

2. Control the partitioner and de-partitioner circuits, i.e., the Partitioner-1 and Partitioner-2 at the source by the CS_T signal and the Departitioner-1 and Departitioner-2 at the destination by the CS_R signal, to select the number of packets to send the HP and LP streams depending on the current SNR in the channel;

3. Count the number of transmitted frames and check the CSI per video frame. When the number of transmitted video frames reaches the allocated GoP, the control units select the scheme and change the SW_T, SW_R, CS_T and CS_R signals for that purpose.

3.3.5 Error Protection

Two LDPC codes with variable channel coding rates are employed to protect the HP and LP streams. Usually, the channel distortion, D_{c_L}, D_{c_R} and D_{c_D}, can be minimized with an appropriate design of LDPC codec. Moreover, the operations of LDPC encoding and decoding must be efficient and simple. Hence, an encoding algorithm of the approximate lower triangular form (ALTF) and a decoding method of sum-product algorithm (SPA) are utilized to achieve this goal [92, 96].

The ALTF algorithm is based on row and column permutations only. This operation performs as many transformations as possible in order to reduce the gap (g) in the ALTF matrix, where the encoding complexity is proportional to the gap size.

The SPA algorithm is a soft decision algorithm that calculates the *a priori* probabilities of the received code bits and uses *a posteriori* probabilities for decoding operation. These probabilities are known as *log-likelihood ratios*.

3.3.6 Error Resilient Methods

In the proposed system in Figure 3.1, two error-resilient video methods are combined to overcome the effects of noisy channels.

The first method depends on resynchronization patterns. In this method, special information in the video packet header is exploited by the video decoder to isolate the effect of error propagation. The length of header information is around 20 bytes and in a hexadecimal form 00 00 FF FF FF FF 80, which exists in most packets, e.g., SPS, PPS, I and even P frame packets. This pattern is utilized to maintain the synchronization with the video encoder by restarting the decoding operation when the error occurs in the video packet. The error propagation could be detected easily by a cyclic redundancy check (CRC) at the decoder side. In this procedure, the decoder depends on the CRC to determine the corrupt packets and discard them. Thus, restarting the video decoder is necessary to minimize the error effect and isolate the error propagation between the video packets.

The second method uses the CSI signal to control the LDPC encoders to achieve adaptive video transmission. In this approach, the 3-D video transmitter allocates different code rates to the LDPC encoders corresponding to the UEP schemes or the same code rates for the EEP scheme.

3.3.7 Cooperative MIMO-OFDM Systems

A wireless network with M+2 nodes is considered, where M is the number of relays between the source and destination. In particular, there is one source node which communicates with one destination node. In the cooperative scenario, the destination can share its information with the partner which is operating as a relay (R). The relay node among M nodes, is willing to assist this communication by amplifying and forwarding (AF) the received signal to the destination without any further signal processing. Every node is equipped with two antennae and adopts a full diversity using Alamouti's scheme [55]. All nodes are assumed to adopt a half-duplex mode such that a node cannot transmit and receive simultaneously, but on different time slots.

As shown in Figure 3.1, the HP and LP bits after LDPC encoders are mapped into a sequence of symbols belonging to a constant modulus constellation such as M-ary phase shift keying. In the first hop, the symbols are encoded by space-time block encoder and sent simultaneously over the channel in multiple consecutive OFDM symbol intervals to the destination and the relay (R). Let $\mathbf{d} \triangleq [d[0], d[1], \cdots, d[N-1]]^T$ denote the symbol vector. In the first hop, the OFDM symbol is sent to the destination and the relay. For the direct link between the source and destination, the jth element of the received signal vector r_j^{SD} at the destination is given by [5, 7]

$$r_j^{SD} = \left(\sum_{i=1}^{N_{TX}} H_{j,i}^{SD} d_i \right) + n_j^{SD}, \quad j = 1, 2, ..., N_{RX} \tag{3.7}$$

where $H_{j,i}^{SD}$ is the channel frequency response between the jth receive antenna at the destination and the ith transmit antenna at the source, d_i is the sample of the OFDM symbol at the ith transmit antenna (with $i = 1, 2, \cdots, N_{TX}$), N_{TX} denotes the number of antennae at the source, $n_j^{SD} \sim \mathcal{CN}(0, \sigma_{SD}^2)$ for $j = 1, 2, \cdots, N_{RX}$ is AWGN and its elements are independent and identically distributed (i.i.d.), and N_{RX} denotes the number of antennae at the destination.

The received signal at the relay r^{SR} at kth relay antenna is given by:

$$r_k^{SR} = \left(\sum_{i=1}^{N_{TX}} H_{k,i}^{SR} d_i \right) + n_k^{SR}, \quad k = 1, 2, ..., N_R \tag{3.8}$$

where $H_{k,i}^{SR}$ is the channel frequency response between the ith transmit antenna at the source and the kth relay antenna at the relay, and is modeled as quasi-static Rayleigh fading channels and remain constant over the period of a transmit

OFDM symbol, $n_k^{SR} \sim \mathcal{CN}\big(0, \sigma_{SR}^2\big)$ for $k = 1, 2, \ldots, N_R$, and N_R denotes the number of antennas at the relay.

In the second hop, the relay performs the AF operation on the received signals (r^{SR}), where the relay first normalizes the received signals to yield normalized signal r_k^{SR} with $\mathbf{E}[|r_k^{SR_{best}}|^2] = 1$ and multiplies the received signal r_k^{SR} by the following gain factor [5, 7]:

$$G_k = \frac{1}{\sqrt{\left(\sum_{i=1}^{N_{TX}} |H_{k,i}^{SR}|^2\right) + \sigma_{SR}^2}}, \quad k = 1, 2, \ldots, N_R \tag{3.9}$$

Then, the relay forwards the signal to the destination. The jth element of the received signals r^{rd} at the destination is given by

$$\begin{aligned} r_j^{RD} &= \sum_{k=1}^{N_R} H_{j,k}^{R_{best}D} G_k r_k^{SR} + n_j^{RD} \\ &= \left(\sum_{k=1}^{N_R} \frac{H_{j,k}^{RD} \left(\sum_{i=1}^{N_{TX}} H_{k,i}^{SR} d_i \right)}{\sqrt{\left(\sum_{i=1}^{N_{TX}} |H_{k,i}^{SR}|^2\right) + \sigma_{SR}^2}} \right) \\ &\quad + \left(\sum_{k=1}^{N_R} \frac{H_{j,k}^{RD} n_k^{SR}}{\sqrt{\left(\sum_{i=1}^{N_{TX}} |H_{k,i}^{SR}|^2\right) + \sigma_{SR}^2}} + n_j^{RD} \right) \\ &\quad j = 1, 2, \ldots, N_{RX} \end{aligned} \tag{3.10}$$

where $n_j^{RD} \sim \mathcal{CN}\big(0, \sigma_{RD}^2\big)$ for $j = 1, 2, \ldots, N_{RX}$.

The received signals r_j^{SD} in (3.7) and r_j^{RD} in (3.10) are applied to the DFT operation. Maximal ratio combining (MRC) is utilized in the destination to obtain cooperative diversity gains by adding the decoding samples of the direct and relay links coherently.

3.4 Proposed UEP Schemes and Problem Formulation

Significant UEP schemes are proposed to solve three problems design for the 3-D video system.

3.4.1 Proposed UEP Schemes

The UEP Schemes are proposed to enhance the video transmission and reduce the data rates for transmission. These schemes classify the packets inside the each view of MVC. In addition, they classify the packets inside the colour and depth for the VpD. For MVC, the summary of each scheme is follows.

1. The first scheme, called partitioning-multi-view coding (P-MVC), employs packet partitioning, where SPS, PPS and I-frame packets in the first and second layer sequences are classified as HP packets while P-frame packets are considered as LP packets;

2. The second scheme, called P-MVC-1/4, considers the g_1 and I-frame packets in the first and second layers as the HP packets;

3. The third method, called P-MVC-1/2, considers g_1, g_2 and I-frame packets in both layers as the HP packets.

For VpD, the same classifications of packets are applied. Therefore, three UEP schemes, P-VpD, P-VpD-1/4 and P-VpD-1/2 are considered.

Note that for direct schemes, the D-MVC and D-VpD respectively denote direct-multi-view coding and direct-view plus schemes.

3.4.2 Problem Formulation and Solution

The proposed UEP schemes solve three problems which are:

3.4.2.1 The complexity of channel encoding and decoding

The LDPC performance in terms of the BER is shown in Figure 3.4 for the set of code length 2048 and fifty maximum iterations with variable coding rates $R = 8/16, 9/16, \ldots, 13/16$ under BPSK modulation.

The gap values are determined for each coding rate as shown in Table 3.3.

As can be observed from Figure 3.4, decreasing the code rates reduces the BER. On the other hand, it also increases the size of the gap as shown in Table 3.3. This leads to increased computational complexity for channel encoding and decoding. Therefore, the best method to solve this problem is to adopt the low code rates at low SNRs, and the moderate and high code rates at moderate and high SNRs, respectively. In this approach, high video quality is maintained at different SNRs and reduced the complexity of the system with improve of SNR

Table 3.3: Gap values at various code rates

Coding rates	Column weight(j)	Row weight (k)	Gap (g)
13/16	3	16	6
12/16	3	12	12
11/16	3	10	13
10/16	3	8	21
9/16	3	7	29
8/16	3	6	38

in the wireless channel. Therefore, a switching operation between the proposed UEP schemes is proposed to overcome this problem. This depends on increasing the code rate with an improvement of SNR in the wireless channel.

3.4.2.2 Direct transmission requires high bandwidth for transmission

In general, the direct schemes require more bandwidth for transmission compared to packets partitioning schemes. To overcome this problem, a packets partitioning method is proposed which significantly reduces the required bandwidth for transmission compared to the direct schemes.

To illustrate this point, the required data rate is measured to transmit MVC and VpD under different schemes. Table 3.4 shows the required data rates in Mbps for different MVC and VpD schemes, where the total date rate $R_T = \frac{R_{HP}}{r_{HP}} + \frac{R_{LP}}{r_{LP}}$ in bps, R_{HP} and R_{LP} are the bit rates for the HP and LP streams, respectively, r_{HP} and r_{LP} respectively are channel code rates for the HP-LDPC and LP-LDPC encoders as shown in Figure 3.1.

As shown in Table 3.4, it can be concluded that the packet partitioning schemes either for MVC or VpD significantly reduce the required data rates for transmission compared to the direct schemes. For example, the P-MVC-1/2 scheme at r_{HP}=4/16 requires less 0.7115 Mpbs than the D-MVC-1/2 scheme at r_{HP}=4/16 for the 'Car' sequence, 1.1894 and 0.48 Mpbs for the 'Hands' and 'Horse' sequences, respectively.

3.4.2.3 The different performance of direct and packets partitioning

The packets partitioning schemes are more reliable than direct schemes. However, the direct schemes are simpler than the partitioning schemes. Therefore, the best

Table 3.4: Comparison results of bitrate allocation for the proposed transmission schemes

Sequence	Scheme	r_{HP}	r_{LP}	R_T(MVC)	R_T(VpD)
Car	D-MVC	4/16	13/16	7.01	6.91
		8/16		3.76	3.844
		13/16		2.51	2.66
	P-MVC	8/16	13/16	3.029	3.027
	P-MVC-1/4			3.29	3.37
	P-MVC-1/2			3.56	3.7
	P-MVC	4/16	13/16	4.368	3.97
	P-MVC-1/4			5.332	5.21
	P-MVC-1/2			6.306	6.39
Hands	D-MVC	4/16	13/16	9.4384	8.27
		8/16		5.0932	4.28
		13/16		3.422	2.75
	P-MVC	8/16	13/16	3.963	3.44
	P-MVC-1/4			4.368	3.71
	P-MVC-1/2			4.762	3.97
	P-MVC	4/16	13/16	5.369	5.25
	P-MVC-1/4			6.829	6.21
	P-MVC-1/2			8.249	7.13
Horse	D-MVC	4/16	13/16	7.948	10.95
		8/16		4.466	6.13
		13/16		3.1266	4.288
	P-MVC	8/16	13/16	4.29	4.69
	P-MVC-1/4			4.481	5.25
	P-MVC-1/2			4.675	5.82
	P-MVC	4/16	13/16	7.336	5.76
	P-MVC-1/4			7.23	7.78
	P-MVC-1/2			7.8	9.81

solution for this problem is to strike a trade-off between the complexity of the partitioning schemes and the simplicity of the direct schemes. This is achieved by adopting the partitioning schemes at low and moderate SNRs, and the direct schemes at high SNRs. In this approach, high video quality is maintained at low and moderate SNRs and reduced the complexity of the system at high SNRs. This point will be explained in more details in subsequent sections.

3.5 Experimental Results and Discussion

To evaluate the performance of the proposed system and schemes, several experiments are conducted with typical 3-D video sequences of 'Car', 'Hands' and 'Horse' in [95], with 30 frames per second (fps) of 432×240 pixels and a GoP of 10. Each GoP is divided into four groups ($Ng = 4$) g_1, g_2,g_3, g_4. In this chapter, the MVC codec based on H.264 in [21, 37] is adopted for encoding the left and right views, while the H.264 reference software JM version (13.2) in [36] is used for encoding the right (colour) and depth sequences. The cooperative MIMO-OFDM system is designed according to its model in Section 3.3.7. Note that, in this chapter, the proposed schemes are evaluated under the assumption of the perfect knowledge of channel variations in terms of amplitude, phase and frequency variations. However, in Chapter 6, the channel variations is taken into account and the proposed schemes are evaluated over time-varying fading channels against the channel variations in terms of time varying phase noise and carrier frequency offset. Table 3.5 shows the simulation configurations.

To simulate the cooperative MIMO system with LDPC codes and OFDM technique, the following steps are taken: 1) The model of the cooperative MIMO system in (3.7)-(3.10) is simulated without LDPC codes and OFDM technique; 2) The simulation model is compared with the analytical model in ([97], Equation (33)) as shown in Figure 3.5 in terms of BER; 3) The LDPC codes and OFDM technique are added to the simulation model. As shown in Figure 3.5, there is strong agreement between the simulation results and the theoretical curve.

3.5.1 VpD Transmission Performance Compared to MRSC and SC Schemes

VpD is more sensitive to error propagation, since error bits in colour information propagate to the reconstructed left view. However, noise effects are not substantially noticed on the reconstructed 3-D video sequence when the right (colour)

Table 3.5: The simulation configurations

System parameters	Value
Source coding	H.264/AVC [36], H.264/MVC [21, 37]
Tested sequence	'Car', 'Hands' and 'Horse' [95]
Video sequence dimensions	(432x240) pixels
Down sampling factor	2:1
GoP	10
Channel	Quasi-static Rayleigh fading
Noise	AWGN
Relay protocol	AF
No. of antennae for source	2
No. of antennae for relay	2
No. of antennae for destination	2
CRC	16
Coding rates	4/16, 8/16 and 13/16 for UEP 13/16 for EEP
Diversity technique	Alamouti scheme
Guard period ratio	1/4
OFDM sub-channels	1024

view is perfectly reconstructed. For example, Figure 3.6 shows the performance of VpD compared to SC and MRSC formats at different percentage of corrupted packets and assumptions that the colour view is perfectly reconstructed and noise only affects the depth sequence. As shown in Figure 3.6, VpD is less affected by noise than other 3-D video coding techniques because of the depth sequence is only gray scales ranging from 0 to 255.

For video transmission over wireless channels, the required data rate to transmit SC, MRSC and VpD formats under different UEP and EEP schemes is firstly measured. Table 3.6 shows the required data rates for VpD using direct and packet partitioning schemes compared to SC and MRSC transmission, where the code rates $R_{HP} = 8/16$ and $R_{LP} = 13/16$ are adopted in this table.

Table 3.6: Required data rates for VpD transmission using direct and packet partitioning schemes compared to SC and MRSC transmission

Scheme	R_T for UEP	R_T for EEP
D-SC	4.027	3.047
D-MRSC	3.342	2.362
D-VpD	2.987	2.062
P-VpD	2.364	2.062
P-VpD-1/4	2.625	2.062
P-VpD-1/2	2.876	2.062

As illustrated in Table 3.6, the D-VpD scheme possesses better data rates than the D-SC and D-MRSC schemes. In addition, packet partitioning schemes for VpD have lower data rates compared to D-VpD.

Figure 3.7 compares the PSNR performance of D-VpD scheme with the D-SC and D-MRSC schemes. The results show that the performance of the D-VpD using UEP schemes is better than the D-SC and D-MRSC schemes because the depth sequence is not deeply affected by noise. Hence, it can be concluded that if the right (colour) view is reconstructed perfectly, the left view could be reconstructed acceptably even if the noise effects have spread in the depth sequence. This fact is clearly observed when the colour receives more error protection than the depth using the UEP technique. Moreover, decreasing the data rates reduces the video signal protection, which makes the video signal more sensitive to error propagation. This fact can be clearly seen in the VpD, SC and MRSC using EEP scheme;

It is clear from the results in Figure 3.7 that the VpD has better PSNR performance compared to SC and MRSC formats and is more suitable for 3-D video transmission.

3.5.2 Performance Comparison between Partitioning and Direct Schemes using VpD and MVC Schemes

Figures 3.8 and 3.9 plot the average decoded 3-D video quality in terms of PSNR with different direct and packets partitioning schemes for MVC and VpD for 'Car', 'Hands' and 'Horse' sequences, respectively. The results lead to the following observations:

1. In Figure 3.8, the performance of the packets partitioning schemes (P-MVC, P-MVC-1/4,..., etc.) either for r_{HP}=4/16 or r_{HP}=8/16 significantly improve the system performance compared to the direct schemes at different SNRs (-9 (minus 9) to -2 dB). For example, the P-MVC-1/2 (r_{HP}=4/16) and P-MVC-1/4 (r_{HP}=4/16) schemes in Figure 3.8-(a) improve the PSNR with 7.8 and 2.94 dB compared to D-MVC-1/2(r_{HP}=4/16) at SNR=-7 dB;

2. In Figure 3.9, the performance of the packets partitioning schemes (P-VpD, P-VpD-1/4,..., etc.) compared to direct schemes (D-VpD) is very close and improves the PSNR at different SNRs. For example, in Figure 3.9-(a), the difference PSNR between the P-VpD-1/2 and D-VpD-1/2 at r_{HP}=4/16 is 0.3 dB at SNR=-8 dB, while their performance is very close with the increasing of SNRs. In addition, if the P-VpD-1/4(r_{HP}=4/16) is compared with D-VpD(r_{HP}=8/16) at SNR=-8 dB, the improvement of PSNR=4.13 dB;

3. The packets partitioning schemes maintain the system to provide high PSNR although the SNRs are changed in the wireless channel. For example, in Figure 3.8-(a), the P-MVC-1/2(r_{HP}=4/16) scheme enhances the system to achieve PSNR between 32.51 to 38.45 dB over SNRs from -9 to -2 dB. In addition, in Figure 3.9-(c), the P-MVC-1/2 (r_{HP}=4/16) scheme maintains the system with PSNR=34.41 to 37.96 dB at different SNRs. This regards to the isolation method of HP packets inside the right (colour) view and left/depth sequence. In this case, the noise only affects the LP packets which do not affect on the overall reconstructed video quality; and

4. The decreasing in the data rate reduces video signal protection, which makes the video signal more sensitive to error propagation. This fact can be seen clearly seen in the D-MVC and D-VpD schemes at r_{HP}=13/16. Therefore, the system has to resort to UEP schemes for enhancing the system at different SNRs. However, the UEP schemes make the channel encoding and decoding operations more complicated, and require high data rates for transmission. Therefore, with suitable allocation of the channel code rates based on the channel's SNR, the high system performance with a lower computational complexity of encoding and decoding operations, and data rates can be achieved. Therefore, the Switch-1, Switch-2, Switch-3 and Switch-4 circuits are proposed as shown in Figure 3.1 that switch to the packets partitioning schemes (P-MVC, P-MVC-1/2,. . . , P-VpD, P-VpD-1/2,. . . ,etc.) at low and moderate SNRs, while they switch to direct schemes at high SNRs. Thus, this adaptive technique achieves a trade-off between the display the 3-D video signal with high video quality at low and moderate SNRs and reducing the complexity of the encoding and decoding operations as well as the required data rates at high SNRs.

3.5.3 The 3-D Video Protocol

In Figures 3.8 and 3.9, the performance of P-MVC-1/2 (r_{HP}=4/16) or P-VpD-1/2 (r_{HP}=4/16) scheme is better than other schemes at low SNRs between -9 to -5 dB, while their performances are close and match with other schemes at moderate and high SNRs (-5 to -3 dB), respectively. Based on this observation, it can be considered the SNR=-5 and -3 dB as SNR thresholds which can be exploited to make the control unit switch the system from a scheme to another to keep high video quality with reducing the data rates and system complexity according to the improvement of SNRs. Therefore, the control unit controls the system to adopt the following 3-D video protocol to achieve high video quality at different channel states with the lowest bandwidth and system complexity. This protocol is: the P-MVC-1/2 (r_{HP}=4/16) or P-VpD-1/2 (r_{HP}=4/16) scheme is adopted for transmission between SNR=-9 and less than -5 dB, the P-MVC-1/4(r_{HP}=8/16) or P-VpD-1/4(r_{HP}=8/16) is used between SNR=-5 and less than -3 dB, and the D-MVC (r_{HP}=13/16) or D-VpD (r_{HP}=13/16) scheme is utilized when SNR is greater than or equal to -3 dB.

For comparative purposes, Figure 3.10 shows the reconstructed left and right pictures for the 'Car' video sequence at frame 19 under different transmission

schemes in the protocol at different SNRs. According to the proposed protocol and Figure 3.10, the proposed system is highly flexible in adapting to the quality of the underlying wireless channel.

3.5.4 Performance Comparison between VpD and MVC Schemes

If Figure 3.8 is compared with Figure 3.9 at different video sequences and schemes, it is seen that VpD schemes either using direct or packet partitioning are better than MVC schemes at low SNRs (-9 to -5 dB), while their performance are close at moderate and high SNRs (-5 to -2 dB). For example, in Figures 3.8-(b) and 3.9-(b), the P-VpD-1/2 (r_{HP}=4/16) scheme achieves PSNR=30.02 dB at SNR=-9 dB, while P-MVC-1/2 (r_{HP}=4/16) achieves PSNR=26.31 dB. This fact is due to the depth structure which is less affected by noise. Therefore, the VpD is more appropriate for 3-D video transmission at low SNRs. These SNRs values (-5 and -3 dB) are called as SNR thresholds that make the system switch from one scheme to another.

3.5.5 Threshold SNR Selection

The SNR thresholds are determined by the design of the wireless system such as the cooperative MIMO-OFDM system in this chapter. To apply this threshold approach in more general cases, the control unit can be made to respond to the number of packets which are lost at the video decoder and the positions of these packets in the GoP. This is easily achieved using CRC. For example, if the D-MVC scheme is adopted and the decoder loses the g_1 and g_2 packets in a certain GoP. This means the SNR in the channel is low. Therefore, the control unit will switch the transmitter to adopt the P-MVC-1/2 scheme for transmission in the next GoP to overcome the low SNR problem until the SNR improves, then the control unit will switch the transmitter to adopt the D-MVC scheme again.

3.6 Conclusion

This chapter put forward a novel UEP scheme, called video packet partitioning, to transmit 3-D video sequences. Various UEP schemes depending on this scheme were proposed to isolate the important packets inside the right/or colour and left/or depth sequences. A new 3-D video transceiver was proposed. In par-

ticular, the video transceiver adopts various UEP schemes with two error resilient methods to overcome the effects of error propagation in the 3-D video streams. The proposed video transceiver and UEP schemes were tasted over the cooperative MIMO-OFDM system. A new 3-D video protocol was proposed that adopts the best UEP schemes to achieve high video quality at different SNRs with the lowest bandwidth and system complexity. A unique efficient control units in the transmitter and receiver were suggested to perform the many tasks needed to achieve a high video quality. Simulation results on standard video sequences showed that the system is less complex and always provides high PSNR at every SNR compared to the direct schemes. Therefore, the proposed system provides a high level of flexibility and efficiency to adapt to the conditions of the wireless communication channel.

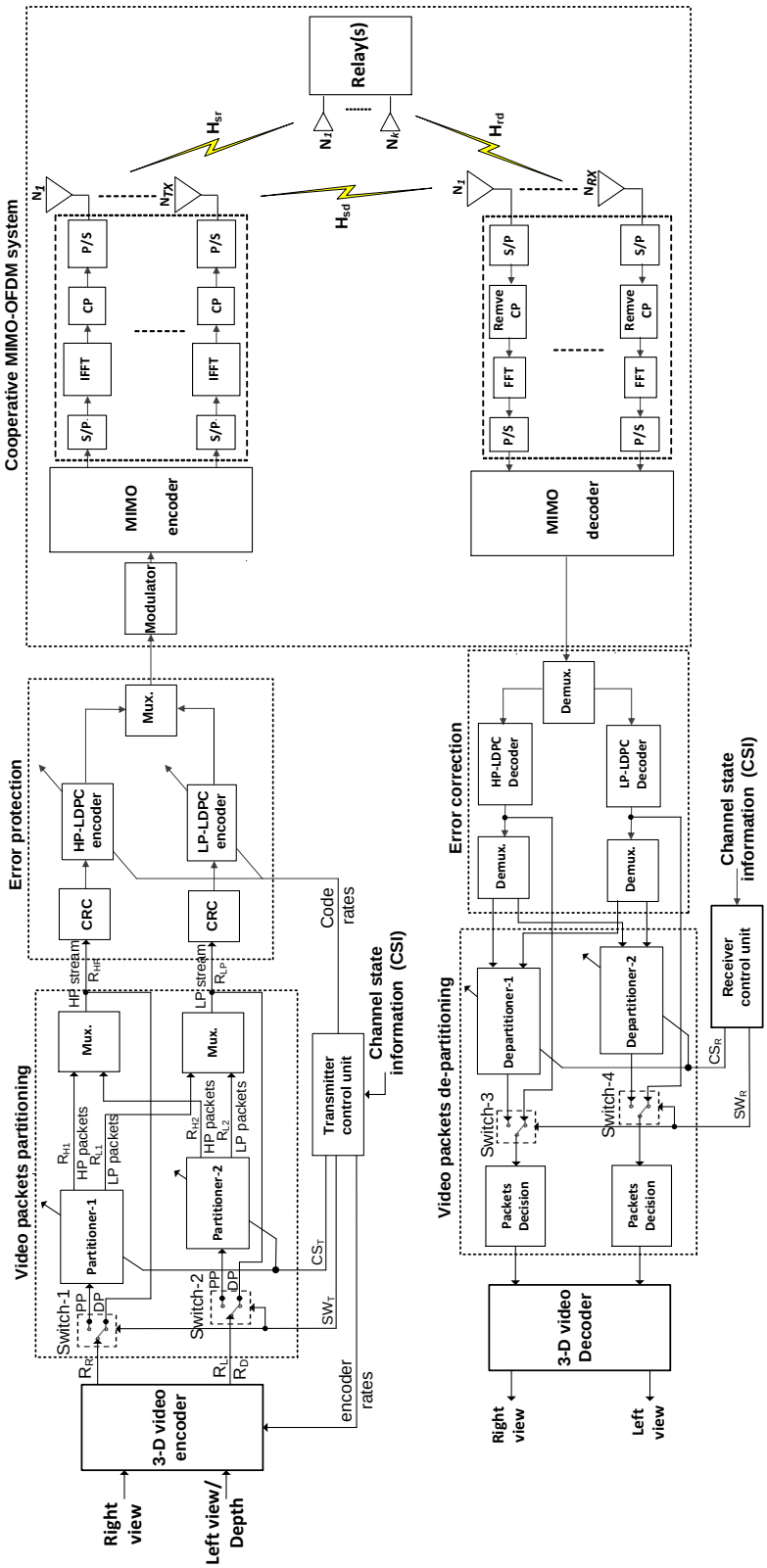

Figure 3.1: Block diagram of the proposed cooperative MIMO-OFDM system for 3-D video transmission.

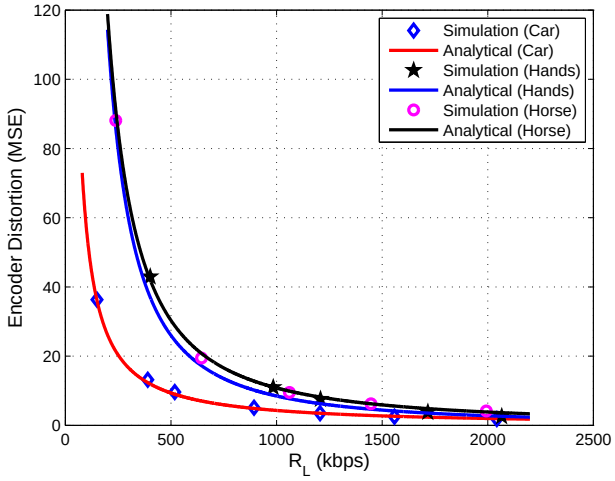

(a) Left view

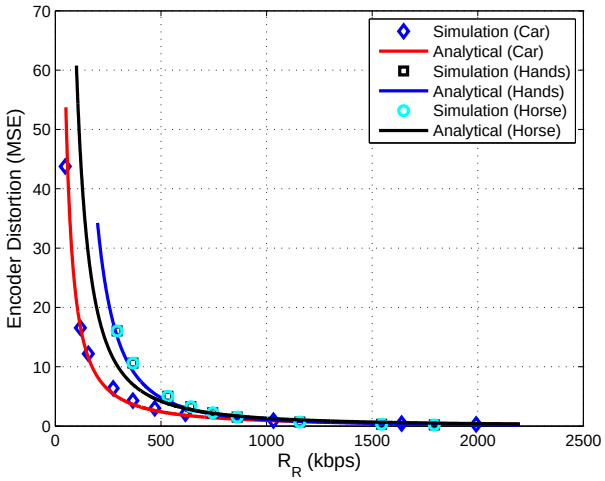

(b) Right view

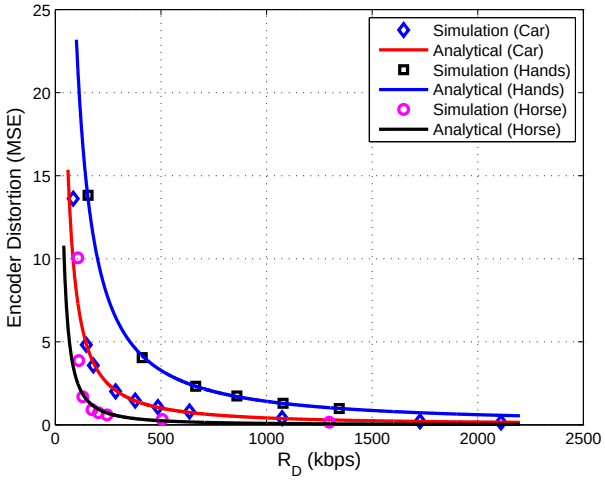

(c) Depth sequence

Figure 3.2: Rate-distortion curves for the left view, the right view and the depth sequence.

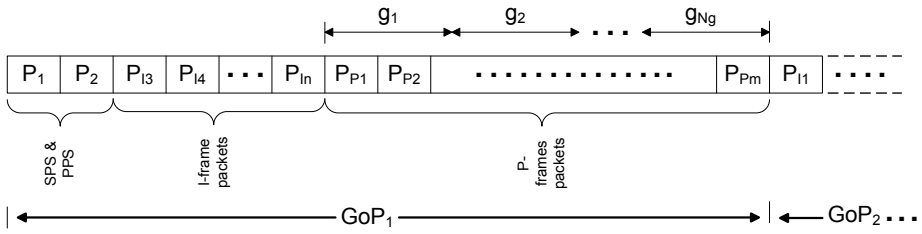

Figure 3.3: Produced video packets and their types after the video encoder.

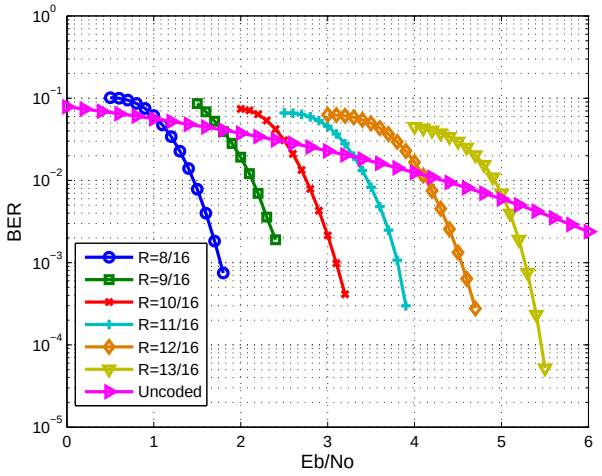

Figure 3.4: Performance of LDPC codes at different coding rates.

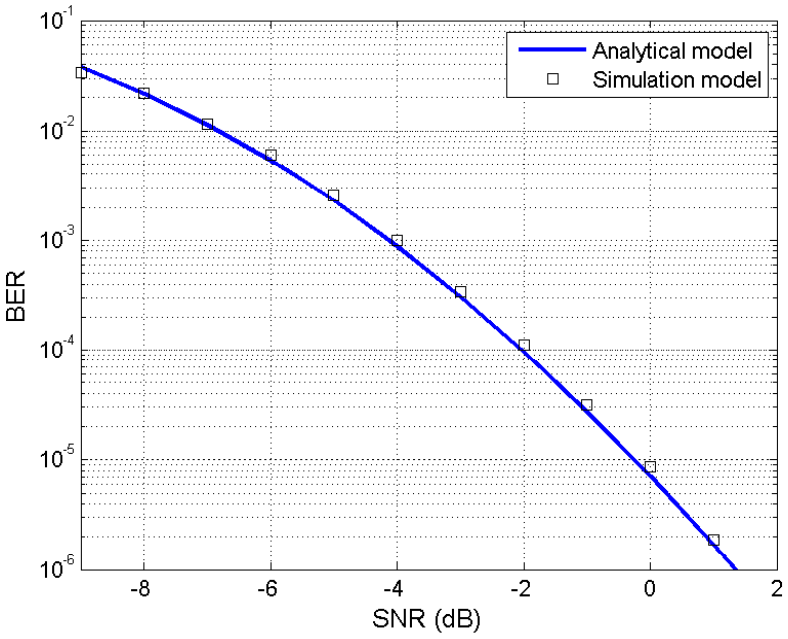

Figure 3.5: Comparison between the simulation model of the cooperative MIMO system and the model in [97].

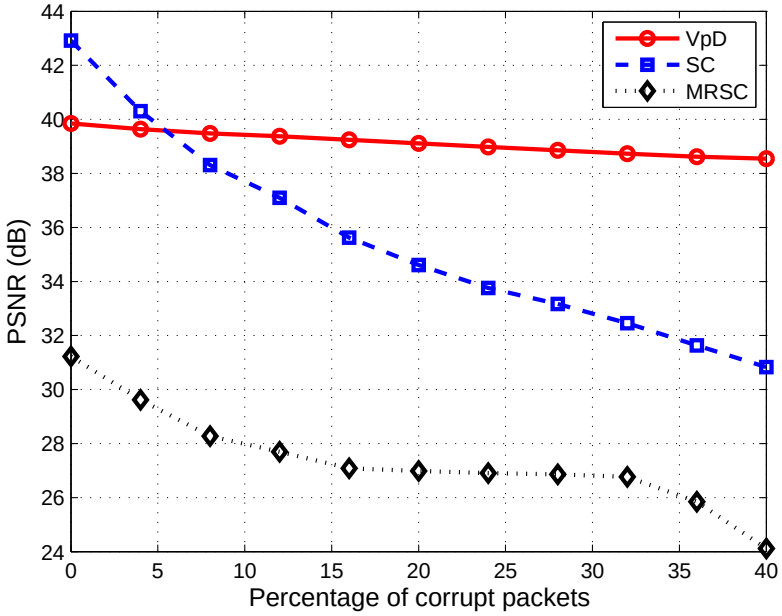

Figure 3.6: Performance of VpD compared to SC and MRSC formats at different percentage of corrupted packets.

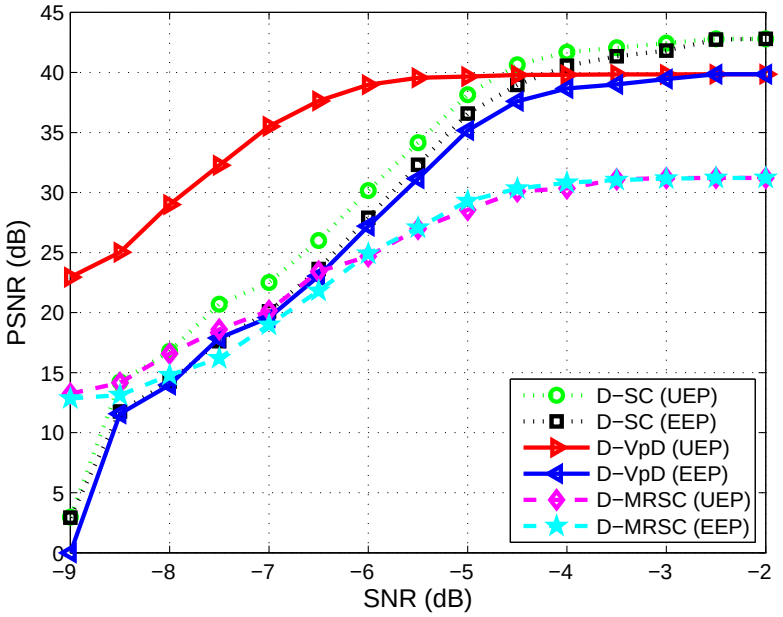

Figure 3.7: PSNR performance for D-VpD scheme compared to D-SC and D-MRSC schemes at $R_{HP} = 8/16$ and $R_{LP} = 13/16$ for UEP and $R_{HP} = R_{LP} = 13/16$ for EEP.

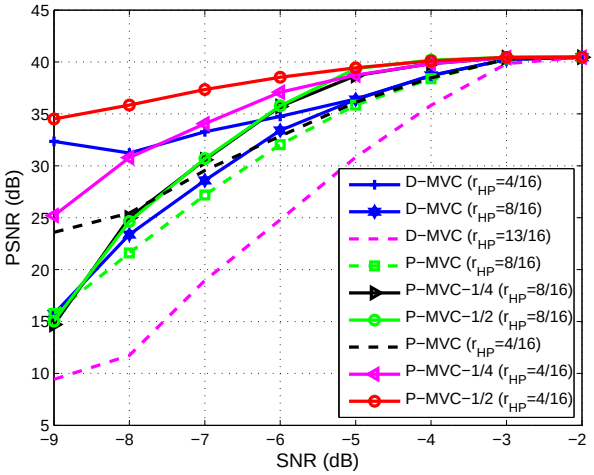

(a) Car sequence

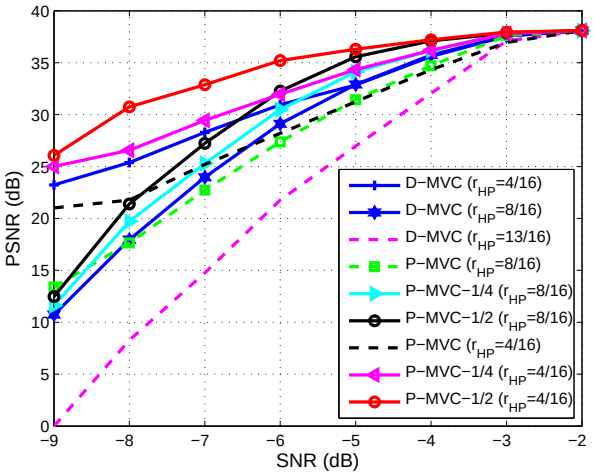

(b) Hands sequence

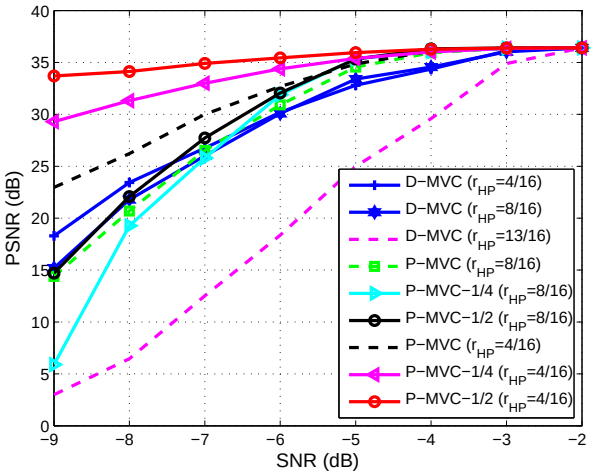

(c) Horse sequence

Figure 3.8: Comparison of the packet partitioning and direct schemes in terms of PSNR for MVC at different video sequences.

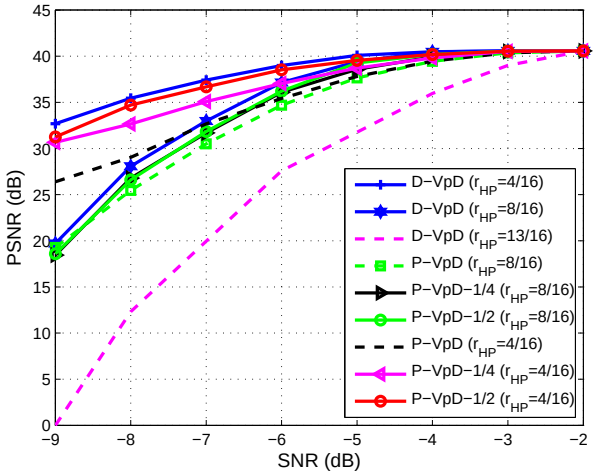

(a) Car sequence

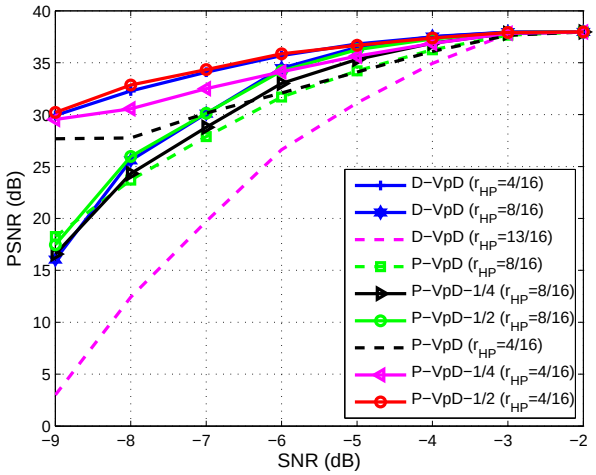

(b) Hands sequence

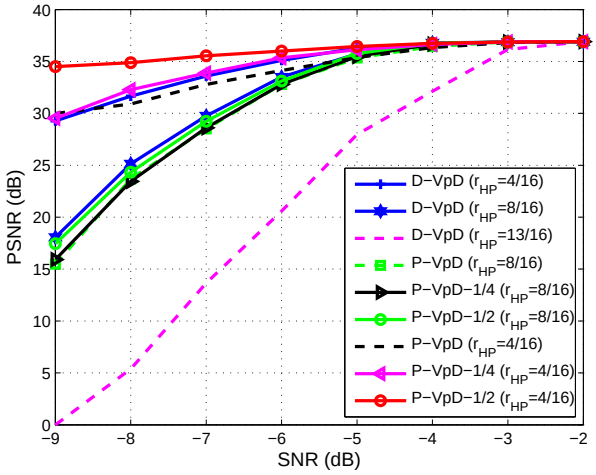

(c) Horse sequence

Figure 3.9: Comparison of the packet partitioning and direct schemes in terms of PSNR for VpD at different video sequences.

(a) Left view (b) Right view

(c) Left view (d) Right view

(e) Left view (f) Right view

Figure 3.10: The reconstructed left and right pictures for the 'Car' video sequence at frame 19 under different transmission schemes in the protocol at different SNRs; (a,b) include P-MVC-1/2 (r_{HP}=4/16) or P-VpD-1/2 (r_{HP}=4/16) at SNR = -8 dB; (c,d) include P-MVC-1/4(r_{HP}=8/16) or P-VpD-1/4(r_{HP}=8/16), at SNR = -4 dB; (c,d) include D-MVC (r_{HP}=13/16) or D-VpD (r_{HP}=13/16) when SNR greater than -3 dB.

Chapter 4

Joint Source-Channel Coding for 3-D Video Transmission over Cooperative Relay Systems

4.1 Introduction

Increasing the number of relays leads to increased time slots required to transmit the signal from the source to the destination, and also leads to a decreased system throughput. To overcome this problem, best relay selection can be adopted. Moreover, in cooperative relay systems, the AF protocol may be more preferable to use than the DF protocol at the relay because it requires lower computational complexity and time delay. This due to the AF protocol which does not require the channel encoding and decoding operations at the relay [60]. Therefore, in this chapter, the AF protocol is considered through the adoption of the best relay selection for video applications.

In the scenario of best relay selection, only a single relay out of the set of available relays is selected based on maximum instantaneous SNR between the source-relay-destination (γ_{SRD}). At each time of relay selection, the γ_{SRD} value is varied as well as the variation of the γ_{SD} value in the source-destination channel. Hence, the end-to-end instantaneous SNR (γ_{coop}) must be communicated to the source and destination, where $\gamma_{coop} \triangleq \gamma_{SD} + \gamma_{SRD}$. The feedback of γ_{coop} can be used to adapt the structure design of the source and destination to the variations of the channels before starting to transmit the video signal. Therefore, the design complexity of the transmitter and receiver, as well as the system performance,

are completely determined by the accuracy of the estimation of the overall SNR (γ_{coop}). This accuracy estimation of γ_{coop} dramatically impacts on the overall performance and complexity of the system. Errors in the estimation of γ_{coop} degrade the overall performance and increase the complexity of the system.

The feedback scenario utilized in [7], is proposed for 2-D video transmission to adapt the system to variations in the channels. However, in [7], the adaptation scheme is based on the assumption that γ_{coop} is *perfectly* known at the source and destination. The study of the impact of feedback estimation (γ_{coop}) on the system performance for 3-D video transmission over cooperative systems has not been addressed in the literature to date.

The existing JSCC algorithms focus on sharing R_{budget} between the source and channel coding operations based only on fixed UEP operations [20, 21]. Here, an end-to-end rate-distortion (R-D) model is proposed for MVC to achieve the optimal encoder bit rates and channel code rates. Moreover, the UEP is performed on a fixed structure of three MVC layers, called layer 0, layer 1 and layer 2, with a fixed number of frames in each layer. However, this restricted model makes the video system unable to be adapted to the variations in wireless channels. In [22], the JSCC algorithm is proposed for the VpD transmission over WiMax systems. However, the UEP scheme adopted for transmission based on direct schemes, which requires high data rates for transmission and has lower performance compared to packet partitioning schemes. Moreover, the JSCC algorithm in [22] depends on certain values of source and channel code rates. In addition, the proposed system in [22] used a single antenna and did not utilize any type of diversity techniques to improve the system performance. More importantly, UEP based on packet partitioning schemes for 3-D video transmission has not been considered in the proposed JSCC algorithms in [20–22]. Moreover, the unequal importance of packets inside the right (colour) and left/depth is not considered in [20–22] in formatting the HP and LP streams of JSCC algorithms.

In the existing literature such as [98, 99], the problem of cross-layer design of joint video encoding rate control, power control, relay selection and channel assignment for cognitive ad hoc networks and cooperative relays is addressed. Moreover, the problem of joint optimization of power and cache control to support real-time video streaming is addressed in [100]. However, the proposed algorithms in [98–100] are only applicable for 2-D video applications. More importantly, UEP schemes based on packet partitioning are not considered in [98–100].

To the best of author's knowledge, the framework of the estimation procedures of the end-to-end instantaneous SNR for cooperative systems based on the best

relay selection, and efficient JSCC algorithms for cross-layer optimization based on packet partitioning schemes, is not addressed in the literature. In addition, the simulation results show that JSCC approaches reported in the literature are significantly outperformed by the JSCC algorithm proposed in this chapter.

It is worth mentioning that this chapter does not exploit any advanced estimation techniques for γ_{coop}, since channel estimation techniques are beyond the scope of this chapter. However, some examples of estimation error in γ_{coop} are provided to show that there is an additional factor related to the accuracy of estimation of γ_{coop} that directly affects the performance of cooperative video systems and has to be considered in the design of multimedia cooperative communication systems with feedback.

4.2 Contributions

The contributions of this chapter are four-fold:

1. A novel JSCC optimization algorithm is proposed based on Lagrange multipliers, which is controlled by the R_{budget} and the estimated γ_{coop}.

2. The proposed algorithm simultaneously optimizes the application layer parameter, quantization parameters (Q_p), and the network layer parameters, these are the number of packets of HP and LP streams and other physical layer parameters, these are the channel code rates.

3. Several experiments are carried out with different typical 3-D video sequences to investigate the performance of the proposed JSCC algorithm at different R_{budget} and γ_{coop} values.

4. The impact of γ_{coop} estimation on the video system performance and complexity is investigated. Experimental results show that the performance and complexity of wireless video systems are very sensitive to accurate estimation of γ_{coop}.

The remainder of this chapter is organized as follows. Section 4.3 describes the system model. Section 4.4 presents problem formulation and solution. Section 4.5 provides experiential results and discussion. Section 4.6 shows the impact of γ_{coop} estimation on video system performance. Finally, Section 4.7 concludes this chapter.

4.3 System Model

A cooperative system with $M+2$ nodes, which consists of one source node communicating with one destination node and M relays, as illustrated Figure 4.1 is considered. The best relay node with maximum γ_{SRD}, namely R_{best} among M relay nodes, is willing to assist this communication by the AF protocol.

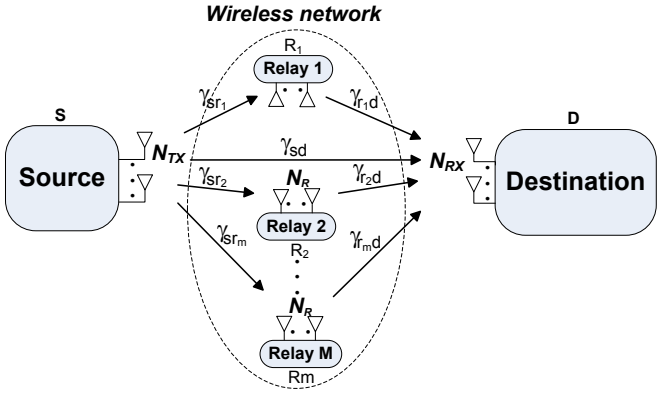

Figure 4.1: Wireless cooperative MIMO relay network.

The description of the system model is similar to that detailed in Chapter 3, and is not presented here to avoid repetition. In the following sub-sections, some parts of the system proposed in Chapter 3 are explained in greater detail from the point-of-view of the proposed JSCC algorithm.

4.3.1 Video Packet Partitioning

As mentioned in Chapter 3 and shown in Figure 4.2, the packets in GOP can be classified to HP packets (N_{HP}) and LP packets (N_{LP}) according to their effect on the total video quality at the video decoder. As explained in Chapter 3 and shown in Figure 4.2, the GOP packets include I and P slice packets as well as the packets of SPS and PPS. According to the tests in Chapter 3, the priority order of the GoP packets for error protection from high to low is P_1, P_2, P_{I_3},..., P_{P_m}.

In this chapter, the proposed JSCC algorithm is designed to allocate as much as possible of the prior packets of a GOP (N_{HP}) to the HP stream when the available γ_{coop} is low. At high γ_{coop}, the JSCC algorithm is designed to use the direct schemes, which depend on transmitting whole video packets without

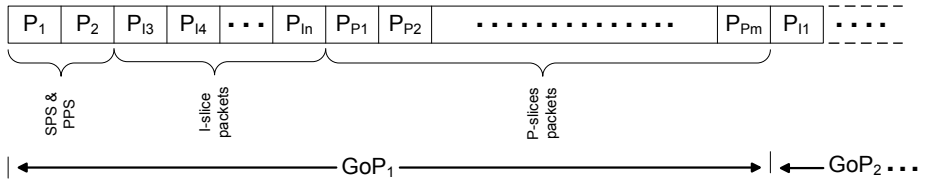

Figure 4.2: Produced video packets and their types after the video encoder.

using packet partitioning, to reduce the complexity associated with the packet partitioning operation.

4.3.2 Error Protection

As explained in Chapter 3, decreasing the code rates reduces the BER. On the other hand, it also increases the computational complexity of the channel encoding and decoding operations. Therefore, the JSCC algorithm proposed in this chapter is designed to use high code rates whilst maintaining high video quality in order to reduce the complexity.

4.3.3 Control Units

As explained in Chapter 3, the proposed system utilizes two control units at the network layer of the source and destination.

Note that in this chapter, a block-fading channel model is used, where the channel is invariant for several time slots. This channel model can be exploited by the proposed control units to maximize the system performance, while minimizing the complexity. However, if the channel varies quickly (as may occur in mobile applications), the system will resort to using one of UEP schemes based on the packet partitioning in Chapter 3. The UEP schemes in Chapter 3 can achieve high PSNR at different SNRs. However, they require a high data rate and computational complexity in the channel encoding and decoding operations. As can be observed from the simulation results in Chapter 3, the system can adopt the P-VpD-1/2 or P-MVC-1/2 scheme for the transmission and neglect to use feedback, with a corresponding increase in the data rate and system complexity.

4.3.4 Cooperative MIMO-OFDM Systems

In this chapter, a time division multiplexing (TDM) protocol is adopted for transmission between the source, relays and destination. Therefore, each node is allowed to transmit the signals in one time slot. Moreover, a frame of several time slots is required to transmit the training symbols for estimating the γ_{coop} throughout the system and sending the video data through the relays to the destination. Figure 4.3 shows the organization of time slots for the proposed framework of the estimation procedures of γ_{coop} and the transmission of video bitstreams. As shown in Figure 4.3, each frame is composed of five time slots, denoted by t_1, t_2, t_3, t_4 and t_5. The first three time slots in each frame, i.e., t_1, t_2 and t_3 are used to estimate γ_{coop}. The fourth and fifth time slots, i.e., t_4, t_5 are used to transmit the video bitstreams to the best relay and destination.

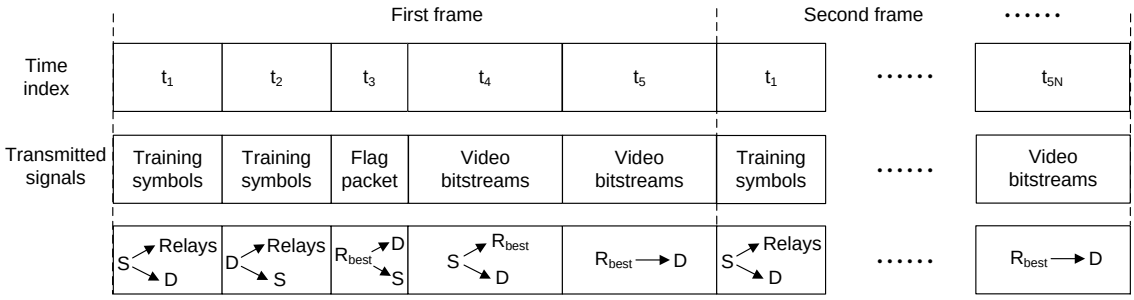

Figure 4.3: Organization of time slots of the proposed framework.

The estimation procedures of γ_{coop} will be explained in detail in Section 4.4.1, while the video transmission scenario during the fourth and fifth time slots, t_4 and t_5, is presented in Chapter 3 (Section 3.3.7) and is not presented here to avoid repetition.

In this chapter, the following set of assumptions are adopted: A1) All nodes adopt a half-duplex mode such that a node cannot transmit and receive simultaneously, but on different time slots; A2) The link channel is modeled as a slow fading frequency-selective channel. That is the channel is assumed to be quasi-static block fading and is constant during the time slots (t_1, t_2, t_3, t_4 and t_5, as shown in Figure 4.3) of the frame, and changes from frame to frame following a complex Gaussian distribution; A3) The best relay node with maximum γ_{SRD}, namely R_{best} among M relay nodes, is willing to assist this communication by amplifying and forwarding (AF) the received signal to the destination without

any further signal processing; A4) Every node is equipped with two antennae and adopts a full diversity approach using Alamouti's scheme [55].

Note that assumptions A1 and A2 are in line with previous studies in [7, 101–104] and applicable for mobile terminals moving at walking speed. Furthermore, assumptions A3 and A4 are adopted in [7, 32, 33, 61–65].

4.4 Problem Formulation and Solution

The two main problems which have to be considered in the design of a cooperative system for 3-D video applications are as follows:

4.4.1 Procedures to Estimate γ_{coop}

As explained in Chapter 3, the video source and destination nodes have to feed the estimated γ_{coop} to the control units before beginning to send the video signal. In this chapter, procedures to estimate γ_{coop} is proposed based on estimating the instantaneous SNRs for the channels of the source-destination (γ_{SD}), and source-relay-destination (γ_{SRD}). As mentioned earlier and shown in Figure 4.3, the estimation procedures require three time slots, t_1, t_2 and t_3, for estimation by sending the training symbols throughout the cooperative system.

The procedures to estimate γ_{coop} for video applications are illustrated in Figure 4.4, as follows:

1. In the first time slot, as shown in Figure 4.4-(a), the source sends training symbols to all the relays and the destination, where the relays and destination are in listening mode. The training symbols are known for all the nodes in the system. Each relay can estimate the channel coefficients ($H_{SR_m}, m = 1, \ldots, M$) of the source-relay channel, while the destination can estimate the channel coefficients (H_{SD}) of the source-destination channel. In this time slot, the destination will have good knowledge of the link quality between the source and destination;

2. In the second time slot, as shown in Figure 4.4-(b), the destination sends training symbols to the all the relays and the source. In this time slot, the relays and the source are in listening mode. Therefore, each relay can estimate the channel coefficients ($H_{R_m D}, m = 1, \ldots, M$) of the channel between the destination and the relay (R_m). Meanwhile, the source can estimate the coefficients (H_{SD}) of the source-destination channel. Therefore, the source

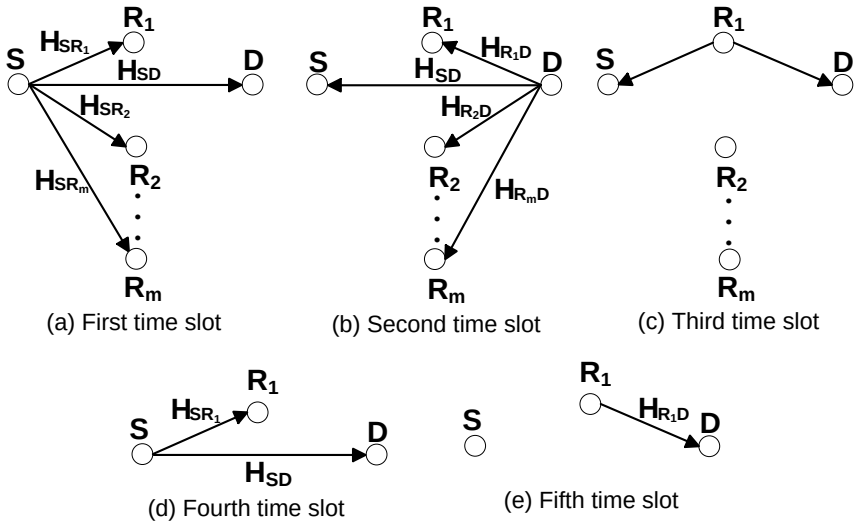

Figure 4.4: (a)-(c) Show procedures to estimate the γ_{coop} for video applications, while (d) and (e) show the required time slots for the transmission.

will have good knowledge of the link quality between the source and destination;

3. In the third time slot, as shown in Figure 4.4-(c), each relay depends on the estimated channel coefficients in the first and second time slots to calculate the instantaneous SNR value between the source and relay (γ_{SR_m}), and the instantaneous SNR values between the destination and relay (γ_{DR_m}). These two values are used to calculate the total instantaneous SNR between the source-relay-destination (γ_{SR_mD}) as in [5]

$$\gamma_{SR_mD} = \frac{\gamma_{SR_m}\gamma_{R_mD}}{\gamma_{SR_m} + \gamma_{R_mD} + 1}, \tag{4.1}$$

As explained in ([61], Section II), each relay utilizes a timer, which is set to be inversely proportional to the γ_{SR_mD}. The best relay, which has a maximum γ_{SR_mD}, will expire first and send a short duration *flag* packet to inform the source and destination that is ready to communicate the source with the destination, while the remaining relays will be backed-off. The *flag* packet can also be exploited to inform the source and destination of

the instantaneous SNR ($\gamma_{SR_{best}D}$) of the source-best relay (R_{best})-destination channel; and

4. In the fourth time slot, the source and destination calculate the end-to-end instantaneous SNR as

$$\begin{aligned} \gamma_{coop} &= \gamma_{SD} + \max_{m \in M} \Big[\frac{\gamma_{SR_m} \gamma_{R_m D}}{\gamma_{SR_m} + \gamma_{R_m D} + 1} \Big], \\ &= \gamma_{SD} + \frac{\gamma_{SR_{best}} \gamma_{R_{best} D}}{\gamma_{SR_{best}} + \gamma_{R_{best} D} + 1} \end{aligned} \tag{4.2}$$

where M is the number of users, $\gamma_{SR_{best}}$ is the instantaneous SNR between the source and the best relay (R_{best}), and $\gamma_{R_{best}D}$ is the instantaneous SNR between the R_{best} and the destination.

The source and destination feed the estimated γ_{coop} to the control units. Then, in the fourth time slot as shown in Figure 4.4-(d), the source will start to broadcast the 3-D video signal to the best relay and destination simultaneously. In the fifth time slot as shown in Figure 4.4-(e), the best relay will start to broadcast the amplified video signal to the destination.

To calculate γ_{coop} in (4.2), the γ_{SD} and γ_{SR_mD} have to be estimated. As shown in Figure 4.4, the source, each relay and the destination can estimate the instantaneous SNR of the source-destination (γ_{SD}), source-relay (γ_{SR_m}) and relay-destination (γ_{R_mD}) during the first, second and third time slots. According to these time slots, the system model for each slot is similar to traditional MIMO-OFDM systems. Therefore, the instantaneous SNR for the MIMO-OFDM system can be estimated by adopting one of the proposed methods in the literature such as the estimation methods in [105–107].

Finally, the framework of estimation procedures of γ_{coop} and the scenario of video transmission over the cooperative system is summarized in Figure 4.5.

It is worth mentioning that: 1) The procedures as shown in Figure 4.4 are repeated automatically after broadcasting the GOPs of the 3-D video signal. The broadcasting of the video signal is performed in the fourth and fifth time slots, i.e., t_4 and t_5, as illustrated in Figure 4.3, after estimating γ_{coop} in the first three time slots of the frame (t_1, t_2, t_3). Therefore, the best relay selection is performed automatically at the start of each frame and the best relay is updated from frame to frame. Hence, the control units can change the design of the source and the destination to track the variations of the wireless channels from frame to frame; 2) The length of training symbols is usually 256 subcarriers, and each of which is

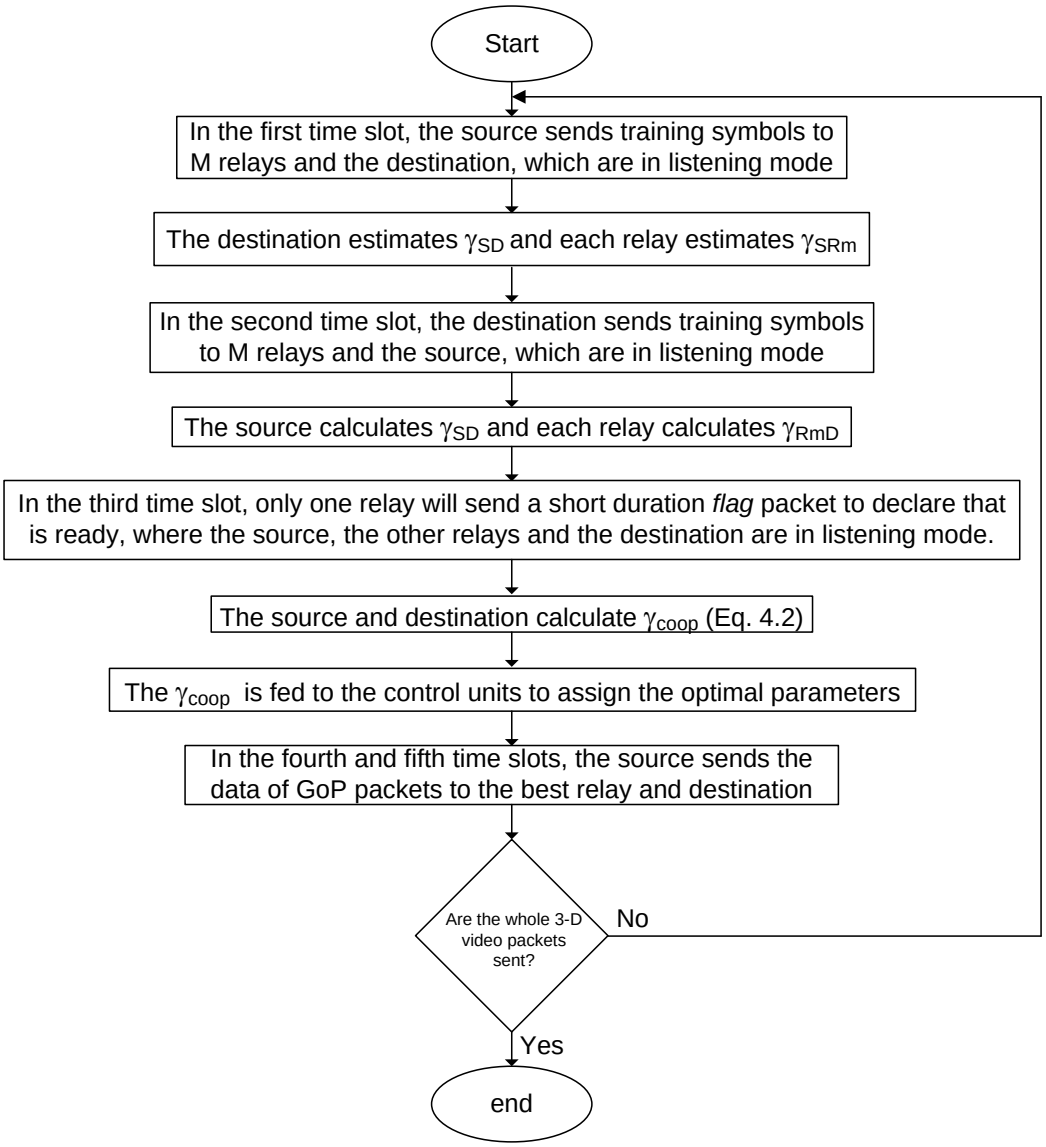

Figure 4.5: Summarization of γ_{coop} estimation for video applications and γ_{coop} estimation is updated after broadcasting GOPs of 3-D video signal per second.

modulated by QPSK modulation [105]. The number of data symbols is normally greater than the number of training symbols. For example, if the number of training symbols is 256 and the length of the source data vector is set to 2560 symbols during the data packet, the resulting overhead is 9 %; 3) It is observed in [105–107] that the performance of SNR estimators can achieve a MSE between

10^{-2} to 10^{-3}, where MSE $\triangleq (\hat{\gamma} - \gamma)^2$, $\hat{\gamma}$ and γ are the estimated and actual instantaneous SNR, respectively. Therefore, γ_{coop} will be directly affected by the accuracy of SNR estimator. To illustrate the impact of estimated γ_{coop} on the video system performance, examples of the estimation error for γ_{coop} are given in Section 4.6.

4.4.2 Practical Scenarios of using Relays for Video Transmission

Best relay selection can be considered as the best method for prioritizing the relays in cooperative networks. However, this method poses some obstacles including extra overhead and scheduling in distributing feedback [108]. To reduce the overhead, two transmission approaches can be followed. The first approach, which is adopted by the 802.11 standard, includes each relay sending a back off signal in randomly selected periods of time, which are uniformly distributed in a range, called the contention window. The second approach is adopted in [108] and depends on assigning high priority relays a smaller contention window than lower priority relays. Thus, the high priority relays are more likely to transmit packets first.

4.4.3 Rate-Distortion Analysis for 3-D Video System

As explained in Chapter 3, the total end-to-end distortion (D_T) can be minimized by adopting suitable source and channel code rates for the video and LDPC encoders that minimize video distortion of the source and channel in the reconstructed left and right views. In addition, the video packet partitioning reduces the total data rates for transmission and improves the video system performance.

4.4.3.1 Source and channel rates for the proposed system

As shown in the proposed system in Chapter 3, two LDPC codes, i.e., HP-LDPC and LP-LDPC encoders, are utilized to protect the HP and LP streams with different or equal code rates. The total bit rate (R_T) in bps is given by

$$R_T = \frac{R_{HP}}{r_1} + \frac{R_{LP}}{r_2} \tag{4.3}$$

where R_{HP} and R_{LP} are the bit rates for the HP and LP streams, respectively, r_1 and r_2 are channel code rates for the HP-LDPC and LP-LDPC encoders, respectively.

As explained in Chapter 3, the R_{HP} and R_{LP} are determined according to the transmission scheme adopted, i.e., direct or packet partitioning schemes, which are usually adopted according to the end-to-end instantaneous SNR (γ_{coop}). Therefore, the R_{HP} and R_{LP} can be calculated as:

$$R_{HP} = \begin{cases} R_{H_1} + R_{H_2} & \gamma_{coop} < \gamma_{th} \\ R_R & \gamma_{coop} \geq \gamma_{th} \end{cases} \tag{4.4}$$

$$R_{LP} = \begin{cases} R_{L_1} + R_{L_2} & \gamma_{coop} < \gamma_{th} \\ R_L(\text{MVC}) \text{ or } R_D(\text{VpD}) & \gamma_{coop} \geq \gamma_{th} \end{cases} \tag{4.5}$$

where R_R, R_L and R_D are the bit rates of the right, left and depth sequences, respectively. After Partitioner-1, R_{H_1} and R_{L_1} are the bit rates of the HP and LP streams, respectively. In addition, after Partitioner-2, the R_{H_2} and R_{L_2} are the bit rates of HP and LP streams, respectively, and γ_{th} represents a certain value of γ_{coop} that is exploited by the control units to switch the system from direct to packet partitioning schemes or vice versa.

If it is assumed that the system change the number of HP packets (N_{HP}) and LP packets (N_{LP}) for each time of relay selection, then the (4.4) and (4.5) can be rewritten as

$$R_{HP} = \begin{cases} \frac{N_f}{L_g}\left[\sum_{i=1}^{i=N_{HP}} L_{p_i}^{R} + \sum_{i=1}^{i=N_{HP}} L_{p_i}^{L,D}\right] & \gamma_{coop} < \gamma_{th} \\ \frac{N_f}{L_g}\sum_{i=1}^{N_p} L_{p_i}^{R} & \gamma_{coop} \geq \gamma_{th} \end{cases} \tag{4.6}$$

$$R_{LP} = \begin{cases} \frac{N_f}{L_g}\left[\sum_{i=1}^{i=N_{LP}} L_{p_i}^{R} + \sum_{i=1}^{i=N_{LP}} L_{p_i}^{L,D}\right] & \gamma_{coop} < \gamma_{th} \\ \frac{N_f}{L_g}\sum_{i=1}^{N_p} L_{p_i}^{L,D} & \gamma_{coop} \geq \gamma_{th} \end{cases} \tag{4.7}$$

where N_f is the total number of video frames per second, L_g is the length of GoP, N_p is the total number of video packets per GoP, N_{HP} is the number of HP packets per GoP, $N_{LP} = N_p - N_{HP}$ is the number of LP packets per GoP, $L_{p_i}^{R}$ and $L_{p_i}^{L,D}$ are the length of ith packet of the right and left (or depth) view packets in bits, respectively.

4.4.3.2 Video distortion for the proposed system

As explained in Chapter 3, video distortion generally consists of source distortion (D_s) and channel distortion (D_c). D_s is due to the compression process in the

video encoder. It is related to the value of Q_P in the video encoder, and is reduced with a lower of Q_P value. D_c is caused by video packet losses introduced by the wireless channel. It is related to the code rates used in the LDPC encoders, and reduced with a reduction in the channel code rates. Hence, the total distortion of the right (D_R) and left (D_L) views can be formed as:

$$D_R = D_{s_R} + D_{c_R} \tag{4.8}$$

and

$$D_L = D_{s_L} + D_{c_L} \tag{4.9}$$

where D_{s_R} and D_{s_L} respectively denote the MSE at the source encoder output for the right and left views. Meanwhile, D_{c_R} and D_{c_L} are the right and left sequences distortion induced by the wireless channel, respectively.

The average distortion of the 3-D video signal (D_T) can be calculated as [3, 32]

$$D_T = \frac{D_R + D_L}{2} \tag{4.10}$$

where D_R and D_L can be measured by computing the MSE between the original video sequence and decoded video sequence after the right and left video decoders, respectively [22, 32].

It can be concluded from Sections 4.4.3.1 and 4.4.3.2 that the use of an optimal value of source rate, number packets for packet partitioning, and channel code rates for the video and LDPC encoders can minimize the D_{s_R},D_{s_L}, D_{c_R} and D_{c_L}. The choice of the optimal values is performed by JSCC algorithm which is constrained by R_{budget} and available γ_{coop} in the wireless channel.

4.4.4 Problem Formulation and Lagrangian Multiplier for Optimum Solution

A method which attempts to solve the packet partitioning optimization problem is now introduced. Given an overall rate of R_{budget} at certain value of γ_{coop} in the wireless channels, it is wanted to optimally allocate bits between the source and channel with optimal allocation for HP and LP packets to minimize the overall

distortion D_T. That is,

$$\min_{(R_{HP},R_{LP},r_1,r_2)} \underbrace{\frac{D_R + D_L}{2}}_{D_T} \tag{4.11a}$$

$$\text{subject to } \underbrace{\frac{R_{HP}}{r_1} + \frac{R_{LP}}{r_2}}_{R_T} \leq R_{budget}, \tag{4.11b}$$

where the design variables, R_{HP}, R_{LP}, r_1 and r_2, follow the conditions

$$\begin{aligned} &0 < R_{HP} < R_{HP_{max}}, \\ &0 < R_{LP} < R_{LP_{max}}, \\ &0 < r_1 < 1, \\ &0 < r_2 < 1, \end{aligned} \tag{4.12}$$

and $R_{HP_{max}}$ and $R_{LP_{max}}$ are the upper bounds of bit rates for the HP and LP streams, respectively.

The solution of the optimum problem in (4.11) is a point in the design space that satisfies the constraints form in (4.11) and the conditions in (4.12). Since the solution of the optimum problem is not an easy task, an iterative algorithm which results in a suboptimal solution is proposed. By starting from an initial point in the design space, the algorithm updates the design variables at each iteration and gradually moves towards the optimum point. It cannot be guaranteed that it will always converge to the global optimum [109]. Moreover, if the algorithm is initialized in a region suitably close to the global minimization, then sequence of the design variables converges monotonically to the global solution.

Simulation results in Section 4.5 demonstrate that the JSCC algorithm monotonically decreases total video distortion at every iteration. Figure 4.6 shows the performance of the JSCC algorithm at different γ_{coop} for 3-D video sequences using VpD and MVC. The results demonstrate the validity of our JSCC algorithm since it optimizes the video system after a small number of iterations.

To solve the system optimum problem, the iterative Lagrange multiplier algorithm proposed in [110] is adopted and developed for the problem at hand. The new algorithm jointly optimizes the Q_p, the number of packets of HP and LP streams, and the channel code rates. The proposed algorithm simultaneously assigns source and channel coding rates, and number of HP and LP packets, based on maximizing the quality of video at the receiver, whilst minimizing the complexity of the channel encoding and decoding operations, subject to constraints

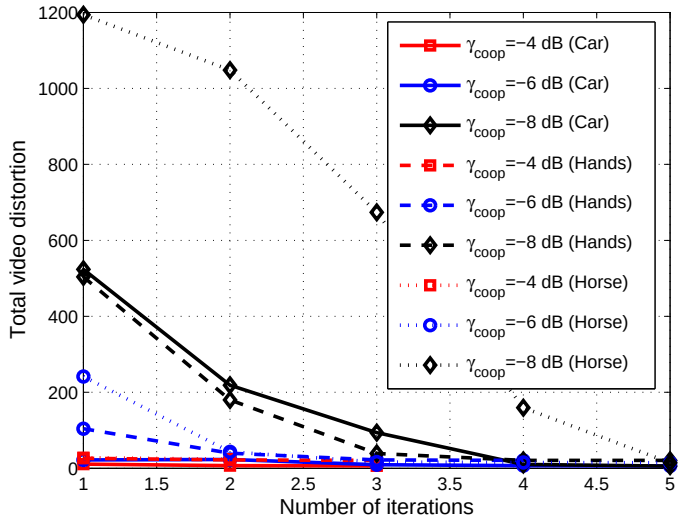

(a) ***VpD***

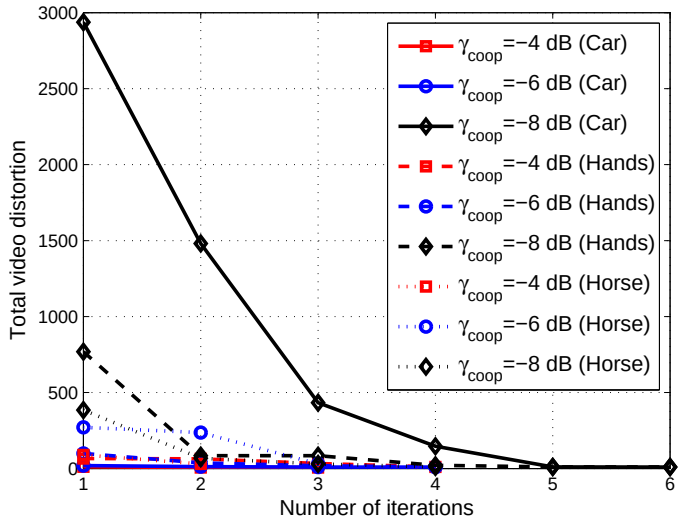

(b) ***MVC***

Figure 4.6: Total video distortion versus number of iterations in the proposed JSCC algorithm at different γ_{coop} and video sequences using VpD and MVC.

of R_{budget} and available γ_{coop}. Following [110], the iterative Lagrange multiplier algorithm is used in the following form:

$$L = D_T - \lambda_{R_{HP}} g_{R_{HP}} - \lambda_{R_{LP}} g_{R_{LP}} - \lambda_{r_1} g_{r_1} - \lambda_{r_2} g_{r_2} \tag{4.13}$$

where

- D_T is the total end-to-end video distortion and is implicitly determined by the available γ_{coop} in the wireless channel as well as R_{budget};
- $\lambda_{R_{HP}}$, $\lambda_{R_{LP}}$, λ_{r_1} and λ_{r_2} are Lagrangian parameters; and
- $g_{R_{HP}}$, $g_{R_{LP}}$, g_{r_1} and g_{r_2} are constraints of R_{HP}, R_{LP}, r_1 and r_2, respectively which follow the constraints form

$$g = \underbrace{\frac{R_{HP}}{r_1} + \frac{R_{LP}}{r_2}}_{R_T} - R_{budget}, \tag{4.14}$$

To obtain an optimum solution, we take the derivative of (4.13) with respect to R_{HP}, R_{LP}, r_1 and r_2, and equate the results to zero, yielding

$$\frac{\partial D_T}{\partial R_{HP}} - \lambda_{R_{HP}} \frac{\partial g_{R_{HP}}}{\partial R_{HP}} - \lambda_{R_{LP}} \frac{\partial g_{R_{LP}}}{\partial R_{HP}} - \lambda_{r_1} \frac{\partial g_{r_1}}{\partial R_{HP}} - \lambda_{r_2} \frac{\partial g_{r_2}}{\partial R_{HP}} = 0 \tag{4.15}$$

$$\frac{\partial D_T}{\partial R_{LP}} - \lambda_{R_{HP}} \frac{\partial g_{R_{HP}}}{\partial R_{LP}} - \lambda_{R_{LP}} \frac{\partial g_{R_{LP}}}{\partial R_{LP}} - \lambda_{r_1} \frac{\partial g_{r_1}}{\partial R_{LP}} - \lambda_{r_2} \frac{\partial g_{r_2}}{\partial R_{LP}} = 0 \tag{4.16}$$

$$\frac{\partial D_T}{\partial r_1} - \lambda_{R_{HP}} \frac{\partial g_{R_{HP}}}{\partial r_1} - \lambda_{R_{LP}} \frac{\partial g_{R_{LP}}}{\partial r_1} - \lambda_{r_1} \frac{\partial g_{r_1}}{\partial r_1} - \lambda_{r_2} \frac{\partial g_{r_2}}{\partial r_1} = 0 \tag{4.17}$$

$$\frac{\partial D_T}{\partial r_2} - \lambda_{R_{HP}} \frac{\partial g_{R_{HP}}}{\partial r_2} - \lambda_{R_{LP}} \frac{\partial g_{R_{LP}}}{\partial r_2} - \lambda_{r_1} \frac{\partial g_{r_1}}{\partial r_2} - \lambda_{r_2} \frac{\partial g_{r_2}}{\partial r_2} = 0 \tag{4.18}$$

Following [110] and rearranging (4.15), (4.16), (4.17) and (4.18), and multiplying (4.15) by $(R_{HP})^{n_1}$, (4.16) by $(R_{LP})^{n_2}$, (4.17) by $(r_1)^{n_3}$ and (4.18) by $(r_2)^{n_4}$, and then taking the roots, the R_{HP}, R_{LP}, r_1 and r_2 at the [k+1]th iteration is given by:

$$R_{HP}^{[k+1]} = R_{HP}^{[k]} \left[\frac{\lambda_{R_{HP}} \frac{\partial g_{R_{HP}}}{\partial R_{HP}} + \lambda_{R_{LP}} \frac{\partial g_{R_{LP}}}{\partial R_{HP}} + \lambda_{r_1} \frac{\partial g_{r_1}}{\partial R_{HP}} + \lambda_{r_2} \frac{\partial g_{r_2}}{\partial R_{HP}}}{\frac{\partial D_T}{\partial R_{HP}}} \right]^{\frac{1}{n_1}} \tag{4.19}$$

$$R_{LP}^{[k+1]} = R_{LP}^{[k]} \left[\frac{\lambda_{R_{HP}} \frac{\partial g_{R_{HP}}}{\partial R_{LP}} + \lambda_{R_{LP}} \frac{\partial g_{R_{LP}}}{\partial R_{LP}} + \lambda_{r_1} \frac{\partial g_{r_1}}{\partial R_{LP}} + \lambda_{r_2} \frac{\partial g_{r_2}}{\partial R_{LP}}}{\frac{\partial D_T}{\partial R_{LP}}} \right]^{\frac{1}{n_2}} \tag{4.20}$$

$$r_1^{[k+1]} = r_1^{[k]} \left[\frac{\lambda_{R_{HP}} \frac{\partial g_{R_{HP}}}{\partial r_1} + \lambda_{R_{LP}} \frac{\partial g_{R_{LP}}}{\partial r_1} + \lambda_{r_1} \frac{\partial g_{r_1}}{\partial r_1} + \lambda_{r_2} \frac{\partial g_{r_2}}{\partial r_1}}{\frac{\partial D_T}{\partial r_1}} \right]^{\frac{1}{n_3}} \tag{4.21}$$

$$r_2^{[k+1]} = r_2^{[k]} \left[\frac{\lambda_{R_{HP}} \frac{\partial g_{R_{HP}}}{\partial r_2} + \lambda_{R_{LP}} \frac{\partial g_{R_{LP}}}{\partial r_2} + \lambda_{r_1} \frac{\partial g_{r_1}}{\partial r_2} + \lambda_{r_2} \frac{\partial g_{r_2}}{\partial r_2}}{\frac{\partial D_T}{\partial r_2}} \right]^{\frac{1}{n_4}} \tag{4.22}$$

where the items in (4.19), (4.20), (4.21) and (4.22) as $\partial g_{R_{HP}}/\partial R_{HP}$, $\partial g_{R_{LP}}/\partial R_{HP}$, $\partial g_{r_1}/\partial R_{HP}$, $\partial g_{r_2}/\partial R_{HP}$, $\partial g_{R_{HP}}/\partial R_{LP}$, $\partial g_{R_{LP}}/\partial R_{LP}$, $\partial g_{r_1}/\partial R_{LP}$, $\partial g_{r_2}/\partial R_{LP}$, $\partial g_{R_{HP}}/\partial r_1$, $\partial g_{R_{LP}}/\partial r_1$, $\partial g_{r_1}/\partial r_1$, $\partial g_{r_2}/\partial r_1$, $\partial g_{R_{HP}}/\partial r_2$, $\partial g_{R_{LP}}/\partial r_2$, $\partial g_{r_1}/\partial r_2$ and $\partial g_{r_2}/\partial r_2$ are obtained from the constraints form in (4.14). For example, to obtain the third item in (4.19), i.e., $\partial g_{r_1}/\partial R_{HP}$, we have to compute the variations of r_1, i.e., ∂r_1, with respect to the variations of R_{HP} between $R_{HP}^{(i+1)}$ and $R_{HP}^{(i)}$ in the constraints form, g, in (4.14). Here, ∂g_{r_1} denotes the variations of r_1 in the constraints form, g, in (4.14), while other variables in (4.14) remain as

$$\frac{\partial g_{r_1}}{\partial R_{HP}} = \frac{\partial R_{HP}}{\partial r_1} + \frac{R_{LP}^{[k]}}{r_2^{[k]}} - R_{budget} = 0, \tag{4.23}$$

Rearranging (4.23) gives

$$\begin{aligned} \partial r_1 &= \frac{\partial R_{HP}}{\left[R_{budget} - \frac{R_{LP}^{[k]}}{r_2^{[k]}} \right]}, \\ &= \frac{R_{HP}^{(i+1)} - R_{HP}^{(i)}}{\left[R_{budget} - \frac{R_{LP}^{[k]}}{r_2^{[k]}} \right]}, \end{aligned} \tag{4.24}$$

After computing ∂r_1 in (4.24), the result represents the variations of r_1 within the constraint, g, in (4.14), i.e., $\partial g_{r_1} \equiv \partial r_1$. Then $\partial g_{r_1}/\partial R_{HP}$ using

$$\frac{\partial g_{r_1}}{\partial R_{HP}} = \frac{\partial g_{r_1}}{R_{HP}^{(i+1)} - R_{HP}^{(i)}}. \tag{4.25}$$

Following similar steps as in (4.23)-(4.25), we can find the remaining items in (4.19), (4.20), (4.21) and (4.22). $R_{HP}^{[k]}$, $R_{LP}^{[k]}$, $r_1^{[k]}$ and $r_2^{[k]}$ are obtained from the previous $[k]$th iteration, n_1, n_2, n_3 and n_4 are known as the step sizes and their

values are selected prior to initiating the JSCC algorithm, k is the number of iterations.

Next, the Lagrange multipliers, $\lambda_{R_{HP}}$, $\lambda_{R_{LP}}$, λ_{r_1} and λ_{r_2} are:

$$\lambda_{R_{HP}}^{[k+1]} = \lambda_{R_{HP}}^{[k]} \left[\frac{R_{HP}^{[k]}}{R_{HP_{max}}} \right]^{\frac{1}{m}}, \tag{4.26}$$

$$\lambda_{R_{LP}}^{[k+1]} = \lambda_{R_{LP}}^{[k]} \left[\frac{R_{LP}^{[k]}}{R_{LP_{max}}} \right]^{\frac{1}{m}}, \tag{4.27}$$

$$\lambda_{r_1}^{[k+1]} = \lambda_{r_1}^{[k]} \left[\frac{r_1^{[k]}}{r_{1max}} \right]^{\frac{1}{m}}, \tag{4.28}$$

$$\lambda_{r_2}^{[k+1]} = \lambda_{r_2}^{[k]} \left[\frac{r_2^{[k]}}{r_{2max}} \right]^{\frac{1}{m}}, \tag{4.29}$$

where m is a constant and its value is selected prior to initiating the JSCC algorithm, and $R_{HP_{max}}$, $R_{LP_{max}}$, r_{1max} and r_{2max} are the upper bounds.

The gradients, $\partial D_T/\partial R_{HP}$, $\partial D_T/\partial R_{LP}$, $\partial D_T/\partial r_1$ and $\partial D_T/\partial r_2$ can be represented as

$$\partial D_T/\partial R_{HP} = \frac{D_T^{(i+1)} - D_T^{(i)}}{R_{HP}^{(i+1)} - R_{HP}^{(i)}}, \tag{4.30}$$

$$\partial D_T/\partial R_{LP} = \frac{D_T^{(i+1)} - D_T^{(i)}}{R_{LP}^{(i+1)} - R_{LP}^{(i)}}, \tag{4.31}$$

$$\partial D_T/\partial r_1 = \frac{D_T^{(i+1)} - D_T^{(i)}}{r_1^{(i+1)} - r_1^{(i)}}, \tag{4.32}$$

$$\partial D_T/\partial r_2 = \frac{D_T^{(i+1)} - D_T^{(i)}}{r_2^{(i+1)} - r_2^{(i)}}, \tag{4.33}$$

where $R_{HP}^{(i,i+1)} = R_{HP}^{[k]} \mp \triangle R_{HP}$, $R_{LP}^{(i,i+1)} = R_{LP}^{[k]} \mp \triangle R_{LP}$, $r_1^{(i,i+1)} = r_1^{[k]} \mp \triangle r_1$ and $r_2^{(i,i+1)} = r_2^{[k]} \mp \triangle r_2$, and $\triangle R_{HP}$, $\triangle R_{LP}$, $\triangle r_1$ and $\triangle r_2$ are the step sizes and their values are selected prior to initiating the JSCC algorithm. $\partial D_T/\partial R_{HP}$, $\partial D_T/\partial R_{LP}$, $\partial D_T/\partial r_1$ and $\partial D_T/\partial r_2$ in (4.30)-(4.33) are obtained by measuring the difference between the total video distortion D_T at two different values of the R_{HP}, R_{LP}, r_1 and r_1, respectively. For example, $D_T^{(i+1)}$ in (4.30) is measured at the kth iteration when the R_{HP} is the only variable, i.e., $R_{HP}^{(i+1)} = R_{HP}^{[k]} + \triangle R_{HP}$ and other design variables R_{LP}, r_1 and r_2 are based on their latest updated values obtained from the previous iteration.

The overall proposed JSCC algorithm is summarized in algorithm 1.

Algorithm 1 Joint optimization of source rates, number of packets based on packet partitioning schemes and channel code rates

Initialization

$R_{HP}^{[k]}$, $R_{LP}^{[k]}$,N_{HP}, Qp, $r_1^{[k]}$, $r_2^{[k]}$, n_1, n_2, n_3, n_4, $\lambda_{R_{HP}}^{[k]}$, $\lambda_{R_{LP}}^{[k]}$, $\lambda_{r_1}^{[k]}$, $\lambda_{r_2}^{[k]}$, $\triangle R_{HP}$, $\triangle R_{LP}$, $\triangle r_1$ and $\triangle r_2$,

while $\frac{R_{HP}^{[k]}}{r_1^{[k]}} + \frac{R_{LP}^{[k]}}{r_2^{[k]}} < R_{budget}$ **do**

calculate Qp, N_{HP} and N_{LP} to satisfy $R_{HP}^{[k]}$ and $R_{LP}^{[k]}$

$\frac{\partial D_T}{\partial R_{HP}} = \frac{D_T^{(i+1)} - D_T^{(i)}}{R_{HP}^{(i+1)} - R_{HP}^{(i)}}$

$\frac{\partial D_T}{\partial R_{LP}} = \frac{D_T^{(i+1)} - D_T^{(i)}}{R_{LP}^{(i+1)} - R_{LP}^{(i)}}$

$\frac{\partial D_T}{\partial r_1} = \frac{D_T^{(i+1)} - D_T^{(i)}}{r_1^{(i+1)} - r_1^{(i)}}$

$\frac{\partial D_T}{\partial r_2} = \frac{D_T^{(i+1)} - D_T^{(i)}}{r_2^{(i+1)} - r_2^{(i)}}$

$\partial g_{R_{HP}}/\partial R_{HP}$, $\partial g_{R_{LP}}/\partial R_{HP}$, $\partial g_{r_1}/\partial R_{HP}$, $\partial g_{r_2}/\partial R_{HP}$, $\partial g_{R_{HP}}/\partial R_{LP}$, $\partial g_{R_{LP}}/\partial R_{LP}$, $\partial g_{r_1}/\partial R_{LP}$, $\partial g_{r_2}/\partial R_{LP}$, $\partial g_{R_{HP}}/\partial r_1$, $\partial g_{R_{LP}}/\partial r_1$, $\partial g_{r_1}/\partial r_1$, $\partial g_{r_2}/\partial r_1$, $\partial g_{R_{HP}}/\partial r_2$, $\partial g_{R_{LP}}/\partial r_2$, $\partial g_{r_1}/\partial r_2$ and $\partial g_{r_2}/\partial r_2$ are obtained from (4.14) similar to steps as in (4.23)-(4.25),

$$R_{HP}^{[k+1]} = R_{HP}^{[k]} \left[\frac{\lambda_{R_{HP}} \frac{\partial g_{R_{HP}}}{\partial R_{HP}} + \lambda_{R_{LP}} \frac{\partial g_{R_{LP}}}{\partial R_{HP}} + \lambda_{r_1} \frac{\partial g_{r_1}}{\partial R_{HP}} + \lambda_{r_2} \frac{\partial g_{r_2}}{\partial R_{HP}}}{\frac{\partial D_T}{\partial R_{HP}}} \right]^{\frac{1}{n_1}}$$

$$R_{LP}^{[k+1]} = R_{LP}^{[k]} \left[\frac{\lambda_{R_{HP}} \frac{\partial g_{R_{HP}}}{\partial R_{LP}} + \lambda_{R_{LP}} \frac{\partial g_{R_{LP}}}{\partial R_{LP}} + \lambda_{r_1} \frac{\partial g_{r_1}}{\partial R_{LP}} + \lambda_{r_2} \frac{\partial g_{r_2}}{\partial R_{LP}}}{\frac{\partial D_T}{\partial R_{LP}}} \right]^{\frac{1}{n_2}}$$

$$r_1^{[k+1]} = r_1^{[k]} \left[\frac{\lambda_{R_{HP}} \frac{\partial g_{R_{HP}}}{\partial r_1} + \lambda_{R_{LP}} \frac{\partial g_{R_{LP}}}{\partial r_1} + \lambda_{r_1} \frac{\partial g_{r_1}}{\partial r_1} + \lambda_{r_2} \frac{\partial g_{r_2}}{\partial r_1}}{\frac{\partial D_T}{\partial r_1}} \right]^{\frac{1}{n_3}}$$

$$r_2^{[k+1]} = r_2^{[k]} \left[\frac{\lambda_{R_{HP}} \frac{\partial g_{R_{HP}}}{\partial r_2} + \lambda_{R_{LP}} \frac{\partial g_{R_{LP}}}{\partial r_2} + \lambda_{r_1} \frac{\partial g_{r_1}}{\partial r_2} + \lambda_{r_2} \frac{\partial g_{r_2}}{\partial r_2}}{\frac{\partial D_T}{\partial r_2}} \right]^{\frac{1}{n_4}}$$

$$\lambda_{R_{HP}}^{[k+1]} = \lambda_{R_{HP}}^{[k]} \left[\frac{R_{HP}^{[k]}}{R_{HP_{max}}} \right]^{\frac{1}{m}}$$

$$\lambda_{R_{LP}}^{[k+1]} = \lambda_{R_{LP}}^{[k]} \left[\frac{R_{LP}^{[k]}}{R_{LP_{max}}} \right]^{\frac{1}{m}}$$

$$\lambda_{r_1}^{[k+1]} = \lambda_{r_1}^{[k]} \left[\frac{r_1^{[k]}}{r_{1_{max}}} \right]^{\frac{1}{m}}$$

$$\lambda_{r_2}^{[k+1]} = \lambda_{r_2}^{[k]} \left[\frac{r_2^{[k]}}{r_{2_{max}}} \right]^{\frac{1}{m}}$$

end while

4.5 Experimental results and Discussion

In this section, the performance of the proposed system and JSCC algorithm are evaluated at different video sequences, available SNR γ_{coop}, and R_{budget}. The impact of γ_{coop} on video system performance is also investigated. For the cooperative MIMO-OFDM system, the simulation configurations in Chapter 3 are employed and is not presented here to avoid repetition.

4.5.1 Experimental Settings

4.5.1.1 Video encoder setting

Several experiments are conducted using standard 3-D video sequences 'Car', 'Hands' and 'Horse' in [95], with 30 frames per second (fps) of 432×240 pixels and a GOP of 10. The packets number per GOP is fixed to 140 packets. The MVC codec based on H.264 in [21] and [37] is adopted for encoding the left and right views, while the H.264 reference software JM version (13.2) in [36] is used for encoding the right (colour) and depth sequences.

4.5.1.2 Choice of initial values for JSCC algorithm

Before starting the recursion of the JSCC algorithm, the initial values should be initialized with appropriate values to optimize the system in as few iterations as possible so as to achieve the UEP between the HP and LP streams and reduce the complexity of the channel encoding and decoding operations. The R_{HP} and R_{LP} are firstly measured at different quantization and packets partitioning values which are allocated to HP and LP streams. Figures. 4.7 and 4.8 show the comparison between the variations of R_{HP} and R_{LP} at different values of Q_p and N_{HP} for different VpD and MVC sequences. In Figures 4.7 and 4.8, the following can be observed:

1. There is no effect from increasing or decreasing N_{HP} on R_{HP} and R_{LP} values, when the values of Q_p are high, i.e., $Q_p > 40$, because the system video performance, at $Q_p > 40$, is limited by the source distortion rather than the channel distortion. Therefore, the JSCC algorithm has to keep the system operating at $Q_p < 40$, and the algorithm can easily control R_{HP} and R_{LP} by changing the packet allocation for the HP and LP streams;

2. The step sizes $\triangle R_{HP}$, $\triangle R_{LP}$, $1/n_1$ and $1/n_2$ have to be greater than the step sizes $\triangle r_1$, $\triangle r_2$, $1/n_3$ and $1/n_4$. This is useful to keep the JSCC

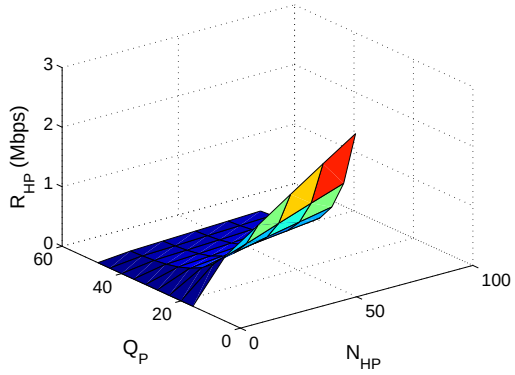

(a) R_{HP} versus Q_p and N_{HP} (Car)

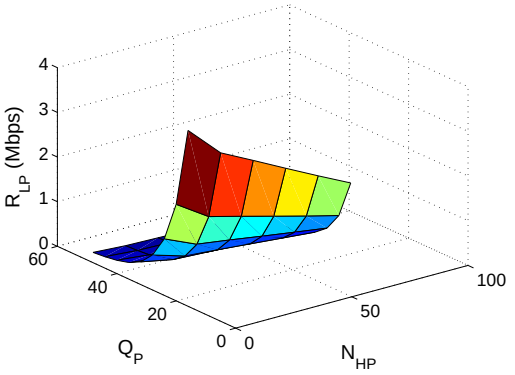

(b) R_{LP} versus Q_p and N_{HP} (Car)

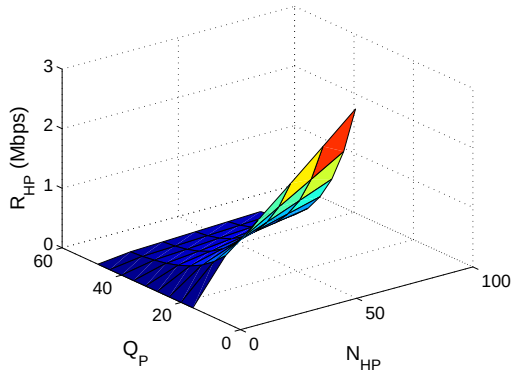

(c) R_{HP} versus Q_p and N_{HP} (Hands)

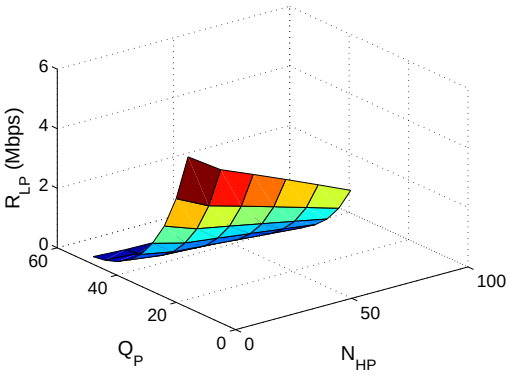

(d) R_{LP} versus Q_p and N_{HP} (Hands)

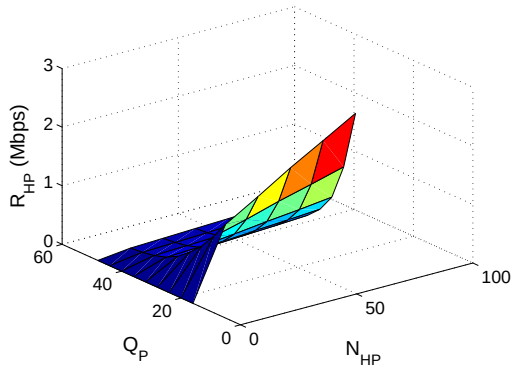

(e) R_{HP} versus Q_p and N_{HP} (Horse)

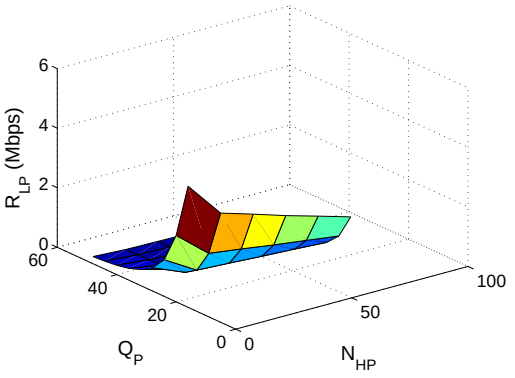

(f) R_{LP} versus Q_p and N_{HP} (Horse)

Figure 4.7: Comparison of the variation of R_{HP} and R_{LP} at different values of Q_p and N_{HP} for different VpD sequences.

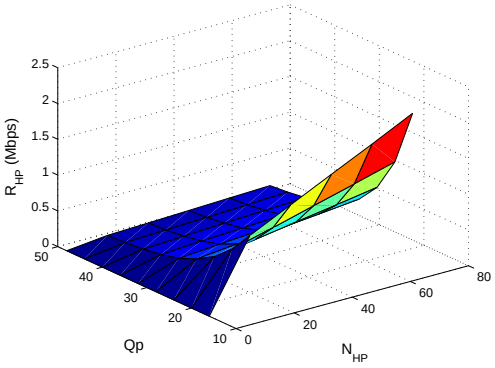

(a) R_{HP} versus Q_p and N_{HP} (Car)

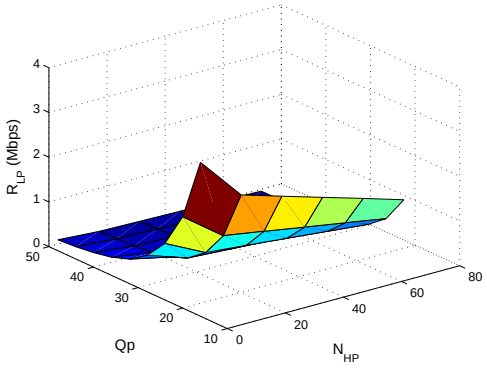

(b) R_{LP} versus Q_p and N_{HP} (Car)

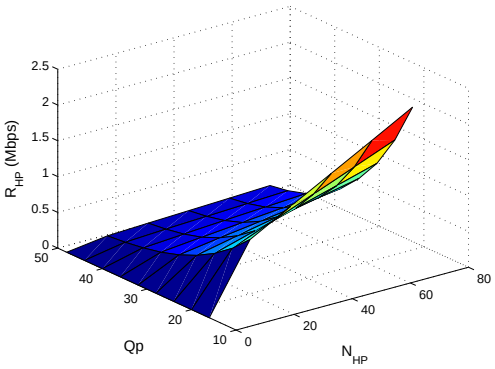

(c) R_{HP} versus Q_p and N_{HP} (Hands)

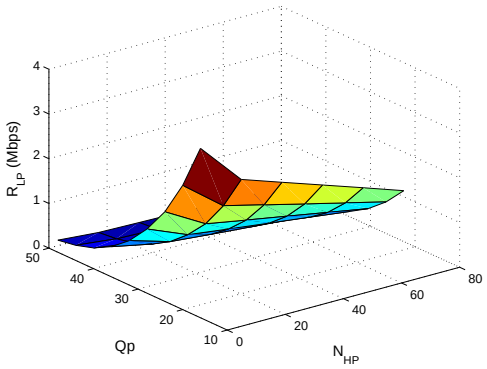

(d) R_{LP} versus Q_p and N_{HP} (Hands)

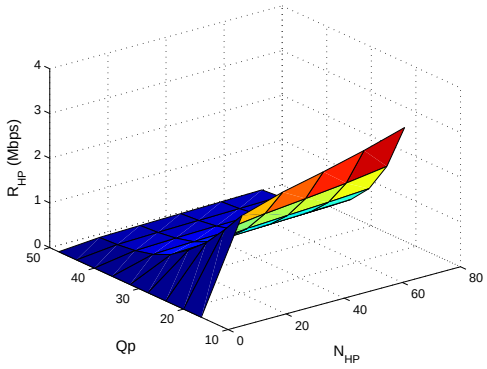

(e) R_{HP} versus Q_p and N_{HP} (Horse)

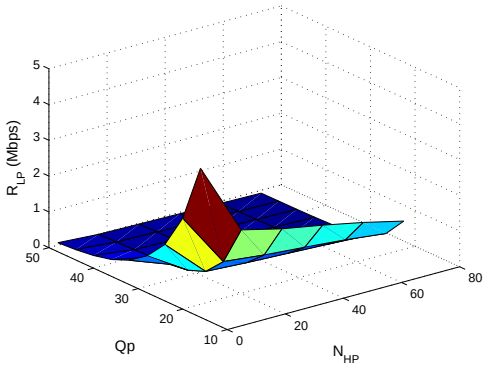

(f) R_{LP} versus Q_p and N_{HP} (Horse)

Figure 4.8: Comparison of the variation of R_{HP} and R_{LP} at different values of Q_p and N_{HP} for different MVC sequences.

algorithm allocating a high N_{HP} to the HP stream instead of resorting to reduce r_1 and r_2 values to minimize the total video distortion. Therefore, the algorithm can reduce the complexity of channel encoding and decoding by increasing the N_{HP} with a slight decrease in the $\triangle r_1$ and $\triangle r_2$ steps;

3. To achieve the UEP between the HP and LP streams, the JSCC algorithm has to be initialized with ${r_1}^{[0]} < {r_2}^{[0]}$.

As shown in Figures. 4.7 and 4.8 and explained above, the JSCC algorithm can be initialized with the following values: $R_{HP}^{[0]}$=0.4 Mbps, $R_{LP}^{[0]}$=0.2 Mbps, $r_1^{[0]}$=0.8125, $r_2^{[0]}$=0.875, $1/n_1$=0.04, $1/n_2$=0.04, $1/n_3$=-0.01, $1/n_4$=-0.01, $\lambda_{R_{HP}}^{[0]}$=10, $\lambda_{R_{LP}}^{[0]}$=10, $\lambda_{r_1}^{[0]}$=10, $\lambda_{r_2}^{[0]}$=10, $\triangle R_{HP} = 0.125\ R_{HP}^{[0]}$, $\triangle R_{LP} = 0.125\ R_{LP}^{[0]}$, $\triangle r_1$=0.0625 and $\triangle r_2$=0.0625.

The selection of initial values achieve the above conditions. For example, the initial value, $R_{HP}^{[0]} = 0.4$ Mbps is selected to start the proposed JSCC algorithm with a moderate value of Q_p, i.e., $Q_p < 40$ and its value is gradually reduced in each iteration of the JSCC algorithm. Thus, the algorithm can allocate more video packets in the HP stream corresponding to the reduction of Q_p in each iteration. This assumption is consistent with the above first condition. Moreover, the initial value, $r_1^{[0]}$, is selected to be lower than the initial value, $r_2^{[0]}$ to achieve the UEP between the HP and LP video streams and the selection of initial values of r_1 and r_2 is consistent with the above third condition. The simulation results in Figure 4.6 show that the proposed JSCC algorithm is computationally efficient since it achieves the terminal condition, i.e., $R_{HP}^{[k]}/r_1^{[k]} + R_{LP}^{[k]}/r_2^{[k]} \approx R_{budget}$, and optimizes the system within five iterations. For example, at $\gamma_{coop} = -6$ dB, the JSCC algorithm stops after three iterations only, while it stops after two iterations only at $\gamma_{coop} = -4$ dB.

4.5.2 Experimental results

4.5.2.1 Evaluation of JSCC algorithm

The proposed JSCC algorithm is evaluated to obtain the optimal number of packets for the HP stream (N_{HP}) and LP stream (N_{LP}), Q_p, and channel code rates r_1 and r_2 for the HP-LDPC and LP-LDPC encoders, respectively, subject to constraints on the R_{budget} and the available γ_{coop} of the wireless channels. Several experiments are conducted for MVC and VpD for 'Car', 'Hands' and 'Horse' sequences, respectively, when $R_{budget} \in \{1, 2, 4(\text{Mbps})\}$ at different γ_{coop} values which are varied from low γ_{coop}, medium γ_{coop} to high γ_{coop}, i.e., $\gamma_{coop} \in$

$\{-8$ (minus 8), $-6, -4$ (dB)$\}$. Tables 4.1 and 4.2 present the optimal values of N_{HP}, N_{LP}, Q_p, r_1 and r_2 at different γ_{coop} and R_{budget}.

The results lead to the following observations:

1) The available γ_{coop}, which is determined by the available relay in the wireless network, plays a significant role in determining the system complexity as follows: a) An increase of γ_{coop} leads to an increase of the code rates r_1 and r_2 and a reduction of the complexity of channel encoding and decoding. For example, in the 'Car' sequence at 4.1, the system adopts the UEP scheme with low code rates $r_1 = 0.2339$ and $r_2 = 0.3463$ at γ_{coop}=-8 dB, while it adopts medium code rates $r_1 = 0.4797$ and $r_2 = 0.586$ and high code rates $r_1 = 0.691$ and $r_2 = 0.714$ at γ_{coop}=-6 and -4 dB, respectively. Therefore, as long as the system achieves a high γ_{coop} by the selecting the best relay in the network, the system complexity is reduced in the proportional to the increase of LDPC code rates; b) An increase in γ_{coop} from low to high values leads to switching of the system to the direct scheme, which is of lower complexity compared to the partitioning schemes. For example, as shown in Tables 4.1 and 4.2, the system adopts the direct transmission when γ_{coop} is high, i.e., γ_{coop}=-4 dB, while the system resorts to the packet partitioning operation and increase the complexity of the system at low γ_{coop}, i.e., γ_{coop}=-8 dB, in order to overcome the low γ_{coop}, which is instantaneously available in the wireless channel. Therefore, the system does not use the packet partitioning operation when γ_{coop} is high;

2) The available γ_{coop} plays a significant factor in determining the system performance in terms of PSNR. The solid lines in Figure 4.9 show the impact of the available γ_{coop} on video system performance when R_{budget}= 4 Mbps at different video sequences using either the VpD or MVC technique. As shown in Figure 4.9 (the solid lines), the system can achieve high PSNR as long as the system can select a relay with high instantaneous SNR. For example, as shown in Figure 4.9-(a) at the 'Car' sequence, the PSNR is improved with 3.2 dB when γ_{coop} value changes from -8 to -4 dB, respectively;

In Figure 4.9, the solid lines compared to the dashed lines show a performance comparison of the proposed JSCC algorithm and the algorithms in [22] and [21]. As can be seen from Figure 4.9, the proposed JSCC algorithm significantly outperforms existing algorithms in terms of PSNR performance at different video sequences and γ_{coop}. For example, as shown in Figure 4.9 at the 'Car' sequence and γ_{coop}= -6 dB, the proposed algorithm outperforms the algorithms in [22] and [21] by 5 dB and 7 dB, respectively.

Figure 4.10 shows a comparison of the reconstructed frame 19 of the proposed

Table 4.1: The optimal values of the encoder rates, packets number for packet partitioning and channel encoder rates at different γ_{coop}, R_{budget} and video sequences using VpD.

Sequence	Adopted scheme	γ_{coop} (dB)	N_{HP}	N_{LP}	r_1	r_2	Q_p	R_{budget} (Mbps)	R_T (Mbps)	PSNR (dB)
Car	Packet partitioning	-8	130	150	0.2339	0.3463	26	4	3.87	38.07
							30	2	1.86	36.8
							43	1	0.97	30.5
		-6	132	148	0.4797	0.586	20	4	3.97	40.58
							26	2	1.89	38.07
							32	1	0.99	35.17
	Direct	-4	140	140	0.691	0.714	18	4	3.99	41.28
							26	2	1.78	38.98
							29	1	0.97	36.7
Hands	Packet partitioning	-8	140	140	0.2147	0.355	32	4	3.99	31.51
							39	2	1.94	29.15
							48	1	0.99	25.76
		-6	92	188	0.4554	0.5192	26	4	3.95	33.26
							33	2	1.95	31.26
							40	1	0.92	28.77
	Direct	-4	140	140	0.6422	0.6566	23	4	3.98	34.07
							30	2	1.99	32.14
							37	1	0.97	29.95
Horse	Packet partitioning	-8	136	144	0.2748	0.4397	24	4	3.92	34.65
							31	2	1.97	31.62
							40	1	0.99	27.52
		-6	118	162	0.4546	0.515	22	4	3.99	36.4
							27	2	1.84	33.73
							34	1	0.98	30.11
	Direct	-4	140	140	0.6448	0.6709	19	4	3.92	37.3
							24	2	1.88	35.06
							30	1	0.98	32.16

Table 4.2: The optimal values of the encoder rates, packets number for packet partitioning and channel encoder rates at different γ_{coop}, R_{budget} and video sequences using MVC.

Sequence	Adopted scheme	γ_{coop} (dB)	N_{HP}	N_{LP}	r_1	r_2	Q_p	R_{budget} (Mbps)	R_T (Mbps)	PSNR (dB)
Car	Packet partitioning	-8	140	140	0.26	0.361	25	4	3.98	34.47
							32	2	1.89	28.96
							40	1	0.99	24.1
		-6	82	198	0.4269	0.52	21	4	3.84	37.56
							27	2	1.92	32.67
							34	1	0.99	27.74
	Direct	-4	140	140	0.7	0.7	18	4	3.8	39.9
							24	2	1.8	34.94
							30	1	0.93	29.95
Hands	Packet partitioning	-8	80	200	0.27	0.32	28	4	3.68	26.26
							35	2	1.8	21.33
							44	1	0.98	17.05
		-6	12	268	0.509	0.5839	22	4	3.88	31.5
							28	2	1.94	26.26
							35	1	0.91	21.33
	Direct	-4	140	140	0.7	0.7	20	4	3.82	34.4
							25	2	1.97	28.85
							32	1	0.97	23.08
Horse	Packet partitioning	-8	122	158	0.24	0.33	32	4	3.81	29.04
							38	2	1.98	24.67
							46	1	0.99	19.9
		-6	62	218	0.43	0.4609	25	4	3.97	34.09
							34	2	1.85	27.73
							41	1	0.94	22.59
	Direct	-4	140	140	0.67	0.67	21	4	3.83	37.29
							29	2	1.94	31.26
							37	1	0.93	25.54

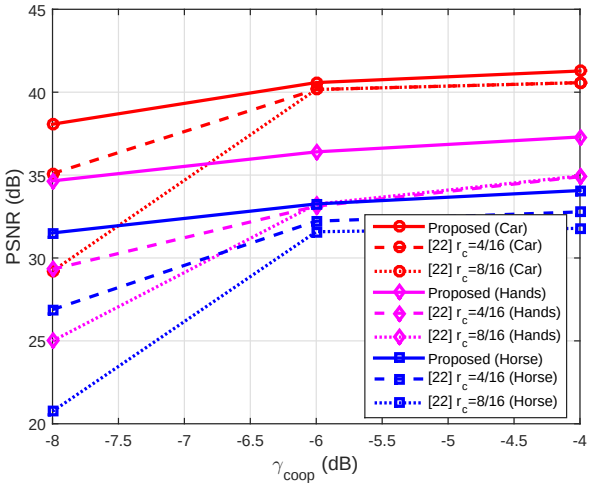

(a) PSNR versus γ_{coop} using VpD.

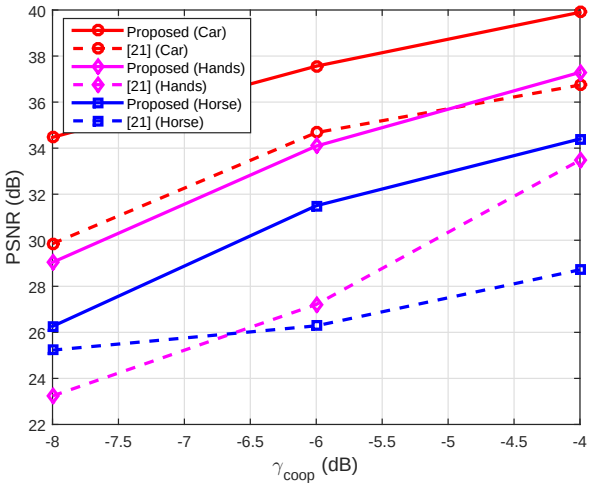

(b) PSNR versus γ_{coop} using MVC.

Figure 4.9: The solid lines, labeled "Proposed", show the impact of γ_{coop} on the proposed system performance in terms of PSNR values for different video sequences at R_{budget}= 4 Mbps. The dashed lines compared to the solid lines, show a performance comparison of proposed JSCC algorithm and the algorithms in [22] and [21], where the code rates of color sequence r_c=4/16, 8/16, and r_d=13/16 for depth sequence are adopted in [22], while the code rates 4/16, 8/16 and 13/16 are respectively adopted for the layer 0, layer 1 and layer 2 in [21].

algorithm at SNR= -8 dB with the existing algorithms in [22] and [21]. The results in Figures 4.9 and 4.10 show that the proposed JSCC algorithm significantly improves the overall system performance compared to that of [22] and [21];

3) The available γ_{coop} causes the JSCC algorithm to assign the R_{budget} between the source and channel rates. As shown in Tables 4.1 and 4.2 for different cases, the most R_{budget} is assigned to the channel rates, i.e., r_1 and r_1 when the available γ_{coop} is low. In contrast, higher source codes rates are assigned, i.e., Q_p values are reduced, when the available γ_{coop} is high;

4) The system tends to change the protection level in terms of the number of prior packets of GoP (N_{HP}) according to the available γ_{coop}. For example, as shown in the 'Hands' sequence at Table 4.1, the system is adopted to protect half of the GoP packets N_{HP}=140, i.e., 70 packets per GoP from the right view and 70 packets from depth sequence, with high protection and the second N_{LP}=140 with low protection at low γ_{coop}=-8 dB. Meanwhile, it reduces the number of N_{HP} to 92 at medium γ_{coop}=-6 dB. Therefore, this adaptive method ensures the achievement of high video quality when γ_{coop} is low, and reduce the complexity of the system when γ_{coop} is higher;

5) The system resorts to the use of UEP schemes at low and medium γ_{coop} values. However, the UEP schemes make the channel encoding and decoding operations more complicated. Therefore, the system has to switch the equal error protection (EEP) scheme at high γ_{coop} to overcome this problem. For example, as shown in Tables 4.1 and 4.2 at different video sequences, the channel code rates $r_1 = r_2 \approx 0.7$ are used at high γ_{coop}=-4 dB;

6) The channel code rates r_1 and r_2 are still restricted by the available γ_{coop} for different data budgets. This fact can be clearly seen when R_{budget} is varied from 1 to 4 Mbps. This is anticipated since the channel distortion (D_c), which is caused by video packet losses in the wireless channel can be minimized by adopting suitable code rates at the channel LDPC encoders. Therefore, if the JSCC algorithm allocates the optimal channel code rates at a certain value of γ_{coop} and achieves minimal channel distortion, the improvement in rate budgets can be used to allocate more rate to the source to mitigate the source distortion (D_s), since the allocated channel code rates are already enough to minimize the D_c. For example, in the 'Car' sequence at Table 4.1, the R_{budget} varied from 1 to 4 Mbps at γ_{coop}=-8 dB, while r_1 and r_2 remained at 0.2339 and 0.3463, respectively. Thus, it can be concluded that r_1 and r_2 are restricted by the available γ_{coop} to resist the channel degradations;

7) The system performance in terms of PSNR improves with the gradual

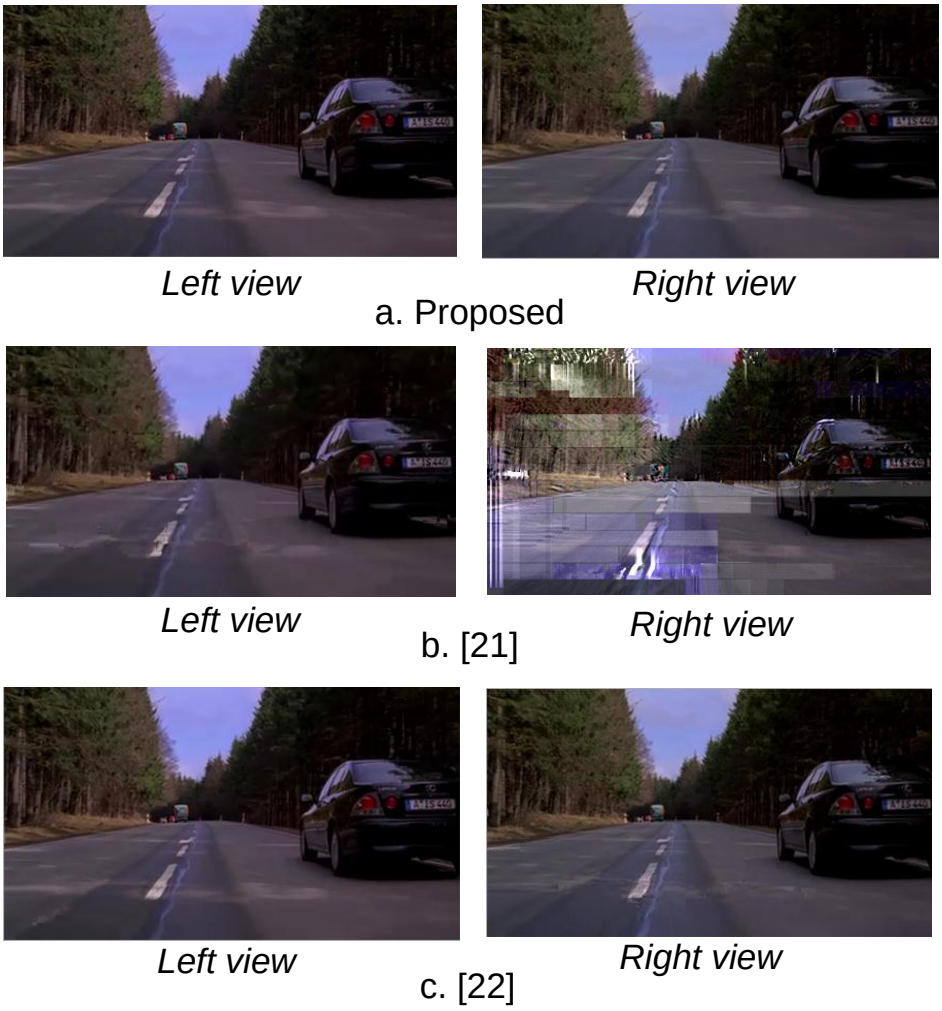

Figure 4.10: Comparison of reconstructed frame 19 of 'Car' sequence at SNR= -8 dB using proposed JSCC algorithm and the algorithms in [21] and [22], where the code rates 4/16, 8/16 and 13/16 are respectively adopted for the layer 0, layer 1 and layer 2 in [21], while the code rates of colour sequence r_c=4/16, and r_d=13/16 for depth sequence are adopted in [22].

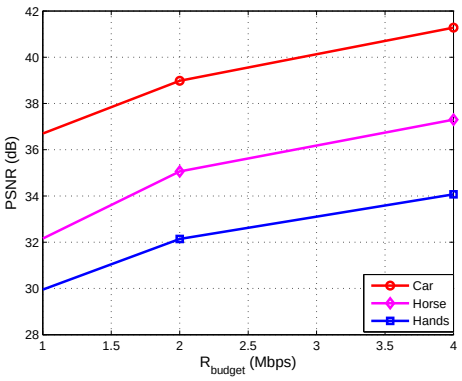

(a) PSNR versus R_{budget} using VpD.

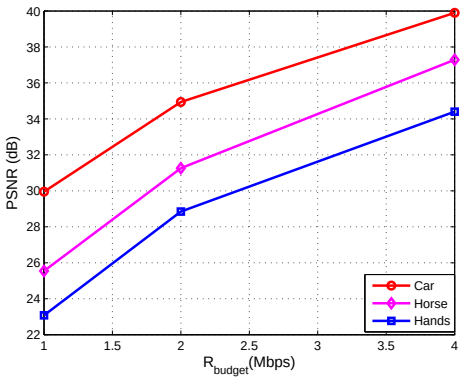

(b) PSNR versus R_{budget} using MVC.

Figure 4.11: PSNR performances of the proposed system under different rate budget constraints at γ_{coop}= -4 dB.

relaxation of R_{budget}. Figure 4.11 shows the PSNRs of the proposed system under different R_{budget} and video sequences using either VpD or MVC technique at γ_{coop}= -4 dB. As shown in Figure 4.11, all the PSNR-rate curves keep rising, which demonstrates the adaptation of the proposed JSCC algorithm to the gradual relaxation of the rate budget constraint.

4.6 Impact of γ_{coop} Estimation on Video System Performance

In this section, some examples of the estimation error in γ_{coop} at different MSEs are presented to show that there is an additional factor related to the accurate estimation of γ_{coop}. The accuracy estimation of γ_{coop} is shown to directly affect the performance and complexity of cooperative video systems and has to be considered in the design of multimedia cooperative communication systems with feedback.

The channel code rates, i.e., r_1 and r_2, are increased or decreased with the variation of γ_{coop} in wireless channels. Therefore, the complexity of channel encoding and decoding operations are determined according to the accuracy of γ_{coop} estimation. Meanwhile, the variations of r_1 and r_2 lead to a reduction in the protection of video packets against the packets loss in the channel. This case directly affects the PSNR values. To illustrate this point, some examples of estimation

error in γ_{coop} are given at different MSEs. The goal is to show the effects of SNR estimator performance on the video system performance and complexity.

For the simulation setting, the 'Car' sequence with VpD and MVC coding is adopted, and the simulation parameters are set on γ_{coop}=-6 dB, R_{budget}=4 Mbps and MSE=10^{-2}, 10^{-3}.

Figure 4.12 shows a comparison performance of the video system at different MSEs with VpD and MVC coding. The following observations can be made from

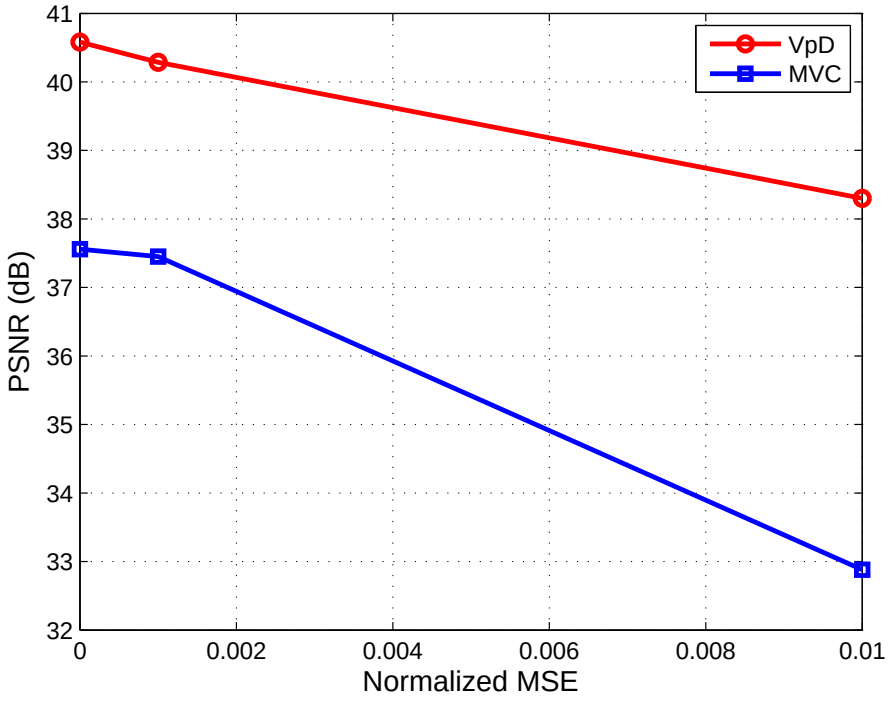

Figure 4.12: The video system performance in terms of PSNR at γ_{coop}=-6 dB and different MSEs with VpD and MVC coding.

Figure 4.12:

1) Even when the performance of the SNR estimator is moderate (of the order of 10^{-3}), there is still some reduction in PSNR. For example, at VpD, the PSNR is reduced from 40.58 to 40.28 dB. The simulation results indicate that there is also an increase in system complexity with a reduction in channel code rates r_1 and r_2 from the actual values 0.4797 and 0.586 to the new values 0.5341 and 0.516, respectively. This due to the JSCC algorithm which adopts wrong γ_{coop}

instead of actual γ_{coop}=-6 dB in the wireless channel;

2) At MSE=10^{-2}, the system performance is worse than with MSE=10^{-3}, since the performance of the SNR estimator is poor. This affects the JSCC algorithm, which assigns the wrong code rates for source and channel. This impairs the ability of the system to achieve high PSNR. For example, at MVC, it is clear that the PSNR is reduced from 37.56 to 32.88 dB, i.e., the performance loss is 4.68 dB. In addition, the simulation results show that the JSCC algorithm assigns the channel code rates $r_1 = 0.6256$ and $r_2 = 0.651$ to the LDPC encoders. These values are greater than the actual values, i.e., $r_1 = 0.4269$ and $r_2 = 0.52$. In this case, the video packets are lost through the channel because the HP and LP streams are protected with LDPC codes higher than the actual values.

3) MVC is more sensitive to the accuracy of γ_{coop} estimation than VpD. This case is clearly seen at MSE=10^{-2}. In this case, the PSNRs for VpD and MVC are respectively reduced from 40.58 to 38.3 dB, and from 37.56 to 32.88 dB, i.e., the PSNRs are reduced for VpD and MVC by 2.28 and 4.68 dB, respectively. This result is anticipated, since the left view in MVC is reconstructed depending on the relationship between the right and left views. Thus, any error in the right view is spread to the reconstructed left view, while the depth structure in VpD is less affected by noise. Therefore, the VpD is more appropriate for 3-D video transmission when the performance of the SNR estimator is low.

Figures. 4.13-4.16 show the original and reconstructed left and right frames of the 'Car' sequence for frame 10 using VpD and MVC at different MSEs. As illustrated in Figs. 4.13-4.16, video distortion appears at high MSE, i.e., 10^{-2}, while it is trivial at medium MSE value, i.e., $10^{-3.}$.

Finally, it can be concluded that the accuracy of estimation of γ_{coop} can be considered a significant factor in in the determination of performance and complexity of cooperative video systems.

4.7 Conclusion

In this chapter, a new joint source-channel coding algorithm is proposed, which depends on the end-to-end video distortion, available instantaneous SNR (γ_{coop}) and the allocated rate budget (R_{budget}) to jointly optimize the application, network and physical layer parameters. The parameters which are optimized are the quantization parameters, number of packets of high-priority and low-priority streams and channel code rates. The algorithm is based on the Lagrange multiplier algorithm, and it maximized the video quality at the destination whilst

(a) Left view **(b)** Right view

Figure 4.13: Original left and right frames of 'Car' sequence for frame 10.

(a) Left view **(b)** Right view

Figure 4.14: Reconstructed left and right frames of 'Car' sequence for frame 10 using VpD and MVC at MSE=0 and 10^{-3}.

(a) Left view **(b)** Right view

Figure 4.15: Reconstructed left and right frames of 'Car' sequence for frame 10 at MSE=10^{-2} using VpD coding.

(a) Left view **(b)** Right view

Figure 4.16: Reconstructed left and right frames of 'Car' sequence for frame 10 at MSE=10^{-2} using MVC coding.

minimizing the complexity of the channel encoding and decoding operations. In addition, the proposed algorithm is effective into covering a wide range of γ_{coop} and R_{budget} values. New procedures to estimate γ_{coop} were proposed. The impact of γ_{coop} estimation on the performance of video system was investigated. Simulation results demonstrate the video system performance, in terms of PSNR and system complexity, is very sensitive to the accuracy of instantaneous signal-to-noise ratio estimation. The results also show that instantaneous SNR and rate budget represent the main factors in determining the complexity of the system with respect to channel code rates.

Chapter 5

Joint Channel, Phase Noise and Frequency Offset Estimation and Data Detection in OFDM Systems

5.1 Introduction

In this chapter, a computationally efficient training based approach for joint channel, CFO, and PHN estimation in OFDM systems is presented. An iterative receiver is proposed for the detection of data symbols in the presence of time-varying PHN and CFO.

In practice, OFDM systems require timing offset estimation, CFO estimation, PHN tracking as well as channel estimation. Timing synchronization for OFDM systems has been well investigated over the past two decades [111, 112]. Compared to timing offsets, OFDM is very sensitive to CFO and PHN, which arise due to instabilities and the thermal noise in the local oscillator, respectively [113]. CFO and time varying PHN result in a CPE and ICI at the receiver, degrading the performance of OFDM systems [12, 13, 23, 76, 77, 114]. In particular, the impact of PHN in systems operating at higher carrier frequencies, e.g., V-band/60 GHz and E-band/70–80 GHz, can be even more profound [70]. Thus, as wireless communication systems and standards, e.g., IEEE 802.11ad, migrate to millimeter-wave frequencies to take advantage of the large bandwidth in this band and adopt higher order modulations and closely spaced sub-carriers to achieve higher spectral efficiencies, it is increasingly important to develop efficient and accurate estimation and detection algorithms that compensate for the

effect of CFO and PHN in OFDM systems.

To jointly estimate channel, CFO, and time varying PHN, training signals are used in OFDM systems. In the context of point-to-point systems, joint channel and CFO estimation based on the expectation-maximization (EM) approach was proposed in [115]. However, in [115], the authors do not take the effect of PHN into account. In [23] and [24], a MAP estimator was used for joint estimation of channel, CFO, and PHN. However, the estimation approach in [23] and [24] is based on a small angle approximation (single-order Taylor series expansion of PHN), that adversely affects the performance of the estimation and data detection algorithms, especially for higher order modulations. In addition, as shown in this chapter, the approach in [23] and [24] can be computationally very complex. Recently, the authors in [25] proposed a joint channel, CFO, and PHN estimation algorithm based on the sequential Monte Carlo and EM approaches. However, as explained in [116], the estimation complexity of Monte Carlo based method in [25] is very high. More importantly, in [23–25], the hybrid Cramér-Rao lower bound (HCRB) for the joint estimation of channel impulse response (CIR), PHN, and CFO in OFDM systems is not derived and the performances of the proposed estimators are not benchmarked against their respective estimation performance bounds. Recently, the problem of joint estimation of channel, CFO, and PHN was considered in the context of OFDM relay networks in [15]. However, the approach in [15] is also based on the *maximum a posteriori* (MAP) criterion, which is computationally very complex.

Given the time-varying nature of PHN, it needs to be tracked, not only during the training interval, but also during the data transmission interval. Hence, following the training period, a receiver structure for joint data detection and PHN mitigation in the data transmission period is required. In the existing literature, joint data detection and PHN mitigation was analyzed in [26, 27, 114, 117]. However, the algorithms proposed in [114] and [27] are based on the assumption of perfect knowledge of channel and CFO. Moreover, the PHN tracking and data detection approach presented in [26] is computationally complex and suffers from performance degradation for higher order modulations. The PHN tracking in [117] requires the application of pilots throughout an OFDM symbol, which adversely affects the bandwidth efficiency of the system. In addition, our simulations show that the approach in [117] is outperformed by the receiver structure proposed in this chapter.

5.2 Contributions

The major contributions of this chapter can be summarized as follows:

1. The proposal of an ECM based estimator for jointly obtaining the channel, CFO, and PHN parameters in OFDM systems. The ECM based estimation is carried out in two steps. In the expectation or E-step, an *extended Kalman filter* (EKF) based estimator is utilized to accurately track the PHN over the training OFDM symbol. During the maximization or M-step, the channel and CFO parameters are estimated by minimizing the derived negative log likelihood function (cf. (5.7)).

2. The derivation of an expression for the HCRB for the joint estimation of the channel, CFO and PHN in OFDM systems. Simulation results show that, compared to the existing algorithms in the literature, the MSE of the proposed algorithm is closer to the HCRB and the proposed algorithm outperforms the existing estimation algorithms at moderate-to-high SNR.

3. The proposal of a new iterative algorithm based on the EKF for data detection and tracking the unknown time-varying PHN throughout the OFDM data packet.

4. Demonstration that the proposed estimation and detection algorithms are computationally efficient, compared to existing algorithms in the literature. In addition, the proposed estimation and detection algorithms outperform existing algorithms in terms of both the uncoded and the coded BER performance.

The remainder of this chapter is organized as follows. Section 5.3 describes the system model and the assumptions used in this work. Section 5.4 derives the HCRB for the joint channel, CFO and PHN estimation in OFDM systems. Section 5.5 describes the proposed ECM based estimator while Section 5.6 presents the proposed receiver for joint data detection and PHN tracking. Section 5.6 analyzes the complexity of the proposed estimation and data detection algorithms and compares it with the existing schemes. Section 5.8 provides numerical and simulation results. Finally, Section 5.9 concludes this chapter.

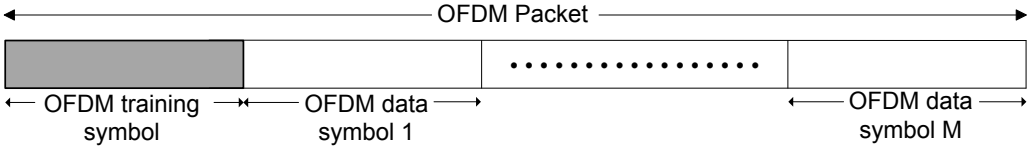

Figure 5.1: Timing diagram for transmission of training and data symbols within an OFDM packet.

5.3 System model

An OFDM packet of $(M+1)$ symbols, which consists of one training symbol and M data symbols, is considered as illustrated in Figure 5.1. In this chapter, the following set of assumptions are adopted:

A1. The channel is modeled as a slow fading frequency-selective channel, i.e., the channel is assumed to be quasi-static, which is constant and *unknown* over the OFDM packet duration and changes from packet to packet following a complex Gaussian distribution.

A2. The time-varying PHN changes from symbol to symbol and is modeled as a Wiener process, i.e., $\theta_n = \theta_{n-1} + \delta_n$, $\forall\ n$, where θ_n is the PHN at the nth instant, $\delta_n \sim \mathcal{N}(0, \sigma_\delta^2)$ is the PHN innovation and σ_δ^2 is the variance of the innovation process [71, 72].

A3. The CFO is modeled as a *deterministic unknown parameter* over a packet and is assumed to change from packet to packet.

A4. The training symbol is assumed to be *known* at the receiver.

A5. The timing offset is assumed to be perfectly estimated. Hence, it is not considered in this chapter.

Note that assumptions A1, A2, A3, and A5 are in line with the previous channel, CFO and PHN estimation algorithms in [12, 13, 23, 25, 26, 72, 117]. In addition, Assumption A5 can be safely assumed since the timing offset in practical systems is commonly estimated using autocorrelation based metrics [23, 26, 111, 112], which are not effected by disturbances of PHN and CFO. Assumption A2 is also reasonable in many practical scenarios to describe the behavior of practical oscillators [23, 71]. Furthermore, assumption A4 is adopted in the IEEE 802.11ac/ad standards to estimate channel and CFO in [10, 11, 23, 114, 117–119].

The complex baseband OFDM signal is given by

$$x_n = \frac{1}{\sqrt{N}} \sum_{k=0}^{N-1} d_k e^{j2\pi kn/N} \qquad n = 0, 1, \ldots, N-1, \tag{5.1}$$

where d_k, for $k = 1, \ldots, N$, is the modulated training symbol, x_n is the nth sample of the transmitted OFDM symbol, N is the number of subcarriers, and k denotes the subcarrier index. At the receiver, after removing the cyclic prefix, the complex baseband received signal, r_n, is given by

$$r_n = e^{j(\bar{\theta}_n + 2\pi n\epsilon/N)} \bar{s}_n + \eta_n \tag{5.2a}$$

$$= e^{j(\theta_n + 2\pi n\epsilon/N)} s_n + \eta_n, \tag{5.2b}$$

where $\bar{s}_n \triangleq \bar{h}_n \otimes x_n$ is the received OFDM training symbol, $\{\bar{\theta}_n\}_{n=0}^{N-1}$ is the discrete-time PHN sequence, ϵ is the normalized CFO, $\{\bar{h}_l\}_{l=0}^{L-1}$ is the channel impulse response, L is the channel length, and $\bar{h}_l \sim \mathcal{CN}(\mu_{h_l}, \sigma^2_{h_l})$. Note that (5.2b) is an equivalent system model representation of (5.2a), where $s_n \triangleq h_n \otimes x_n$, $h_n \triangleq e^{j\bar{\theta}_0}\bar{h}_n$ and $\theta_n \triangleq \bar{\theta}_n - \bar{\theta}_0$. This equivalent system model helps to distinguish between the phase disturbance caused by PHN and the channel phase for the first sample, which in turn resolves the phase ambiguity in the joint estimation problem as indicated in Section 5.5. In addition, $\{\eta_n\}_{n=0}^{N-1}$ is the complex AWGN with zero-mean and known variance σ_w^2. The received signal, $\mathbf{r} \triangleq [r_0, r_1, \ldots, r_{N-1}]^T$, in vector form is given by

$$\mathbf{r} = \mathbf{EPF}^H\mathbf{DWh} + \boldsymbol{\eta}, \tag{5.3}$$

where

- $\mathbf{E} \triangleq \text{diag}([1, e^{(j2\pi\epsilon/N)}, \ldots, e^{(j2\pi\epsilon/N)\times(N-1)}]^T)$ is the $N \times N$ CFO matrix,
- $\mathbf{P} \triangleq \text{diag}([e^{j\theta_0}, e^{j\theta_1}, \ldots, e^{j\theta_{N-1}}]^T)$ is the $N \times N$ PHN matrix,
- $\mathbf{F}$ is an $N \times N$ discrete Fourier transform (DFT) matrix, i.e., $[\mathbf{F}]_{l,n} \triangleq (1/\sqrt{N})e^{-j(2\pi nl/N)}$ for $n, l = 0, 1, \cdots, N-1$,
- $\mathbf{D} \triangleq \text{diag}(\mathbf{d}), \mathbf{d} \triangleq [d_0, d_1, \cdots, d_{N-1}]^T$ is the modulated training vector,
- $\mathbf{W}$ is an $N \times L$ DFT matrix, i.e., $\mathbf{W} \triangleq \mathbf{F}(1:N, 1:L)$,
- L denotes the number of channel taps,
- $\mathbf{h} \triangleq [h_0, h_1, \ldots, h_{L-1}]^T$ is the channel impulse response (CIR), and
- $\boldsymbol{\eta} \triangleq [\eta_0, \eta_1, \cdots, \eta_{N-1}]^T$ is the noise vector.

5.4 Derivation of the Hybrid Cramér-Rao Bound

In this section, the HCRB for the joint estimation of the CIR, PHN, and CFO parameters in OFDM systems is derived. The HCRB is a lower bound on the joint estimation of random, e.g., PHN, and deterministic, e.g., CIR and CFO parameters. Let $\boldsymbol{\lambda} = [\boldsymbol{\theta}^T \ \Re\{\mathbf{h}\}^T \ \Im\{\mathbf{h}\}^T \ \epsilon]^T$ be the vector of hybrid parameters of interest, where $\boldsymbol{\theta} \triangleq [\theta_1, \ldots, \theta_{N-1}]^T$ is a vector of random PHN parameters and the channel vector, $\mathbf{h}$, and the CFO, ϵ, are modeled as deterministic parameters. Note that it is clear from (5.2b) that there is no need to estimate θ_0. The accuracy of estimating $\boldsymbol{\lambda}$ is lower bounded by the HCRB, $\boldsymbol{\Omega}$, as [79, pp. 1-85]

$$\mathbb{E}_{\mathbf{r},\boldsymbol{\theta}|\epsilon}\left[(\hat{\boldsymbol{\lambda}}(\mathbf{r}) - \boldsymbol{\lambda})(\hat{\boldsymbol{\lambda}}(\mathbf{r}) - \boldsymbol{\lambda})^T\right] \succeq \boldsymbol{\Omega}. \tag{5.4}$$

Let us define $\boldsymbol{\Omega} \triangleq \mathbf{B}^{-1}$. Here, $\mathbf{B}$ is an $(N+2L) \times (N+2L)$ hybrid information matrix (HIM), which is determined according to the following theorem.

Theorem 5.1: The closed-form HIM for joint estimation of CIR, PHN, and CFO is given by

$$\mathbf{B} = \frac{2}{\sigma_w^2}\Re\left\{\begin{bmatrix} \mathbf{B}_{11} & \mathbf{B}_{12} & \mathbf{B}_{13} & \mathbf{b}_{14} \\ \mathbf{B}_{21} & \mathbf{B}_{22} & \mathbf{B}_{23} & \mathbf{b}_{24} \\ \mathbf{B}_{31} & \mathbf{B}_{32} & \mathbf{B}_{33} & \mathbf{b}_{34} \\ \mathbf{b}_{41} & \mathbf{b}_{42} & \mathbf{b}_{43} & \mathrm{b}_{44} \end{bmatrix}\right\}, \tag{5.5}$$

where

- $\mathbf{B}_{11} \triangleq \bar{\mathbf{Q}}_1^H \bar{\mathbf{Q}}_1 + \boldsymbol{\Lambda}$ is the $(N-1) \times (N-1)$ HIM for the estimation of $\boldsymbol{\theta}$, $\mathbf{Q}_1 = \mathrm{diag}(\mathbf{F}^H\mathbf{D}\mathbf{W}\mathbf{h})$, and $\bar{\mathbf{Q}}_1 = \mathbf{Q}_1(2:N, 2:N)$,
- $\boldsymbol{\Lambda}$ is an $(N-1) \times (N-1)$ tridiagonal matrix with diagonal elements given by $\frac{\sigma_w^2}{2\sigma_\delta^2}[1, 2, \ldots, 2, 1]$ and off-diagonal elements given by $\frac{-\sigma_w^2}{2\sigma_\delta^2}[1, \ldots, 1]$,
- $\mathbf{B}_{22} \triangleq \mathbf{Q}_2^H\mathbf{Q}_2$ is an $L \times L$ information matrix for the estimation of real part of $\mathbf{h}$, and $\mathbf{Q}_2 = \mathbf{F}^H\mathbf{D}\mathbf{W}$,
- $\mathbf{B}_{33} \triangleq \mathbf{Q}_2^H\mathbf{Q}_2$ is an $L \times L$ information matrix for the estimation of imaginary part of $\mathbf{h}$,
- $\mathrm{b}_{44} \triangleq \mathbf{q}_5^H\mathbf{q}_5$ is a scalar representing the information for the estimation of CFO, ϵ, $\mathbf{q}_5 = \sqrt{\mathbf{M}}\mathbf{F}^H\mathbf{D}\mathbf{W}\mathbf{h}$, and $\mathbf{M} \triangleq \mathrm{diag}\left(\left[(2\pi\frac{0}{N})^2, \ldots, (2\pi\frac{N-1}{N})^2\right]^T\right)$,
- $\mathbf{B}_{12} = \mathbf{B}_{21}^H \triangleq -j\bar{\mathbf{Q}}_1^H\bar{\mathbf{Q}}_2$, $\bar{\mathbf{Q}}_2 = \mathbf{Q}_2(2:N, 1:L)$,

- $\mathbf{B}_{13} = \mathbf{B}_{31}^H \triangleq \bar{\mathbf{Q}}_1^H \bar{\mathbf{Q}}_2$,
- $\mathbf{b}_{14} = \mathbf{b}_{41}^H \triangleq \bar{\mathbf{Q}}_4^H \bar{\mathbf{q}}_3$, $\mathbf{Q}_4 = \text{diag}(\sqrt{\mathbf{M}}\mathbf{F}^H\mathbf{DWh})$, $\bar{\mathbf{Q}}_4 = \mathbf{Q}_4(2:N, 2:N)$, $\mathbf{q}_3 = \mathbf{F}^H\mathbf{DWh}$, and $\bar{\mathbf{q}}_3 = \mathbf{q}_3(2:N)$,
- $\mathbf{B}_{23} = \mathbf{B}_{32}^H \triangleq j\mathbf{Q}_2^H \mathbf{Q}_2$,
- $\mathbf{b}_{24} = \mathbf{b}_{42}^H \triangleq j\mathbf{Q}_2^H \mathbf{q}_5$, and
- $\mathbf{b}_{34} = \mathbf{b}_{43}^H \triangleq \mathbf{Q}_2^H \mathbf{q}_5$.

Proof: The proof is given in Appendix (A.1).

Finally, the HCRB, $\mathbf{\Omega}$, is given by the inverse of the HIM. i.e., $\mathbf{\Omega} = \mathbf{B}^{-1}$. Note that the HCRB of the channel, $\mathbf{h}$, is obtained by adding the HCRB for real and imaginary parts of channels.

Remark 1: It is difficult to find the closed-form HCRB due to the complicated structure of the BIM. However, to obtain analytical insights, we consider a simple case, $N = 2$, $L = 1$, and derive the closed-form HCRB for the joint estimation of CIR, PHN, and CFO. Due to space limitation, the details are omitted and the final results for the closed-form HCRB of the CIR and the CFO estimation are given below

$$\text{HCRB}_{\text{CIR}}|_{N=2} = \frac{(2\gamma + \alpha)N^2\sigma_w^2}{2(\alpha + \gamma)\gamma}, \tag{5.6a}$$

$$\text{HCRB}_{\text{CFO}}|_{N=2} = \frac{N^2\left((\alpha + \gamma)N^2\sigma_w^2 + 2\gamma\alpha|h|^2\sigma_\delta^2\right)}{8\alpha\gamma|h|^2\pi^2}, \tag{5.6b}$$

where $\alpha \triangleq |d_1 + d_2 e^{j\frac{2\pi}{N}}|^2$ and $\gamma \triangleq |d_1 + d_2|^2$. It can be observed from (5.6a) that the HCRB for CIR estimation is independent of the PHN variance, σ_δ^2. Moreover, according to (5.6b), HCRB for CFO estimation is determined by PHN variance, σ_δ^2, at high SNR. This interesting insight is also reflected through simulations results in Figure 5.4 and Figure 5.5, respectively, in Section 5.8.

5.5 Proposed ECM based Estimator

In this section, an ECM based algorithm that utilizes the OFDM training symbol to jointly estimate the CIR, CFO and PHN at the receiver is derived. Joint data detection and PHN tracking during data transmission interval is analyzed in Section 5.6.

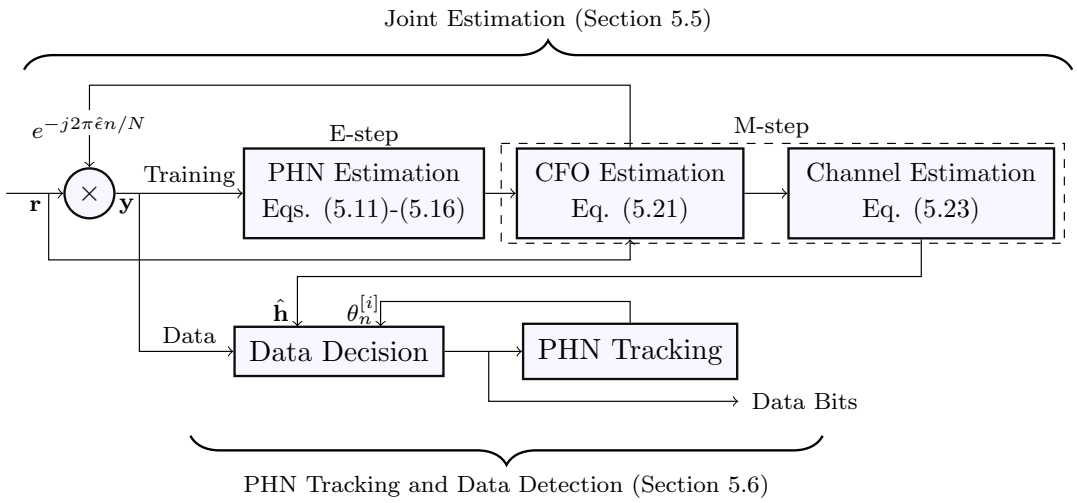

Figure 5.2: Proposed estimator based on an ECM algorithm and data detection.

Figure 5.2 depicts the block diagram of the overall system employing the proposed ECM based estimator and the joint data detection and PHN mitigation algorithm. As illustrated in Figure 5.2, the proposed ECM based estimator applies the training OFDM symbol at the beginning of each packet to estimate the CIR and CFO in the presence of PHN. Next, the data detection is performed by: 1) mitigating the impact of CFO over the length of the packet by multiplying the received packet with the complex conjugate of the estimated CFO coefficients determined using the proposed ECM estimator; 2) tracking the PHN parameters using an *iterative* algorithm that utilizes an EKF; 3) mitigating the effect of PHN over the received packet; and 4) detecting data symbols using the estimated CIR and hard decision decoding.

As shown in Figure 5.2, the ECM algorithm iterates between the expectation step (E-step) and the maximization step (M-step). In the E-step, an EKF is used to update the PHN vector at the $(i+1)$th iteration, $\boldsymbol{\theta}^{[i+1]}$, using the CIR and CFO estimates, $\hat{\mathbf{h}}^{[i]}$ and $\hat{\epsilon}^{[i]}$, respectively, obtained from the previous iteration, i.e., ith iteration. Next, in the M-step, the estimates of the CIR and CFO at the $i+1$th iteration, $\hat{\mathbf{h}}^{[i+1]}$ and $\hat{\epsilon}^{[i+1]}$, respectively are obtained.

For the given problem, the incomplete data set is given by the $N \times 1$ vector $\mathbf{s} \triangleq \mathbf{F}^H\mathbf{D}\mathbf{W}\mathbf{h} = [s_0, s_1, \ldots, s_{N-1}]^T$ and the received data, $\mathbf{r}$ in (5.3). Following [120], the hidden variable is chosen to be $\boldsymbol{\theta}$. Thus, the complete data set is defined as $\mathbf{z} \triangleq [\mathbf{r}^T \ \boldsymbol{\theta}^T]^T$. Moreover, the negative log likelihood function (LLF) of

the complete data, $\log p(\mathbf{z};\epsilon,\mathbf{h})$, is given by

$$\log p(\mathbf{z};\epsilon,\mathbf{h}) = \mathrm{C} + \frac{1}{\sigma_w^2}\sum_{n=0}^{N-1} \parallel r_n - e^{j2\pi\epsilon n/N} e^{j\theta_n} s_n \parallel^2 + \log p(\theta_0) + \sum_{n=0}^{N-1} \log p(\theta_n|\theta_{n-1}), \tag{5.7}$$

where C is a constant. Note that s_n (defined below (5.2b)) in (5.7) includes the CIR. The E and M-steps for estimating the CIR, CFO, and PHN in the training interval are detailed in the following subsections.

5.5.1 E-step

In this step, the received signal r_n is first multiplied by $e^{-j2\pi\hat{\epsilon}^{[i]}n/N}$. Subsequently, the signal $y_n \triangleq e^{-j2\pi n\epsilon^{[i]}/N} r_n$ is used to estimate the PHN vector, where $\hat{\epsilon}^{[i]}$ is the latest CFO estimate obtained from the previous iteration. An EKF during the E-step is proposed to estimate the PHN samples $\boldsymbol{\theta}$. The intuition behind choosing the EKF will be explained shortly after (5.9).

The signal y_n can be written as

$$y_n = e^{-j2\pi n\epsilon^{[i]}/N} r_n = e^{j2\pi n\Delta\hat{\epsilon}/N} e^{j\theta_n} s_n^{[i]} + \tilde{w}_n, \tag{5.8}$$

where $s_n^{[i]}$ is the nth symbol of the vector $\mathbf{s}^{[i]} \triangleq \mathbf{F}^H\mathbf{D}\mathbf{W}\hat{\mathbf{h}}^{[i]}$, $\Delta\hat{\epsilon} \triangleq \epsilon - \hat{\epsilon}^{[i]}$, and $\tilde{w}_n \triangleq w_n e^{-j2\pi n\hat{\epsilon}^{[i]}/N}$. The state and observation equations at time n are given by

$$\theta_n = \theta_{n-1} + \delta_n, \tag{5.9}$$

$$y_n = z_n + w_n = e^{j\theta_n} s_n + \tilde{w}_n, \tag{5.10}$$

respectively. Since the observation equation in (5.10) is a non-linear function of the unknown state vector $\boldsymbol{\theta}$, the EKF is used instead of the simple Kalman filtering. The EKF uses the Taylor series expansion to linearize the non-linear observation equation in (5.10) about the current estimates [78]. Thus, the Jacobian of z_n, $\dot{z}_n$, is evaluated by computing the first order partial derivative of z_n with respect to θ_n as

$$\begin{aligned}\dot{z}_n = \frac{\partial z(\theta_n)}{\partial\theta_n}\Big|_{\theta_n=\hat{\theta}_{n|n-1}} &= jz(\hat{\theta}_{n|n-1}) \\ &= je^{j\hat{\theta}_{n|n-1}^{[i]}}\hat{s}_n.\end{aligned} \tag{5.11}$$

The first and second moments of the state vector at the ith iteration denoted by $\hat{\theta}^{[i]}_{n|n-1}$ and $M^{[i]}_{n|n-1}$, respectively, are given by

$$\hat{\theta}^{[i]}_{n|n-1} = \hat{\theta}^{[i]}_{n-1|n-1}, \tag{5.12}$$

$$M^{[i]}_{n|n-1} = M^{[i]}_{n-1|n-1} + \sigma^2_{\delta}. \tag{5.13}$$

Given the observation y_n, the Kalman gain K_n, posteriori state estimate $\hat{\theta}^{[i]}_{n|n}$, and the filtering error covariance, $M^{[i]}_{n|n}$ are given by

$$K_n = M^{[i]}_{n|n-1}\dot{z}^*(\theta_{n|n-1})\big(\dot{z}(\theta_{n|n-1})M^{[i]}_{n-1|n-1}\dot{z}^*(\theta_{n|n-1}) + \sigma^2_w\big)^{-1}, \tag{5.14}$$

$$\hat{\theta}^{[i]}_{n|n} = \hat{\theta}^{[i]}_{n|n-1} + \Re\big\{K_n\big(y_n - e^{j\hat{\theta}^{[i]}_{n|n-1}}\hat{s}^{[i]}_n\big)\big\}, \tag{5.15}$$

$$M^{[i]}_{n|n} = \Re\big\{M^{[i]}_{n|n-1} - K_n\dot{z}(\theta_{n|n-1})M^{[i]}_{n|n-1}\big\}, \tag{5.16}$$

respectively. Before starting the EKF recursion (5.11)−(5.16), $\hat{\theta}^{[0]}_{1|0}$ and $M^{[0]}_{1|0}$ are initialized to $\hat{\theta}^{[0]}_{1|0} = 0$ and $M^{[0]}_{1|0} = \sigma^2_{\delta}$. The initialization choice for the PHN follows from the assumption that the complex channel parameter takes into account the PHN corresponding to the first symbol.

5.5.2 M-step

In this step, the CIR and CFO are estimated by minimizing the LLF in (5.7). In order to further reduce the complexity associated with the M-step, the minimization in (5.7) is carried out with respect to one of the parameters while keeping the remaining parameters at their most recently updated values [121, 122]. First, by using the channel estimate at the ith iteration, $\hat{\mathbf{h}}^{[i]}$, and the PHN vector estimate from the E-step, $\hat{\boldsymbol{\theta}}^{[i+1]}$, the LLF in (5.7) is minimized with respect to ϵ to obtain the CFO estimate for the $(i+1)$th iteration, $\hat{\epsilon}^{[i+1]}$, as

$$\hat{\epsilon}^{[i+1]} = \arg\min_{\epsilon} \sum_{n=0}^{N-1} \parallel r_n - e^{j2\pi\epsilon n/N}e^{j\theta_n}s_n \parallel^2 \Big|_{\theta_n=\hat{\theta}^{[i]}_n, \mathbf{h}=\hat{\mathbf{h}}^{[i]}}. \tag{5.17}$$

After simplifying (5.17), we have

$$\hat{\epsilon}^{[i+1]} = \arg\max_{\epsilon} \sum_{n=0}^{N-1} \Re\{(r_n)^*\hat{S}^{[i]}_n e^{j2\pi\epsilon n/N}\}, \tag{5.18}$$

where $\hat{S}_n^{[i]} = e^{j\hat{\theta}_n^{[i]}}\hat{s}_n$. In order to resolve the nonlinearity in (5.18), we can approximate the term $e^{j2\pi\epsilon n/N}$ using a second order Taylor series expansion around the pervious CFO estimate, $\hat{\epsilon}^{[i]}$, as

$$e^{j2\pi\epsilon n/N} = e^{j2\pi\hat{\epsilon}^{[i]}n/N} + (\epsilon - \hat{\epsilon}^{[i]})(j\frac{2\pi}{N}n)e^{j2\pi\hat{\epsilon}^{[i]}n/N} + \frac{1}{2}(\epsilon - \hat{\epsilon}^{[i]})^2(j\frac{2\pi}{N}n)^2 e^{j2\pi\hat{\epsilon}^{[i]}n/N}. \tag{5.19}$$

Substituting (5.19) into (5.18), $\hat{\epsilon}^{[i+1]}$ is given by

$$\begin{aligned}\hat{\epsilon}^{[i+1]} = \arg\max_{\epsilon}\Bigg\{ &\sum_{n=0}^{N-1} \Re\big\{(r_n)^* \hat{S}_n^{[i]} e^{j2\pi\hat{\epsilon}^{[i]}n/N} \\ &+ (\epsilon - \hat{\epsilon}^{[i]}) \sum_{n=0}^{N-1} \Re\big\{(r_n)^* \hat{S}_n^{[i]} (j\frac{2\pi}{N}n) e^{j2\pi\hat{\epsilon}^{[i]}n/N}\big\} \\ &+ \frac{1}{2}(\epsilon - \hat{\epsilon}^{[i]})^2 \sum_{n=0}^{N-1} \Re\big\{(r_n)^* \hat{S}_n^{[i]} (j\frac{2\pi}{N}n)^2 e^{j2\pi\hat{\epsilon}^{[i]}n/N}\big\}\Bigg\}. \end{aligned} \tag{5.20}$$

Taking the derivative of (5.20) with respect to ϵ and equating the result to zero, the estimate of ϵ at the $(i+1)$th iteration is given by

$$\hat{\epsilon}^{[i+1]} = \hat{\epsilon}^{[i]} + \frac{N}{2\pi}\frac{\sum_{n=0}^{N-1} n\Im\big\{(r_n)^* \hat{S}_n^{[i]} e^{j2\pi\hat{\epsilon}^{[i]}n/N}\big\}}{\sum_{n=0}^{N-1} n^2\Re\big\{(r_n)^* \hat{S}_n^{[i]} e^{j2\pi\hat{\epsilon}^{[i]}n/N}\big\}}. \tag{5.21}$$

Next, by setting $\boldsymbol{\theta}$ and ϵ to their latest updated values, the updated value of $\hat{\mathbf{h}}$ at the $(i+1)$th iteration, $\hat{\mathbf{h}}^{[i+1]}$, is determined as outlined below.

Based on the vector form of the received signal in (5.3), the negative LLF, in (5.7), can be written as

$$\log p(\mathbf{z};\epsilon) = \mathrm{C}_1 + \parallel \mathbf{r} - \mathbf{EP\Gamma h} \parallel^2 + \log p(\boldsymbol{\theta}). \tag{5.22}$$

where $\boldsymbol{\Gamma} \triangleq \mathbf{F}^H\mathbf{DW}$ and C_1 is a constant. Taking the derivative of (5.22) with respect to $\mathbf{h}$ and equating the result to zero, the estimate of $\mathbf{h}$ at the $(i+1)$th iteration is given by

$$\hat{\mathbf{h}}^{[i+1]} = (\boldsymbol{\Gamma}^H\boldsymbol{\Gamma})^{-1}\boldsymbol{\Gamma}^H\hat{\mathbf{P}}^H\hat{\mathbf{E}}^H\mathbf{r}, \tag{5.23}$$

where $\hat{\mathbf{E}} \triangleq \mathrm{diag}([e^{(j2\pi\hat{\epsilon}^{[i+1]}/N)\times 0}, e^{(j2\pi\hat{\epsilon}^{[i+1]}/N)}, \ldots, e^{(j2\pi\hat{\epsilon}^{[i+1]}/N)\times(N-1)}]^T)$ and $\hat{\mathbf{P}} \triangleq \mathrm{diag}([e^{j\hat{\theta}_0^{[i]}}, e^{j\hat{\theta}_1^{[i]}}, \ldots, e^{j\hat{\theta}_{N-1}^{[i]}}]^T)$. Note that $\hat{\epsilon}^{[i+1]}$ and $\hat{\boldsymbol{\theta}}^{[i]} \triangleq [\hat{\theta}_1^{[i]}, \ldots, \hat{\theta}_{N-1}^{[i]}]^T$ are determined as in (5.21) and (5.15), respectively.

Using (5.15), (5.21), and (5.23), the proposed algorithm iteratively updates the PHN, CFO, and CIR estimates, respectively. The algorithm is terminated when the difference between the likelihood functions of two iterations is smaller than a threshold ζ, i.e.,

$$\left| \sum_{n=0}^{N-1} \left\| r_n - e^{j2\pi\hat{\epsilon}^{[i+1]}n/N} e^{j\hat{\theta}_n^{[i+1]}} s_n^{[i+1]} \right\|^2 - \sum_{n=0}^{N-1} \left\| r_n - e^{j2\pi\hat{\epsilon}^{[i]}n/N} e^{j\hat{\theta}_n^{[i]}} s_n^{[i]} \right\|^2 \right| \leq \zeta. \tag{5.24}$$

5.5.3 Initialization and Convergence

The appropriate initialization of CFO and CIR, i.e., $\hat{\epsilon}^{[0]}$ and $\hat{\mathbf{h}}^{[0]}$, respectively, is essential to ensure the global convergence of the proposed estimator [123]. The initialization process can be summarized as follows:

- The initial CFO estimate is obtained by applying an exhaustive search for the value of ϵ that minimizes the cost function, $\sum_{n=0}^{N-1} \parallel r_n - e^{j2\pi\hat{\epsilon}n/N}\hat{s}_n \parallel^2$. Here, $\hat{s}_n$ is the nth symbol of the vector $\hat{\mathbf{s}} \triangleq \mathbf{F}^H\mathbf{D}\mathbf{W}\hat{\mathbf{h}}$ with $\hat{\mathbf{h}} \triangleq (\mathbf{\Gamma}^H\mathbf{\Gamma})^{-1}\mathbf{\Gamma}^H \hat{\mathbf{E}}^H\mathbf{r}$. Note that this exhaustive search needs to be only carried out at the system start up to initialize the estimation process. Simulations in Section 5.8 indicate that an exhaustive search with a coarse step size of 10^{-2} is sufficient for the initialization of the proposed estimator.

- Using $\hat{\epsilon}^{[0]}$, the initial channel estimate, $\hat{\mathbf{h}}^{[0]}$, is obtained by applying the relationship, $\hat{\mathbf{h}}^{[0]} = (\mathbf{\Gamma}^H\mathbf{\Gamma})^{-1}\mathbf{\Gamma}^H(\hat{\mathbf{E}}^{[0]})^H\mathbf{r}$. Here, $\hat{\mathbf{E}}^{[0]} = \hat{\mathbf{E}}|_{\hat{\epsilon}=\hat{\epsilon}^{[0]}}$.

Note that, based on the equivalent system model in (5.2b) and the simulation results in Section 5.8, it can be concluded that the proposed ECM algorithm converges globally when the PHN vector $\hat{\boldsymbol{\theta}}$ is initialized as $\hat{\boldsymbol{\theta}}^{[0]} = \mathbf{0}_{N-1\times 1}$.

Simulation results in Section 5.8 show that at SNR of 20 dB or higher the proposed ECM-based estimator always converges to the true estimates in only 2 iterations.

5.6 Joint Data Detection and PHN Mitigation

In this section, an iterative detector that utilizes an EKF to the track the PHN parameters during the data transmission interval is proposed.

At first, using the estimated CFO value, the effect of CFO on the received data symbol, $\mathbf{r}$, in (5.3) is compensated. As shown Figure 5.2, the resulting

signal, $\mathbf{y} \triangleq [y_1, \ldots, y_n]$, where y_n is defined in (5.10), passes through an *iterative* data detection and PHN estimation block. An EKF is proposed for tracking the PHN samples, $\boldsymbol{\theta}$, over the data symbols. The PHN estimation is similar to that in (5.11)-(5.16) and is not presented here to avoid repetition. However, instead of training-based PHN tracking, the PHN estimation is followed in a decision-directed fashion for the received data symbols. In other words, the estimate of the data symbol in the previous iteration, $\hat{\mathbf{d}}^{[i-1]}$, is used to update the symbol's PHN estimate at the current iteration $\hat{\boldsymbol{\theta}}^{[i]}$. Particularly, $\mathbf{s}^{[i]}$ in (5.10), is calculated as $\mathbf{s}^{[i]} = \mathbf{F}^H \hat{\mathbf{D}}^{[i-1]} \mathbf{W} \hat{\mathbf{h}}$, where $\hat{\mathbf{h}}$ is the CIR vector estimate obtained from the ECM estimator during the training interval, and $\hat{\mathbf{D}}^{[i-1]} \triangleq \text{diag}(\hat{\mathbf{d}}^{[i-1]})$. Next, the data vector estimate is updated for the ith iteration. Following [26] and based on the received signal in (5.3), the negative LLF for the CFO compensated signal, $\mathbf{y}$, can be written as

$$\log p(\mathbf{y}, \hat{\mathbf{d}}, \hat{\boldsymbol{\theta}}) = \text{C} + \frac{1}{2\sigma_w^2} \parallel \mathbf{y} - \hat{\mathbf{P}} \mathbf{F}^H \hat{\boldsymbol{\Upsilon}} \hat{\mathbf{d}} \parallel^2 + \frac{1}{2\xi_d} \parallel \hat{\mathbf{d}} \parallel^2 + \log p(\boldsymbol{\theta}), \tag{5.25}$$

where C is a constant and

- $\hat{\boldsymbol{\Upsilon}} \triangleq \text{diag}(\mathbf{W}\hat{\mathbf{h}})$ is the estimated channel frequency response,
- $\hat{\mathbf{d}} \triangleq [\hat{d}_0, \hat{d}_1, \cdots, \hat{d}_{N-1}]^T$ is the estimate of the modulated data vector, and
- ξ_d is the average transmitted symbol power and normalized to 1,

Taking the derivative of (5.25) with respect to $\mathbf{d}$ and equating the result to zero, the estimate of $\mathbf{d}$ at the ith iteration, $\hat{\mathbf{d}}^{[i]}$ is given by

$$\hat{\mathbf{d}}^{[i]} = (\hat{\boldsymbol{\Upsilon}}^H \hat{\boldsymbol{\Upsilon}} + \frac{\sigma_w^2}{\xi_d} \mathbf{I}_N)^{-1} \hat{\boldsymbol{\Upsilon}}^H \mathbf{F} \hat{\mathbf{P}}^H \mathbf{y}, \tag{5.26}$$

where $\hat{\mathbf{P}} \triangleq \text{diag}([e^{j\theta_0}, e^{j\hat{\theta}_1^{[i]}}, \ldots, e^{j\hat{\theta}_{N-1}^{[i]}}]^T)$ and $\hat{\boldsymbol{\theta}}^{[i]} \triangleq [\hat{\theta}_1^{[i]}, \ldots, \hat{\theta}_{N-1}^{[i]}]^T$ are obtained via the EKF based estimator.

Using the EKF set of equations (5.11)−(5.16) and (5.26), the proposed algorithm iteratively updates the PHN and data estimates, respectively, and stops when the difference between likelihood functions of two iterations is smaller than a threshold ζ, i.e.,

$$\left| \sum_{n=0}^{N-1} \left\| y_n - e^{j\hat{\theta}_n^{[i+1]}} \hat{s}_n^{[i+1]} \right\|^2 - \sum_{n=0}^{N-1} \left\| y_n - e^{j\hat{\theta}_n^{[i]}} \hat{s}_n^{[i]} \right\|^2 \right| \leq \zeta. \tag{5.27}$$

Let $\hat{\mathbf{d}}^{[0]}$ denote the initial estimate of the transmitted data vector. Appropriate initialization of $\hat{\mathbf{d}}^{[0]}$ results in the proposed iterative detector to converge quickly. In our algorithm, the initial data estimate is obtained using $\hat{\mathbf{d}}^{[0]} = (\hat{\boldsymbol{\Upsilon}}^H\hat{\boldsymbol{\Upsilon}} + \frac{\sigma_w^2}{\xi_d}\mathbf{I}_N)^{-1}\hat{\boldsymbol{\Upsilon}}^H\mathbf{F}\hat{\mathbf{P}}_{[m-1]}^H\mathbf{y}$, where $\hat{\mathbf{P}}_{[m-1]}$ is the PHN matrix estimate obtained from the previous OFDM symbol. Simulation results in Section 5.8 indicate that at SNR= 20 dB the proposed detector, on average, converges after 2 iterations. The overall estimation and detection algorithm is summarized in Algorithm 2 on the next page.

5.7 Complexity Analysis

In this section, the computational complexity of the proposed estimator and detector is compared with that of [23] and [26]. Throughout this section, computational complexity is defined as the number of complex additions and multiplications [124].

Let us denote the computational complexity of the proposed estimator by $C_{\text{EST}} = C_{\text{EST}}^{[M]} + C_{\text{EST}}^{[A]}$, where $C_{\text{EST}}^{[M]}$ and $C_{\text{EST}}^{[A]}$ denote the number of complex multiplications and additions used by the estimator, respectively. $C_{\text{EST}}^{[M]}$ and $C_{\text{EST}}^{[A]}$ are determined as

$$\begin{aligned} C_{\text{EST}}^{[M]} =& \big[\underbrace{N}_{(5.11)} + \underbrace{5N}_{(5.14)} + \underbrace{2N}_{(5.15)} + \underbrace{2N}_{(5.16)} + \underbrace{7N}_{(5.21)} + \underbrace{LN(2N+1)}_{(5.23)} + \underbrace{N(N^2+L(N+1))}_{s_n \text{in}(5.15)}\big] \\ & t_{\text{ECM}} + \big[\underbrace{3N}_{\sum_{n=0}^{N-1}\|r_n - e^{j2\pi\hat{\epsilon}n/N}\hat{s}_n\|^2} + \underbrace{LN(2N+1)}_{\hat{\mathbf{h}}\triangleq\xi_d{}^{-1}\boldsymbol{\Gamma}^H\hat{\mathbf{E}}^H\mathbf{r}} + \underbrace{N(N^2+L(N+1))}_{\hat{\mathbf{s}}\triangleq\mathbf{F}^H\mathbf{D}\mathbf{W}\hat{\mathbf{h}}}\big]t_{\text{initialize}} \\ & + \underbrace{N^2(N+L)}_{\boldsymbol{\Gamma}\text{in}(5.23)}, \end{aligned} \tag{5.28}$$

$$\begin{aligned} C_{\text{EST}}^{[A]} =& \big[\underbrace{N}_{(5.13)} + \underbrace{N}_{(5.14)} + \underbrace{2N}_{(5.15)} + \underbrace{N}_{(5.16)} + \underbrace{2N+1}_{(5.21)} + \underbrace{L(N-1)(2N+1)}_{(5.23)} \\ & + \underbrace{N(N-1)(L+1)+N(L-1)}_{s_n \text{in}(5.15)}\big]t_{\text{ECM}} \\ & + \big[\underbrace{2N}_{\sum_{n=0}^{N-1}\|r_n - e^{j2\pi\hat{\epsilon}n/N}\hat{s}_n\|^2} + \underbrace{L(N-1)(2N+1)}_{\hat{\mathbf{h}}\triangleq\xi_d{}^{-1}\boldsymbol{\Gamma}^H\hat{\mathbf{E}}^H\mathbf{r}} \\ & + \underbrace{N(N-1)(L+1)+N(L-1)}_{\hat{\mathbf{s}}\triangleq\mathbf{F}^H\mathbf{D}\mathbf{W}\hat{\mathbf{h}}}\big]t_{\text{initialize}} + \underbrace{N(N-1)(N+L)}_{\boldsymbol{\Gamma}\text{in}(5.23)}, \end{aligned} \tag{5.29}$$

Algorithm 2 PROPOSED ECM ESTIMATOR AND DATA DETECTION ALGORITHM

ECM ESTIMATOR

Initialization

$\hat{\theta}_{1|0}^{[0]} = 0$ and $M_{1|0}^{[0]} = \sigma_\delta^2$ and obtain $\hat{\epsilon}^{[0]}$ and $\hat{\mathbf{h}}^{[0]}$ using an exhaustive search and (5.23) with coarse step size i.e., 10^{-2}

while $\left| \sum_{n=0}^{N-1} \left\| r_n - e^{j2\pi\hat{\epsilon}^{[i+1]}n/N} e^{j\hat{\theta}_n^{[i+1]}} s_n^{[i+1]} \right\|^2 - \sum_{n=0}^{N-1} \left\| r_n - e^{j2\pi\hat{\epsilon}^{[i]}n/N} e^{j\hat{\theta}_n^{[i]}} s_n^{[i]} \right\|^2 \right| > \zeta$. **do**

for $n = 0, 1, \ldots, N-1$ **do**

(5.11)−(5.16)

end for

for $n = 0, 1, \ldots, N-1$ **do**

$\hat{\epsilon}^{[i+1]} = \hat{\epsilon}^{[i]} + \frac{N}{2\pi} \frac{\sum_{n=0}^{N-1} n\Im\left\{(r_n)^* \hat{S}_n^{[i]} e^{j2\pi\hat{\epsilon}^{[i]}n/N}\right\}}{\sum_{n=0}^{N-1} n^2\Re\left\{(r_n)^* \hat{S}_n^{[i]} e^{j2\pi\hat{\epsilon}^{[i]}n/N}\right\}}$

end for

$\hat{\mathbf{h}}^{[i+1]} = (\mathbf{\Gamma}^H\mathbf{\Gamma})^{-1}\mathbf{\Gamma}^H\hat{\mathbf{P}}^H\hat{\mathbf{E}}^H\mathbf{r}$

$\hat{\mathbf{h}}^{[i]} = \hat{\mathbf{h}}^{[i+1]}$, $\hat{\boldsymbol{\theta}}^{[i]} = \hat{\boldsymbol{\theta}}^{[i+1]}$, $\hat{\epsilon}^{[i]} = \hat{\epsilon}^{[i+1]}$

end while

DATA DETECTION

for $m = 1, \ldots, M$ **do**

Initialization

Obtain $\hat{\mathbf{d}}^{[0]} = (\hat{\mathbf{\Upsilon}}^H\hat{\mathbf{\Upsilon}} + \frac{\sigma_w^2}{\xi_d}\mathbf{I}_N)^{-1}\hat{\mathbf{\Upsilon}}^H\mathbf{F}\hat{\mathbf{P}}_{[m-1]}^H\mathbf{y}$

Replace $\hat{\mathbf{d}}^{[0]}$ by its hard decision.

while $\left| \sum_{n=0}^{N-1} \left\| y_n - e^{j\hat{\theta}_n^{[i+1]}} \hat{s}_n^{[i+1]} \right\|^2 - \sum_{n=0}^{N-1} \left\| y_n - e^{j\hat{\theta}_n^{[i]}} \hat{s}_n^{[i]} \right\|^2 \right| > \zeta$ **do**

Using the EKF set of equation in Section 5.5.1 to estimate the PHN parameters,

$\hat{\mathbf{d}}^{[i]} = (\hat{\mathbf{\Upsilon}}^H\hat{\mathbf{\Upsilon}} + \frac{\sigma_w^2}{\xi_d}\mathbf{I}_N)^{-1}\hat{\mathbf{\Upsilon}}^H\mathbf{F}\hat{\mathbf{P}}^H\mathbf{y}$.

Replace $\hat{\mathbf{d}}^{[i]}$ by its hard decision.

$\hat{\mathbf{d}}^{[i]} = \hat{\mathbf{d}}^{[i+1]}$

end while

end for

where t_{ECM} is the number of iterations in the ECM estimator and $t_{\text{initialize}}$ is the number of iterations required to initialize the ECM algorithm. The latter depends on the step size of the exhaustive search used to initialize the CFO estimates.

Similarly, the computational complexity of the proposed detector is denoted by $C^{[M]}_{\text{DATA DET}}$ and $C^{[A]}_{\text{DATA DET}}$, where $C^{[M]}_{\text{DATA DET}}$ and $C^{[A]}_{\text{DATA DET}}$ denote the number of complex multiplications and additions used by the detector, respectively. $C^{[M]}_{\text{DATA DET}}$ and $C^{[A]}_{\text{DATA DET}}$ are determined as

$$C^{[M]}_{\text{DATA DET}} = \big[\underbrace{N}_{(5.11)} + \underbrace{5N}_{(5.14)} + \underbrace{2N}_{(5.15)} + \underbrace{2N}_{(5.16)} + \underbrace{N(N^2+L(N+1))}_{s_n \text{in}(5.15)} + \underbrace{N^2(5N+1)}_{(5.26)}\big] t_{\text{DATA DET}} + \underbrace{N^2(5N+1)}_{\hat{\mathbf{d}}^{[0]}=(\hat{\boldsymbol{\Upsilon}}^H\hat{\boldsymbol{\Upsilon}}+\frac{\sigma_w^2}{\xi_d}\mathbf{I}_N)^{-1}\hat{\boldsymbol{\Upsilon}}^H\mathbf{F}\mathbf{P}^H_{[m-1]}\mathbf{y}} + \underbrace{NL}_{\hat{\boldsymbol{\Upsilon}}\text{in}(5.26)}, \tag{5.30}$$

$$\begin{aligned} C^{[A]}_{\text{DATA DET}} = \big[&\underbrace{N}_{(5.13)} + \underbrace{N}_{(5.14)} + \underbrace{2N}_{(5.15)} + \underbrace{N}_{(5.16)} + \underbrace{N(N-1)(L+1)+N(L-1)}_{s_n \text{in}(5.15)} \\ &+ \underbrace{N(N^2+N(N-1)(4N+1))}_{(5.26)}\big] t_{\text{DATA DET}} \\ &+ \underbrace{N(N^2+N(N-1)(4N+1))}_{\hat{\mathbf{d}}^{[0]}=(\hat{\boldsymbol{\Upsilon}}^H\hat{\boldsymbol{\Upsilon}}+\frac{\sigma_w^2}{\xi_d}\mathbf{I}_N)^{-1}\hat{\boldsymbol{\Upsilon}}^H\mathbf{F}\mathbf{P}^H_{[m-1]}\mathbf{y}} + \underbrace{N(L-1)}_{\hat{\boldsymbol{\Upsilon}}\text{in}(5.26)}, \end{aligned} \tag{5.31}$$

where $t_{\text{DATA DET}}$ is the number of iterations required by the detector in (5.27).

Following similar steps as in (5.28)-(5.31), we can find the computational complexity of the estimator in [23] as

$$C^{[M]}_{[23,\text{EST}]} = \big[N^2(11N+7)+2N\big] t_{[8]} + N^2(9N+4L+1) + LN \tag{5.32}$$

$$\begin{aligned} C^{[A]}_{[23,\text{EST}]} = &\big[2N^3+(N-1)(9N^2+7N+2)+1\big] t_{[8]} + 2N^3 \\ &+ (N-1)(N(7N+4L+1)+L) \end{aligned} \tag{5.33}$$

where $t_{[23]}$ is the number of iterations required for estimating the CFO via an exhaustive search in [23]. Moreover, the notations $C^{[M]}_{[23,\text{EST}]}$ and $C^{[A]}_{[23,\text{EST}]}$ are used to denote the number of complex multiplications and additions used by the estimator in [23], respectively.

The computational complexity of the detector in [26] is given by

$$C^{[M]}_{[26,\text{ DATA DET}]} = \big[N^2(11N+6)\big] t_{[26]} + N^2(6N+1) \tag{5.34}$$

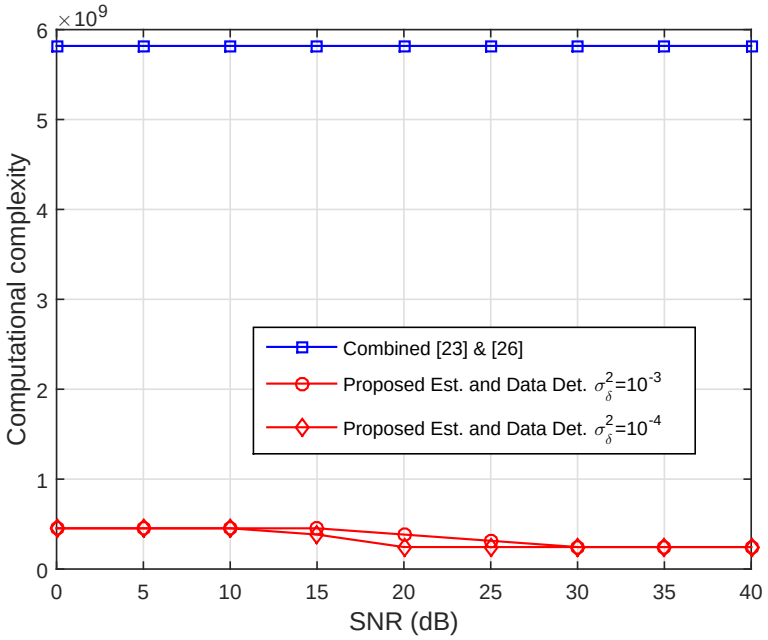

Figure 5.3: Comparison of the computational complexity of the proposed algorithms and the algorithms in [23] and [26] for PHN variance, $\sigma_\delta^2 = [10^{-3}, 10^{-4}]$ rad^2.

$$C^{[A]}_{[26,\ \text{DATA DET}]} = \big[N(N-1)(9N+6) + N^2(2N+1)\big]t_{[26]} + N^2(6N-5) + N(N-1) \tag{5.35}$$

where $t_{[26]}$ is the number of iterations used by the detector in [26]. Note that since the estimation approach of [23] and [24] are similar, the computational complexity of the estimation algorithm in [24] can be calculated using (5.32) and (5.33). Note that the computational complexity of the algorithm in [117] is not presented since the approach in [117] only considers channel and PHN estimation while assuming that no CFO is present.

Figure 5.3 compares the computational complexity of the proposed algorithm ((27)-(30)) and the existing algorithms in [23] and [26] ((31)-(34)) for PHN variance, $\sigma_\delta^2 = [10^{-3}, 10^{-4}]$ rad^2. Note that the combined algorithm, [23] & [26], is used because the authors (Lin et. al.) have proposed the estimation algorithm in [23] and the data detection algorithm in [26]. For the comparison, the number of iterations, t_{ECM}, $t_{\text{DATA DET}}$ and $t_{\text{initialize}}$ for the proposed algorithm and $t_{[23]}$ and $t_{[26]}$ for the existing algorithms are determined as follows. *For the proposed algorithm*, simulations indicate that (i) at low SNR, i.e., $SNR < 10$ dB,

on average, the proposed estimator and detector converge after $t_{\text{ECM}} = 3$ and $t_{\text{DATA DET}} = 5$ iterations, respectively, (ii) the number of iterations decreases to $t_{\text{ECM}} = t_{\text{DATA DET}} = 2$ at $SNR \geq 20$ dB for $\sigma_\delta^2 = 10^{-4}$ rad^2 and $SNR \geq 30$ dB for $\sigma_\delta^2 = 10^{-3}$ rad^2, and (iii) the proposed ECM algorithm converges to the true estimates when the CFO estimates are initialized with a step size of 10^{-2}, i.e., $t_{\text{initialize}} = 10^2$. *For the existing algorithms*, the results in Section 5.8 indicate that in order to reach an appropriate estimation accuracy and system performance, the algorithm in [23] requires the step size for the exhaustive search to be set to 10^{-3}, i.e., $t_{[23]}$=10^3. In addition, the data detector in [26] requires $t_{[26]} = 4$ iterations to converge for the PHN variance of $\sigma_\delta^2 = [10^{-3}, 10^{-4}]$ rad^2. Using these values for the number of iterations, the results shown in Figure 5.3 can be obtained. It can be seen that the proposed estimation and data detection algorithms are computationally more efficient compared to the combined algorithms in [23] and [26], e.g., by a factor of 23.8 for SNR = 20 dB, $\sigma_\delta^2 = 10^{-4}$ rad^2, $L = 4$ and $N = 64$. Moreover, the total number of real multiplications and additions in our proposed algorithms is 3.97×10^7 and 3.43×10^8, respectively, while they are 2.92×10^9 and 2.89×10^9, respectively, for the combined algorithms in [23] and [26].

5.8 Simulation Results and Discussions

In this section, simulation results are presented to evaluate the performance of the proposed estimation and data detection algorithms. An OFDM packet consisting of $m = 6$ OFDM symbols is considered, comprising an OFDM training symbol followed by 5 data symbols. The data symbols are drawn from normalized 64, 128, or 256 quadrature amplitude modulation (QAM). In the simulations, the symbol SNR is defined as $\xi_d/\sigma_w^2 = 1/\sigma_w^2$. The sampling rate of the OFDM signal is 20 MHz, corresponding to the OFDM sampling duration of $T_s = 50$ nanoseconds. The channel impluse response (CIR) is assumed to be a Rayleigh fading multipath channel with a delay of $L = 4$ taps and an exponentially decreasing power delay profile with the average channel power = $[-1.52 - 6.75 - 11.91 - 17.08]$ dB. The Wiener PHN is generated with PHN variances of $\sigma_\delta^2 = [10^{-3}, 10^{-4}]$ rad^2. The unknown normalized CFO is assumed to be uniformly distributed over the range $\epsilon \in (-0.5, 0.5)$ for each simulation. Unless specified otherwise, an OFDM training symbol size of $N = 64$ subcarriers is used with each subcarrier modulated in *quadrature phase-shift keying (QPSK)* with subcarrier spacing = 312.5 kHz. The simulation results are averaged over 1×10^5 Monte Carlo simulation runs. Finally,

the MSE performance of the proposed estimator and the BER performance of the overall OFDM system are investigated in the following subsections.

5.8.1 Estimation Performance

In this subsection, the performance of the proposed ECM estimator is compared with the HCRB in Theorem 5.1 and the MAP estimator in [23]. Figures 5.4, 5.5, and 5.6 plot the HCRB and the MSE for estimating the CIR, PHN, and CFO, respectively. The HCRB in (5.7) is numerically evaluated for two different PHN variance, e.g., $\sigma_\delta^2 = [10^{-3}, 10^{-4}]$ rad^2. The following observations can be made from the figures:

1. The HCRB for PHN and CFO estimation and the estimator's MSE are dependent on the variance of the PHN process. Note that, $\sigma_\delta^2 = 10^{-3}$ rad^2, corresponds to the presence of a very strong PHN [125].

2. Figure 5.4 shows that the HCRB for the channel estimation does not suffer from an error floor, which is inline with Remark 1 in Section 5.4. However, Figures 5.5 and 5.6 show that the HCRB for CFO and PHN suffer from

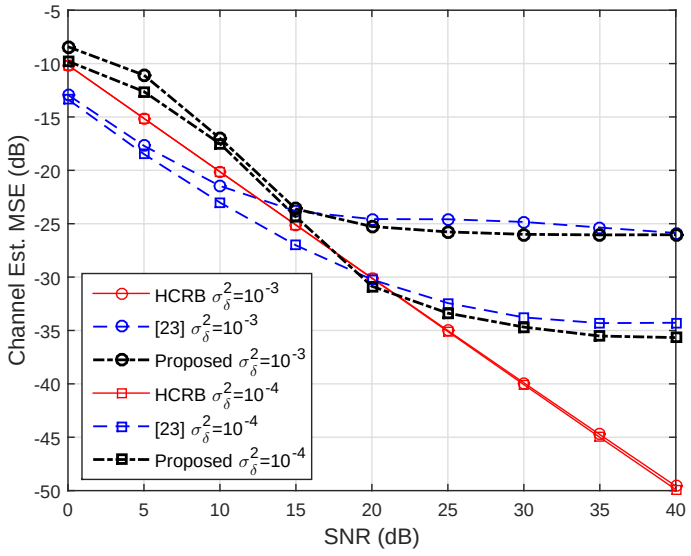

Figure 5.4: Channel estimation MSE for the proposed and MAP estimators for PHN variance, $\sigma_\delta^2 = [10^{-3}, 10^{-4}]$ rad^2.

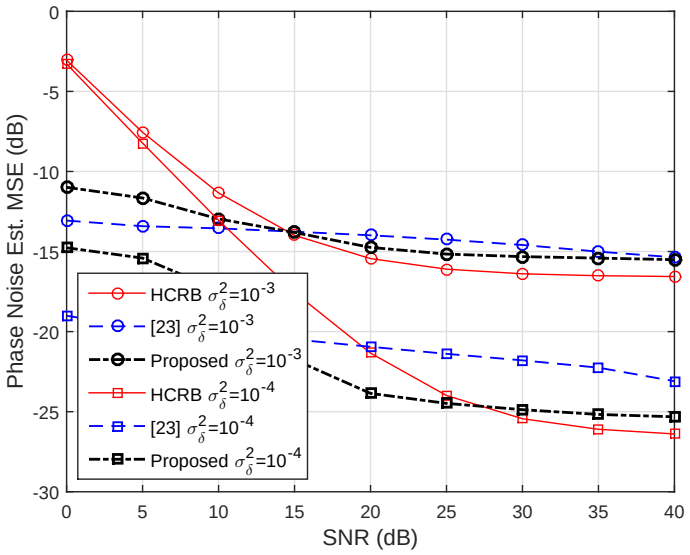

Figure 5.5: PHN estimation MSE for the proposed and MAP estimators for PHN variance, $\sigma_\delta^2 = [10^{-3}, 10^{-4}]$ rad^2.

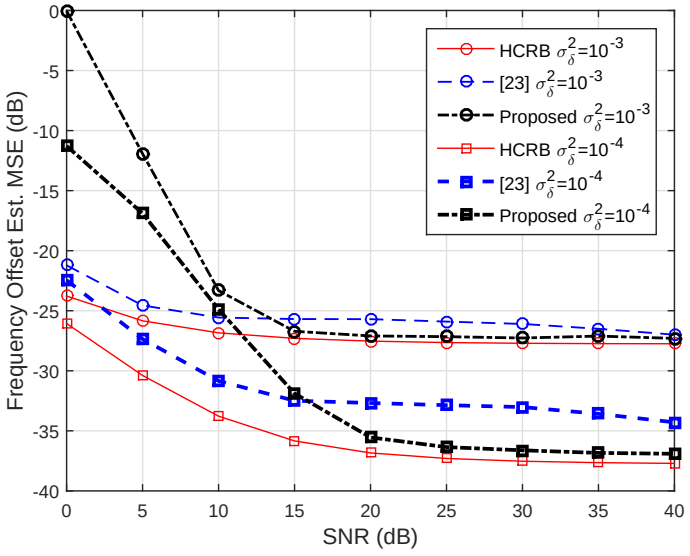

Figure 5.6: CFO estimation MSE for the proposed and MAP estimators for PHN variance, $\sigma_\delta^2 = [10^{-3}, 10^{-4}]$ rad^2.

an error floor, which is directly related to the variance of the PHN process. This is due to the fact that at low SNR the performance of the system is dominated by AWGN, while at high SNR the performance of the proposed estimator is limited by PHN and the resulting ICI.

3. Figures 5.4, 5.5, and 5.6 show that at low SNR, i.e., $SNR < 15$ dB, the proposed estimator is outperformed by the estimation algorithm in [23]. This outcome can be attributed to the different linearization approaches that are applied in this thesis. In [23], a first order Taylor series approximation is applied to linearize the signal model with respect to the PHN parameters over the whole OFDM symbol. However, the proposed algorithm uses an EKF algorithm that linearizes the observation sequence sample by sample, i.e., the estimate of the previous sample's PHN is used to linearize the current sample's PHN within the OFDM symbol. Thus, the proposed algorithm is less severely impacted by the residual error introduced by the first order Taylor series approximation. This results in significantly better estimation performance at high SNRs, where the estimator's performance is mainly impacted by PHN and not the AWGN. However, the estimator in [23] is based on the maximum a posterior (MAP) criterion that utilizes an exhaustive search to obtain the PHN parameters after applying the first order Taylor series approximation. Although this estimator is very complex, it is well-known that a MAP estimator is an optimal estimator for tracking random parameters and outperforms an EKF [126]. Hence, at low SNR, where the performance of the estimator is dictated by the AWGN noise, the MAP estimator in [23] is capable of more accurately tracking the PHN parameters compared to the EKF based estimator in this chapter.

   It is important to note that, compared to [23], the comparatively poor performance of the proposed estimator at low SNR does not result in significant degradation in the overall BER performance of an OFDM system (see Figures 5.7-5.10). This can be attributed to the fact that at low SNR the overall BER of the system is not dictated by the PHN estimation error but is bounded by the AWGN. However, at high SNR, where the overall performance of an OFDM system is PHN limited, the proposed algorithm demonstrates a significantly better BER performance due to the lower error associated with the estimation of PHN parameters compared to [23].

4. Figures 5.4, 5.5, and 5.6 show that the proposed estimator outperforms the estimation algorithm in [23] at moderate-to-high SNR. The biggest gain is

achieved in the MSE of PHN estimation, followed by the MSE of CFO and channel estimation. For example, for $\sigma_\delta^2 = 10^{-4}$ rad^2 and at high SNR, the proposed estimator results in a 2–3 dB performance gain compared to that of [23] while estimating PHN or CFO. This performance gain is in addition to the lower complexity of the proposed estimator as shown in Section 5.7.

Note that in Figure 5.5, the PHN estimation MSE of the proposed estimator and the estimator in [26] are lower than the HCRB at low SNR. This is due to the fact that the HCRB cannot be derived in closed-form while taking into account the prior knowledge of the range of CFO values, i.e., $(-0.5, 0.5)$. However, the proposed estimator and the estimator in [26] take into account this prior information while estimating the PHN, CFO, and the channel paraments.

5.8.2 Comparison with Existing Work

In the following, the combined estimation and data detection performance is examined in terms of the uncoded BER of the OFDM system. The following system setups are considered for comparison:
(i) The proposed estimation and data detection algorithm (labelled as "Proposed Est. and Data Det.").
(ii) The estimation and data detection algorithm in [23] and [26], respectively (labelled as "[23] & [26]").
(iii) The data detection in [117] combined with the proposed estimation algorithm (labelled as "[Proposed estimation, 114] ").
(iv) The estimation algorithm in [23] combined with the proposed data detection algorithm (labelled as "[23, Proposed data detection] ").
(v) As a reference, a system that applies the proposed estimation algorithm but utilizes no PHN tracking during OFDM data symbols (labelled as "No CFO cancel. and PHN track.").
(vi) As a lower-bound on the BER performance, a system assuming perfect channel, PHN, and CFO estimation (labelled as "Perf. CIR, PHN & CFO est.").

Figure 5.7 depicts the uncoded BER performance of the OFDM systems listed above. The following observations can be made from Figure 5.7:

1. The results demonstrate that without phase tracking and CFO cancellation throughout the packet, the OFDM system performance deteriorates significantly. On the other hand, by combining the proposed estimation and data detection algorithms, the BER performance of an OFDM system

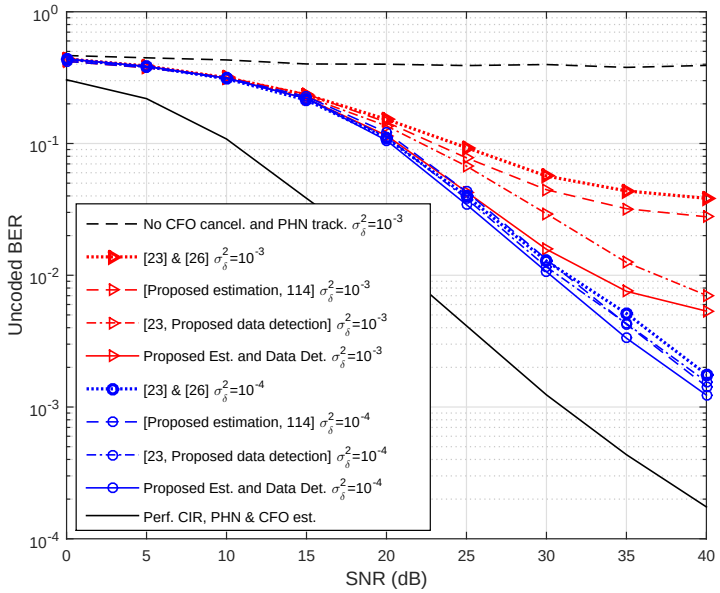

Figure 5.7: Comparison of uncoded BER of the proposed algorithms for PHN variance, $\sigma_\delta^2 = [10^{-3}, 10^{-4}]$ rad^2 and 64-QAM modulation with the algorithms in [23] & [26] and [114].

is shown to improve considerably even in the presence of very strong PHN, e.g., $\sigma_\delta^2 = 10^{-3}$ rad^2.

2. Compared to existing algorithms, the BER performance of an OFDM system using the proposed algorithms is closer to the ideal case of perfect CIR, PHN, and CFO estimation (a performance gap of 10 dB at SNR = 20 dB).

3. It can be clearly observed that the proposed receiver structure outperforms the algorithms in [23] and [26]. This performance improvement can be attributed to the fact that instead of single order Taylor series approximation applied directly to the whole OFDM symbol [23], the proposed estimation and detection algorithms apply EKF to linearize the PHN, which uses the most recent estimated PHN values to obtain an updated PHN estimate sample by sample. This linearization using EKF helps in achieving better system performance at high SNR.

4. It is clear that the performance of the proposed data detection algorithm outperforms the algorithm in [117]. This result is anticipated, since at high

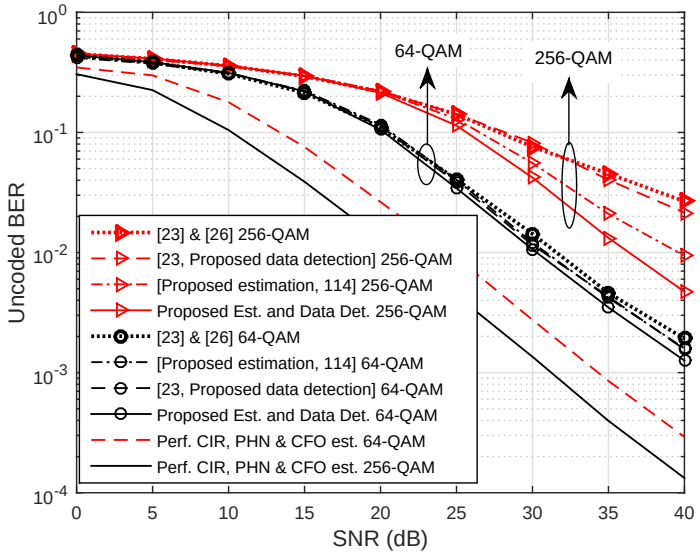

Figure 5.8: Comparison of uncoded BER of the proposed algorithms for 64-QAM and 256-QAM modulations with the algorithm in [23] & [26] and [114] at PHN variance, $\sigma_\delta^2 = 10^{-4}$ rad^2.

PHN variance, the approximation of PHN parameters using linear interpolation in [117] highly deviates from the true PHN parameters. Therefore, the linear interpolation approach in [117] may not be used in the presence of very strong PHN, e.g., $\sigma_\delta^2 = 10^{-3}$ rad^2.

5. It can be seen that the performance of the proposed estimator outperforms that of [23] even when the latter is combined with the proposed data detection algorithm. This is because the estimation based on EKF outperforms the estimation in [23] at high SNR. Thus, at high SNR, where the system performance is determined by the PHN estimation performance, the proposed estimation and detection algorithms achieve better BER results.

6. Finally, Figure 5.7 shows that in the presence of PHN, the overall BER performance of an OFDM system suffers from an error floor at high SNR, since at high SNR the performance of an OFDM system is dominated by PHN, which cannot be completely eliminated.

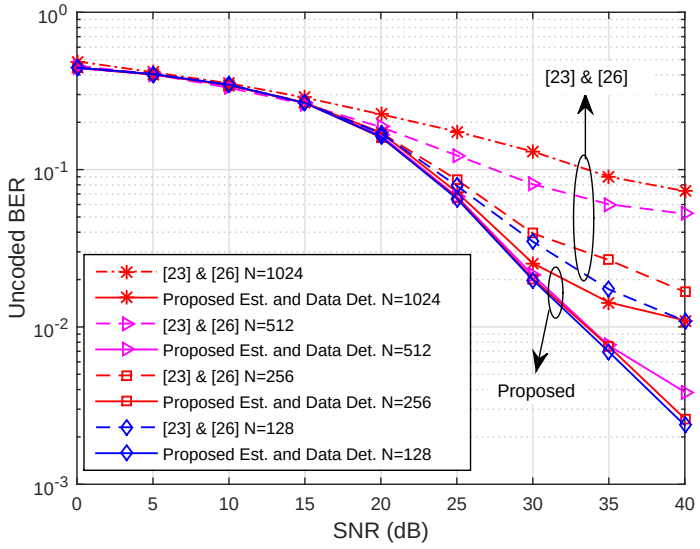

Figure 5.9: Comparison of uncoded BER of the proposed algorithms with the algorithm in [23] & [26] for varying training symbol lengths N= 128, 256, 512 and 1024, at $\sigma_\delta^2 = 10^{-4}$ rad^2 and 128-QAM modulation.

5.8.3 Effect of Modulation and OFDM System Parameter

Figure 5.8 illustrates the uncoded BER performance of an OFDM system for higher order modulations, i.e., 256-*quadrature amplitude modulation* (256-QAM). The results in Figure 5.8 shows that even for a denser constellation, the proposed estimation and data detection algorithms significantly improve the overall system performance compared to that of [23, Proposed data detection], [26] and [117]. For example, to achieve a BER of 3×10^{-2} with a PHN variance of 10^{-4} rad^2, the proposed algorithm outperforms the algorithms in [23, Proposed data detection] and [26] by a margin of 6 dB and 7 dB, respectively. In addition, the proposed algorithm outperforms the algorithm in [117] by a margin of 3 dB at a BER of 10^{-2} with a PHN variance of 10^{-4} rad^2. In addition, this gap widens at higher SNR values.

Figure 5.9 illustrates the uncoded BER performance of an OFDM system for different number of subcarriers, e.g., $N = 128, 256, 512$ and 1024, within an OFDM symbol. Based on the results in Figure 5.9, it can be concluded that the proposed algorithm is not sensitive to the subcarrier spacing at low-to-medium SNRs while at high SNRs, the BER degrades as one moves to $N = 1024$

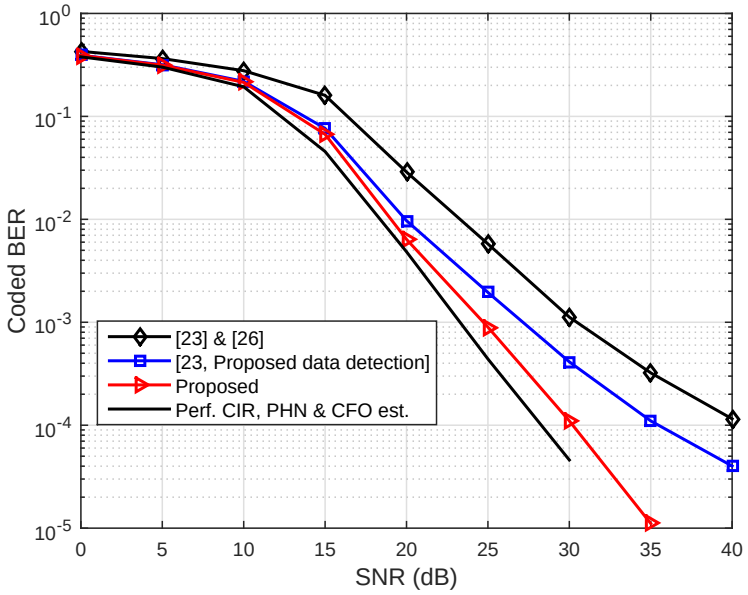

Figure 5.10: Comparison of coded BER of the proposed algorithms with the algorithms in [23] & [26] and [23, Proposed data detection] for PHN variance, $\sigma_\delta^2 = 10^{-4}$ rad^2 and 64-QAM modulation.

subcarriers. This is because increasing the number of subcarriers results in more ICI that is caused by the residual PHN and CFO. More importantly, the BER performance of an OFDM system using the proposed algorithms outperforms that of [23] and [26] for any value of N. For instance, at BER $= 10^{-2}$ and $N = 128$, the SNR gain for the proposed algorithms is almost 8 dB compared to the algorithms in [23] and [26].

Finally, the coded BER performance is shown in Figure 5.10. A low-density parity-check (LDPC) code is employed with a channel coding rate of 1/2 and codeword length of 1296 bits. The algorithm in [92] is used for encoding. The soft-decision iterative decoding algorithm, based on a sum-product algorithm in [96] is utilized for decoding the estimated data vector in (5.26). The results in Figure 5.10 show that, the proposed estimation and data detection algorithms improve the overall system performance compared to the existing algorithms in [23] and [26]. For example, to achieve a BER of 10^{-4} with a PHN variance of 10^{-4} rad^2, the proposed algorithm outperforms the algorithms in "[23, Proposed data detection]" and "[23] & [26]" by a margin of 5 dB and 10 dB, respectively.

In addition, compared to existing algorithms, the coded BER performance of an OFDM system using the proposed algorithm is closer to that of the ideal case of perfect CIR, PHN, and CFO estimation (a performance gap of 2 dB at BER of 10^{-4}).

5.9 Conclusion

In this chapter, an ECM based algorithm has been proposed for joint estimation of channel, PHN, and CFO in OFDM systems. The signal model for the estimation problem is outlined in detail and the HCRB for the joint estimation of channel, PHN, and CFO in OFDM systems is derived. Simulation results indicate that the estimation MSE of the proposed algorithm is closer to the derived HCRB and outperforms the existing estimation algorithms at moderate-to-high SNR. Next, an *iterative* algorithm for joint data detection and PHN mitigation is proposed for the OFDM data symbols. The proposed algorithm employs an EKF based approach to track the time-varying PHN parameters throughout the OFDM data symbols. The performance of the proposed estimation and detection algorithms has been evaluated for different PHN variances $\sigma_\delta^2 = [10^{-3}, 10^{-4}]\text{rad}^2$, different number of subcarriers $N = [64, 128, 256, 512, 1024]$, and different modulation schemes, $64, 128, 256$-QAM. Numerical results show that the proposed ECM based estimator and the iterative data detection algorithm are not only computationally efficient compared to the existing algorithms but also outperform existing algorithms in terms of both the uncoded and the coded BER performance. For example, the uncoded BER for the proposed algorithms has an SNR gain of almost 8 dB compared to the existing algorithms at an BER of 10^{-2} with $N = 128$. In addition, the coded BER performance using the proposed algorithms is closer to the ideal case of perfect CIR, PHN, and CFO estimation with a performance gap of only 2 dB at BER of 10^{-4} and PHN variance, $\sigma_\delta^2 = 10^{-4}$ rad^2.

Chapter 6

Synchronization of Cooperative OFDM Communication Systems and Its Effects on 3-D Video Applications

6.1 Introduction

In the last chapter, an ECM based algorithm for joint estimation of channel, PHN, and CFO was proposed. In addition, the HCRB for the joint estimation problem was presented. An iterative receiver based on an EKF for joint data detection and PHN tracking was also proposed. In this chapter, an iterative pilot-aided algorithm based on ECM for joint estimation of multipath channels, Wiener PHNs, and CFOs, the HCRB and the data detection in DF and AF based cooperative OFDM systems will be investigated, as well the effects of synchronization impairments on 3-D video applications.

Relay based cooperative communication schemes using single-antenna transceivers provide spatial diversity by forming virtual MIMO systems [58, 60]. In contrast to conventional MIMO systems, which resulting single PHN and CFO since the antenna elements are co-located on a single device, the cooperative networks have multiple distributed nodes and each one has its own local oscillator. Thus, this gives rise to multiple PHNs and multiple CFOs. In addition, such diversity gains are only possible if synchronization, e.g., accurate estimation of channel, phase noises (PHNs), and carrier frequency offsets (CFOs) exists among all communication nodes [127]. Moreover, It is shown that a small phase shift at

the output of the local oscillator in each node can significantly reduce the overall cooperative system performance [14].

OFDM systems, which are employed to enhance bandwidth efficiency and mitigate the effect of frequency-selective fading, are more severely impacted by PHN. Moreover, CFOs and PHNs result in a CPE and ICI at the destination [13]. In addition, the estimation of the CIR for each link becomes challenging in the presence of CFOs and PHNs [23]. Furthermore, the accurate estimation of these multiple impairments, i.e., CIR, CFOs, and time-varying PHNs, is required for coherent detection of OFDM signals at the destination.

Most of the existing work in the literature focuses on estimating either CFOs while assuming perfect estimation of PHNs [28–30] or targeting the estimation PHN parameters while assuming perfect CFOs estimation [14]. More specifically, in [28], the channel estimation in the presence of CFOs is analyzed in DF and AF cooperative systems. However, the authors in [28] do not take the effect of PHN into account. In [29] and [30], the CFOs estimation is investigated for DF and AF cooperative systems, respectively. However, the proposed algorithms in [29] and [30] are based on the assumption of perfect knowledge of channels. Moreover, in [30], a minimum mean square error (MMSE) equalizer is used to equalize the ICI, which is computationally very complex. In [14], the channel estimation in the presence of PHN are investigated. However, the CFOs effects are not take into account. More importantly, [14, 28–30] do not provide the HCRB for joint estimation of multiple impairments in cooperative OFDM systems, which would provide essential information about the absolute performance of the estimation scheme. The problem of joint channel, CFO, and PHN estimation is considered in the context of OFDM relay networks in [15]. However, the relaying approach and system model are totally different from the one in this chapter. Moreover, the estimation approach in [15] is based on the *maximum a posteriori* (MAP) criterion, which is computationally very complex.

Given the time-varying nature of PHN, we need to track it not only during the training interval but also during the data transmission interval. Hence, following the training period, a receiver structure for joint data detection and PHN mitigation in the data transmission period is required. In the existing literature, joint data detection and PHN mitigation is analyzed in [14] and [15]. However, the PHN tracking in [14] and [15] requires the application of pilots throughout an OFDM symbol to compensate the CPE. This adversely affects the bandwidth efficiency and data detection performance. Furthermore, our simulations show that the approach in [14] and [15] is outperformed by the receiver structure proposed

in this chapter.

In the context of 3-D video transmission, this chapter shows that the performance of cooperative communication systems for video applications is adversely impacted by synchronization impairments such as imperfect channel estimation, PHNs and CFOs, as they can result in ICI and rotation of the video signal constellation.

Most of the existing work on video transmission is based on the assumption that channels, PHNs and CFOs are *accurately* known at the video transceiver. In [7, 31–35], the proposed video transceiver is based on the assumption that the channels are *perfectly* known at the source and destination. Moreover, in [7, 31–35], the study of the impact of imperfect channel, PHN and CFO estimation on the system performance for video transmission, has not been addressed.

6.1.1 Contributions

The major contributions of this chapter can be summarized as follows:

- The proposal of an iterative pilot-aided algorithm based on the ECM in both DF and AF cooperative OFDM networks in the presence of *unknown* channel gains, PHNs and CFOs. In the E-step, an *extended Kalman filter* (EKF) estimator that is shown to accurately track the time varying PHN over the transmission packet is proposed. In the M-step, a closed form estimator is derived to estimate the CFO and channel parameters. Through simulations, it has been found that the proposed ECM based estimator only requires a few iterations to track the multiple impairments over the transmission packet.

- Addressing of the effects of PHNs and CFOs on an OFDM-based AF and DF relay network. Through simulations, it has been found that PHNs and CFOs significantly degrade the overall BER performance in the AF relay network compared to the DF relay network and non-cooperative systems.

- The presentation of an expression for the HCRB for the joint estimation of the channel, CFO and PHN in OFDM cooperative systems for both DF and AF. Simulation results show that the MSE of the proposed algorithm is closer to the HCRB at moderate-to-high SNR.

- The proposal of a new iterative algorithm based on the EKF for data detection and tracking the *unknown* time-varying PHN throughout the OFDM data packet.

- The investigation of the performance of the proposed estimator and the detector through simulations. These simulation results demonstrate that, at different values of SNRs, the combined estimation algorithm and iterative receiver can significantly improve average bit-error rate performance compared to the existing algorithms, the conventional cooperative[1] and non-cooperative systems, i.e., the single-hop link (direct link) $S \rightarrow D$.

- The investigation of the effects of PHNs and CFOs on 3-D video applications over an OFDM-based AF relay network. Through simulations, it has been found that proposed estimator and detector significantly improve the PSNR performance with a variety of PHN variances. In addition, simulation results show that the the conventional approaches, which ignore PHNs and CFOs in data detection, for video transmission are significantly outperformed by the system proposed in this chapter.

The rest of this chapter is organized as follows: Section 6.2 describes the system model, the scenario under consideration, and the assumptions in this work, Section 6.3.1.1 presents problem formulation, Section 6.4 derives HCRB. Section 6.5 derives the proposed estimator, Section 6.6 presents the joint data detection and PHN mitigation, Section 6.7 illustrates the complexity analysis of the proposed system while Section 6.8 provides simulation results that investigate the performance of the proposed estimator and detector. Finally, Section 6.9 concludes the chapter and summarizes its key findings.

6.2 Signal Model

A cooperative system with $M + 2$ nodes is considered. It consists of one source node which communicates with one destination node and M relays. The time division multiple access (TDMA)-based relay protocol is considered, where during the first time slot, the source node broadcasts the information to the mth relay and destination node, while during the second time slot, the mth relay node decodes and re-encodes or amplifies and forwards the source information to the destination node. In order to guarantee the advantages of cooperative diversity, there is a need to estimate the channel gains, time varying PHNs, and CFOs for the received signal at the destination node during both time slots. In this chapter, the following set of assumptions are adopted:

[1]This means ignoring PHN and CFO in channel estimation and detection as in [14].

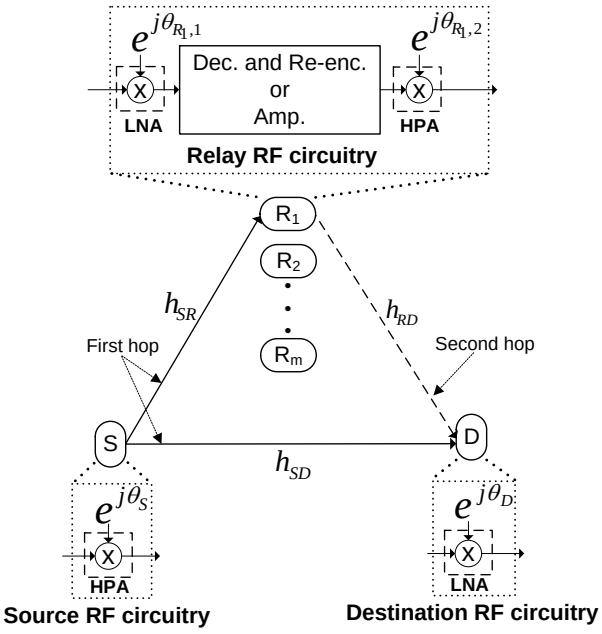

Figure 6.1: System block diagram of a cooperative system with $M + 2$ nodes

A1. All nodes adopt a half-duplex mode such that a node cannot transmit and receive simultaneously, but on different time slots. This means the source node broadcasts the signal to the relay and the destination in the first hop (i.e., first transmission time slot). In the second hop, the relay applies either the AF or DF protocol on the received signal and forwards it to the destination while the source is silent as shown in Figure 6.1. Since there is no collision between the received signals during the two consecutive hops at the destination, this transmission protocol maintains orthogonality at the expense of a loss in spectral efficiency.

A2. The channels are modeled as a slow fading frequency-selective channel, i.e., the channels are assumed to be quasi-static Rayleigh fading and they are constant and *unknown* over the OFDM packet duration and change from packet to packet following a complex Gaussian distribution;

A3. Carrier frequency offsets (CFOs) are modeled as *unknown deterministic parameters* over a packet, and change from packet to packet.

A4. The time-varying PHN changes from symbol to symbol and is modeled as a Wiener process, i.e., $\theta_n = \theta_{n-1} + \delta_n$, $\forall\ n$, where θ_n is the PHN at the nth instant, $\delta_n \sim \mathcal{N}(0, \sigma_\delta^2)$ is PHN innovation and σ_δ^2 is the variance of the innovation process [71, 72].

A5. The training symbol is assumed to be *known* at the destination.

A6. The timing offsets are assumed to be perfectly estimated, hence it is not considered.

Note that assumptions A1, A2, A3, A4 and A6 are in line with previous studies and channel, CFO and PHN estimation algorithms in [14, 23, 25, 26, 28–30, 72, 117]. Assumption A4 is also reasonable in many practical scenarios to describe the behaviour of practical oscillators [23, 71]. In addition, assumption A5 is adopted in the IEEE 802.11ac/ad standards to estimate channel and CFO in [10, 11, 23, 114, 117–119].

The time-invariant composite CIR between any pair of nodes a and b is modeled as $\bar{h}_{a,b}(\tau) = \sum_{l=0}^{L-1} \bar{h}_{a,b}(l)\delta(\tau - lT_s)$, where $\bar{h}_{a,b}(l)$ is the channel gain for the lth tap, and $\delta(x)$ is the unit impulse function. L is the channel order, and $T_s = 1/B$, where B represents the total bandwidth. The channel order L is the same for any pair of nodes. For brevity, we define $\bar{\mathbf{h}}_{a,b} \triangleq [\bar{h}_{a,b}(0), \bar{h}_{a,b}(1), \ldots, \bar{h}_{a,b}(L -$

$1)]^T$ and the channel gains $\bar{h}_{a,b}(l)$ are modeled as complex Gaussian zero-mean random variables. The frequency-domain channel coefficient matrix is $\mathbf{H}_{a,b} = \text{diag}\{H_{a,b}[0], H_{a,b}[1], \ldots, H_{a,b}[N-1]\}$, where $H_{a,b}[n] = \sum_{d=0}^{L-1} \bar{h}_{a,b}(d) e^{-(j2\pi nd/N)}$ is the channel frequency response on the nth subcarrier and N is the number of subcarriers.

The input data bits are first mapped to the complex symbols drawn from a signal constellation such as phase-shift keying (PSK) or quadrature amplitude modulation (QAM). Next, the source node S transmits the modulated training symbol vector $\mathbf{d}_S = [d_S(0), d_S(1), \ldots, d_S(N-1)]^T$. Note that, because the joint channel, PHN and CFO estimation algorithm is similar performed for each relay, the relay index m is omitted in this section.

6.2.1 First Time Slot

The received samples at the destination D and the relay R in time domain are given by

$$y_{D,1}(n) = e^{j(\bar{\theta}_{S,D}(n)+2\pi n\epsilon_{S,D}/N)}(\bar{h}_{S,D}(n) \otimes x(n)) + w_{D,1}(n) \tag{6.1a}$$
$$= e^{j(\theta_{S,D}(n)+2\pi n\epsilon_{S,D}/N)}(h_{S,D}(n) \otimes x(n)) + w_{D,1}(n), \tag{6.1b}$$

$$y_{R,1}(n) = \sqrt{g_{S,R}} e^{j(\bar{\theta}_{S,R_1}(n)+2\pi n\epsilon_{S,R}/N)}(\bar{h}_{S,R}(n) \otimes x(n)) + w_R(n) \tag{6.2a}$$
$$= \sqrt{g_{S,R}} e^{j(\theta_{S,R_1}(n)+2\pi n\epsilon_{S,R}/N)}(h_{S,R}(n) \otimes x(n)) + w_R(n), \tag{6.2b}$$

where

- $x(n) = \frac{1}{\sqrt{N}} \sum_{k=0}^{N-1} d_S(k) e^{j2\pi kn/N}$ is the complex baseband OFDM signal at nth sample of the transmitted OFDM symbol for $n = 0, 1, \ldots, N-1$, and k denotes the subcarrier index,

- $\{\bar{h}_{S,D}(l)\}_{l=0}^{L-1}$ and $\{\bar{h}_{S,R}(l)\}_{l=0}^{L-1}$ are the channel impulse response from $S \to D$ and $S \to R$, respectively. Note that (6.1b) and (6.2b) are an equivalent system model representation of (6.1a) and (6.2a), respectively, $h_{S,D}(n) \triangleq e^{j\bar{\theta}_{S,D}(0)}\bar{h}_{S,D}(n)$, $h_{S,R}(n) \triangleq e^{j\bar{\theta}_{S,R}(0)}\bar{h}_{S,R}(n)$, $\theta_{S,D}(n) \triangleq \bar{\theta}_{S,D}(n) - \bar{\theta}_{S,D}(0)$, and $\theta_{S,R_1}(n) \triangleq \bar{\theta}_{S,R_1}(n) - \bar{\theta}_{S,R_1}(0)$. This equivalent system model helps to distinguish between the phase disturbance caused by PHN and the channel phase for the first sample, which in turn resolves the phase ambiguity in the joint estimation problem as indicated in Section 6.5,

- $g_{S,R}$=$(d_{S,D}/d_{S,R})^{\gamma}$ is the large-scale fading gain, where we assume that the distance between the source and the relay is smaller than the distance between the source and the destination (see Figure 6.1). $d_{S,D}$ and $d_{S,R}$ are the physical distances from $S \rightarrow D$ and $S \rightarrow R$, respectively, γ is the large-scale fading exponent,

- $\theta_{S,D}(n) = \theta_S(n) + \theta_D(n)$ and $\theta_{S,R_1}(n) = \theta_S(n) + \theta_{R_1}(n)$ are the PHN processes between S and D and S and R, respectively, during the first time slot, $\theta_k(n)$ for $k \in \{S, R, D\}$, is generated using a Wiener process, i.e., $\theta(n) = \theta(n-1) + \delta(n)$, $\forall\ n$, where $\delta(n) \sim \mathcal{N}(0, \sigma_\delta^2)$ is the PHN innovation and σ_δ^2 is the variance of the innovation process [71],

- $\epsilon_{S,R}$ and $\epsilon_{R,D}$ denote the normalized CFOs between the S and R and R and D nodes, respectively,

- $w_{D,1}(n)$ and $w_R(n)$ are the additive white Gaussian noise (AWGN) samples with $\{w_{D,1}(n),$
  $w_R(n)\} \sim \mathcal{N}(0, \sigma_w^2)$.

Using (6.1) and (6.2) the received signals at D and R, $\mathbf{y}_{D,1} = [y_{D,1}(0), y_{D,1}(1),$ $\ldots, y_{D,1}(N-1)]^T$ and $\mathbf{y}_{R,1} = [y_{R,1}(0), y_{R,1}(1), \ldots, y_{R,1}(N-1)]^T$, respectively, in vectorial form are given by

$$\mathbf{y}_{D,1} = \mathbf{E}_{S,D}\mathbf{P}_{S,D}\mathbf{F}^H\mathbf{D}_S\mathbf{F}_L\mathbf{h}_{S,D} + \mathbf{w}_{D,1}, \tag{6.3}$$

$$\mathbf{y}_{R,1} = \sqrt{g_{S,R}}\mathbf{E}_{S,R}\mathbf{P}_{S,R_1}\mathbf{F}^H\mathbf{D}_S\mathbf{F}_L\mathbf{h}_{S,R} + \mathbf{w}_R, \tag{6.4}$$

where

- $\mathbf{P}_{S,D} \triangleq \text{diag}([e^{j\theta_{S,D}(0)}, e^{j\theta_{S,D}(1)}, \ldots, e^{j\theta_{S,D}(N-1)}]^T)$ and $\mathbf{P}_{S,R_1} \triangleq \text{diag}([e^{j\theta_{S,R_1}(0)},$ $e^{j\theta_{S,R_1}(1)}, \ldots, e^{j\theta_{S,R_1}(N-1)}]^T)$ are $N \times N$ PHN matrices from $S \rightarrow D$ and $S \rightarrow R$, respectively,

- $\mathbf{E}_{S,D}$ and $\mathbf{E}_{S,R}$ are $N \times N$ CFO matrices from $S \rightarrow D$, and from $S \rightarrow R$, respectively, i.e., $\mathbf{E}_{a,b} \triangleq \text{diag}([e^{(j2\pi\epsilon_{ab}/N)\times 0}, e^{(j2\pi\epsilon_{ab}/N)}, \ldots, e^{(j2\pi\epsilon_{ab}/N)\times(N-1)}]^T)$, $a, b \in \{S, R, D\}$,

- $\mathbf{F}$ is an $N \times N$ DFT matrix, i.e., $[\mathbf{F}]_{l,m} \triangleq (1/\sqrt{N})e^{-j(2\pi ml/N)}$ for $m, l = 0, 1, \cdots, N-1$,

- $\mathbf{D}_S \triangleq \text{diag}(\mathbf{d}_S[n])$,

- $\mathbf{F}_L$ is an $N \times L$ DFT matrix, i.e., $\mathbf{F}_L \triangleq \mathbf{F}(1:N, 1:L)$,
- $\mathbf{w}_{D,1} = [w_{D,1}(0), w_{D,1}(1), \ldots, w_{D,1}(N-1)]^T$ and $\mathbf{w}_R = [w_R(0), w_R(1), \ldots, w_R(N-1)]^T$ are AWGN vectors.

6.2.2 Second Time Slot

In this time slot, the relay applies either AF or DF protocol on the received signal and forwards it to the destination while the source is silent.

6.2.2.1 AF-relaying protocol

In this protocol, the relay simply amplifies and forwards the received signal to the destination. By adopting the low phase noise variance assumption, as explained in [14], the approximated received signal at D is given by

$$\begin{aligned}\mathbf{y}_{D,2} &= \sqrt{g_{R,D}\frac{\mathbb{E}[|\mathbf{d}_S|^2]}{\mathbb{E}[|\mathbf{y}_{R,1}|^2]}}\mathbf{E}_{R,D}\mathbf{P}_{R_2,D}\mathbf{F}^H\mathbf{H}_{R,D}\mathbf{F}\mathbf{y}_{R,1} + \mathbf{w}_{D,2} \\ &= \sqrt{\frac{g_{R,D}g_{S,R}\xi_D}{g_{S,R}\xi_D\sigma_h^2 + \sigma_w^2}}\mathbf{E}_{R,D}\mathbf{E}_{S,R}\mathbf{P}_{R_2,D}\mathbf{P}_{S,R_1}\mathbf{F}^H\mathbf{H}_{S,R}\mathbf{H}_{R,D}\mathbf{d}_S \\ &+ \sqrt{\frac{g_{R,D}\xi_D}{g_{S,R}\xi_D\sigma_h^2 + \sigma_w^2}}\mathbf{E}_{R,D}\mathbf{P}_{R_2,D}\mathbf{F}^H\mathbf{H}_{R,D}\mathbf{F}\mathbf{w}_R + \mathbf{w}_{D,2} \end{aligned} \tag{6.5}$$

Equation (6.5) can further be simplified as

$$\mathbf{y}_{D,2} = \mathrm{q}_1\mathbf{E}_{S,R,D}\mathbf{P}_{S,R,D}\mathbf{F}^H\mathbf{D}_S\mathbf{F}_{(2L-1)}\mathbf{h}_{S,R,D} + \mathrm{q}_2\mathbf{E}_{R,D}\mathbf{P}_{R_2,D}\mathbf{F}^H\mathbf{H}_{R,D}\mathbf{F}\mathbf{w}_R + \mathbf{w}_{D,2} \tag{6.6}$$

where

- $\mathrm{q}_1 \triangleq \sqrt{\frac{g_{R,D}g_{S,R}\xi_D}{g_{S,R}\xi_D\sigma_h^2+\sigma_w^2}}$ and $\mathrm{q}_2 \triangleq \sqrt{\frac{g_{R,D}\xi_D}{g_{S,R}\xi_D\sigma_h^2+\sigma_w^2}}$,
- σ_h^2=$\mathbb{E}[|h_{S,R}|^2]$ is the variance of CIR vector,
- $g_{R,D}$=$(d_{S,D}/d_{R,D})^\gamma$ is the large-scale fading gain and $d_{R,D}$ is the distance from $R \to D$,
- $\mathbf{w}_{D,2}$ is the AWGN vector at the destination,
- $\mathbf{E}_{S,R,D}$=$\mathbf{E}_{R,D}\mathbf{E}_{S,R}$ is the effective CFO matrix during the first and the second hops from $S \to R \to D$,

- $\mathbf{P}_{R_2,D} \triangleq \text{diag}([e^{j\theta_{R_2,D}(0)}, \ldots, e^{j\theta_{R_2,D}(N-1)}]^T)$, $\theta_{R_2,D}(n) \triangleq \bar{\theta}_{R_2,D}(n) - \bar{\theta}_{R_2,D}(0)$ is $N \times N$ PHN matrix during the second hop from $R \to D$,
- $\mathbf{P}_{S,R,D} \triangleq \text{diag}([e^{j\theta_{S,R,D}(0)}, \ldots, e^{j\theta_{S,R,D}(N-1)}]^T)$, $\theta_{S,R,D}$=$\theta_S + \theta_{R,1} + \theta_{R,2} + \theta_D$ is the effective PHN matrix during the first and the second hops from $S \to R \to D$,
- $g_{R,D}$=$(d_{S,D}/d_{R,D})^\gamma$, $d_{R,D}$ is the distance from $R \to D$,
- $\mathbf{F}_{(2L-1)}$ is an $N \times (2L-1)$ DFT matrix, i.e., $\mathbf{F}_{(2L-1)} \triangleq \mathbf{F}(1:N, 1:(2L-1))$, L is the channel length,
- $\mathbf{h}_{R,D}(n) \triangleq e^{j\bar{\theta}_{R,D}(0)}\bar{\mathbf{h}}_{R,D}(n)$ and $\bar{\mathbf{h}}_{R,D}$ is CIR between the relay and destination,
- $\mathbf{h}_{S,R,D} \triangleq \mathbf{h}_{S,R} \star \mathbf{h}_{R,D}$ is a $2L-1 \times 1$ vector,
- $\mathbf{H}_{R,D} \triangleq \text{diag}\,(\mathbf{F}_L \mathbf{h}_{R,D})$, and $\mathbf{H}_{S,D} \triangleq \text{diag}\,(\mathbf{F}_L \mathbf{h}_{S,D})$.

The received signal vector at D, $\mathbf{y}_{D,2}$ in (6.6), is a circularly symmetric complex Gaussian random variable, i.e., $\mathbf{y}_{D,2} \sim \mathcal{CN}(\boldsymbol{\mu}_{\mathbf{y}_{D,2}}, \boldsymbol{\Sigma}_{\mathbf{y}_{D,2}})$, with mean $\boldsymbol{\mu}_{\mathbf{y}_{D,2}} = \mathrm{q}_1 \mathbf{E}_{S,R,D}\mathbf{P}_{S,R,D}\mathbf{F}^H\mathbf{D}_S\mathbf{F}_{(2L-1)}\mathbf{h}_{S,R,D}$ and covariance matrix $\boldsymbol{\Sigma}_{\mathbf{y}_{D,2}} = (\mathrm{q}_2^2\sigma_w^2\sigma_h^2 + \sigma_w^2)\mathbf{I}_N$, where $\boldsymbol{\mu}_{\mathbf{y}_{D,2}}$ and $\boldsymbol{\Sigma}_{\mathbf{y}_{D,2}}$ are derived in (A.2).

6.2.2.2 DF-relaying protocol

In the DF protocol, each relay firstly receives the signal in (6.4) and performs the joint estimation of the channel gains, PHN and CFO during the training interval and compensated the impairments. Next, the relay decodes the received data packet by the joint data detection and PHN mitigation. Then, the decoded signal is forwarded to the destination. The received signal in the destination can be defined as

$$\mathbf{y}_{D,2} = \sqrt{g_{R,D}}\mathbf{E}_{R,D}\mathbf{P}_{R_2,D}\mathbf{F}^H\bar{\mathbf{D}}_S\mathbf{F}_L\mathbf{h}_{R,D} + \mathbf{w}_{D,2} \tag{6.7}$$

where $\bar{\mathbf{D}}_S \triangleq \text{diag}(\bar{\mathbf{d}}_S[n])$ and $\bar{\mathbf{d}}_S$ is the decoded and then remodulated training symbol vector from the relay. In this chapter, the relay can use the ECM estimator for joint estimation of channel, PHN and CFO. Moreover, the iterative data detection algorithm based on EKF can be used to detect the data and track the PHN throughout the OFDM packet.

6.3 Problem Formulation

6.3.1 AF and DF Relaying for Cooperative Networks

6.3.1.1 AF relaying

In order to gain the advantages of cooperative diversity, the destination receiver needs to decode the received signals, $\mathbf{y}_{D,1}$ in (6.3), and $\mathbf{y}_{D,2}$ in (6.6), during first and second time slots, respectively. This in turn requires the estimation of $\boldsymbol{\theta}_{S,D} \triangleq [\theta_{S,D}(1), \ldots, \theta_{S,D}(N-1)]^T$, $\mathbf{h}_{S,D} \triangleq [h_{S,D}(0), \ldots, h_{S,D}(L-1)]^T$ and $\epsilon_{S,D}$ during the first time slot and the estimation of $\boldsymbol{\theta}_{S,R,D} \triangleq [\theta_{S,R,D}(1), \ldots, \theta_{S,R,D}(N-1)]^T$, $\mathbf{h}_{S,R,D} \triangleq [h_{S,R,D}(0), \ldots, h_{S,R,D}(2L-1)]^T$ and $\epsilon_{S,R,D}$ during second time slot.

6.3.1.2 DF relaying

Similarly, the relay and destination receivers need to decode the received signals, $\mathbf{y}_{D,1}$ in (6.3), $\mathbf{y}_{R,1}$ in (6.4), and $\mathbf{y}_{D,2}$ in (6.7), during the first and second time slots, respectively. This in turn requires the estimation of $\boldsymbol{\theta}_{S,D} \triangleq [\theta_{S,D}(1), \ldots, \theta_{S,D}(N-1)]^T$, $\mathbf{h}_{S,D} \triangleq [h_{S,D}(0), \ldots, h_{S,D}(L-1)]^T$ and $\epsilon_{S,D}$, and $\boldsymbol{\theta}_{S,R_1} \triangleq [\theta_{S,R_1}(1), \ldots, \theta_{S,R_1}(N-1)]^T$, $\mathbf{h}_{S,R} \triangleq [h_{S,R}(0), \ldots, h_{S,R}(L-1)]^T$ and $\epsilon_{S,R}$ during first time slot and $\boldsymbol{\theta}_{R_2,D} \triangleq [\theta_{R_2,D}(1), \ldots, \theta_{R_2,D}(N-1)]^T$, $\mathbf{h}_{R,D} \triangleq [h_{R,D}(0), \ldots, h_{R,D}(L-1)]^T$ and $\epsilon_{R,D}$ during second time slot.

Note that it is clear from (6.1b) and (6.2b) that there is no need to estimate $\theta_{S,D}(0)$ and $\theta_{S,R,D}(0)$ in AF protocol or $\theta_{S,R_1}(0)$ and $\theta_{R_2,D}(0)$ in DF protocol.

6.3.2 Performance of the Estimation and Detection Algorithms

The estimation and detection algorithms have to be of low computational complexity and suitable for video applications. As shown in Chapter 5, both the proposed ECM estimator and data detection algorithm based on EKF outperform existing algorithms in terms of the MSE and the BER. In addition, they have lower computational complexity and are suitable for video application.

6.3.3 Relaying Protocol for Video Applications

Usually, the AF protocol is preferred in relay for video applications as it requires lower complexity and time processing in processing the received signal [60]. Moreover, the channel encoding and decoding operations at the relay are not required

in the AF protocol [5]. However, AF relaying networks in the presence of PHNs and CFOs achieve lower performance than the DF relaying networks as the channel estimation is performed at the destination and is affected by the PHN and additive noise from channels which are amplified and forwarded to the destination [14]. Therefore, efficient estimation and data detection techniques for channel estimation in the presence of PHNs and CFOs are required to enhance the application of AF relaying protocol for video applications.

6.4 Hybrid Cramér-Rao Bound

In this section, the HCRB for joint estimation of channel gains, PHNs, and CFOs for DF and AF-relaying cooperative networks are presented.

6.4.1 HCRB for AF Relaying

In the case of AF relaying, only the overall channel gains, $\mathbf{h}_{S,R,D}$, PHNs, $\boldsymbol{\theta}_{S,R,D}$, and CFOs, $\epsilon_{S,R,D}$, need to be estimated. As a result, the parameter vector of interest for AF relaying, $\boldsymbol{\lambda}$, is given by $\boldsymbol{\lambda} = [\boldsymbol{\theta}_{S,R,D}^T \ \Re\{\mathbf{h}_{S,R,D}\}^T \ \Im\{\mathbf{h}_{S,R,D}\}^T \ \epsilon_{S,R,D}]^T$. Note that the $\boldsymbol{\lambda}$ comprises both random and deterministic parameters, e.g., PHN, $\boldsymbol{\theta}_{S,R,D} \triangleq [\theta_{S,R,D}(1), \ldots, \theta_{S,R,D}(N-1)]^T$, is random while CIR, $\mathbf{h}_{S,R,D}$, and CFO, $\epsilon_{S,R,D}$, are deterministic parameters. Thus, HCRB instead of standard CRB must be derived. The accuracy of estimating $\boldsymbol{\lambda}$ is lower bounded by the HCRB ($\boldsymbol{\Omega}$) as [79, pp. 1-85]

$$\mathbb{E}_{\mathbf{u},\boldsymbol{\theta}_{S,R,D}|\mathbf{h}_{S,R,D},\epsilon_{S,R,D}} \left[(\hat{\boldsymbol{\lambda}}(\mathbf{u}) - \boldsymbol{\lambda})(\hat{\boldsymbol{\lambda}}(\mathbf{u}) - \boldsymbol{\lambda})^T \right] \succeq \boldsymbol{\Omega}. \tag{6.8}$$

Let us define $\boldsymbol{\Omega} = \mathbf{B}^{-1}$ and $\mathbf{B}$ is an $(N + 2(2L-1)) \times (N + 2(2L-1))$ hybrid information matrix (HIM), which is given in the following theorem.

Theorem 6.1: The HIM for joint estimation of CIR, PHN and CFO is given by

$$\mathbf{B} = \frac{2}{\sigma_w^2} \Re \left\{ \begin{bmatrix} \mathbf{B}_{11} & \mathbf{B}_{12} & \mathbf{B}_{13} & \mathbf{b}_{14} \\ \mathbf{B}_{21} & \mathbf{B}_{22} & \mathbf{B}_{23} & \mathbf{b}_{24} \\ \mathbf{B}_{31} & \mathbf{B}_{32} & \mathbf{B}_{33} & \mathbf{b}_{34} \\ \mathbf{b}_{41} & \mathbf{b}_{42} & \mathbf{b}_{43} & \mathrm{b}_{44} \end{bmatrix} \right\}, \tag{6.9}$$

where

- $\mathbf{B}_{11} \triangleq \mathrm{q}_1^2 \bar{\mathbf{Q}}_1^H \bar{\mathbf{Q}}_1 + \boldsymbol{\Lambda}$ is the $(N-1) \times (N-1)$ HIM for the estimation of $\boldsymbol{\theta}_{S,R,D}$, $\mathbf{Q}_1 = \mathrm{diag}(\mathbf{F}^H \mathbf{D}_S \mathbf{F}_{(2L-1)}$ $\mathbf{h}_{S,R,D})$, and $\bar{\mathbf{Q}}_1 = \mathbf{Q}_1(2:N, 2:N)$,

- $\mathbf{\Lambda}$ is an $(N-1)\times(N-1)$ tridiagonal matrix with diagonal elements given by $\frac{\tilde{\sigma}_w^2}{2\sigma^2_{\delta_{S,R,D}}}[1,2,\ldots,2,1]$ and off-diagonal elements given by $\frac{-\tilde{\sigma}_w^2}{2\sigma^2_{\delta_{S,R,D}}}[1,\ldots,1]$, and $\sigma^2_{\delta_{S,R,D}} \triangleq \sigma^2_{\delta_S}+\sigma^2_{\delta_{R_1}}+\sigma^2_{\delta_{R_2}}+\sigma^2_{\delta_D}$ is the total PHN variance of the innovation process from $S\rightarrow R\rightarrow D$,
- $\mathbf{B}_{22} \triangleq \mathrm{q}_1^2\mathbf{Q}_2^H\mathbf{Q}_2$ is an $(2L-1)\times(2L-1)$ information matrix for the estimation of real part of $\mathbf{h}_{S,R,D}$, and $\mathbf{Q}_2=\mathbf{F}^H\mathbf{D}_S\mathbf{F}_{(2L-1)}$,
- $\mathbf{B}_{33} \triangleq \mathrm{q}_1^2\mathbf{Q}_2^H\mathbf{Q}_2$ is an $(2L-1)\times(2L-1)$ information matrix for the estimation of imaginary part of $\mathbf{h}_{S,R,D}$,
- $\mathrm{b}_{44} \triangleq \mathrm{q}_1^2\mathbf{q}_5^H\mathbf{q}_5$ is a scalar representing the information for the estimation of CFO, ϵ, $\mathbf{q}_5=\sqrt{\mathbf{M}}\mathbf{F}^H\mathbf{D}_S\mathbf{F}_{(2L-1)}$ $\mathbf{h}_{S,R,D}$, and $\mathbf{M}\triangleq \mathrm{diag}\left(\left[(2\pi\frac{0}{N})^2,(2\pi\frac{1}{N})^2,\ldots,(2\pi\frac{N-1}{N})^2\right]^T\right)$,
- $\mathbf{B}_{12}=\mathbf{B}_{21}^H \triangleq -j\mathrm{q}_1^2\bar{\mathbf{Q}}_1^H\bar{\mathbf{Q}}_2$, $\bar{\mathbf{Q}}_2=\mathbf{Q}_2(2:N,1:L)$
- $\mathbf{B}_{13}=\mathbf{B}_{31}^H \triangleq \mathrm{q}_1^2\bar{\mathbf{Q}}_1^H\bar{\mathbf{Q}}_2$,
- $\mathbf{b}_{14}=\mathbf{b}_{41}^H \triangleq \mathrm{q}_1^2\bar{\mathbf{Q}}_4^H\bar{\mathbf{q}}_3$, $\mathbf{Q}_4=\mathrm{diag}(\sqrt{\mathbf{M}}\mathbf{F}^H\mathbf{D}_S\mathbf{F}_{(2L-1)}\mathbf{h}_{S,R,D})$, $\bar{\mathbf{Q}}_4=\mathbf{Q}_4(2:N,2:N)$, $\mathbf{q}_3=\mathbf{F}^H\mathbf{D}_S\mathbf{F}_{(2L-1)}\mathbf{h}_{S,R,D}$, and $\bar{\mathbf{q}}_3=\mathbf{q}_3(2:N)$,
- $\mathbf{B}_{23}=\mathbf{B}_{32}^H \triangleq j\mathrm{q}_1^2\mathbf{Q}_2^H\mathbf{Q}_2$,
- $\mathbf{b}_{24}=\mathbf{b}_{42}^H \triangleq j\mathrm{q}_1^2\mathbf{Q}_2^H\mathbf{q}_5$, and
- $\mathbf{b}_{34}=\mathbf{b}_{43}^H \triangleq \mathrm{q}_1^2\mathbf{Q}_2^H\mathbf{q}_5$.

Finally, the HCRB, $\mathbf{\Omega}$, is given by the inverse of the HIM. i.e., $\mathbf{\Omega}=\mathbf{B}^{-1}$. Note that the detailed derivation can be pursued by using similar steps given in Appendix (A.1).

6.4.2 HCRB for DF Relaying

Similar to the case of AF relaying, the received signal vector in general between any pair of transmitted node a and received node b, $\mathbf{y}_b\sim\mathcal{CN}(\boldsymbol{\mu}_{\mathbf{y}_b},\mathbf{\Sigma}_{\mathbf{y}_b})$, with mean $\boldsymbol{\mu}_{\mathbf{y}_b}=\mathbf{E}_{a,b}\mathbf{P}_{a,b}\mathbf{F}^H\mathbf{D}_S\mathbf{F}_L\mathbf{h}_{a,b}$ and covariance matrix $\mathbf{\Sigma}_{\mathbf{y}_b}=\sigma_w^2\mathbf{I}_N$, where $a,b\in\{S,R,D\}$. The parameter vector of interest between any pair of transmitted node a and received node b, is given by $\boldsymbol{\lambda}=[\boldsymbol{\theta}_{a,b}^T\ \mathbf{h}_{a,b}^T\ \epsilon_{a,b}]^T$. The accuracy of estimating $\boldsymbol{\lambda}$ is lower bounded by the HCRB ($\mathbf{\Omega}$) as [79]

$$\mathbb{E}_{\mathbf{y},\boldsymbol{\theta_{a,b}}|\mathbf{h}_{a,b},\epsilon_{a,b}}\left[(\hat{\boldsymbol{\lambda}}(\mathbf{y})-\boldsymbol{\lambda})(\hat{\boldsymbol{\lambda}}(\mathbf{y})-\boldsymbol{\lambda})^T\right]\succeq\mathbf{\Omega}. \tag{6.10}$$

Let us define $\mathbf{\Omega} = \mathbf{B}^{-1}$ and $\mathbf{B}$ is an $(N+L)\times(N+L)$ hybrid information matrix (HIM) and can be calculated similar to the AF case of equation (6.9). However, in (6.9) $\mathbf{F}_L$ is used instead of $\mathbf{F}_{(2L-1)}$ and q_1^2 is removed. Thus, the HCRB in (6.10) can be used for the parameter vector of interest between $S \to D$ in (6.3), $S \to R$ in (6.4), and $R \to D$ in (6.7), i.e., $\boldsymbol{\lambda} = [\boldsymbol{\theta}_{S,D}^T \ \mathbf{h}_{S,D}^T \ \epsilon_{S,D}]^T$, $\boldsymbol{\lambda} = [\boldsymbol{\theta}_{S,R_1}^T \ \mathbf{h}_{S,R}^T \ \epsilon_{S,R}]^T$, and $\boldsymbol{\lambda} = [\boldsymbol{\theta}_{R_2,D}^T \ \mathbf{h}_{R,D}^T \ \epsilon_{R,D}]^T$, respectively.

6.5 Joint Parameter Estimation

In this section, the ECM based estimator is proposed for the joint estimation of channel parameters, PHNs and CFOs for DF-and AF-relay networks, and its computational complexity is analyzed.

6.5.1 Proposed ECM based Estimator for AF Cooperative Networks

The ECM algorithm at the destination receiver iterates between the expectation step (E-step) and the maximization step (M-step). In E-step, EKF is proposed to update the PHN vector at $(i+1)$th iteration, $\boldsymbol{\theta}_{S,R,D}^{[i+1]}$, using the CIR and CFO estimates, $\hat{\mathbf{h}}_{S,R,D}^{[i]}$ and $\hat{\epsilon}_{S,R,D}^{[i]}$, respectively, obtained from the previous (ith) iteration, while in M-step, closed-form estimators are derived to update the CIR and CFO estimates, $\hat{\mathbf{h}}_{S,R,D}^{[i+1]}$ and $\hat{\epsilon}_{S,R,D}^{[i+1]}$, respectively. The proposed ECM algorithm at the ith iteration is given as follows.

For the given problem, the data set is given by $\mathbf{s} \triangleq \mathrm{q}_1\mathbf{F}^H\mathbf{D}_S\mathbf{F}_{(2L-1)}\mathbf{h}_{S,R,D} = [s(0),\ldots,s(N-1)]^T$ and is $N\times 1$ vector and re-write $\mathbf{y}_{D,2}$ in (6.6) as follows

$$\mathbf{u} = \mathbf{E}_{S,R,D}\mathbf{P}_{S,R,D}\mathbf{s} + \mathbf{v}; \tag{6.11}$$

where the overall noise vector $\mathbf{v} \triangleq [v(0),\ldots,v(N-1)]^T = \mathrm{q}_2\mathbf{E}_{R,D}\mathbf{P}_{R_2,D}\mathbf{F}^H\mathbf{H}_{R,D}\mathbf{F}\mathbf{w}_R + \mathbf{w}_{D,2}$ is distributed as $\mathbf{v} \sim \mathcal{CN}(\mathbf{0}, \tilde{\sigma}_w^2\mathbf{I}_N)$ and $\tilde{\sigma}_w^2 \triangleq \mathrm{q}_2^2\sigma_w^2\sigma_h^2 + \sigma_w^2$. Following [120], the complete data is defined as $\mathbf{z} \triangleq [\mathbf{u}^T \ \boldsymbol{\theta}_{S,R,D}^T]^T$ and the negative log likelihood function of the complete data, $\log p(\mathbf{z};\epsilon_{S,R,D})$, is given by

$$\log p(\mathbf{z};\epsilon_{S,R,D}) = \mathrm{C1} + \frac{1}{\tilde{\sigma}_w^2}\sum_{n=0}^{N-1} \parallel u(n) - e^{j2\pi\epsilon_{S,R,D}n/N} \times e^{j\theta_{S,R,D}(n)}s(n) \parallel^2$$
$$+ \log p(\theta_{S,R,D}(0)) + \sum_{n=0}^{N-1}\log p(\theta_{S,R,D}(n)|\theta_{S,R,D}(n-1)), \tag{6.12}$$

where C1 is a constant. The detailed E-step and M-step for estimating the CIR, PHN, and CFO are as follows:

E-step: In this step, the received signal $u(n)$ is first multiplied by $e^{-j2\pi\hat{\epsilon}^{[i]}_{S,R,D}n/N}$. Next, the signal $r(n) \triangleq e^{-j2\pi n\epsilon^{[i]}_{S,R,D}/N}u(n)$ is used to estimate the PHN vector, where $\hat{\epsilon}^{[i]}_{S,R,D}$ is the latest CFO estimate obtained from the previous iteration. First, we propose to use EKF during E-step to estimate the PHN samples $\boldsymbol{\theta}_{S,R,D}$. The signal $r(n)$ can be written as

$$r(n) = e^{-j2\pi n\epsilon^{[i]}_{S,R,D}/N}u(n) = e^{j2\pi n\Delta\hat{\epsilon}_{S,R,D}/N}e^{j\theta_{S,R,D}(n)}s^{[i]}(n) + \tilde{v}(n), \tag{6.13}$$

where $s^{[i]}(n)$ is nth symbol of the vector $\mathbf{s}^{[i]} \triangleq \mathrm{q}_1\mathbf{F}^H\mathbf{D}_S\mathbf{F}_{(2L-1)}\mathbf{h}^{[i]}_{S,R,D}$, $\Delta\hat{\epsilon}_{S,R,D} \triangleq \epsilon_{S,R,D} - \hat{\epsilon}^{[i]}_{S,R,D}$, and $\tilde{v}(n) \triangleq v(n)e^{-j2\pi n\hat{\epsilon}^{[i]}_{S,R,D}/N}$. The state and observation equations at time n are given by

$$\theta_{S,R,D}(n) = \theta_{S,R,D}(n-1) + \delta_{S,R,D}(n), \tag{6.14}$$

$$r(n) = z(n) + \tilde{v}(n) = e^{j\theta_{S,R,D}(n)}s(n) + \tilde{v}(n). \tag{6.15}$$

Since the observation equation in (6.15) is a non-linear function of the unknown state vector $\boldsymbol{\theta}_{S,R,D}$, the EKF is used instead of simple Kalman filtering. The EKF uses Taylor series expansion to linearize the non-linear observation equation in (6.15) about the current estimates [78]. Thus, the Jacobian of $z(n)$ is evaluated by computing the first order partial derivative of $z(n)$ with respect to $\theta_{S,R,D}(n)$ as

$$\begin{aligned}\dot{z}(n) = \left.\frac{\partial z(\theta_{S,R,D}(n))}{\partial\theta_{S,R,D}(n)}\right|_{\theta_{S,R,D}(n)=\hat{\theta}_{S,R,D}(n|n-1)} &= jz(\hat{\theta}_{S,R,D}(n|n-1)) \\ &= je^{j\hat{\theta}^{[i]}_{S,R,D}(n|n-1)}\hat{s}(n),\end{aligned} \tag{6.16}$$

where $\dot{z}$ denotes the Jacobian of z evaluated at $\theta_{S,R,D}(n)$. The first and second moments of the state vector at the $(i+1)$th iteration denoted by $\hat{\theta}^{[i+1]}_{S,R,D}(n|n-1)$ and $M^{[i+1]}(n|n-1)$, respectively, are given by

$$\hat{\theta}^{[i+1]}_{S,R,D}(n|n-1) = \hat{\theta}^{[i+1]}_{S,R,D}(n-1|n-1), \tag{6.17}$$

$$M^{[i+1]}(n|n-1) = M^{[i+1]}(n-1|n-1) + \sigma^2_{\delta_{S,R,D}}, \tag{6.18}$$

Given the observation $x(n)$, the Kalman gain $K(n)$, posteriori state estimate

$\hat{\theta}^{[i+1]}_{S,R,D}(n|n)$, and the filtering error covariance, $M^{[i+1]}(n|n)$ are given by

$$\begin{aligned} K(n) &= M^{[i+1]}(n|n-1)\dot{z}^*(\theta_{S,R,D}(n|n-1)) \\ &\times \Big(\dot{z}(\theta_{S,R,D}(n|n-1)) \times M^{[i+1]}(n-1|n-1) \\ &\times \dot{z}^*(\theta_{S,R,D}(n|n-1)) + \tilde{\sigma}^2_w\Big)^{-1}, \end{aligned} \tag{6.19}$$

$$\hat{\theta}^{[i+1]}_{S,R,D}(n|n) = \hat{\theta}^{[i+1]}_{S,R,D}(n|n-1) + \Re\big\{K_n\big(r(n) - e^{j\hat{\theta}^{[i+1]}_{S,R,D}(n|n-1)}\hat{s}^{[i]}(n)\big)\big\}, \tag{6.20}$$

$$M^{[i+1]}(n|n) = \Re\big\{M^{[i+1]}(n|n-1) - K(n)\dot{z}(\theta_{S,R,D}(n|n-1)) \times M^{[i+1]}(n|n-1)\big\}, \tag{6.21}$$

where $\hat{s}^{[i]}(n)$ is nth symbol of the vector $\hat{\mathbf{s}}^{[i]} \triangleq \mathrm{q}_1\mathbf{F}^H\mathbf{D}_S\mathbf{F}_{(2L-1)}\hat{\mathbf{h}}^{[i]}_{S,R,D}$. Before starting the EKF recursion (6.16)-(6.21), $\hat{\theta}^{[1]}_{S,R,D}(1|0)$ and $M^{[1]}(1|0)$ are initialized by $\hat{\theta}^{[1]}_{S,R,D}(1|0) = 0$ and $M^{[1]}(1|0) = \sigma^2_{\delta_{S,R,D}}$.

M-step: In this step, the CIR and CFO from $S \to R \to D$ are estimated by minimizing the log likelihood function in (6.12). In order to further reduce the complexity associated with the M-step, the minimization in (6.12) is done with respect to one of the estimation parameter while keeping the other parameter at its most recently updated value [122]. We first minimize the log likelihood function in (6.12) with respect to $\epsilon_{S,R,D}$ to update the CFO estimate for $(i+1)$th iteration, $\hat{\epsilon}^{[i+1]}_{S,R,D}$, while channel is kept constant at its ith iteration value, $\hat{\mathbf{h}}^{[i]}_{S,R,D}$ and updated PHN vector, $\hat{\boldsymbol{\theta}}^{[i+1]}_{S,R,D}$, is obtained from the E-step. Thus, the CFO estimate update, $\hat{\epsilon}^{[i+1]}_{S,R,D}$, is given by

$$\hat{\epsilon}^{[i+1]}_{S,R,D} = \arg\min_{\epsilon_{S,R,D}} \sum_{n=0}^{N-1} \parallel u(n) - e^{j2\pi\epsilon_{S,R,D}n/N}e^{j\theta_{S,R,D}(n)}s(n) \parallel^2 \Big|_{\substack{\theta_{S,R,D}(n)=\hat{\theta}^{[i+1]}_{S,R,D}(n),\\ \mathbf{h}_{S,R,D}=\hat{\mathbf{h}}^{[i]}_{S,R,D}}} \tag{6.22}$$

After simplifying (6.22), we have

$$\hat{\epsilon}^{[i+1]}_{S,R,D} = \arg\max_{\epsilon_{S,R,D}} \sum_{n=0}^{N-1} \Re\{(u(n))^*\hat{S}^{[i]}(n)e^{j2\pi\epsilon_{S,R,D}n/N}\} \tag{6.23}$$

where $\hat{S}^{[i]}(n) = e^{j\hat{\theta}^{[i+1]}_{S,R,D}(n)}\hat{s}^{[i]}(n)$. In order to handle the nonlinearity of (6.23), the term $e^{j2\pi\epsilon_{S,R,D}n/N}$ can be approximated using Taylor series expansion around the

pervious CFO estimate, $\hat{\epsilon}_{S,R,D}^{[i]}$, up to the second order term as

$$e^{j2\pi\epsilon_{S,R,D}n/N} = e^{j2\pi\hat{\epsilon}_{S,R,D}^{[i]}n/N} + (\epsilon_{S,R,D} - \hat{\epsilon}_{S,R,D}^{[i]})\left(j\frac{2\pi}{N}n\right) \times e^{j2\pi\hat{\epsilon}_{S,R,D}^{[i]}n/N} + \frac{1}{2}(\epsilon_{S,R,D} - \hat{\epsilon}_{S,R,D}^{[i]})^2\left(j\frac{2\pi}{N}n\right)^2 \times e^{j2\pi\hat{\epsilon}_{S,R,D}^{[i]}n/N} \tag{6.24}$$

Substituting (6.24) into (6.23), $\hat{\epsilon}_{S,R,D}^{[i+1]}$ is given by

$$\begin{aligned}\hat{\epsilon}_{S,R,D}^{[i+1]} = \arg\max_{\epsilon_{S,R,D}}\Bigg\{ &\sum_{n=0}^{N-1}\Re\big\{(u(n))^*\hat{S}^{[i+1]}(n)e^{j2\pi\hat{\epsilon}_{S,R,D}^{[i]}n/N} \\ &+ (\epsilon_{S,R,D} - \hat{\epsilon}_{S,R,D}^{[i]})\sum_{n=0}^{N-1}\Re\big\{(u(n))^*\hat{S}^{[i+1]}(n)\left(j\frac{2\pi}{N}n\right) \\ &e^{j2\pi\hat{\epsilon}_{S,R,D}^{[i]}n/N}\big\} + \frac{1}{2}(\epsilon_{S,R,D} - \hat{\epsilon}_{S,R,D}^{[i]})^2 \\ &\sum_{n=0}^{N-1}\Re\big\{(u(n))^*\hat{S}^{[i+1]}(n)\left(j\frac{2\pi}{N}n\right)^2 e^{j2\pi\hat{\epsilon}_{S,R,D}^{[i]}n/N}\big\}\Bigg\}\end{aligned} \tag{6.25}$$

Taking the derivative of (6.25) with respect to $\epsilon_{S,R,D}$ and equating the result to zero, the estimate of $\epsilon_{S,R,D}$ at the $(i+1)$th iteration is given by:

$$\hat{\epsilon}_{S,R,D}^{[i+1]} = \hat{\epsilon}_{S,R,D}^{[i]} + \frac{N}{2\pi}\frac{\sum_{n=0}^{N-1} n\Im\big\{(u(n))^*\hat{S}^{[i+1]}(n)e^{j2\pi\hat{\epsilon}_{S,R,D}^{[i]}n/N}\big\}}{\sum_{n=0}^{N-1} n^2\Re\big\{(u(n))^*\hat{S}^{[i+1]}(n)e^{j2\pi\hat{\epsilon}_{S,R,D}^{[i]}n/N}\big\}}, \tag{6.26}$$

Next, by setting $\boldsymbol{\theta}_{S,R,D}$ and $\epsilon_{S,R,D}$ to their latest updated values, the updated value of $\hat{\mathbf{h}}_{S,R,D}$ at the $(i+1)$th iteration, $\hat{\mathbf{h}}_{S,R,D}^{[i+1]}$, is calculated. Based on the vectorial form of received signal in (6.11), the negative log likelihood function, in (6.12), can be written as

$$\log p(\mathbf{z};\epsilon_{S,R,D}) = \mathrm{C1} + \parallel \mathbf{u} - \mathrm{q}_1\mathbf{E}_{S,R,D}\mathbf{P}_{S,R,D}\boldsymbol{\Gamma}\mathbf{h}_{S,R,D} \parallel^2 + \log p(\boldsymbol{\theta}_{S,R,D}), \tag{6.27}$$

where $\boldsymbol{\Gamma} \triangleq \mathrm{q}_1\mathbf{F}^H\mathbf{D}_S\mathbf{F}_{(2L-1)}$. Taking the derivative of (6.27) with respect to $\mathbf{h}_{S,R,D}$ and equating the result to zero, the estimate of $\mathbf{h}_{S,R,D}$ at the $(i+1)$th iteration is given by:

$$\hat{\mathbf{h}}_{S,R,D}^{[i+1]} = (\boldsymbol{\Gamma}^H\boldsymbol{\Gamma})^{-1}\boldsymbol{\Gamma}^H\hat{\mathbf{P}}_{S,R,D}^H\hat{\mathbf{E}}_{S,R,D}^H\mathbf{u}, \tag{6.28}$$

where $\hat{\mathbf{E}}_{S,R,D} \triangleq \text{diag}([e^{(j2\pi\hat{\epsilon}^{[i+1]}_{S,R,D}/N)\times 0}, e^{(j2\pi\hat{\epsilon}^{[i+1]}_{S,R,D}/N)}, \ldots, e^{(j2\pi\hat{\epsilon}^{[i+1]}_{S,R,D}/N)\times(N-1)}]^T)$, and $\hat{\epsilon}^{[i+1]}_{S,R,D}$ is obtained from (6.26), $\hat{\mathbf{P}}_{S,R,D} \triangleq \text{diag}([e^{j\hat{\theta}^{[i+1]}_{S,R,D}(0)}, e^{j\hat{\theta}^{[i+1]}_{S,R,D}(1)}, \ldots, e^{j\hat{\theta}^{[i+1]}_{S,R,D}(N-1)}]^T)$, and $\hat{\boldsymbol{\theta}}^{[i+1]}_{S,R,D} \triangleq [\hat{\theta}^{[i+1]}_{S,R,D}(0), \hat{\theta}^{[i+1]}_{S,R,D}(1), \ldots, \hat{\theta}^{[i+1]}_{S,R,D}(N-1)]^T$ is obtained from (6.20).

Using (6.20), (6.26) and (6.28), the proposed algorithm iteratively updates the PHN and CFO and CIR paramors in E-step and M-step of the algorithm, respectively, and stops when the difference between likelihood functions of two iterations is smaller than a threshold ζ, i.e.,

$$\left| \sum_{n=0}^{N-1} \left\| u(n) - e^{j2\pi\hat{\epsilon}^{[i+1]}_{S,R,D}n/N} e^{j\hat{\theta}^{[i+1]}_{S,R,D}(n)} s^{[i+1]}(n) \right\|^2 - \sum_{n=0}^{N-1} \left\| u(n) - e^{j2\pi\hat{\epsilon}^{[i]}_{S,R,D}n/N} e^{j\hat{\theta}^{[i]}_{S,R,D}}(n) s^{[i]}(n) \right\|^2 \right| \leq \zeta. \tag{6.29}$$

The appropriate initialization of CFO and CIR, i.e., $\hat{\epsilon}^{[0]}_{S,R,D}$ and $\hat{\mathbf{h}}^{[0]}_{S,R,D}$, respectively, can help the proposed estimator to estimate the CIR, CFO, and PHN parameters in a few iterations. The initial CFO estimate is obtained by applying a linear search for the value of $\epsilon_{S,R,D}$ that minimizes the cost function, $\sum_{n=0}^{N-1} \parallel u(n) - e^{j2\pi\hat{\epsilon}_{S,R,D}n/N}\hat{s}(n) \parallel^2$, where $\hat{s}(n)$ is nth symbol of the vector $\hat{\mathbf{s}} \triangleq \mathrm{q}_1\mathbf{F}^H\mathbf{D}_S\mathbf{F}_{(2L-1)}\hat{\mathbf{h}}_{S,R,D}$, $\hat{\mathbf{h}}_{S,R,D} \triangleq (\boldsymbol{\Gamma}^H\boldsymbol{\Gamma})^{-1}\boldsymbol{\Gamma}^H\hat{\mathbf{E}}^H_{S,R,D}\mathbf{u}$ and linear search is made with a coarse step size of 10^{-2}. Next, using the initial CFO estimate $\hat{\epsilon}^{[0]}_{S,R,D}$, initial channel estimate, $\hat{\mathbf{h}}^{[0]}_{S,R,D}$, is obtained by applying the equation, $\hat{\mathbf{h}}^{[0]}_{S,R,D} \triangleq (\boldsymbol{\Gamma}^H\boldsymbol{\Gamma})^{-1}\boldsymbol{\Gamma}^H(\hat{\mathbf{E}}^{[0]}_{S,R,D})^H\mathbf{u}$, where $\hat{\mathbf{E}}^{[0]}_{S,R,D} = \hat{\mathbf{E}}_{S,R,D}|_{\hat{\epsilon}_{S,R,D}=\hat{\epsilon}^{[0]}_{S,R,D}}$. The simulation results show that the proposed estimator always converges to true estimates, e.g., at $SNR = 20$ dB and with threshold $\zeta = 10^{-3}$, on average, the estimator converges after 2 iterations only.

6.5.2 Proposed ECM based Estimator for DF Cooperative Networks

Similar to the case of AF relaying, bth node receiver between any pair of transmitted node a and received node b has to jointly estimate the CIR, PHN and CFO between $a \rightarrow b$. The ECM algorithm at bth node receiver iterates between the expectation step (E-step) and the maximization step (M-step). The ECM algorithm is not presented here to avoid repetition. Therefore, using (6.20), (6.26) and (6.28), the proposed algorithm iteratively updates the parameters of PHN, $\boldsymbol{\theta}^{[i+1]}_{a,b}$, CFO, $\hat{\epsilon}^{[i+1]}_{a,b}$, and CIR, $\hat{\mathbf{h}}^{[i+1]}_{a,b}$ and stops when the difference between likelihood func-

tions of two iterations is smaller than a threshold ζ as in (6.29). Thus, (6.20), (6.26) and (6.28) can be used to estimate the parameters, $\boldsymbol{\theta}_{S,D}, \mathbf{h}_{S,D}, \epsilon_{S,D}$ between $S \rightarrow D$ in (6.3), $\boldsymbol{\theta}_{S,R_1}, \mathbf{h}_{S,R}, \epsilon_{S,R}$ between $S \rightarrow R$ in (6.4), and $\boldsymbol{\theta}_{R_2,D}, \mathbf{h}_{R,D}, \epsilon_{R,D}$ between $R \rightarrow D$ in (6.7), respectively.

6.6 Joint Data Detection and PHN Mitigation

In order to decode the received signal at the destination and relay in the presence of PHNs and CFOs, an iterative detector based EKF for both DF and AF relay cooperative systems is proposed.

6.6.1 Decoding in AF-Relaying Networks

In this section, an iterative detector that utilizes an EKF is proposed to track the PHN parameters during the data transmission interval.

At first, using the estimated CFO value, the effect of CFO on the received data symbol, $\mathbf{u}$, in (6.11) is compensated. The resulting signal, $\mathbf{r} \triangleq [r_1, \ldots, r_n]$, where r_n is defined in (6.15), passes through an *iterative* algorithm of data detection and PHN mitigation. An EKF is used to track the PHN samples, $\boldsymbol{\theta}_{S,R,D}$, over the data symbols. The PHN estimation is similar to that in (6.16)-(6.21) and is not presented here to avoid repetition. However, instead of training-based PHN tracking, the PHN estimation is followed in a decision-directed fashion for the received data symbols. In other words, the estimate of the data symbol in the previous iteration, $\hat{\mathbf{d}}_S^{[i-1]}$, is used to update the symbol's PHN estimate at the current iteration $\hat{\boldsymbol{\theta}}^{[i]}$. Particularly, $\mathbf{s}^{[i]}$ in (6.11), is calculated as $\mathbf{s} = \mathbf{F}^H \mathbf{D}_S \mathbf{F}_{(2L-1)} \hat{\mathbf{h}}_{S,R,D}$, where $\hat{\mathbf{h}}_{S,R,D}$ is the overall CIR vector estimate obtained from the ECM estimator during the training interval, and $\hat{\mathbf{D}}_S^{[i-1]} \triangleq \text{diag}(\hat{\mathbf{d}}_S^{[i-1]})$. Next, the data vector estimate is updated for the ith iteration. Following [26] and based on the received signal in (6.15), the negative LLF for the CFO compensated signal, $\mathbf{r}$, can be written as

$$\log p(\mathbf{r}, \hat{\mathbf{d}}_S, \hat{\boldsymbol{\theta}}_{S,R,D}) = \text{C} + \frac{1}{2\tilde{\sigma}_w^2} \parallel \mathbf{r} - \text{q}_1 \hat{\mathbf{P}}_{S,R,D} \mathbf{F}^H \hat{\boldsymbol{\Upsilon}} \hat{\mathbf{d}}_S \parallel^2 + \frac{1}{2\xi_{d_S}} \parallel \hat{\mathbf{d}}_S \parallel^2 + \log p(\boldsymbol{\theta}_{S,R,D}), \tag{6.30}$$

where

- $\hat{\boldsymbol{\Upsilon}} \triangleq \text{diag}(\mathbf{F}_{(2L-1)} \hat{\mathbf{h}}_{S,R,D})$ is the estimated channel frequency response,

- $\hat{\mathbf{d}}_S \triangleq [\hat{d}_S(0), \hat{d}_S(1), \cdots, \hat{d}_S(N-1)]^T$ is the estimate of the modulated data vector, and

- ξ_{d_S} is the average transmitted symbol power and normalized to 1,

Taking the derivative of (6.30) with respect to $\mathbf{d}_S$ and equating the result to zero, the estimate of $\mathbf{d}_S$ at the ith iteration, $\hat{\mathbf{d}}^{[i]}$ is given by

$$\hat{\mathbf{d}}_S^{[i]} = \mathrm{q}_1(\mathrm{q}_1^2 \hat{\boldsymbol{\Upsilon}}^H \hat{\boldsymbol{\Upsilon}} + \frac{\tilde{\sigma}_w^2}{\xi_{d_S}} \mathbf{I}_N)^{-1} \hat{\boldsymbol{\Upsilon}}^H \mathbf{F} \hat{\mathbf{P}}_{S,R,D}^H \mathbf{r}, \tag{6.31}$$

where $\hat{\mathbf{P}}_{S,R,D} \triangleq \mathrm{diag}([e^{j\hat{\theta}_{S,R,D}^{[i]}(0)}, e^{j\hat{\theta}_{S,R,D}^{[i]}(1)}, \ldots, e^{j\hat{\theta}_{S,R,D}^{[i]}(N-1)}]^T)$ and $\hat{\boldsymbol{\theta}}_{S,R,D}^{[i]} \triangleq [\hat{\theta}_{S,R,D}^{[i]}(0), \hat{\theta}_{S,R,D}^{[i]}(1), \ldots, \hat{\theta}_{S,R,D}^{[i]}(N-1)]^T$ are obtained via the EKF based estimator.

Using the EKF set of equations (6.16)-(6.21) and (6.31), the proposed algorithm iteratively updates the PHN and data estimates, respectively, and stops when the difference between the likelihood functions of two iterations is smaller than a threshold ζ, i.e.,

$$\left| \sum_{n=0}^{N-1} \left\| r(n) - e^{j\hat{\theta}_{S,R,D}^{[i+1]}(n)} \hat{s}^{[i+1]}(n) \right\|^2 - \sum_{n=0}^{N-1} \left\| r(n) - e^{j\hat{\theta}_{S,R,D}^{[i]}(n)} \hat{s}^{[i]}(n) \right\|^2 \right| \leq \zeta. \tag{6.32}$$

Let $\hat{\mathbf{d}}_S^{[0]}$ denote the initial estimate of the transmitted data vector. Appropriate initialization of $\hat{\mathbf{d}}_S^{[0]}$ results in the proposed iterative detector to converge quickly. In our algorithm, the initial data estimate is obtained using $\hat{\mathbf{d}}_S^{[0]} = \mathrm{q}_1(\mathrm{q}_1^2 \hat{\boldsymbol{\Upsilon}}^H \hat{\boldsymbol{\Upsilon}} + \frac{\tilde{\sigma}_w^2}{\xi_{d_S}} \mathbf{I}_N)^{-1} \hat{\boldsymbol{\Upsilon}}^H \mathbf{F} \hat{\mathbf{P}}_{S,R,D}^{H[m-1]} \mathbf{r}$, where $\hat{\mathbf{P}}_{S,R,D}^{[m-1]}$ is the PHN matrix estimate obtained from the previous OFDM symbol. Simulation results in Section 6.8 indicate that at SNR= 20 dB the proposed detector, on average, converges after 2 iterations.

6.6.2 Decoding in DF-Relaying Networks

Similar to the AF case, the bth node receiver between any pair of transmitted node a and received node b can use the estimated CFO value to compensate the effect of CFO on the received data symbol. Then, the resulting signal passes through an *iterative* algorithm of data detection and PHN mitigation similar the EKF set of equations (6.16)-(6.21) and (6.31). Therefore, the same approach can be used to decode the data at the destination and the relay from the received signal in (6.3) and (6.4), respectively.

6.7 Complexity analysis

In this subsection, the computational complexity of the proposed ECM, iteration algorithm for data detection in both DF-and AF-relaying multi-relay cooperative systems are analyzed. Throughout this section, computational complexity is defined as the number of complex additions plus number of multiplications [124].

6.7.1 AF Relaying

Let the computational complexity of AF link, i.e., from $S \rightarrow R \rightarrow D$, of the ECM algorithm is denoted by $C_{\text{EST}}^{\text{AF}} = C_{\text{EST}}^{\text{AF},[M]} + C_{\text{EST}}^{\text{AF},[A]}$. The notations $C_{\text{EST}}^{\text{AF},[M]}$ and $C_{\text{EST}}^{\text{AF},[A]}$ are used to denote the number of complex multiplications and additions, respectively, used by the ECM estimator and are determined as

$$\begin{aligned} C_{\text{EST}}^{\text{AF},[M]} = \big[& \underbrace{N}_{(6.16)} + \underbrace{5N}_{(6.19)} + \underbrace{2N}_{(6.20)} + \underbrace{2N}_{(6.21)} + \underbrace{7N}_{(6.26)} + \underbrace{N(2L-1)(2N+1)}_{(6.28)} \\ & + \underbrace{N(N^2+(2L-1)(N+1))}_{s_n \text{in}(6.20)} \big] t_{\text{ECM}} + \big[\underbrace{3N}_{\sum_{n=0}^{N-1} \|u(n) - e^{j2\pi \hat{\epsilon}_{S,R,D} n/N} \hat{s}(n)\|^2} \\ & + \underbrace{N(2L-1)(2N+1)}_{\hat{\mathbf{h}}_{S,R,D} \triangleq \xi_d{}^{-1} \mathbf{\Gamma}^H \hat{\mathbf{E}}_{S,R,D}^H \mathbf{u}} + \underbrace{N(N^2+(2L-1)(N+1))}_{\hat{\mathbf{s}} \triangleq \mathrm{q}_1 \mathbf{F}^H \mathbf{D}_S \mathbf{F}_{(2L-1)} \hat{\mathbf{h}}_{S,R,D}} \big] t_{\text{initialize}} \\ & + \underbrace{N^2(N+(2L-1))}_{\mathbf{\Gamma} \text{in}(6.28)} \end{aligned} \tag{6.33}$$

$$\begin{aligned} C_{\text{EST}}^{\text{AF},[A]} = \big[& \underbrace{N}_{(6.18)} + \underbrace{N}_{(6.19)} + \underbrace{2N}_{(6.20)} + \underbrace{N}_{(6.21)} + \underbrace{2N+1}_{(6.26)} + \underbrace{(N-1)(2L-1)(2N+1)}_{(6.28)} \\ & + \underbrace{N(N-1)((2L-1)+1) + N((2L-1)-1)}_{s_n \text{in}(6.20)} \big] t_{\text{ECM}} \\ & + \big[\underbrace{2N}_{\sum_{n=0}^{N-1} \|u(n) - e^{j2\pi \hat{\epsilon}_{S,R,D} n/N} \hat{s}(n)\|^2} + \underbrace{(2L-1)(N-1)(2N+1)}_{\hat{\mathbf{h}}_{S,R,D} \triangleq \xi_d{}^{-1} \mathbf{\Gamma}^H \hat{\mathbf{E}}_{S,R,D}^H \mathbf{u}} \\ & + \underbrace{N(N-1)((2L-1)+1) + N((2L-1)-1)}_{\hat{\mathbf{s}} \triangleq \mathrm{q}_1 \mathbf{F}^H \mathbf{D}_S \mathbf{F}_{(2L-1)} \hat{\mathbf{h}}_{S,R,D}} \big] t_{\text{initialize}} \\ & + \underbrace{N(N-1)(N+(2L-1))}_{\mathbf{\Gamma} \text{in}(6.28)} \end{aligned} \tag{6.34}$$

where t_{ECM} is the number of iterations in ECM algorithm and $t_{\text{initialize}}$ is the number of iterations in coarse estimation to obtain the initial estimate of CFO.

Similarly, the computational complexity of the proposed data detection algorithm based on EKF is denoted by $C^{\text{AF},[M]}_{\text{DATA DET}}$ and $C^{\text{AF},[A]}_{\text{DATA DET}}$, where $C^{\text{AF},[M]}_{\text{DATA DET}}$ and $C^{\text{AF},[A]}_{\text{DATA DET}}$ denote the number of complex multiplications and additions used by the detector. $C^{\text{AF},[M]}_{\text{DATA DET}}$ and $C^{\text{AF},[A]}_{\text{DATA DET}}$ are determined as

$$\begin{aligned} C^{\text{AF},[M]}_{\text{DATA DET}} = \big[& \underbrace{N}_{(6.16)} + \underbrace{5N}_{(6.19)} + \underbrace{2N}_{(6.20)} + \underbrace{2N}_{(6.21)} + \underbrace{N(N^2 + (2L-1)(N+1))}_{s_n \text{in}(6.20)} \\ & + \underbrace{N^2(5N+1)}_{(6.31)} \big] t_{\text{DATA DET}} + \underbrace{N^2(5N+1)}_{\hat{\mathbf{d}}_S^{[0]} = \mathrm{q}_1(\mathrm{q}_1^2 \hat{\boldsymbol{\Upsilon}}^H \hat{\boldsymbol{\Upsilon}} + \frac{\tilde{\sigma}_w^2}{\xi_{d_S}} \mathbf{I}_N)^{-1} \hat{\boldsymbol{\Upsilon}}^H \mathbf{F} \mathbf{P}_{S,R,D}^{H[m-1]} \mathbf{r}} \\ & + \underbrace{N(2L-1)}_{\hat{\boldsymbol{\Upsilon}} \text{in}(6.31)} \end{aligned} \tag{6.35}$$

$$\begin{aligned} C^{\text{AF},[A]}_{\text{DATA DET}} = \big[& \underbrace{N}_{(6.18)} + \underbrace{N}_{(6.19)} + \underbrace{2N}_{(6.20)} + \underbrace{N}_{(6.21)} \\ & + \underbrace{N(N-1)((2L-1)+1) + N((2L-1)-1)}_{s_n \text{in}(6.20)} \\ & + \underbrace{N(N^2 + N(N-1)(4N+1))}_{(6.31)} \big] t_{\text{DATA DET}} \\ & + \underbrace{N(N^2 + N(N-1)(4N+1))}_{\hat{\mathbf{d}}_S^{[0]} = \mathrm{q}_1(\mathrm{q}_1^2 \hat{\boldsymbol{\Upsilon}}^H \hat{\boldsymbol{\Upsilon}} + \frac{\tilde{\sigma}_w^2}{\xi_{d_S}} \mathbf{I}_N)^{-1} \hat{\boldsymbol{\Upsilon}}^H \mathbf{F} \mathbf{P}_{S,R,D}^{H[m-1]} \mathbf{r}} + \underbrace{N((2L-1)-1)}_{\hat{\boldsymbol{\Upsilon}} \text{in}(6.31)} \end{aligned} \tag{6.36}$$

6.7.2 DF Relaying

Similar to the AF case of equations (6.33), (6.34), (6.35) and (6.36), the computational complexity between any pair of transmitted node a and received node b, i.e., from $a \to b$, can be calculated. Therefore, the computational complexity of the proposed ECM algorithm and the data detection algorithm based on EKF are denoted by $C^{ab}_{\text{EST}} = C^{ab,[M]}_{\text{EST}} + C^{ab,[A]}_{\text{EST}}$ and $C^{ab}_{\text{DATA DET}} = C^{ab,[M]}_{\text{DATA DET}} + C^{ab,[A]}_{\text{DATA DET}}$, respectively. The notations $C^{ab,[M]}_{\text{EST}}$ and $C^{ab,[M]}_{\text{DATA DET}}$, and $C^{ab,[A]}_{\text{EST}}$ and $C^{ab,[A]}_{\text{DATA DET}}$ are used to denote the number of complex multiplications and additions, respectively, used by the ECM estimator and the data detection algorithm based on EKF and are determined similar to equations (6.33), (6.34), (6.35) and (6.36). However, L is used instead of $(2L-1)$ in (6.33), (6.34), (6.35) and (6.36).

Figure 6.2 shows the average number of iterations, i.e., t_{ECM} and $t_{\text{DATA DET}}$ required by the proposed algorithms in both AF and DF relaying networks and

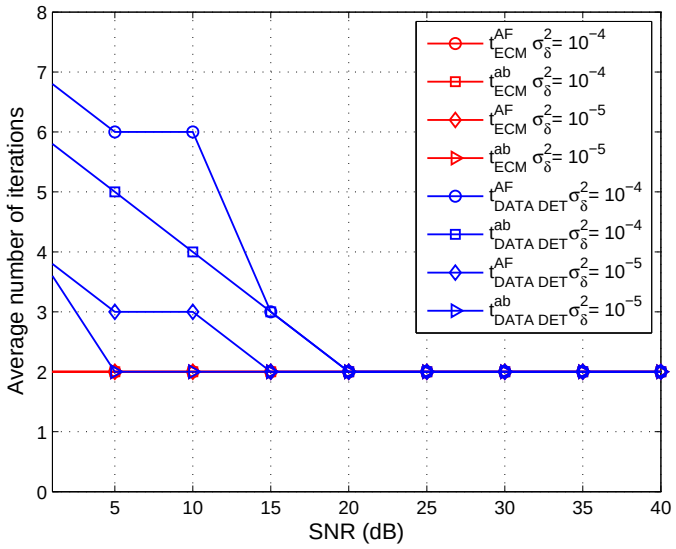

Figure 6.2: Average number of iterations for the proposed ECM algorithm and the data detection algorithm based on EKF in DF and AF cooperative networks for phase noise variance $\sigma^2_\delta = [10^{-4}, 10^{-5}]$ rad^2 and 16-QAM modulation.

PHN variance, $\sigma^2_\delta = [10^{-4}, 10^{-5}]$ rad^2 and 16-QAM modulation. For the comparison in Figure 6.2, the number of iterations of AF link, i.e., from $S \rightarrow R \rightarrow D$, are donated by t^{AF}_{ECM}, $t^{AF}_{\text{DATA DET}}$, while the number of iterations of DF link between any pair of transmitted node a and received node b, are donated by t^{ab}_{ECM}, $t^{ab}_{\text{DATA DET}}$. It can be observed from the results in Figure 6.2 that (i) at low SNR, i.e., $SNR < 20$ dB, on average, the proposed detector converges after $t_{\text{DATA DET}}$ more than 2 iterations, (ii) the proposed detector in AF relaying networks requires more number of iterations at low SNR, i.e., $SNR < 20$ dB. This due to the irreducible error of channel, PHN and CFO estimation from source to relays and the noise at the relays which is amplified and forwarded to the destination, (iii) the number of iterations decreases to $t_{\text{ECM}} = t_{\text{DATA DET}} = 2$ at $SNR \geq 20$ dB, and (iv) the proposed ECM algorithm converges to the true estimates when the CFO estimates are initialized with a step size of 10^{-2}, i.e., $t_{\text{initialize}} = 10^2$. Using these values for the number of iterations, we get the computational complexity of the proposed algorithms for both DF and AF multi-relay cooperative networks with $M = 4$ relays as shown in Figure 6.3. The results in Figure 6.3 show that (i) at low SNR, i.e., $SNR < 20$ dB, the computational complexity of

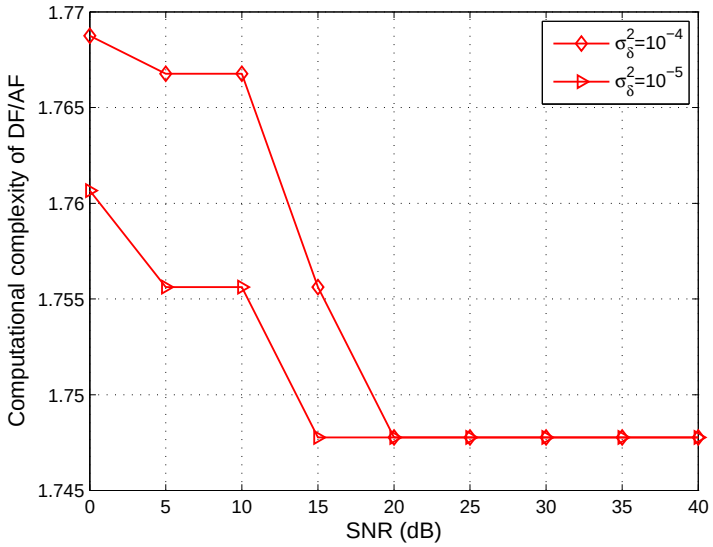

Figure 6.3: Comparison of the computational complexity of the proposed algorithms in DF over AF cooperative networks for phase noise variance $\sigma_\delta^2 = [10^{-4}, 10^{-5}]$ rad^2, 16-QAM modulation, $L = 4$ and $M = 4$ relays.

the proposed algorithms in DF and AF cooperative networks are dependent on the variance of the PHN process, since at low SNR the performance of the proposed estimator and detector is dominated by AWGN and PHN variance, while at moderate-to-high SNR, i.e., $SNR > 20$ dB the performance of the system is limited by residual PHN and CFO, (ii) at moderate-to-high SNR compared to low SNR, the proposed estimation and data detection algorithms are computationally more efficient. These results are anticipated, since the proposed estimation and data detection algorithms require few iterations at moderate-to-high SNR as shown in Figure 6.2.

6.8 Simulation Results and Discussions

In this section, simulation results are presented to evaluate the performance of the proposed estimation and data detection algorithms for both DF and AF relay systems. In addition, an investigation is carried out to investigate the effects of PHNs and CFOs on 3-D video transmission. A multipath Rayleigh fading channel with a delay of $L = 4$ taps and an exponentially decaying power

delay profile is assumed between each pair of nodes. A training symbol size of $N = 64$ subcarriers is used, where each subcarrier is modulated using the QPSK scheme. The Wiener PHN is generated with different PHN variances, e.g. $\sigma_\delta^2 = [10^{-4}, 10^{-5}]\text{rad}^2$, where $\sigma_{\delta_S}^2 = \sigma_{\delta_D}^2 = \sigma_{\delta_{R_m,1}}^2 = \sigma_{\delta_{R_m,2}}^2 = \sigma_\delta^2$. Note that, $\sigma_\delta^2 = 10^{-4}$ rad^2, corresponds to a high phase noise variance [125]. Since carrier frequency offsets from source to relays, ϵ_{S,R_m}, are carried over to the destination, ϵ_{S,R_m} and $\epsilon_{R_m,D}$ have the range (-0.25,0.25) in order to limit the total frequency offset from source to destination, $\epsilon_{S,D}$ to the range (-0.5, 0.5). Similar to the parameter setting adopted in [14], the large-scale channel fading parametrization is set as γ=2, $d_{S,D}$=1, d_{S,R_m}=0.5, $d_{R_m,D}$=0.72, g_{S,R_m}=4 and $g_{R_m,D}$=1.9. The data symbols are drawn from normalized 16 or 64 QAM. The MSE performance of ECM estimator and the BER performance of the overall multi-relay cooperative network compared to the single-hop link, $S \rightarrow D$, is detailed in the following subsections. To evaluate the PSNR performance of the proposed system, several experiments are conducted with typical 3-D video "Car" sequence in [95], with 432×240 pixels and a GoP of 8. Each GoP is divided into four groups ($Ng = 4$) g_1, g_2,g_3, g_4. In this chapter, the H.264 reference software JM version (13.2) in [36] is used for encoding the colour and depth sequences. The adopted LDPC is set of a code length of 1296 and 50 maximum iterations with variable coding rates = 13/16, 8/16 and 4/16. The simulation results are averaged over 1×10^5 Monte Carlo simulation runs.

6.8.1 Estimation Performance

In this subsection, the performance of the proposed ECM estimator is compared with the HCRB in Theorem 6.1. Figures. 6.4, 6.5 and 6.6 plot the HCRB and MSE for estimating the CIR, PHN, and CFO, respectively, using the proposed algorithm. Note that, in Figures 6.4, 6.5 and 6.6, the label, $S \rightarrow D$, represents the performance of the estimator of each link in the DF system, while the the label, $S \rightarrow R \rightarrow D$, represents the performance of the estimator of each link in the AF system.

The results lead to the following observations:

1) The HCRB and the proposed estimators MSE are dependent on the variance of the PHN process and are lower for a lower PHN variance;

2) Figures 6.4, 6.5 and 6.6 show that CIR, CFO and PHN estimation performances suffer from an error floor, which is directly related to the variance of the PHN process. This occurs as, at low SNR, the performance of the system is dominated

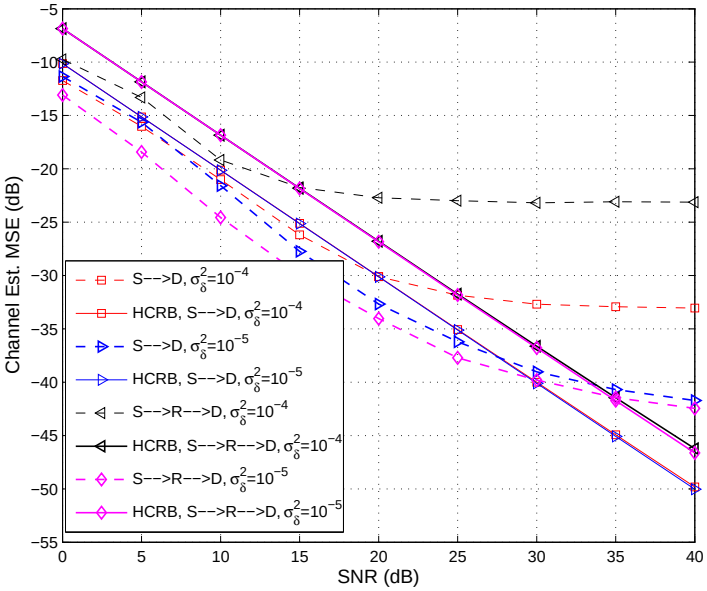

Figure 6.4: MSE of channel estimation for the proposed estimator compared to HCRB for phase noise variance $\sigma_\delta^2 = [10^{-4}, 10^{-5}]$ rad^2.

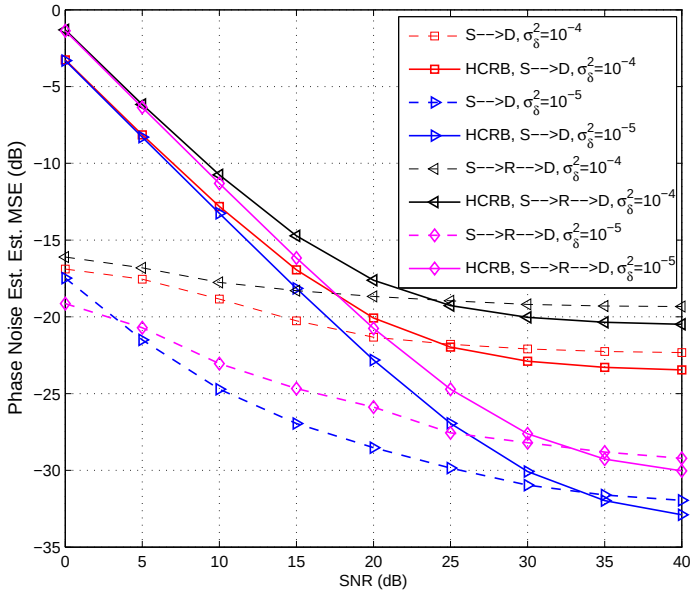

Figure 6.5: MSE of phase noise estimation for the proposed estimator compared to HCRB for phase noise variance $\sigma_\delta^2 = [10^{-4}, 10^{-5}]$ rad^2.

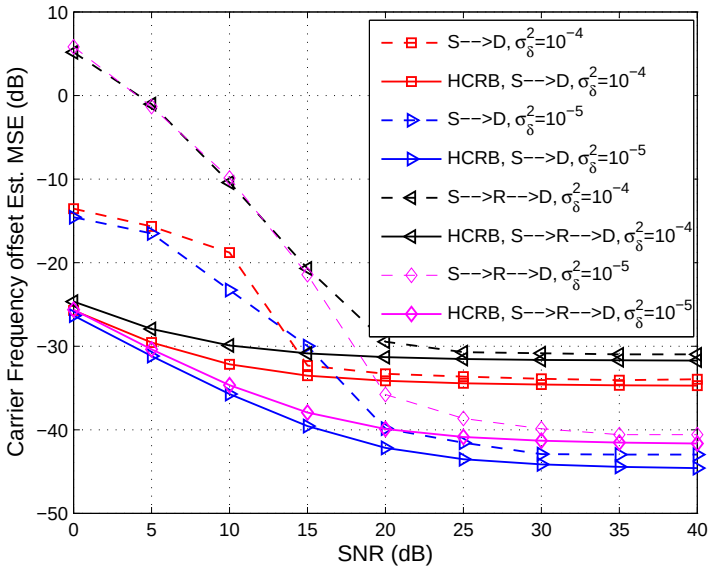

Figure 6.6: MSE of frequency offset estimation for the proposed estimator compared to HCRB for phase noise variance $\sigma_\delta^2 = [10^{-4}, 10^{-5}]$ rad^2.

by AWGN, while at high SNR the performance of the proposed estimator is limited by PHN and the resulting ICI;

3) The estimation performance and HCRB for the single-hop link (direct link), $S \rightarrow D$, are better than those of the relay link, i.e., $S \rightarrow R \rightarrow D$. This is due to the noise at the relays which is amplified and forwarded to the destination. The difference of estimator performance in terms of MSE between the $S \rightarrow D$ and $S \rightarrow R \rightarrow D$ adversely affects the performance of data detection algorithms. Therefore, the DF cooperative systems have better BER performance than the AF cooperative systems (see Figures 6.7-6.12);

4) It is shown that the MSEs of the proposed estimator for both direct and relay links are close to their HCRLBs at moderate-to-high SNRs;

5) In Figure 6.5, the MSE of the proposed estimator is lower than the HCRB at lower SNR. This is due to the fact that the HCRB cannot be derived in closed-form while taking into account the range of CFO values, i.e., (-0.25. 0.25), while the estimator takes the advantage of this known prior estimation range. Thus, the HCRB is higher than the MSE of the proposed estimator at lower SNR.

6.8.2 Impact of PHN on Cooperative Performance

After mitigating the PHN and CFO and compensating the channel on the received signals from the direct and relay links, maximal ratio combining (MRC) is utilized in the destination to obtain a cooperative diversity gain by adding the decoding samples of the direct and relay links coherently.

In the following, the combined estimation and data detection performance is examined in terms of the BER of both DF and AF. The following system setups are considered for comparison:

(i) Cooperative systems apply the proposed estimation and data detection algorithms (labelled as "Proposed MRC").

(ii) Cooperative systems apply the data detection in [14] combined with the proposed estimation algorithm (labelled "[[14], data detection]"). Note that the estimation performance of the algorithm in [14] is not presented since the approach in [14] only considers channel and PHN estimation while assuming that no CFO is present. In addition, the estimation performance of the algorithm in [15] is not presented since the relaying approach in [15] is totally different than the relaying approach and system model in this chapter.

(iii) Non-cooperative systems that apply the proposed estimation and data detection algorithm (labelled as "Single-hop").

(iv) As a reference, cooperative systems that apply the proposed estimation and data detection algorithms but utilize no CFO cancelation and PHN tracking during OFDM data symbols (labelled "Conventional MRC").

(v) As a lower-bound on the BER performance, cooperative systems assuming perfect channel, PHN, and CFO estimation (labelled "MRC, Perf. CIR, PHN & CFO est.").

Figures 6.7 and 6.8 show the BER performance with 4 relays for DF and AF cooperative networks for PHN variance, $\sigma_\delta^2 = [10^{-4}, 10^{-5}]$ rad^2 and 16-QAM modulation.

The following observations can be made from Figures 6.7 and 6.8:

1) The results of conventional MRC demonstrate that without phase tracking and CFO cancelation throughout the packet, the OFDM cooperative system performance for both DF and AF deteriorates significantly. On the other hand, by combining the proposed estimation and data detection algorithms, the BER performance of an OFDM cooperative system is shown to improve immensely even in the presence of strong PHN, e.g., $\sigma_\delta^2 = 10^{-4}$ rad^2.

2) Compared to existing algorithms, the BER performance of both DF and AF

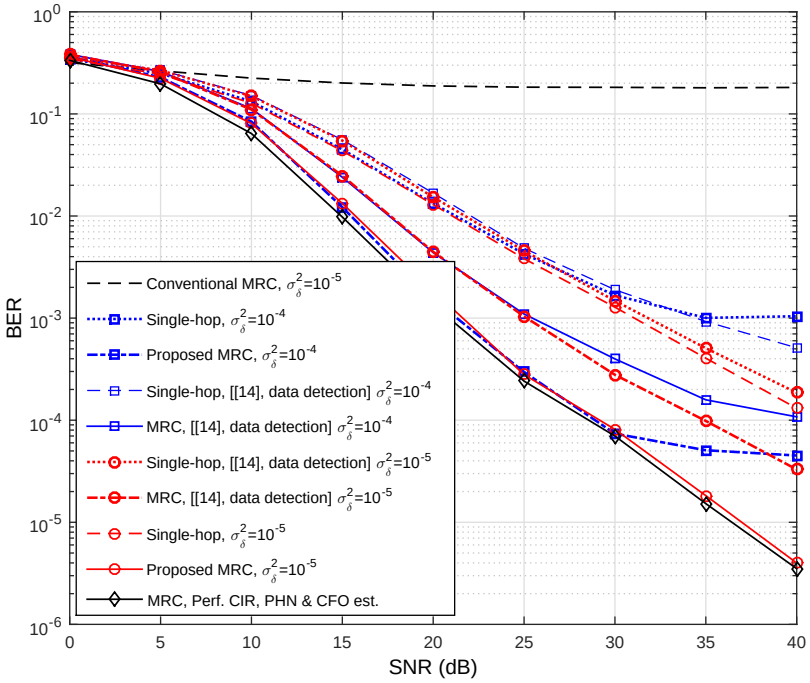

Figure 6.7: BER performance for a DF cooperative system for PHN variance, $\sigma_\delta^2 = [10^{-4}, 10^{-5}]$ rad^2 and 16-QAM modulation with M=4.

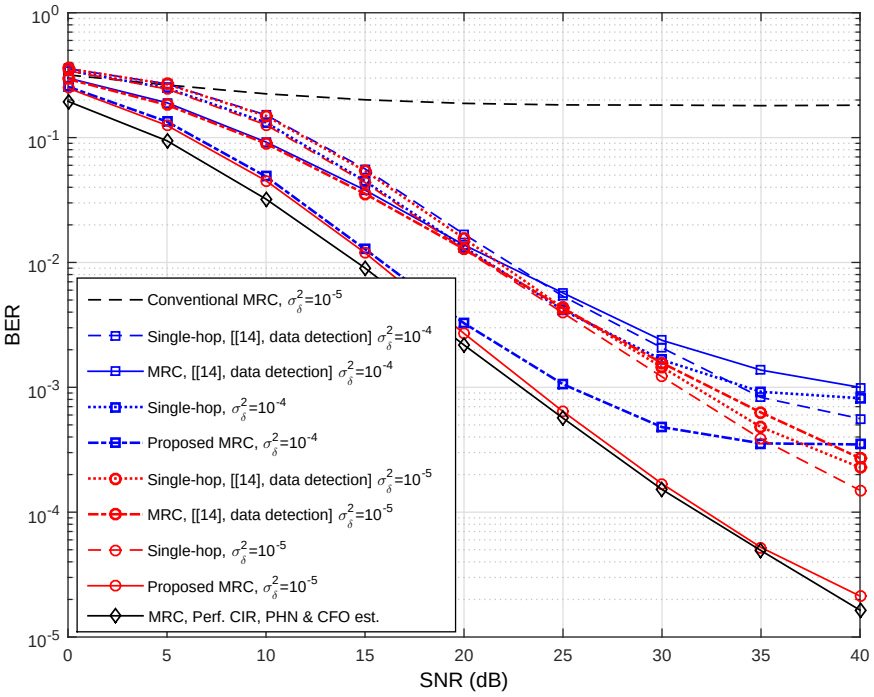

Figure 6.8: BER performance for an AF cooperative system for PHN variance, $\sigma_\delta^2 = [10^{-4}, 10^{-5}]$ rad^2 and 16-QAM modulation with M=4.

relaying cooperative network using the proposed algorithms is close to the ideal case of perfect CIR, PHN and CFO estimation when $\sigma_\delta^2 = 10^{-5}$ rad^2. However, at high PHN variance, i.e., $\sigma_\delta^2 = 10^{-4}$ rad^2, the BER performance of both DF and AF suffer from an error floor at high SNR. This result is anticipated, since at high PHN variance, the performance of a cooperative OFDM system is dominated by PHN, which cannot be completely eliminated.

3) It is clear that the performance of DF relaying cooperative network in Figures 6.7 outperforms the performance of AF in Figure 6.8 at different PHN variance and SNRs. This result is anticipated, since the received signal in the destination using AF suffers from PHN produce from four oscillators, i.e., two oscillators in the source and destination and two oscillators in the relay. However, the received signal between any pair of transmitted node a and received node b using DF suffers only from PHN signals from two oscillators.

4) Finally, the results in Figures 6.8 and 6.7 show that the proposed ECM based estimator and the iterative data detection algorithm outperform existing algorithms in terms of the BER performance. For example, in Figure 6.8, the BER for the proposed algorithms has an SNR gain of almost 12 dB compared to the existing algorithms in [14] at an BER of 10^{-4} and high PHN variance, i.e., $\sigma_\delta^2 = 10^{-4}$ rad^2.

6.8.3 Impact of Increase of Relays on Cooperative Performance

In this subsection, the performance of both DF and AF is examined compared to non-cooperative systems (single-hop) with the increase in diversity gain through increasing the number of relays in the cooperative network.

Figures 6.9 and 6.10 show the BER performance for DF and AF cooperative networks at different numbers of relays, $M = [1, 2, 4]$ for PHN variance, $\sigma_\delta^2 = [10^{-4}, 10^{-5}]$ rad^2 and 16-QAM modulation. The following observations can be made from Figures 6.9 and 6.10 that the cooperative system should use more relays with proportional to increase of PHN variance to achieve better BER performance compared to non-cooperative systems (single-hop). Figures 6.9 and 6.10 clearly show that the DF and AF cooperative system that an the number of relays increases, BER performance improves. In the presence of PHN, the cooperative system can achieve better BER performance by combining the proposed estimation and data detection algorithms and using more than one relay. However, this approach maintains higher performance at the expense of loss in

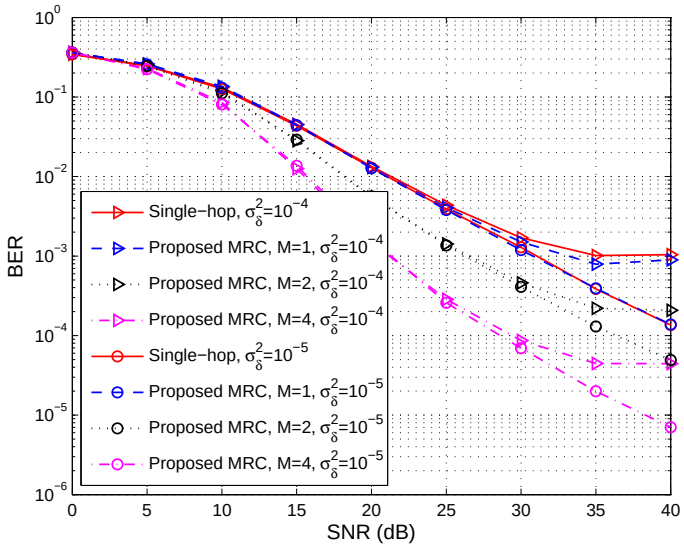

Figure 6.9: BER performance for a DF cooperative system at different number of relays, $M = [1, 2, 4]$ for PHN variance, $\sigma_\delta^2 = [10^{-4}, 10^{-5}]$ rad^2 and 16-QAM modulation.

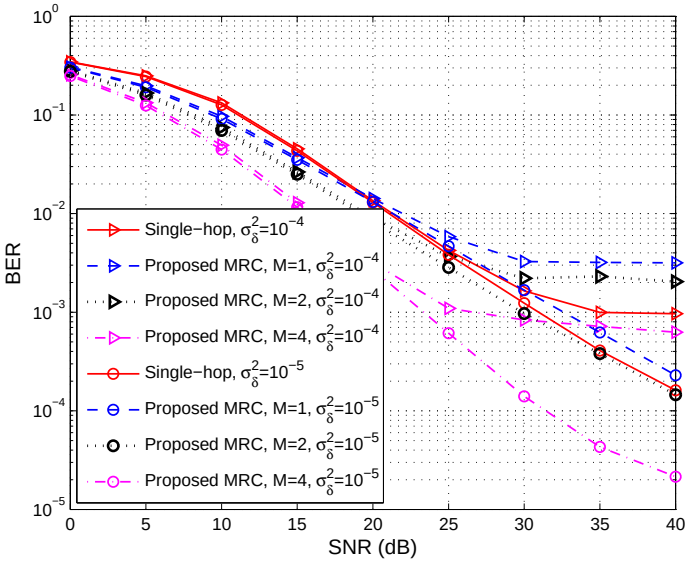

Figure 6.10: BER performance for an AF cooperative system at different number of relays, $M = [1, 2, 4]$ for PHN variance, $\sigma_\delta^2 = [10^{-4}, 10^{-5}]$ rad^2 and 16-QAM modulation.

spectral efficiency.

6.8.4 Impact of Modulation on Cooperative Performance

Figures 6.11 and 6.12 evaluate the BER performances of an OFDM cooperative system for both DF and AF at higher order modulations, i.e., 64-QAM.

The following observations can be made from Figures 6.11 and 6.12:

1) Even for a denser constellation, the proposed estimation and data detection algorithms significantly improve the overall system performance for both DF and AF compared to the non-cooperative system (direct transmission). For example, to achieve a BER of 10^{-2} with a PHN variance of 10^{-5} rad^2 using DF, the performance of cooperative system outperforms the non-cooperative system a margin of 5 dB. More importantly, this gap widens at high SNR values.

2) The BER performance of an OFDM cooperative system using the proposed algorithms is closer to the ideal case of perfect CIR, PHN, and CFO estimation for PHN variance, $\sigma_\delta^2 = 10^{-5}$ rad^2 (a performance gap of 0.6 dB in Figure 6.11 and 1 dB in Figure 6.12 at SNR = 20 dB).

3) It is clearly seen in Figure 6.12 that the performance of the proposed data detection algorithm outperforms the algorithm in [14] for 64-QAM modulation since the overall system performance is less or equal to the single-hop (direct transmission). Therefore, the pilots approach in [14] may not be used for higher order modulations, i.e., 64-QAM.

4) The results in Figures 6.11 and 6.12 shows that, even for a denser constellation, the proposed estimation and data detection algorithms significantly improve the overall system performance compared to that of [[14], data detection]. For example, to achieve a BER of 10^{-3} with a PHN variance of 10^{-5} rad^2 and 64-QAM, the proposed algorithm outperforms the algorithms in [[14], data detection] by a margin of 2 dB and 5 dB, in DF and AF relay networks, respectively.

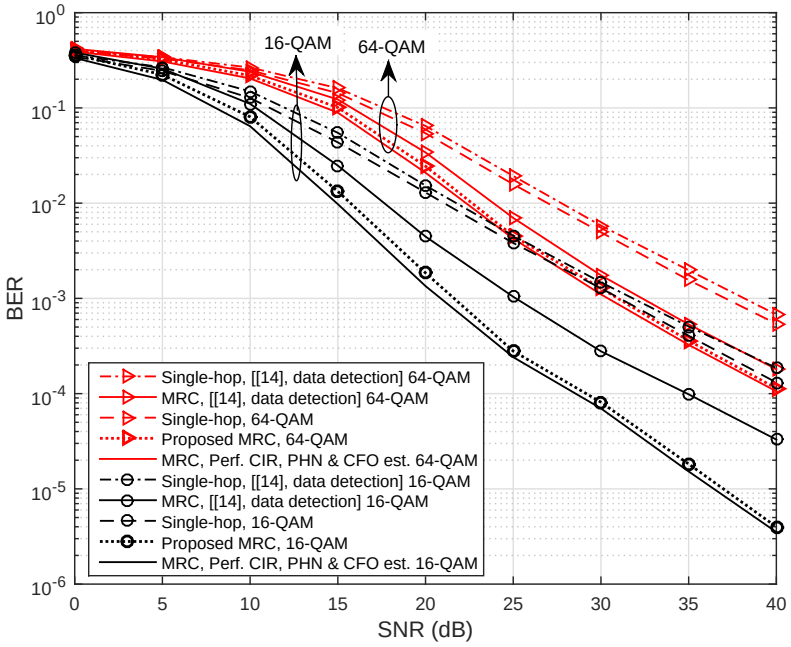

Figure 6.11: BER performance for a DF cooperative system for 64-QAM modulation with M=4 at PHN variance, $\sigma_\delta^2 = 10^{-5}$ rad^2.

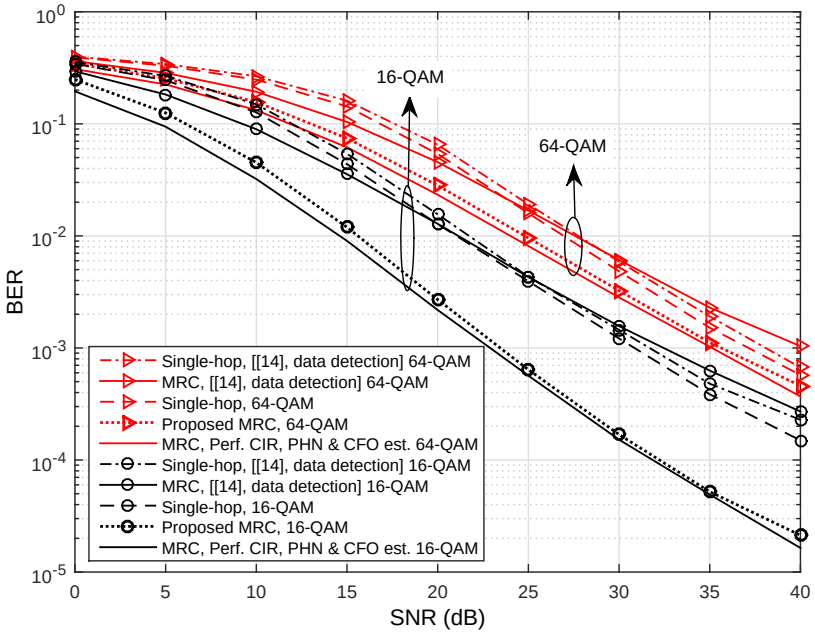

Figure 6.12: BER performance for a AF cooperative system for 64-QAM modulation with M=4 at PHN variance, $\sigma_\delta^2 = 10^{-5}$ rad^2.

6.8.5 Impact of PHN on the PSNR Performance

In this subsection, the effects of PHNs and CFOs on the performance of the AF relay network for 3-D video applications are investigated.

6.8.5.1 Impact of PHN

Figure 6.13 shows the PSNR performance for the proposed system using the UEP scheme, P-VpD-1/2, at code rates of $r_{HP} = 8/16$ and $r_{LP} = 13/16$, for PHN variance of $\sigma_\delta^2 = [10^{-4}, 10^{-5}]$ rad^2 and 16-QAM modulation with $M = 4$ relays.

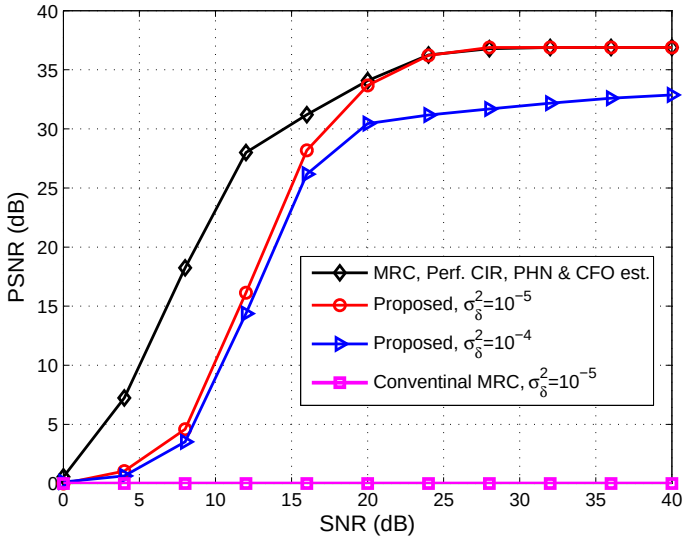

Figure 6.13: PSNR performance for the proposed cooperative system at coding rates, $r_{HP} = 8/16$ and $r_{LP} = 13/16$, for PHN variance, $\sigma_\delta^2 = [10^{-4}, 10^{-5}]$ rad^2 and 16-QAM modulation with M=4.

The following observations can be made from Figure 6.13:
1) The results of conventional MRC demonstrate that, without phase tracking and CFO cancellation at the receiver, the cooperative system performance deteriorates significantly. On the other hand, by combining the proposed estimation and data detection algorithms, the PSNR performance of the cooperative system is shown to improve immensely even in the presence of strong PHN, e.g., $\sigma_\delta^2 = 10^{-4}$ rad^2.
2) The results in Figure 6.13 show that the PSNR performance of the proposed

algorithms is close to that of the ideal case of "MRC, Perf. CIR, PHN & CFO est." with $\sigma_\delta^2 = 10^{-5}$ rad^2.
3) Simulation results in Figure 6.13 show that, at high SNRs and PHN variance $\sigma_\delta^2 = 10^{-4}$ rad^2, the system has lower a PSNR performance compared to its performance with a PHN variance $\sigma_\delta^2 = 10^{-5}$ rad^2. This result is anticipated, since, with high PHN variance, the performance of the cooperative system is dominated by the PHN, which cannot be completely eliminated. For instance, as shown in Figure 6.13, at SNR = 28 dB and PHN variance $\sigma_\delta^2 = 10^{-5}$ rad^2, the PSNR gain for the proposed system is almost 5.2 dB compared to the proposed system at PHN variance, $\sigma_\delta^2 = 10^{-4}$ rad^2.
4) Finally, at the low SNR regime, i.e. $SNR < 20$ dB, there are still some reductions in PSNR even the PHN variance is moderate, i.e., $\sigma_\delta^2 = 10^{-5}$ rad^2. This is because the performance of the ECM estimator is limited by the PHN and AWGN at low SNRs. For example, as shown in Figure 6.13, at SNR = 12 dB and PHN variance, $\sigma_\delta^2 = 10^{-5}$ rad^2, the PSNR is reduced from 28 dB to 16.14 dB, i.e. the performance loss is 11.86 dB.

6.8.5.2 Impact of modulation

Figure 6.14 plots the PSNRs of the proposed system using the UEP scheme, P-VpD-1/2, at higher order modulations, i.e. 64-QAM.

The following observations can be made from Fig 6.14:
i) Even with perfect CIR, PHN, and CFO estimation, the system using 64-QAM performs worse than using 16-QAM at low-to-moderate SNRs. This result is expected since 64-QAM is less robust to channel noise,
ii) At moderate-to-high SNRs, the PSNR performance using the proposed algorithms is closer to the ideal case of perfect CIR, PHN, and CFO estimation (a performance gap of 0.4 dB and 1 dB at SNR = 20 dB using 16-QAM and 64-QAM, respectively),
iii) It is clear from the results in Fig 6.14 that the PHN and the order of modulation play a significant factor in determining the PSNR performance. As shown in Figure 6.14, the system can achieve high PSNR by using lower orders of modulation, e.g. 16-QAM.

6.8.5.3 Impact of channel code rates

In this subsection, the performance of the proposed system with different UEP schemes and channel code rates is presented. Figure 6.15 shows the PSNR perfor-

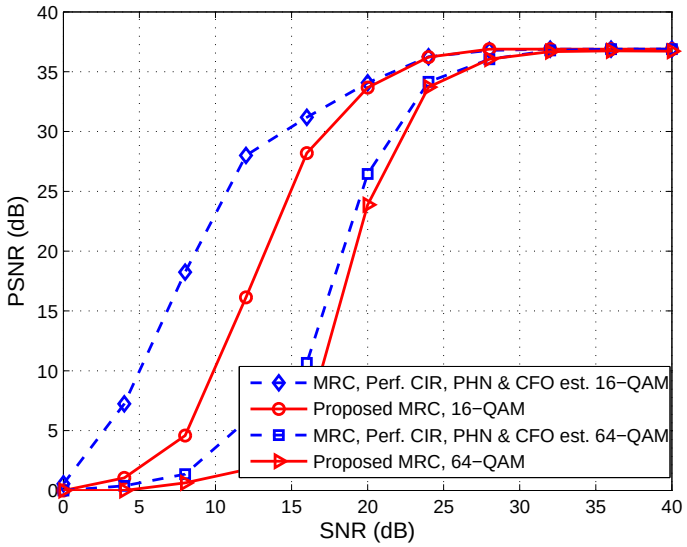

Figure 6.14: PSNR performance for the cooperative system at coding rates, $r_{HP} = 8/16$ and $r_{LP} = 13/16$, for 64-QAM modulation and PHN variance, $\sigma_\delta^2 = 10^{-5}$ rad^2 with M=4.

mance for the proposed cooperative system with different UEP schemes, P-VpD, P-VpD-1/4 and P-VpD-1/2, and channel code rates, $r_{HP} = [4/16, 8/16, 13/16]$ and $r_{LP} = 13/16$ for the PHN variance, $\sigma_\delta^2 = 10^{-5}$ rad^2 and 16-QAM modulation with $M = 4$.

The following observations can be made from Figure 6.15:

1) The system can improve the PSNR performance by reducing the code rate. For instance, at $SNR = 16$ dB and P-VpD-1/2, $r_{HP} = 4/16$, the PSNR gain is almost 5.4 dB compared to P-VpD-1/2 with $r_{HP} = 8/16$. However, this improvement in PSNR is at expense of increased complexity of channel coding.

2) The PSNR performance is enhanced by allocating as much as possible of the prior packets of a GOP to the HP stream. This is clearly shown in low SNRs, i.e., $SNR < 20$ dB. For instance, at $SNR = 12$ dB and $r_{HP} = 4/16$, the PSNR gain is almost 2 dB if the P-VpD-1/2 scheme is adopted for transmission instead of the P-VpD-1/4 scheme. However, this enhancement in PSNR increases the required data rates for transmission which is limited for many practical communication applications.

3) The results in Figure 6.15 show that the performance of P-MVC-1/2 scheme

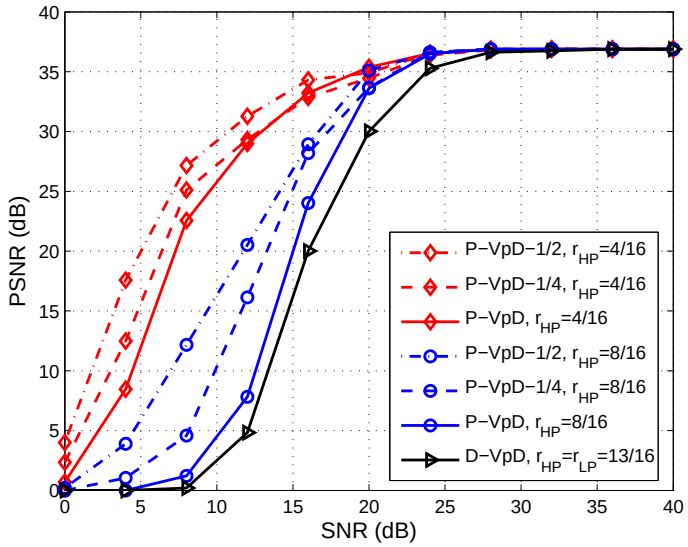

Figure 6.15: PSNR performance for the cooperative system at different coding rates, $r_{HP} = [4/16, 8/16, 13/16]$ and $r_{LP} = 13/16$ for PHN variance, $\sigma_\delta^2 = 10^{-5}$ rad^2 and 16-QAM modulation with M=4.

with r_{HP}=4/16 is better than other schemes at low SNRs, i.e., $SNR < 20$ dB, while its performance is close with other schemes, e.g., P-VpD-1/4 scheme with r_{HP}=8/16 and D-VpD scheme with r_{HP}=13/16 at moderate and high SNRs, i.e., $SNR > 20$ dB and $SNR < 28$ dB, respectively. Based on this observation, the $SNR = 20$ and 28 dB could be considered as SNR thresholds which can be exploited by the control units to switch the system from an UEP scheme to another. This approach maintains high video quality with the reduction of required data rates for transmission and the system complexity corresponding to the improvement of SNRs. Therefore, the control unit controls the system to adopt the following 3-D video protocol in order to achieve high video quality at different SNRs and achieve the lowest bandwidth and system complexity. This protocol is: the P-VpD-1/2 scheme, at channel coding rate, $r_{HP} = 4/16$ is adopted for transmission at low SNR, i.e., $SNR < 20$ dB, and the P-VpD-1/4 scheme at channel coding, r_{HP}=8/16 and the D-VpD scheme, at channel coding rate, r_{HP}=13/16 are adopted at moderate SNR, i.e., $SNR > 20$ dB and high SNR, i.e., $SNR > 28$ dB, respectively.

4) As shown Figure 6.15, by taking advantage of both estimation algorithms and

the UEP schemes based on packet partitioning and balancing the trade-off between complexity and performance, the proposed system can track different channel conditions, e.g., high and low SNRs and phase noise variances and Doppler rates, to achieve a specific system performance.

6.9 Conclusion

In this chapter, the joint estimation of channel parameters, PHNs, and CFOs in cooperative OFDM systems is addressed. The effects of PHNs and CFOs on the performance of relay networks for 3-D video application is also investigated. A new iterative estimator, that jointly estimates the unknown channel gains, PHNs, and CFOs, for both DF-and AF-relaying cooperative OFDM systems has been proposed. The proposed estimator is found to be computationally efficient since it estimates the desired parameters in a few iterations. Simulation results show that the performance of the proposed estimator is close to the derived HCRB at moderate-to-high SNRs. Next, an *iterative* algorithm for joint data detection and PHN mitigation is proposed for the OFDM data symbols. The proposed algorithm employs an EKF based approach to track the time-varying PHN parameters throughout the OFDM data symbols. Numerical results show that the proposed ECM based estimator and the iterative data detection algorithm enhance cooperative systems to outperform the existing algorithms and non-cooperative systems in terms of BER performance. Simulation results also demonstrate that the video system performance, in terms of PSNR, is very sensitive to the accuracy estimation of channel, PHNs and CFOs. In addition, PHNs and CFOs represent the main factors in determining the the system performance in terms of PSNR.

Chapter 7

Conclusions and Future Work

7.1 Summary

This thesis focuses on designing efficient three-dimensional (3-D) video transmission methods and signal processing algorithms to overcome the effects of error-prone wireless channels and impairments in the physical layer. These are unequal error protection (UEP), joint source-channel coding (JSCC), cooperative diversity technique, joint channel, phase noise (PHN) and carrier frequency offset (CFO) estimation, and data detection in the presence of PHN and CFO. An efficient UEP scheme based on video packet partitioning is presented in Chapter 3. A new JSCC algorithm for cross-layer optimization of the application, network, and physical layer is proposed in Chapter 4. Signal processing estimation and detection algorithms based on an expectation conditional maximization (ECM) and the extended Kalman filter (EKF) are proposed for orthogonal frequency division multiplexing (OFDM) systems (Chapter 5) and cooperative systems (Chapter 6).

This chapter summaries the major contributions drawn from this thesis and presents future research directions arising from this work.

7.2 Conclusions

In this thesis, the major contributions are presented and investigated in different chapters.

In Chapter 3, different representations of 3-D video sequences employed by source coding were investigated. The objective was to examine the representa-

tion that is most suitable for video transmission over a wireless channel. Next, an efficient UEP scheme based on video packet partitioning is proposed. The proposed UEP scheme is inspired by the advantage of the protection of video packets inside the 3-D video sequences. In addition, a new 3-D video transceiver is proposed. The proposed transceiver adopts various UEP schemes based on packet partitioning and achieves a trade-off between system complexity and performance using switching operations between the proposed UEP schemes. Two error-resilient video methods were combined to overcome the effects of noisy channels. These methods include resynchronization patterns and the use of the signal of channel state information (CSI) to control the control units in the source and the destination. Experimental results indicate that colour plus depth (VpD) is most suitable for video communication over error-prone channels. In addition, the proposed UEP schemes achieve significantly high peak signal-to-noise ratio (PSNR) at different signal-to-noise ratios (SNRs) over the wireless channel with the lowest possible bandwidth and system complexity. Simulation results also demonstrate that the conventional UEP scheme based on direct transmission of 3-D video sequences is outperformed by the proposed UEP scheme in terms of the quality of the received 3-D video sequences and the data rate required for the video transmission.

In Chapter 4, an algorithm to cross-layer optimization for 3-D video transmission over a cooperative relay systems was proposed. Procedures to estimate the end-to-end instantaneous SNR between the source-destination, and source-relay-destination were proposed. Next, the algorithm was proposed based on Lagrange multipliers. The proposed algorithm exploits the rate budget constraint and the estimated end-to-end instantaneous SNR to simultaneously assign the source code rates for the application layer, the number of high and low priority packets for the network layer, and channel code rates for the physical layer. Simulation results show that the existing algorithms are outperformed by the proposed JSCC algorithm in terms of PSNR. In addition, the proposed JSCC algorithm is found to be computationally more efficient as it can minimize the overall video distortion in a few iterations. Simulation results also show that the accurate estimation of an end-to-end instantaneous SNR can achieve a high PSNR performance of cooperative systems and has to be considered in the design of multimedia cooperative communication systems with feedback.

Bit errors in the data and video bitstreams may occur from noise within the channel or by impairments in the physical layer such as phase noise (PHN) and carrier frequency offset (CFO). These factors can degrade the bit-error-rate

(BER) and PSNR performance of the wireless system.

In Chapter 5, signal processing techniques were employed to mitigate the effects of PHN and CFO in OFDM systems. A computationally efficient expectation conditional maximization (ECM) based algorithm for joint estimation of channel, PHN, and CFO in OFDM systems was proposed. The hybrid Cramér-Rao lower bound (HCRB) was derived to evaluate the performance of the proposed estimator in terms of mean square error (MSE). Next, an iterative algorithm based on an extended Kalman filter (EKF) for joint data detection and PHN mitigation was proposed. Numerical results based on MSE and HCRB show that the proposed estimation algorithm outperforms the existing estimation algorithms at moderate-to-high SNRs for different PHN variances. The combination of the proposed estimation and detection algorithms is computationally more efficient compared to the existing algorithms and significantly improve the average uncoded and coded BER performance. The proposed estimation and data detection algorithms are also shown to coverage quickly, typically in 2-5 iterations.

The performance of cooperative communication systems is adversely impacted by synchronization impairments such as imperfect channel estimation, PHN and CFO. Therefore, reliable data and video applications are only possible if perfect synchronization, i.e., perfect estimation of channel, PHNs, and CFOs exists among the nodes of source, relays and destination. Since the ECM estimator, the iterative algorithm based on an EKF, and the UEP scheme based on video packet partitioning target the solutions to different problems (inter-carrier interference (ICI) mitigation and robustness), it is useful to exploit a combination of these methods to achieve robust 3-D video communications in asynchronous cooperative relaying network.

Chapter 6 advances the work in Chapter 5 by efficiently combining the ECM estimator and the iterative data detection algorithm based on an EKF with cooperative OFDM systems. The signal model for the estimation problem was outlined in detail and the ECM algorithm for the joint estimation of channel, PHNs, and CFOs in OFDM cooperative systems was also proposed. The HCRB expressions for cooperative OFDM systems were presented. Next, an iterative algorithm based on an EKF for joint data detection and PHN tracking was proposed. The impact of PHNs and CFOs on the performance of OFDM relay networks for 3-D video applications was also investigated. Simulation results show that the proposed estimator achieves MSE performance close to the derived HCRB at moderate-to-high SNR for different PHN variances. In addition, compared to the existing algorithms and non-cooperative systems, a significant improvement in

BER performance was achieved by the combination of the estimation and detection algorithms. Simulation results also demonstrate that the proposed combination of the estimation algorithms and UEP schemes based packet portioning can achieve high PSNR performance over a wide range of SNRs and different PHN variances. Furthermore, the accurate estimation of channel parameters, PHNs and CFOs is shown to have a dramatic impact on the performance and complexity of cooperative systems for video applications. Thus, these impairment factors must be considered in the design of multimedia cooperative communication systems.
Finally, the work in this thesis moves the research on cooperative systems based signal processing techniques a step forward. Efficient design of video transmission methods and signal processing algorithms that overcome the effects of error-prone wireless channels and the impairments in the physical layer for 3-D video applications is proposed. In this thesis, five different approaches were examined namely: UEP, JSCC, cooperative diversity, joint channel, PHN and CFO estimation, and data detection in the presence of PHN and CFO. The work in this thesis provides new insights into streaming 3-D video and is helpful for further study of channel estimation and the improvement of system complexity and PSNR for 3-D video delivery in the presence of PHNs and CFOs in future wireless networks such as 5G networks.

7.3 Future Work

Many future research directions or investigations in the area of cooperative systems based signal processing techniques for 3-D video transmission arise from the topics presented in this thesis.

- **UEP schemes based on video packet partitioning for H.265/HEVC standards:** Currently, there is intensive research activity pursuing 3-D video transmission using H.265/HEVC standards over wireless cooperative systems. The proposed UEP schemes based on video packet partitioning in this thesis are more efficient for use in error-prone channels. Thus, the principles and methodologies proposed in Chapter 3 can be used to develop H.265 standards. Similar to H.264 standards, the corrupted units of the network abstraction layer (NAL) in the video streams can be discarded and the remaining units can be decoded independently.

- **Error probability analysis of OFDM systems in the presence of channel, PHN and CFO estimation:** In Chapters 5 and 6, the same approach was followed as adopted in previous papers in the literature, which compared the BER performance of the proposed estimation and detection algorithms against the BER performance with perfect estimation of channel, PHN and CFO. This can be considered as a theoretical benchmark for the BER performance of the system. Following the works in Chapters 5 and 6, there is a need to obtain theoretical closed-form expressions for the BER of the system in the presence of channel, PHN, and CFO estimation.

- **Phase noise and carrier frequency offset synchronization with channel estimation in cooperative MIMO-OFDM networks and its application to 3-D video streaming:** The estimation and detection algorithms presented in this thesis only analyse to cooperative networks with a single antenna. The proposed estimation and detection algorithms in Chapters 5 and 6 can be modified for application in multi-input multi-output-orthogonal frequency division multiplexing (MIMO-OFDM) cooperative systems, since similar to single-input-single-output (SISO) systems, MIMO-OFDM cooperative systems are also affected by a multiplicative phase noise factor and CFOs. The proposed JSCC algorithm in Chapter 4 can be combined with the cooperative MIMO-OFDM networks to estimate the overall instantaneous SNR over the cooperative network. This combination is expected to achieve high PSNRs performance at different SNRs and PHN variances.

References

[1] A. Vetro, T. Wiegand, and G. J. Sullivan, "Overview of the Stereo and Multiview Video Coding Extensions of the H.264/MPEG-4 AVC Standard," *Proc. IEEE*, vol. 99, pp. 626–642, Apr. 2011.

[2] A. Gotchev, G. B. Akar, T. Capin, D. Strohmeier, and A. Boev, "Three-dimensional media for mobile devices," *Proc. IEEE*, vol. 99, pp. 708–741, 2011.

[3] A. Aksay, M. O. Bici, D. Bugdayci, A. Tikanmaki, A. Gotchev, and G. B. Aksar, "A study on the effect of MPE-FEC for 3D video broadcasting over DVB-H," in *Proc. International Mobile Multimedia Communications Conference*, London, UK, Dec 2009.

[4] H. Wang, L. Kondi, A. Luthra, and S. Ci, *4G wireless video communications*. New York, USA: John Wiley and Sons, 2009.

[5] M. Uysal, *Cooperative communications for improved wireless network transmission: framework for virtual antenna array applications*. Hershey, Pennsylvania, USA: IGI Global, 2010.

[6] C.-H. Kuo, C.-M. Wang, and J.-L. Lin, "Cooperative Wireless Broadcast for Scalable Video Coding," *IEEE Trans. Circuits Syst. Video Technol.*, vol. 21, no. 6, pp. 816–824, Jun. 2011.

[7] H. Xiao, Q. Dai, X. Ji, and W. Zhu, "A novel JSCC framework with diversity-multiplexing-coding gain tradeoff for scalable video transmission over cooperative MIMO," *IEEE Trans. Circuits Syst. Video Technol.*, vol. 20, pp. 994–1006, Jul 2010.

[8] L. Nuaymi, *WiMAX: technology for broadband wireless access*. New York, USA: John Wiley & Sons, 2007.

[9] Y. Zhang and H.-H. Chen, *Mobile wimax: toward broadband wireless metropolitan area networks.* New York, USA: Taylor & Francis Group, 2008.

[10] T. Paul and T. Ogunfunmi, "Wireless LAN comes of age: Understanding the IEEE 802.11n amendment," *IEEE Circuits Syst. Mag.*, vol. 8, no. 1, pp. 28–54, 2008.

[11] X. Zhu, A. Doufexi, and T. Kocak, "Throughput and coverage performance for IEEE 802.11ad millimeter-wave WPANs," in *Proc. IEEE Vehicular Technology Conference (VTC Spring)*, Budapest, Hungary, May 2011, pp. 1–5.

[12] A. Armada and M. Calvo, "Phase noise and sub-carrier spacing effects on the performance of an OFDM communication system," *IEEE Commun. Lett.*, vol. 2, no. 1, pp. 11 –13, Jan. 1998.

[13] A. Garcia Armada, "Understanding the effects of phase noise in orthogonal frequency division multiplexing (OFDM)," *IEEE Trans. Broadcast.*, vol. 47, no. 2, pp. 153 –159, Jun 2001.

[14] P. Rabiei, W. Namgoong, and N. Al-Dhahir, "On the performance of OFDM-based amplify-and-forward relay networks in the presence of phase noise," *IEEE Trans. Commun.*, vol. 59, no. 5, pp. 1458–1466, May 2011.

[15] R. Wang, H. Mehrpouyan, M. Tao, and Y. Hua, "Channel estimation, carrier recovery, and data detection in the presence of phase noise in OFDM relay systems," *submitted to IEEE Trans. Signal Proc.*, [Online]. Available: http://arxiv.org/pdf/1309.7564.pdf.

[16] C. T. E. R. Hewage, Z. Ahmad, S. Worrall, S. Dogan, and A. Kondoz, "Unequal error protection for backward compatible 3-D video transmission over wimax," in *Proc. IEEE International Symposium on Circuits and Systems*, Taipei, Taiwan, May 2009, pp. 125–128.

[17] B. W. Micallef and C. J. Debono, "An analysis on the effect of transmission errors in real-time H.264-MVC bit-streams," in *Proc. IEEE Mediterranean Electrotechnical Conference*, Valletta, Malta, Apr 2010, pp. 1215–1220.

[18] G. Tech, H. Brust, K. Mller, A. Aksay, and D. Bugdayci, "Development and optimization of coding algorithms for mobile 3DTV," Tampere University of Technology, Tech. Rep.

[19] C. Hellge, D. Gomez-Barquero, T. Schierl, and T. Wiegand, "Layer-aware forward error correction for mobile broadcast of layered media," *IEEE Trans. Multimedia*, vol. 13, no. 3, pp. 551 –562, June 2011.

[20] A. S. Tan, A. Aksay, C. Bilen, G. B. Akar, and E. Arikan, "Rate distortion optimized layered stereoscopic video streaming with raptor codes," in *Proc. Int. Packet Video Workshop*, Lausanne, Switzerland, Nov. 2007, pp. 98 –104.

[21] A. S. Tan, A. Aksay, G. B. Akar, and E. Arikan, "Rate-distortion optimization for stereoscopic video streaming with unequal error protection," *EURASIP J. Adv. Signal Process.*, vol. 2009, pp. 1–14, Jan. 2009.

[22] B. Kamolrat, W. Fernando, M. Mrak, and A. Kondoz, "Joint source and channel coding for 3D video with depth image - based rendering," *IEEE Trans. Consum. Electron.*, vol. 54, pp. 887–894, May 2008.

[23] D. D. Lin, R. Pacheco, T. J. Lim, and D. Hatzinakos, "Joint estimation of channel response, frequency offset, and phase noise in OFDM," *IEEE Trans. Signal Process.*, vol. 54, no. 9, pp. 3542–3554, Sept. 2006.

[24] J. Tao, J. Wu, and C. Xiao, "Estimation of channel transfer function and carrier frequency offset for OFDM systems with phase noise," *IEEE Trans. Veh. Technol.*, vol. 58, no. 8, pp. 4380–4387, Oct. 2009.

[25] R. Carvajal, J. C. Aguero, B. I. Godoy, and G. C. Goodwin, "EM-based maximum-likelihood channel estimation in multicarrier systems with phase distortion," *IEEE Trans. Veh. Technol.*, vol. 62, no. 1, pp. 152 –160, Jan. 2013.

[26] D. D. Lin and T. J. Lim, "The variational inference approach to joint data detection and phase noise estimation in OFDM," *IEEE Trans. Signal Process.*, vol. 55, no. 5, pp. 1862 –1874, May 2007.

[27] Y. Gong and X. Hong, "A new algorithm for OFDM joint data detection and phase noise cancellation," in *Proc. IEEE International Conference on Communications ICC*, Beijing, China, May 2008, pp. 636–640.

[28] Z. Zhang, W. Zhang, and C. Tellambura, "Cooperative OFDM channel estimation in the presence of frequency offsets," *IEEE Trans. Veh. Technol.*, vol. 58, no. 7, pp. 3447–3459, Sep. 2009.

[29] Q. Huang, M. Ghogho, J. Wei, and P. Ciblat, "Practical timing and frequency synchronization for OFDM-based cooperative systems," *IEEE Trans. Signal Process.*, vol. 58, no. 7, pp. 3706–3716, Jul. 2010.

[30] Y. Yao and X. Dong, "Multiple CFO mitigation in amplify-and-forward cooperative OFDM transmission," *IEEE Trans. Commun.*, vol. 60, no. 12, pp. 3844–3854, Dec. 2012.

[31] W. Lee, K. Noh, S. Kim, and J. Heo, "Efficient cooperative transmission for wireless 3D HD video transmission in 60GHz channel," *IEEE Trans. Consum. Electron.*, vol. 56, no. 4, pp. 2481–2488, November 2010.

[32] O. H. Salim and W. Xiang, "A novel unequal error protection scheme for 3-D video transmission over cooperative MIMO-OFDM systems," *EURASIP J. Wirel. Commun. Netw.*, vol. 2012:269, no. doi:10.1186/1687-1499-2012-269, Aug. 2012.

[33] O. H. Salim, W. Xiang, and J. Leis, "An efficient unequal error protection scheme for 3-D video transmission," in *Proc. IEEE Wireless Communications and Networking Conference WCNC*, Shanghai, China, Apr. 2013, pp. 4077–4082.

[34] O. H. Salim and W. Xiang, "Prioritized 3-D video transmission over cooperative MIMO-OFDM systems," in *Proc. IEEE International Conference on Digital Image Computing Techniques and Applications (DICTA)*, Noosa, QLD, Australia, Dec. 2011, pp. 225 –230.

[35] O. H. Salim, W. Xiang, and J. Leis, "Error-resilient video transmission for 3-D signal over cooperative-MIMO system," in *European Signal Processing Conference (EUSIPCO)*, Barcelona, Spain, Aug. 2011, pp. 1372–1376.

[36] H.264/AVC reference software, JM version 13.2. [Online]. Available: http://iphome.hhi.de/suehring/tml.

[37] A. A. C. Bilen and G. B. Akar, "A multi-view video codec based on H.264," in *Proc. IEEE image processing conference(ICIP)*, Atlanta, Ga, USA, Oct 2006, pp. 541–544.

[38] O. H. Salim, W. Xiang, J. Leis, and L. Cao, "Cross-layer optimization for 3-D video transmission over cooperative relay systems," *Signal Processing-Image Communication*, 29 (2014), pp. 1102-1120, doi: 10.1016/j.image.2014.08.003.

[39] O. H. Salim, A. A. Nasir, H. Mehrpouyan, W. Xiang, S. Durrani, and R. A. Kennedy, "Channel, phase noise and frequency offset in OFDM systems: Joint estimation, data detection and hybrid Cramér-Rao lower bound," *IEEE Trans. Commun.*, vol. 62, no. 9, pp. 3311–3325, Sep. 2014.

[40] O. H. Salim, A. A. Nasir, H. Mehrpouyan, and W. Xiang, "Phase noise and carrier frequency offset in OFDM systems: Joint estimation and hybrid Cramér-Rao lower bound," in *IEEE International Workshop on Signal Processing Advances in Wireless Communications (SPAWC)*, Darmstadt, Germany, June 2013, pp. 649–653.

[41] O. H. Salim, A. A. Nasir, W. Xiang, and R. A. Kennedy, "Joint channel, phase noise, and carrier frequency offset estimation in cooperative OFDM systems," in *International Conference on Communications (ICC)*, Sydney, NSW, Australia, June 2014, pp. 4384–4389.

[42] H. Brust, A. Smolic, K. Mueller, G. Tech, and T. Wiegand, "Mixed resolution coding of stereoscopic video for mobile devices," in *Proc. IEEE The True Vision - Capture, Transmission and Display of 3D Video*, Potsdam, Germany, May 2009, pp. 1–4.

[43] C. Fehn, "Depth-image-based rendering (DIBR), compression and transmission for a new approach on 3D-TV," in *Proc. Stereoscopic Displays and Virtual Reality Systems (SPIC)*, San Jose, CA, USA, Jan. 2004, pp. 93–104.

[44] I. E. Richardson, *The H.264 advanced video compression standard.* New York, USA: John Wiley and Sons, 2010.

[45] T. Wiegand, G. J. Sullivan, G. Bjontegaard, and A. Luthra, "Overview of the H.264/AVC video coding standard," *IEEE Trans. Circuits Syst. Video Technol.*, vol. 13, no. 7, pp. 560–576, Jul. 2003.

[46] K. Muller, H. Schwarz, D. Marpe, C. Bartnik, S. Bosse, H. Brust, T. Hinz, H. Lakshman, P. Merkle, F. H. Rhee, G. Tech, M. Winken, and T. Wiegand, "3D High-Efficiency Video Coding for Multi-View Video and Depth Data," *IEEE Trans. Image Process.*, vol. 22, no. 9, pp. 3366–3378, Sep. 2013.

[47] G. J. Sullivan, J.-R. Ohm, W.-J. Han, and T. Wiegand, "Overview of the High Efficiency Video Coding (HEVC) Standard," *IEEE Trans. Circuits Syst. Video Technol.*, vol. 22, no. 12, pp. 1649–1668, Dec. 2012.

[48] S. Kumar, L. Xu, M. Mandal, and S. Panchanathan, "Error resiliency schemes in H.264/AVC standard," *Visual Communication and Image Representation*, vol. 17, pp. 425–450, Apr. 2006.

[49] Nasruminallah, M. F. U. Butt, S. X. Ng, and L. Hanzo, "H.264 wireless video telephony using iteratively-detected binary self-concatenated coding," in *Proc. IEEE Vehicular Technology Conference (VTC Spring)*, Taipei, Taiwan, May 2010, pp. 1–5.

[50] G.-H. Yang, D. Shen, , and V. O. Li, "UEP for video transmission in space-time coded OFDM systems," in *Proc. IEEE Annual Joint Conference of the Computer and Communications Societies*, Hong Kong, China, Mar 2010, pp. 12001210,.

[51] J.-C. Wu, C.-M. Li, and K.-H. Chen, *Digital Video.* Coroatia: InTech, 2010.

[52] Y. Liu, S. Ci, H. Tang, and Y. Ye, "Application-adapted mobile 3D video coding and streaming - a survey," *3D Research Journal, Springer*, vol. 3, no. 1, 2012.

[53] I. E. Telatar, "Capacity of multi-antenna Gaussian channels," Bell lab, Tech. Rep.

[54] G. J. Foschini and M. J. Gans, "On limits of wireless communications in a fading environment when using multiple antennas," *Wireless Personal Communications*, vol. 6, p. 311335, 1998.

[55] S. M. Alamouti, "A simple transmit diversity technique for wireless communications," *IEEE J. Sel. Areas Commun.*, vol. 16, pp. 1451–1458, Oct. 1998.

[56] V. Tarokh, H. Jafarkhani, and A. R. Calderbank, "Space-time block coding for wireless communications: performance results," *IEEE J. Sel. Areas Commun.*, vol. 17, no. 3, pp. 451–460, Mar 1999.

[57] A. Sendonaris, E. Erkip, and B. Aazhang, "User cooperation diversity, Part I and Part II," *IEEE Trans. Commun.*, vol. 51, no. 11, pp. 1927–1948, Nov. 2003.

[58] N. J. Laneman, D. N. Tse, and G. W. Wornell, "Cooperative diversity in wireless networks: Efficient protocols and outage behavior," *IEEE Trans. Inf. Theory*, vol. 50, no. 3, pp. 3062–3080, Dec. 2004.

[59] N. Rahnavard and F. Fekri, "Unequal error protection using low-density parity-check codes," in *Proc. IEEE Int. Symp. Inf. Theory*, Geneva, Switzerland, Jun 2004, p. 449.

[60] Y. Jing and B. Hassibi, "Cooperative diversity in wireless relay networks with multiple-antenna nodes," in *International Symposium on Information ISIT*, Sept. 2005, pp. 815–819.

[61] A. Bletsas, A. Khisti, D. Reed, and A. Lippman, "A simple Cooperative diversity method based on network path selection," *IEEE J. Sel. Areas Commun.*, vol. 24, pp. 659 – 672, March 2006.

[62] A. S. Ibrahim, A. K. Sadek, W. Su, and K. J. R. Liu, "Cooperative communications with relay-selection: when to cooperate and whom to cooperate with?" *IEEE Trans. Wireless Commun.*, vol. 7, pp. 2814–2827, Jul. 2008.

[63] D. S. Michalopoulos and G. K. Karagiannidis, "Performance analysis of single relay selection in rayleigh fading," *IEEE Trans. Wireless Commun.*, vol. 7, pp. 3718–3724, October 2008.

[64] Y. Jing and H. Jafarkhani, "Single and multiple relay selection schemes and their achievable diversity orders," *IEEE Trans. Wireless Commun.*, vol. 7, pp. 1414–1423, March 2009.

[65] D. S. Michalopoulos, A. S. Lioumpas, G. K. Karagiannidis, and R. Schober, "Selective Cooperative Relaying over Time-Varying Channels," *IEEE Trans. Commun.*, vol. 58, pp. 2402–2412, Aug 2010.

[66] L. Hanzo and C. H. Wong, *Adaptive Wireless Transceivers: Turbo-Coded, Turbo-Equalised and Space-Time Coded TDMA, CDMA, MC-CDMA and OFDM Systems*. New York, USA: John Wiley and Sons, Inc, 2002.

[67] K. Fazel and S. Kaiser, *Multi-carrier and spread spectrum systems from OFDM and MC-CDMA to LTE and WiMAX.* Chichester, United Kingdom: Wiley and Sons Ltd, 2008.

[68] T. Pollet, M. V. Bladel, and M. Moeneclaey, "BER sensitivity of OFDM systems to carrier frequency offset and wiener phase noise," *IEEE Trans. Commun.*, vol. 43, no. 234, pp. 191 –193, Feb/Mar/Apr 1995.

[69] T. Schenk, *RF Imperfections in High-rate Wireless Systems.* Springer, 2008.

[70] H. Mehrpouyan, M. R. Khanzadi, M. Matthaiou, A. M. Sayeed, R. Schober, and Y. Hua, "Improving bandwidth efficiency in E-band communication systems," *IEEE Commun. Mag.*, vol. 52, no. 3, pp. 121–128, March 2014.

[71] A. M. A. Demir and J. Roychowdhury, "Phase noise in oscillators: A unifying theory and numerical methods for characterization," *IEEE Trans. Biomed. Circuits Syst.*, vol. 47, pp. 655–674, May 2000.

[72] D. Lin, R. Pacheco, T. J. Lim, and D. Hatzinakos, "Optimal OFDM channel estimation with carrier frequency offset and phase noise," in *Proc. IEEE (WCNC)*, Apr 2006.

[73] P. Murphy, "Design, implementation and characterization of a cooperative communications system," Ph.D. dissertation, Rice University, Houston, Texas, Dec. 2010.

[74] L. Tomba, "On the effect of Wiener phase noise in OFDM systems," *IEEE Trans. Commun.*, vol. 46, no. 5, pp. 580–583, May 1998.

[75] S. Wu and Y. Bar-Ness, "OFDM systems in the presence of phase noise: consequences and solutions," *IEEE Trans. Commun.*, vol. 52, no. 11, pp. 1988–1996, Nov. 2004.

[76] D. Petrovi, W. Rave, and G. Fettweis, "Phase noise suppression in OFDM including intercarrier interference," in *Proc. Int. OFDM Workshop*, 2003, pp. 219–224.

[77] ——, "Phase noise suppression in OFDM using Kalman filter," in *Proc. WPMC*, 2003.

[78] S. M. Kay, *Fundamentals of Statistical Signal Processing, Estimation Theory*. Signal Processing Series: Prentice Hall, 1993.

[79] H. L. van Trees and K. L. Bell, *Bayesian bounds for parameter estimation and nonlinear filtering/tracking*. New York, USA: John Wiley and Sons, 2007.

[80] S. Bay, B. Geller, A. Renaux, J. Barbot, and J. Brossier, "On the hybrid Cramér-Rao bound and its application to dynamical phase estimation," *IEEE Signal Process. Lett.*, vol. 15, pp. 453–456, 2008.

[81] T. Szigeti and C. Hattingh, "End-to-End QoS Network Design: Quality of Service in LANs, WANs, and VPNs (Networking Technology)," Cisco Press, Tech. Rep.

[82] Y. Li, "A Quality Guaranteed Video Dissemination Protocol over Urban Vehicular Ad Hoc Networks," Ph.D. dissertation, University of Ottawa, Ottawa, Canada, 2014.

[83] J.-C. Wu, C.-M. Li, and K.-H. Chen, "Adaptive digital video transmission MIMO systems," in *Proc. IEEE Intelligent Information Technology Application (IITA)*, Shanghai, China, Jan. 2008, pp. 653– 57.

[84] D. Song and C. W. Chen, "Scalable H.264/AVC video transmission over mimo wireless systems with adaptive channel selection based on partial channel information," *IEEE Trans. Circuits Syst. Video Technol.*, vol. 17, pp. 1218–1226, Sep. 2007.

[85] ——, "Maximum-throughput delivery of SVC-based video over MIMO systems with time-varying channel capacity," *Visual Communication and Image Representation*, vol. 19, pp. 520–528, Dec. 2008.

[86] H. Zheng, C. Ru, W. Chen, and L. Yu, "Video transmission over MIMO-OFDM system: MDC and space-time coding-based approaches," *Advances in Multimedia*, vol. 2007, no. 1, pp. Artical ID 61 491, 8 pages, 2007. doi:10.1155/2007/61 491, Jan.

[87] C. H. Kuo, C. S. Kim, and C. C. J. Kuo, "Robust video transmission over wideband wireless channel using space-time coded OFDM systems," in *Proc. IEEE Wireless Communications and Networking (WCNC)*, Orlando, Florida USA, Aug. 2002, pp. 931–936.

[88] S. Lin, A. Stefanov, and Y. Wang, "On the performance of space-time block-coded MIMO video communications," *IEEE Transactions on Vehicular Technology*, vol. 56, no. 3, pp. 1223 –1229, may 2007.

[89] G. B. Akar, A. M. Tekalp, C. Fehn, and M. R. Civanlar, "Transport methods in 3DTV a survey," *IEEE Trans. Circuits Syst. Video Technol.*, vol. 17, pp. 1622–1630, Nov. 2007.

[90] C. Hewage, S. Worrall, S. Dogan, H. Kodikaraarachchi, and A. M. Kondoz, "Stereoscopic TV over IP," in *4th European Conference on Visual Media Production (IETCVMP)*, London, May 2007, pp. 1 – 7.

[91] C. Hewage, S. T. Worrall, S. Dogan, S. Villette, and A. M. Kondoz, "Quality evaluation of color plus depth map-based stereoscopic video," *IEEE J. Sel. Topics Signal Process.*, vol. 3, pp. 304–318, 2009.

[92] T. J. Richardson and R. L. Urbanke, "Efficient encoding of low-density parity-check codes," *IEEE Trans. Inf. Theory*, vol. 47, pp. 638 – 656, Feb. 2001.

[93] A. Smolic, K. Mueller, P. Merkle, P. Kauff, and T. Wiegand, "An overview of available and emerging 3D video formats and depth enhanced stereo as efficient generic solution," in *Proc. IEEE Picture Coding Symposium*, Chicago, USA, May 2009, pp. 1–4.

[94] K. Stuhlmuller, N. Farber, M. Link, and B. Girod, "Analysis of video transmission over lossy channels," *IEEE J. Sel. Areas Commun.*, vol. 18, pp. 1012 – 1032, Jun. 2000.

[95] Mobile 3DTV. [Online]. Available: http://sp.cs.tut.fi/mobile3dtv/video-plus-depth/

[96] S. J. Johnson. Introducing low-density parity-check codes. [Online]. Available: http://sigpromu.org/sarah/SJohnsonLDPCintro.pdf

[97] A. Abdaoui, S. S. Ikki, M. H. Ahmed, and E. Chaatelet, "On the performance analysis of a MIMO-relaying scheme with space-time block codes," *IEEE Trans. Veh. Technol.*, vol. 59, pp. 3604 – 3609, May 2010.

[98] Z. Guan, L. Ding, T. Melodia, and D. Yuan, "On the effect of cooperative relaying on the performance of video streaming applications in cognitive radio networks," in *Proc. IEEE International Conference on Communications (ICC)*, June 2011, pp. 1–6.

[99] Z. Guan, T. Melodia, and D. Yuan, "Jointly optimal rate control and relay selection for cooperative wireless video streaming," *IEEE/ACM Trans. Netw.*, vol. 21, no. 4, pp. 1173–1186, Aug. 2013.

[100] A. Liu and V. K. N. Lau, "Cache-enabled opportunistic cooperative MIMO for video streaming in wireless systems," *IEEE Trans. Signal Process.*, vol. 62, no. 2, pp. 390–402, Jan. 2014.

[101] E. Biglieri, G. Caire, and G. Taricco, "Limiting performance of block-fading channels with multiple antennas," *IEEE Trans. Inf. Theory*, vol. 47, pp. 1273–1289, May 2001.

[102] L. Dong and A. P. Petropulu, "A multichannel cooperative scheme for wireless networks and performance characterization," in *Proc. IEEE International Conference on Acoustics, Speech and Signal Processing (ICASSP)*, Honolulu, Hawaii, U.S.A, Apr. 2007, pp. III–501–III–504.

[103] M. Mardani, J. S. Harsini, and F. Lahouti, "Cross-layer link adaptation design for relay channels with cooperative ARQ protocol," in *Proc. IEEE Workshop on Signal Processing Advances in Wireless Communications (SPAWC)*, Perugia, Italy, Jun. 2009, pp. 504–508.

[104] P. H. Tan, C. K. Ho, and S. Sun, "Joint network-channel code design for block fading cooperative multiple access channel," in *Proc. IEEE Information Theory Workshop (ITW)*, Dublin, Germany, Aug. 2010, pp. 1–5.

[105] S. Boumard, "Novel noise variance and SNR estimation algorithm for wireless MIMO OFDM systems," in *Proc. IEEE Global Telecommunications Conference (GLOBECOM)*, Dec. 2003, pp. 1330–1334.

[106] F. Jiao, R. Guangliang, and Z. Zhe, "A New noise variance and post detection SNR estimation method for MIMO OFDM systems," in *Proc. IEEE International Conference on Communication Technology Proceedings (ICCT)*, Nov. 2008, p. 179182.

[107] M. Zivkovic and R. Mathar, "Preamble-based SNR estimation algorithm for wireless MIMO OFDM systems," in *Proc. IEEE International Symposium on Wireless Communication Systems (ISWCS)*, Siena, Italy, Sep 2009, pp. 96–100.

[108] M.-H. Lu, P. Steenkiste, and T. Chen, "Robust wireless video streaming using hybrid spatial/temporal retransmission," *IEEE J. Sel. Areas Commun.*, vol. 28, no. 3, pp. 476–487, Apr 2010.

[109] B. Hassani and E. Hinton, "A review of homogenization and topology optimization III-topology optimization using optimality criteria," *Computers and Structures*, vol. 69, pp. 739–756, 1998.

[110] M. P. Saka and E. S. Kameshki, "Optimum design of nonlinear elastic framed domes," *Advances in Engineering Software*, vol. 29, no. 79, pp. 519–528, 1998.

[111] P. Chevillat, D. Maiwald, and G. Ungerboeck, "Rapid training of a voiceband data-modem receiver employing an equalizer with fractional-T spaced coefficients," *IEEE Trans. Commun.*, vol. 35, no. 9, pp. 869–876, Sep. 1987.

[112] T. Schmidl and D. Cox, "Robust frequency and timing synchronization for OFDM," *IEEE Trans. Commun.*, vol. 45, no. 12, pp. 1613–1621, Dec. 1997.

[113] A. Chorti and M. Brookes, "A spectral model for RF oscillators with power-law phase noise," *IEEE Trans. Circuits Syst.*, vol. 53, no. 9, pp. 1989–1999, Sep. 2006.

[114] D. Petrovic, W. Rave, and G. Fettweis, "Effects of phase noise on OFDM systems with and without PLL: Characterization and compensation," *IEEE Trans. Commun.*, vol. 55, no. 8, pp. 1607–1616, Aug. 2007.

[115] J.-H. Lee, J. C. Han, and S.-C. Kim, "Joint carrier frequency synchronization and channel estimation for OFDM systems via the EM algorithm," *IEEE Trans. Veh. Technol.*, vol. 55, no. 1, pp. 167–172, Jan. 2006.

[116] F. Septier, Y. Delignon, A. Menhaj-Rivenq, and C. Garnier, "Monte carlo methods for channel, phase noise, and frequency offset estimation with unknown noise variances in OFDM systems," *IEEE Trans. Signal Process.*, vol. 56, no. 8, pp. 3613–3626, Aug. 2008.

[117] P. Rabiei, W. Namgoong, and N. Al-Dhahir, "A non-iterative technique for phase noise ICI mitigation in packet-based OFDM systems," *IEEE Trans. Signal Process.*, vol. 58, no. 11, pp. 5945–5950, Nov. 2010.

[118] S. Wu and Y. Bar-Ness, "A phase noise suppression algorithm for OFDM-based WLANs," *IEEE Commun. Lett.*, vol. 6, no. 12, pp. 535–537, Dec. 2002.

[119] F. Munier, T. Eriksson, and A. Svensson, "An ICI reduction scheme for OFDM system with phase noise over fading channels," *IEEE Trans. Commun.*, vol. 56, no. 12, pp. 1119–1126, Jul. 2008.

[120] E. P. Simon, L. Ros, H. Hijazi, and M. Ghogho, "Joint carrier frequency offset and channel estimation for OFDM systems via the EM algorithm in the presence of very high mobility," *IEEE Trans. Signal Process.*, vol. 60, no. 2, pp. 754 –765, Feb. 2012.

[121] X. L. Meng and D. B. Rubin, "Maximum likelihood estimation via the ECM algorithm: A general framework," *Biometrika*, vol. 8, no. 2, pp. 267–278, Jun. 1993.

[122] G. J. McLachlan and T. Krishnan, *The EM Algorithm and Extensions.* Hoboken, NJ: Wiley, 2008.

[123] T. A. Fesler and A. O. Hero, "Space-alternating generalized expectation maximization algorithm," *IEEE Trans. Signal Process.*, vol. 42, no. 10, pp. 2664–2677, Oct 1994.

[124] H. Mehrpouyan and S. D. Blostein, "Bounds and algorithms for multiple frequency offset estimation in cooperative networks," *IEEE Trans. Wireless Commun.*, vol. 10, no. 4, p. 13001311, Apr. 2011.

[125] H. Mehrpouyan, A. A. Nasir, S. D. Blostein, T. Eriksson, G. K. Karagiannidis, and T. Svensson, "Joint estimation of channel and oscillator phase noise in MIMO systems," *IEEE Trans. Signal Process.*, vol. 60, no. 9, pp. 4790–4807, Sept. 2012.

[126] A. A. Nasir, H. Mehrpouyan, R. Schober, and Y. Hua, "Phase noise in MIMO systems: Bayesian Cramér-Rao bounds and soft-input estimation," *IEEE Trans. Signal Process.*, in press.

[127] A. A. Nasir, S. Durrani, and R. A. Kennedy, "Achieving Cooperative Diversity with Multiple Frequency Offset Estimation," in *Proc. IEEE International Conference on Signal Processing and Communication Systems (ICSPCS)*, Honolulu, USA, Dec. 2011, pp. 12–14.

[128] S. Bay, C. Herzet, J.-M. Brossier, J.-P. Barbot, and B. Geller, "Analytic and asymptotic analysis of Bayesian Cramér-Rao bound for dynamical phase offset estimation," *IEEE Trans. Signal Process.*, vol. 56, no. 1, pp. 61 –70, Jan. 2008.

Appendix A

Proofs

A.1 Derivation of the HCRB

The hybrid information matrix $\mathbf{B}$ can be written as [79, pp. 1-85]

$$\mathbf{B} = \boldsymbol{\Xi}_D + \boldsymbol{\Xi}_P, \tag{A.1}$$

where $\boldsymbol{\Xi}_D \triangleq \mathbb{E}_{\boldsymbol{\theta}}\left[\boldsymbol{\Psi}(\boldsymbol{\theta}, \Re\{\mathbf{h}\}, \Im\{\mathbf{h}\}, \epsilon)\right]$ with $\boldsymbol{\Psi}(\boldsymbol{\theta}, \Re\{\mathbf{h}\}, \Im\{\mathbf{h}\}, \epsilon) \triangleq \mathbb{E}_{\mathbf{r}|\boldsymbol{\theta}, \Re\{\mathbf{h}\}, \Im\{\mathbf{h}\}, \epsilon}\big[-\Delta^{\boldsymbol{\lambda}}_{\boldsymbol{\lambda}} \log p(\mathbf{r}|\boldsymbol{\theta}, \Re\{\mathbf{h}\},\ \Im\{\mathbf{h}\}, \epsilon)|, \Re\{\mathbf{h}\}, \Im\{\mathbf{h}\}, \epsilon\big]$ denoting the Fisher's information matrix (FIM) and $\boldsymbol{\Xi}_P \triangleq \mathbb{E}_{\boldsymbol{\theta}|, \Re\{\mathbf{h}\}, \Im\{\mathbf{h}\}, \epsilon}\big[-\Delta^{\boldsymbol{\lambda}}_{\boldsymbol{\lambda}} \log\ p(\boldsymbol{\theta}|, \Re\{\mathbf{h}\}, \Im\{\mathbf{h}\}, \epsilon)|, \epsilon\big]$ is the prior information matrix with $p(\boldsymbol{\theta}|\mathbf{h}, \boldsymbol{\epsilon})$ denoting the prior distribution of PHN vector given the CIR and CFO. Thus, expressions for matrices $\boldsymbol{\Xi}_D$ and $\boldsymbol{\Xi}_P$ can be obtained.

A.1.1 Computation of $\boldsymbol{\Xi}_D \triangleq \mathbb{E}_{\boldsymbol{\theta}}\left[\boldsymbol{\Psi}(\boldsymbol{\theta}, \Re\{\mathbf{h}\}, \Im\{\mathbf{h}\}, \epsilon)\right]$

To compute FIM, first, the likelihood function $p(\mathbf{r}|\boldsymbol{\theta}, \Re\{\mathbf{h}\}, \Im\{\mathbf{h}\}, \epsilon)$ is given by

$$p(\mathbf{r}|\boldsymbol{\theta}, \Re\{\mathbf{h}\}, \Im\{\mathbf{h}\}, \epsilon) = \mathrm{C} \exp\left[\frac{-1}{\sigma_w^2}(\mathbf{r} - \boldsymbol{\mu})^H(\mathbf{r} - \boldsymbol{\mu})\right], \tag{A.2}$$

where $\mathrm{C} \triangleq (\pi\sigma_w^2)^{-N}$. Given $\boldsymbol{\theta}$, $\Re\{\mathbf{h}\}$, $\Im\{\mathbf{h}\}$, and ϵ, $\mathbf{r}$ is a complex Gaussian vector with mean vector $\boldsymbol{\mu} = \mathbf{EPF}^H\mathbf{DWh}$ and covariance matrix $\sigma_w^2\mathbf{I}_N$. The FIM, $\boldsymbol{\Psi}(\boldsymbol{\theta}, \Re\{\mathbf{h}\}, \Im\{\mathbf{h}\}, \epsilon)$, will be $(N+2L)\times(N+2L)$ matrix for joint estimation of $(N-1)$ PHN parameters $\boldsymbol{\theta}$, $2L$ channel parameters $\Re\{\mathbf{h}\}$ and $\Im\{\mathbf{h}\}$ and one CFO parameter ϵ. Using (A.2), the (i,j)th entry of $\boldsymbol{\Psi}$ can be written as [78]

$$[\boldsymbol{\Psi}]_{i,j} = \frac{2}{\sigma_w^2}\Re\left\{\frac{\partial \boldsymbol{\mu}^H}{\partial \boldsymbol{\lambda}_i}\frac{\partial \boldsymbol{\mu}}{\partial \boldsymbol{\lambda}_j}\right\}, \tag{A.3}$$

where

$$\frac{\partial \boldsymbol{\mu}^H}{\partial \boldsymbol{\lambda}_i} = \begin{cases} \text{diag}(\mathbf{E}\mathbf{F}^H\mathbf{D}\mathbf{W}^H\mathbf{h})\mathbf{a}_i, & i = 1,\ldots,N-1 \;\; (\boldsymbol{\lambda}_i = \theta_i) \\ \mathbf{E}\mathbf{P}\mathbf{F}^H\mathbf{D}\mathbf{W}^H\mathbf{e}_{i-(N-1)}, & i = N,\ldots,N+L-1 \;\; (\boldsymbol{\lambda}_i = \Re\{h_{i-N}\}) \\ j\mathbf{E}\mathbf{P}\mathbf{F}^H\mathbf{D}\mathbf{W}^H\mathbf{e}_{i-(N+L-1)}, & i = N+L,\ldots,N+2L-1 \;\; (\boldsymbol{\lambda}_i = \Im\{h_{i-(N+L)}\}) \\ j\sqrt{\mathbf{M}}\mathbf{E}\mathbf{P}\mathbf{F}^H\mathbf{D}\mathbf{W}^H\mathbf{h}, & i = N+2L \;\; (\boldsymbol{\lambda}_i = \epsilon) \end{cases} \tag{A.4}$$

$\mathbf{a}_i = [0, 0_{1\times i-1}, je^{j\theta_i}, 0_{1\times N-i}]^T$ for $i = 1,\ldots,N-1$, $\mathbf{e}_l = [0_{1\times l-1}, 1, 0_{1\times L-1}]^T$ for $l = 1,\ldots,L$, and $\mathbf{M} \triangleq \text{diag}\big(\big[(2\pi\frac{0}{N})^2, (2\pi\frac{1}{N})^2, \ldots, (2\pi\frac{N-1}{N})^2\big]^T\big)$.

Substituting (A.4) into (A.5), the matrix $\boldsymbol{\Xi}_D$ is obtained as

$$\boldsymbol{\Xi}_D = \frac{2}{\sigma_w^2}\Re\left\{\begin{bmatrix} \bar{\mathbf{Q}}_1^H\bar{\mathbf{Q}}_1 & -j\bar{\mathbf{Q}}_1^H\bar{\mathbf{Q}}_2 & \bar{\mathbf{Q}}_1^H\bar{\mathbf{Q}}_2 & \bar{\mathbf{Q}}_4^H\bar{\mathbf{q}}_3 \\ j\bar{\mathbf{Q}}_2^H\bar{\mathbf{Q}}_1 & \mathbf{Q}_2^H\mathbf{Q}_2 & j\mathbf{Q}_2^H\mathbf{Q}_2 & j\mathbf{Q}_2^H\mathbf{q}_5 \\ \bar{\mathbf{Q}}_2^H\bar{\mathbf{Q}}_1 & -j\mathbf{Q}_2^H\mathbf{Q}_2 & \mathbf{Q}_2^H\mathbf{Q}_2 & \mathbf{Q}_2^H\mathbf{q}_5 \\ \bar{\mathbf{q}}_3^H\bar{\mathbf{Q}}_4 & -j\bar{\mathbf{q}}_5^H\mathbf{Q}_2 & \mathbf{q}_5^H\mathbf{Q}_2 & \mathbf{q}_5^H\mathbf{q}_5 \end{bmatrix}\right\}, \tag{A.5}$$

where $\mathbf{Q}_1 = \text{diag}(\mathbf{F}^H\mathbf{D}\mathbf{W}\mathbf{h})$, $\bar{\mathbf{Q}}_1 = \mathbf{Q}_1(2:N, 2:N)$, $\mathbf{Q}_2 = \mathbf{F}^H\mathbf{D}\mathbf{W}$, $\bar{\mathbf{Q}}_2 = \mathbf{Q}_2(2:N, 1:L)$, $\mathbf{Q}_4 = \text{diag}(\sqrt{\mathbf{M}}\mathbf{F}^H\mathbf{D}\mathbf{W}\mathbf{h})$, $\bar{\mathbf{Q}}_4 = \mathbf{Q}_4(2:N, 2:N)$, $\mathbf{q}_3 = \mathbf{F}^H\mathbf{D}\mathbf{W}\mathbf{h}$, and $\bar{\mathbf{q}}_3 = \mathbf{q}_3(2:N)$, and $\mathbf{q}_5 = \sqrt{\mathbf{M}}\mathbf{F}^H\mathbf{D}\mathbf{W}\mathbf{h}$. Note that the elements of $\boldsymbol{\theta}$ get canceled by their conjugates, hence, there is no need to calculate the explicit expectation of $\boldsymbol{\Psi}$ over $\boldsymbol{\theta}$.

A.1.2 Computation of $\boldsymbol{\Xi}_P \triangleq \mathbb{E}_{\boldsymbol{\theta}|\mathbf{h},\epsilon}\left[-\Delta_{\boldsymbol{\lambda}}^{\boldsymbol{\lambda}}\log p(\boldsymbol{\theta}|\mathbf{h},\epsilon)|\mathbf{h},\epsilon\right]$

The second factor in HIM, defined in (A.1), can be written as:

$$\boldsymbol{\Xi}_P = \mathbb{E}_{\boldsymbol{\theta}|\mathbf{h},\epsilon}\left[-\Delta_{\boldsymbol{\lambda}}^{\boldsymbol{\lambda}}\log p(\boldsymbol{\theta}|\mathbf{h},\epsilon)|\epsilon\right] \triangleq \begin{bmatrix} \boldsymbol{\Xi}_{P_{11}} & \boldsymbol{\Xi}_{P_{12}} & \boldsymbol{\Xi}_{P_{13}} & \boldsymbol{\xi}_{P_{14}} \\ \boldsymbol{\Xi}_{P_{21}} & \boldsymbol{\Xi}_{P_{22}} & \boldsymbol{\Xi}_{P_{23}} & \boldsymbol{\xi}_{P_{24}} \\ \boldsymbol{\Xi}_{P_{31}} & \boldsymbol{\Xi}_{P_{32}} & \boldsymbol{\Xi}_{P_{33}} & \boldsymbol{\xi}_{P_{34}} \\ \boldsymbol{\xi}_{P_{41}} & \boldsymbol{\xi}_{P_{42}} & \boldsymbol{\xi}_{P_{43}} & \boldsymbol{\xi}_{P_{44}} \end{bmatrix} =$$

$$\begin{bmatrix} \mathbb{E}_{\boldsymbol{\theta}}\left[-\Delta_{\boldsymbol{\theta}}^{\boldsymbol{\theta}}\log p(\boldsymbol{\theta})\right] & \mathbb{E}_{\boldsymbol{\theta}}\left[-\Delta_{\boldsymbol{\theta}}^{\Re\{\mathbf{h}\}}\log p(\boldsymbol{\theta})\right] & \mathbb{E}_{\boldsymbol{\theta}}\left[-\Delta_{\boldsymbol{\theta}}^{\Im\{\mathbf{h}\}}\log p(\boldsymbol{\theta})\right] & \mathbb{E}_{\boldsymbol{\theta}}\left[-\Delta_{\boldsymbol{\theta}}^{\epsilon}\log p(\boldsymbol{\theta})\right] \\ \mathbb{E}_{\boldsymbol{\theta}}\left[-\Delta_{\Re\{\mathbf{h}\}}^{\boldsymbol{\theta}}\log p(\boldsymbol{\theta})\right] & \mathbb{E}_{\boldsymbol{\theta}}\left[-\Delta_{\Re\{\mathbf{h}\}}^{\Re\{\mathbf{h}\}}\log p(\boldsymbol{\theta})\right] & \mathbb{E}_{\boldsymbol{\theta}}\left[-\Delta_{\Re\{\mathbf{h}\}}^{\Im\{\mathbf{h}\}}\log p(\boldsymbol{\theta})\right] & \mathbb{E}_{\boldsymbol{\theta}}\left[-\Delta_{\Re\{\mathbf{h}\}}^{\epsilon}\log p(\boldsymbol{\theta})\right] \\ \mathbb{E}_{\boldsymbol{\theta}}\left[-\Delta_{\Im\{\mathbf{h}\}}^{\boldsymbol{\theta}}\log p(\boldsymbol{\theta})\right] & \mathbb{E}_{\boldsymbol{\theta}}\left[-\Delta_{\Im\{\mathbf{h}\}}^{\Re\{\mathbf{h}\}}\log p(\boldsymbol{\theta})\right] & \mathbb{E}_{\boldsymbol{\theta}}\left[-\Delta_{\Im\{\mathbf{h}\}}^{\Im\{\mathbf{h}\}}\log p(\boldsymbol{\theta})\right] & \mathbb{E}_{\boldsymbol{\theta}}\left[-\Delta_{\Im\{\mathbf{h}\}}^{\epsilon}\log p(\boldsymbol{\theta})\right] \\ \mathbb{E}_{\boldsymbol{\theta}}\left[-\Delta_{\epsilon}^{\boldsymbol{\theta}}\log p(\boldsymbol{\theta})\right] & \mathbb{E}_{\boldsymbol{\theta}}\left[-\Delta_{\epsilon}^{\Re\{\mathbf{h}\}}\log p(\boldsymbol{\theta})\right] & \mathbb{E}_{\boldsymbol{\theta}}\left[-\Delta_{\epsilon}^{\Im\{\mathbf{h}\}}\log p(\boldsymbol{\theta})\right] & \mathbb{E}_{\boldsymbol{\theta}}\left[-\Delta_{\epsilon}^{\epsilon}\log p(\boldsymbol{\theta})\right] \end{bmatrix}, \tag{A.6}$$

where $\triangle_{\mathbf{y}}^{\mathbf{x}}$ represents the second-order partial derivative operator and $p(\boldsymbol{\theta})$ is the prior distribution of $\boldsymbol{\theta}$.

1) Computation of $\boldsymbol{\Xi}_{P_{11}} \triangleq \mathbb{E}_{\boldsymbol{\theta}}\left[-\Delta_{\boldsymbol{\theta}}^{\boldsymbol{\theta}} \log p(\boldsymbol{\theta})\right]$: From [128, eq.(19)], the $(N-1)\times(N-1)$ matrix $\mathbb{E}_{\boldsymbol{\theta}}\left[-\Delta_{\boldsymbol{\theta}}^{\boldsymbol{\theta}} \log p(\boldsymbol{\theta})\right]$ can be obtained as

$$\boldsymbol{\Xi}_{P_{11}} = \frac{-1}{\sigma_\delta^2}\begin{bmatrix} -1 & 1 & 0 & \cdots & 0 \\ 1 & -2 & 1 & 0 & \vdots \\ 0 & \ddots & \ddots & \ddots & 0 \\ \vdots & 0 & 1 & -2 & 1 \\ 0 & \cdots & 0 & 1 & -1 \end{bmatrix}. \tag{A.7}$$

2) Computation of remaining terms in (A.6): Since CFO is a deterministic parameter and no prior knowledge of $\mathbf{h}$ is assumed, thus

$$\boldsymbol{\Xi}_{P_{12}} = \boldsymbol{\Xi}_{P_{21}}^T = \mathbf{0}_{(N-1)\times L}, \tag{A.8}$$
$$\boldsymbol{\Xi}_{P_{13}} = \boldsymbol{\Xi}_{P_{31}}^T = \mathbf{0}_{(N-1)\times L}, \tag{A.9}$$
$$\boldsymbol{\Xi}_{P_{22}} = \boldsymbol{\Xi}_{P_{33}} = \boldsymbol{\Xi}_{P_{23}} = \boldsymbol{\Xi}_{P_{32}} = \mathbf{0}_{L\times L}, \tag{A.10}$$
$$\boldsymbol{\xi}_{P_{14}} = \boldsymbol{\xi}_{P_{14}}^T = \mathbf{0}_{(N-1)\times 1}, \tag{A.11}$$
$$\boldsymbol{\xi}_{P_{23}} = \boldsymbol{\xi}_{P_{32}}^T = \mathbf{0}_{L\times 1}, \tag{A.12}$$
$$\boldsymbol{\xi}_{P_{24}} = \boldsymbol{\xi}_{P_{42}}^T = \boldsymbol{\xi}_{P_{34}} = \boldsymbol{\xi}_{P_{43}}^T = \mathbf{0}_{L\times 1}, \tag{A.13}$$
$$\xi_{P_{44}} = 0. \tag{A.14}$$

Using the above results, the HIM in (6.9) can be evaluated, since $\mathbf{B}_{11} = \boldsymbol{\Xi}_{D_{11}} + \boldsymbol{\Xi}_{P_{11}}$, $\mathbf{B}_{22} = \boldsymbol{\Xi}_{D_{22}} + \boldsymbol{\Xi}_{P_{22}} = \boldsymbol{\Xi}_{D_{22}}$, $\mathbf{B}_{33} = \boldsymbol{\Xi}_{D_{33}} + \boldsymbol{\Xi}_{P_{33}} = \boldsymbol{\Xi}_{D_{33}}$, $\mathrm{b}_{44} = \xi_{D_{44}} + \xi_{P_{44}} = \xi_{D_{33}}$, $\mathbf{B}_{12} = \mathbf{B}_{21}^H = \boldsymbol{\Xi}_{D_{12}} + \boldsymbol{\Xi}_{P_{12}} = \boldsymbol{\Xi}_{D_{12}}$, $\mathbf{B}_{13} = \mathbf{B}_{31}^H = \boldsymbol{\Xi}_{D_{13}} + \boldsymbol{\Xi}_{P_{13}} = \boldsymbol{\Xi}_{D_{13}}$, $\mathbf{B}_{23} = \mathbf{B}_{32}^H = \boldsymbol{\Xi}_{D_{23}} + \boldsymbol{\Xi}_{P_{23}} = \boldsymbol{\Xi}_{D_{23}}$, $\mathbf{b}_{14} = \mathbf{b}_{41}^H = \boldsymbol{\xi}_{D_{14}} + \boldsymbol{\xi}_{P_{14}} = \boldsymbol{\xi}_{D_{14}}$, $\mathbf{b}_{24} = \mathbf{b}_{24}^H = \boldsymbol{\xi}_{D_{24}} + \boldsymbol{\xi}_{P_{24}} = \boldsymbol{\xi}_{D_{24}}$, and $\mathbf{b}_{34} = \mathbf{b}_{43}^H = \boldsymbol{\xi}_{D_{34}} + \boldsymbol{\xi}_{P_{34}} = \boldsymbol{\xi}_{D_{34}}$.

A.2 Derivation of the mean and covariance matrix in (6.6)

Given $\mathbb{E}\{\mathbf{w}_R\} = \mathbf{0}_{N\times 1}$ and $\mathbb{E}\{\mathbf{w}_{D,2}\} = \mathbf{0}_{N\times 1}$, the mean of the received signal in (6.6), $\boldsymbol{\mu}_{\mathbf{y}_{D,2}}$, is calculated as

$$\begin{aligned}\boldsymbol{\mu}_{\mathbf{y}_{D,2}} &= \mathbb{E}\big\{\mathrm{q}_1\mathbf{E}_{S,R,D}\mathbf{P}_{S,R,D}\mathbf{F}^H\mathbf{D}_S\mathbf{F}_{(2L-1)}\mathbf{h}_{S,R,D} \\ &\quad +\mathrm{q}_2\mathbf{E}_{R,D}\mathbf{P}_{R_2,D}\mathbf{F}^H\mathbf{H}_{R,D}\mathbf{F}\mathbf{w}_R + \mathbf{w}_{D,2}\big\} \\ &= \mathrm{q}_1\mathbf{E}_{S,R,D}\mathbf{P}_{S,R,D}\mathbf{F}^H\mathbf{D}_S\mathbf{F}_{(2L-1)}\mathbf{h}_{S,R,D}. \end{aligned} \tag{A.15}$$

The covariance matrix, $\boldsymbol{\Sigma}_{\mathbf{y}_{D,2}}$, as

$$\begin{aligned}\boldsymbol{\Sigma}_{\mathbf{y}_{D,2}} &= \mathbb{E}\big\{(\mathbf{y}_{D,2} - \boldsymbol{\mu}_{\mathbf{y}_{D,2}})(\mathbf{y}_{D,2} - \boldsymbol{\mu}_{\mathbf{y}_{D,2}})^H\big\} \\ &= \mathrm{q}_2^2\mathbf{E}_{R,D}\mathbf{P}_{R_2,D}\mathbf{F}^H\mathbf{H}_{R,D}\mathbf{F}\ \mathbb{E}\{\mathbf{w}_R\mathbf{w}_R^H\}\ \mathbf{F}^H\mathbf{H}_{R,D}^H\mathbf{F}\mathbf{P}_{R_2,D}^H\mathbf{E}_{R,D}^H \\ &\quad + \mathbb{E}\{\mathbf{w}_{D,2}\mathbf{w}_{D,2}^H\} \\ &= \mathrm{q}_2^2\sigma_w^2\mathbf{E}_{R,D}\mathbf{P}_{R_2,D}\mathbf{F}^H\mathbf{H}_{R,D}\mathbf{H}_{R,D}^H\mathbf{F}\mathbf{P}_{R_2,D}^H\mathbf{E}_{R,D}^H + \sigma_w^2\mathbf{I}_N \\ &= (\mathrm{q}_2^2\sigma_w^2\sigma_h^2 + \sigma_w^2)\mathbf{I}_N, \end{aligned} \tag{A.16}$$

where $\mathbb{E}\{\mathbf{H}_{R,D}\mathbf{H}_{R,D}^H\} = \sigma_h^2\mathbf{I}_N$, $\mathbf{F}^H\mathbf{F} = \mathbf{I}_N$, $\mathbf{P}_{R_2,D}\mathbf{P}_{R_2,D}^H = \mathbf{I}_N$ and $\mathbf{E}_{R_2,D}\mathbf{E}_{R_2,D}^H = \mathbf{I}_N$.